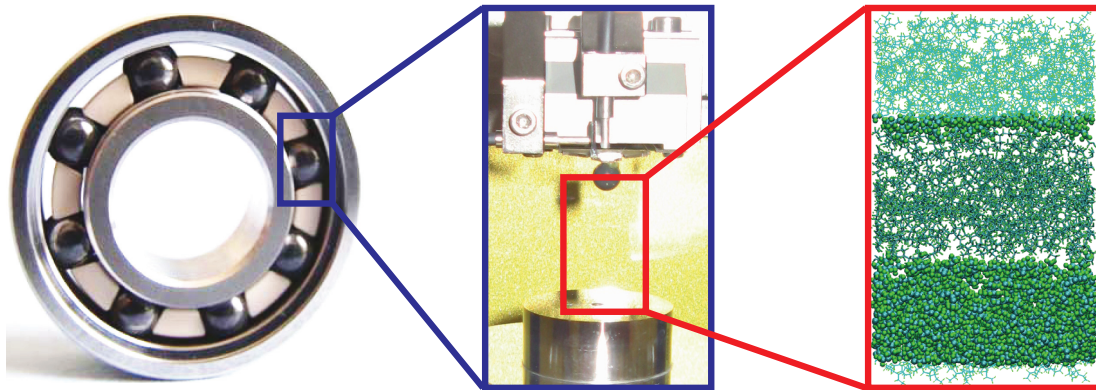


Experimental and Computational Investigation of the
Influence of a Plasma-Enhanced Chemical Vapor Deposition
Amorphous Carbon Fluorine Coating on
Sliding Friction in Hybrid Ball Bearings



Doctoral Thesis by
Markus Rullich

Bremen, October 2012

**Experimental and Computational Investigation of the
Influence of a Plasma-Enhanced Chemical Vapor Deposition
Amorphous Carbon Fluorine Coating on
Sliding Friction in Hybrid Ball Bearings**

Dissertation
zur Erlangung des Grades
Doktor der Naturwissenschaften
Dr. rer. nat.

dem Fachbereich Physik
der Universität Bremen

vorgelegt von
Dipl.-Chem. Markus Rullich
aus Willich

Bremen, Oktober 2012

Erstgutachter: Prof. Dr. Thomas Frauenheim
Zweitgutachter: Prof. Dr. Lucio Colombi Ciacchi

Πρόλογος

“God made the bulk; surfaces were invented by the devil.”

– *Wolfgang Pauli*

While the *bulk* properties of a material can often be described by macroscopic continuum models, the *surfaces* elude general description, because they are highly dependent on the surrounding of a body. The *bulk* of a material also most of the times retains its properties under application conditions, while the *surface* properties may change drastically. Yet the surface properties are highly important for scientific and engineering applications. All chemical catalysis e.g. solely occurs at the surface of the catalytic material. And regarding engineering applications, surface properties e.g. are important for friction, either the minimization or maximization of friction.

Focusing on the minimization of friction, this doctoral thesis is based on work that has been carried out in the framework of the project NANODYN (“Nano-Dynamik tribologischer Paarungen auf plasmastrukturierten Oberflächen und deren Herstellung”). This interdisciplinary project of industry corporations, a Fraunhofer Institute and our university center for computational materials science has been funded by the German Federal Ministry of Education and Research (BMBF). One aim of the project NANODYN was the development of a plasma surface coating for application to hybrid ball bearings, consisting of ceramics balls and steel rings. The coating was meant to reduce the friction moment occurring in the bearing applications. The desired application of these enhanced bearings, which even unmodified offer reduced friction and wear compared to standard steel bearings, is the food and drug industry, the first envisaged application being filling lines. In filling lines the lubrication of a bearing with aqueous media is very common, which is the reason, why the focus of the devoted efforts was on enhancing the tribological properties under water lubrication conditions.

In addition to the design of tribological experiments on sliding friction, computer simulations were planned to be able to depict and gain a deeper understanding of the processes at the molecular level. Consequently, the work underlying this thesis is spread over the part of physics behind the improvement of an engineering component, which is studied experimentally and computationally. This is the reason why the introduction of this thesis tries to cover all aspects of general importance with respect to simulations and experiments on friction in ball bearings, without going into too much detail.

The interdisciplinary scope of this text is also the reason for a comprehensive list of the used abbreviations as well as short explanations of terms, which the reader might not be familiar with, because his / her background is different from the one that is optimal for some sections of this thesis. Furthermore, the meaning of some words with engineering background needs to be defined, because the same word has different meanings for different authors.

This thesis contains three parts, the first part is the introduction, which informs the reader on the topics of friction, contact, plasma surface coating and molecular dynamics simulations. The topic of part II is the presentation of the experimental approach and its results as well as the discussion of the experimental results. Furthermore, in part III the simulation approach including model development followed by computational results and discussion are elaborated on.

Markus Rullich

Bremen, October 2012

Table of Contents

Table of Contents	III
Abbreviations and Nomenclature	VII
I. Introduction	1
1. Friction	4
1.1. Friction in Ball Bearings	6
1.2. The Dependence of Static Friction on the Stationary Time	11
1.3. The Dependence of Kinetic Friction on the Relative Velocity	11
1.4. The Stick-Slip Phenomenon	12
1.5. Friction Measurements	14
2. Contact	17
2.1. The Area of Contact	17
2.2. Load and Deformation	19
2.3. Lubrication	23
2.4. The Squeeze-Out of Lubricant	26
3. Plasma Surface Coating	29
3.1. Chemical Vapor Deposition	29
3.2. Plasma Properties	30
3.3. Plasma-Enhanced Chemical Vapor Deposition	32

4. Classical Force Field Simulations	37
4.1. From Quantum Mechanics to Force Fields	37
4.2. Non-bonded Particle Interactions	40
4.3. Bonded Particle Interactions	41
4.4. Force Field Parameters	42
4.5. Periodic Boundary Conditions	43
4.6. Exact Electrostatics Calculation	45
4.7. Molecular Dynamics	45
4.8. Virtual Spring Pulling	47
4.9. Barostat and Thermostat	48
II. Experimental Investigations	51
5. Experimental Details	53
5.1. Hybrid Ball Bearing Part Coating	53
5.1.1. PECVD a-C:F:H Coating Process	53
5.1.2. Coating Thickness Analytics	53
5.1.3. Chemical Analysis of the Film by XPS	54
5.2. Tribometry	54
5.2.1. Chemicals and Materials	54
5.2.2. Experimental Procedure	55
5.2.2.1. Preparation	55
5.2.2.2. Procedure	57
6. Experimental Results	58
6.1. Coating Analytics Results	58
6.1.1. Coating Thickness	58
6.1.2. Chemical Analysis of the Coating	58
6.2. Tribometry Results	59
6.2.1. Experiments Without Lubrication	60
6.2.2. Experiments with Water Lubrication	61
6.2.3. Experiments with PFPE Lubrication	63

7. Discussion of the Experimental Results	65
8. Conclusions of the Experiments	67
III. Computational Investigations	68
9. Computational Details	75
9.1. Material Models	75
9.1.1. a-C:F Coating Model	75
9.1.2. α -Cristobalite Silicon Dioxide Model	77
9.1.3. PFPE Oil Krytox [®] GPL 104 Model	78
9.2. Simulation Details	85
10. Results and Discussion	90
10.1. The Influence of the Perpendicular Force	90
10.2. The Influence of the Water Layer	101
10.3. The Influence of the Temperature	106
10.4. The Influence of the Sliding Velocity	110
11. Conclusions of the Simulations	116
IV. Summary and Outlook	119
12. Summary	120
13. Outlook	122
14. Acknowledgement	124
References	125
V. Appendix	133
List of Figures	134

List of Tables	144
A. Additional Background	145
A.1. Energy Minimization	145
B. Experimental Results Tables	147
B.1. No Lubrication	147
B.2. Water Lubrication	149
B.3. PFPE Lubrication	152
C. Computational Results Tables	155
C.1. Varying Perpendicular Pressures	155
C.2. Varying Perpendicular Force	166
C.3. Varying Water Layer Thicknesses	179
C.4. Varying Temperatures	183
C.5. Varying Relative Velocities	193

Abbreviations and Nomenclature

α	degree of ionization, ratio of volume electron density to sum of vol. electron density and vol. neutral species density
a-C:F:H	fluorine-containing amorphous hydrogenated carbon, amorphous carbon coating containing a lot more fluorine than hydrogen
a-C:H	amorphous diamond-like hydrogenated carbon, result of a coating process using a carbonaceous precursor that contains hydrogen
a-C	amorphous carbon, result of a PECVD coating process with a carbon source precursor
A_0	apparent area of contact
AES	Auger electron spectroscopy, detecting electrons emitted by rearrangement of electrons after x-ray ionization (Auger effect)
AFM	atomic force microscope, a scanning probe microscope employing atomically sharp tips to determine forces
apparent area of contact	area of contact between two bodies, in which contact possibly occurs but not necessarily does occur
A_{real}	real area of contact
asperity	spot in a surface protruding above the average surface level
average surface level	the average height of a surface, featuring hills, asperities, on top and lower lying valleys, corrugations
axial load / force	force acting along the bearing radius, pressing inner ring and balls together as well as balls and outer ring
BFGS	Broyden–Fletcher–Goldfarb–Shanno method for nonlinear optimizations, employed for energy minimizations

BO	Born-Oppenheimer
boundary lubrication friction	friction under boundary lubrication conditions, quasi-solid lubricant may separate the friction partners
boundary lubrication	lubrication state between surfaces separated by at most a few monolayers of lubricant, which is in a quasi-solid state
box	the simulation volume in molecular dynamics simulations is often referred to as box
Brownian motion	the random movement of molecules solely due to temperature, not because of external forces acting on the particles
CCD	charge-coupled device, electronic light sensor converting light intensity to measurable voltage
charge group	a group of atoms that has a net zero charge, which is considered for electrostatic interactions always as a whole
COF	coefficient of friction, the proportionality constant giving the friction force as function of the normal force
cold-welded junctions	chemical bonds formed between the friction partner asperities, resulting in significant wear
COM	center of mass of a body or system
commensurability	structural likeness of surface profiles, asperities and corrugations may interlock in case of commensurability
component	part of a machine or assembly
creep	the slow rearrangement of atoms, decreasing elastic energy and resulting in plastic deformation
CVD	chemical vapor deposition, creation of coatings by bringing reactive precursor molecules together in proximity of a substrate
δ_{ij}	Kronecker δ , 1 for $i = j$, 0 else
direct contact	direct contact of two bodies without anything between the two
DLC	diamond-like carbon, coating deposited using carbonaceous precursors resulting in sp^3 carbon networks similar to diamond

dry running	operation of a bearing in the absence of lubricant
Δt	time step of a molecular dynamics simulation
ϵ	depth of a Lennard-Jones interaction potential
ϵ_0	the permittivity of vacuum
E	elastic modulus of a material
ϵ_r	the relative permittivity of a material
ESCA	electron spectroscopy for chemical analysis, analyzing the electrons ejected from the specimens by X-rays, also called XPS
F	force
fatigue	the degradation of material integrity, leads to machine failure e.g. by fatigue cracks and finally fracture
FDA	Food and Drug Administration, United States official organization for regulation of food and drugs
F_F	friction force, the force necessary to initiate or perpetuate movement
FF	force field, set of parameters for molecular dynamics simulations
F_N	normal force, the force acting normal to the sliding interface, often called load
force field	empirically determined set of potential parameters for atom-atom interactions to be used in molecular dynamics simulations
Fraunhofer IGB	Fraunhofer Institut für Grenzflächen- und Bioverfahrenstechnik, Stuttgart, Germany
g	gravitational acceleration
H	Hessian matrix of the second derivatives
HDD	hard disk drive, the most common magnetic data storage device in computers

Hertz contact stress	the high stress occurring in the contact area, if two bodies are pressed against each other
hybrid (ball) bearing	(ball) bearing consisting of two steel rings and ceramics balls
hydrodynamic friction	friction resulting from the resistance a liquid poses to bodies moving through the liquid
junction	single spot of direct contact between surface asperities
k	spring constant or force constant of a spring
k_B	Boltzmann constant
kinetic friction	The resistance a moving body poses to the perpetuation of movement
L-BFGS	low-memory BFGS, modified Broyden–Fletcher–Goldfarb–Shanno geometry optimization method using low amounts of memory
lubricant	substance of varying viscosity which makes the friction surfaces slippery, reducing wear and friction
m/z	mass to charge ratio, the x-axis unit of a mass spectrum using time-of-flight detection
MALDI	matrix assisted laser desorption ionization, a method for carefully ionizing macromolecules stabilized in a matrix of photosensitizer
MD	molecular dynamics, simulation approach based on integrating Newton's equation of motion
M	molar mass of a particle
m	mass of the body
μ	coefficient of friction (COF), the proportionality constant giving the friction force as function of the normal force
μ_{kin}	kinetic coefficient of friction (COF)
μ_{static}	static coefficient of friction (COF)
MW	micro wave

n_0	volume neutral species density in a plasma
NANODYN	BMBF-funded industry-related project: Nano-Dynamik tribologischer Paarungen auf plasmastrukturierten Oberflächen und deren Herstellung
n_e	volume electron density in a plasma
NEAT	no addition of lubricant to the tribological system
NMR	Nuclear Magnetic Resonance, often also used as abbreviation for the respective spectroscopy
$n_{T/p}$	thermostat or barostat time step interval integer
ν	Poisson number of a material
ω	eigenfrequency of a system, here the oscillation of stick-slip motion
part	shaped piece of material, part of a component
PECVD	plasma-enhanced chemical vapor deposition, chemical vapor deposition enhanced by a reactivity increase of the precursor induced by plasma
PEEK	Polyether ether ketone, thermoplastic polymer, offering good mechanical properties for a polymer as well as high thermal and chemical resistance
PFPE	perfluoro-polyether, high-performance lubricant, chemically inert and not toxic, approved for direct food contact
pinning	surface asperities clamp one or more lubricant molecules and force them to move along during the sliding process
precursor	a molecule that forms a coating on the desired substrate
PTFE	polytetrafluoroethylene, polymer made almost completely from CF_2 -moieties
\dot{o}	first differentiation with respect to time of the observable o
\ddot{o}	second differentiation with respect to time of the observable o

r	interatomic distance, vector if bold font, absolute value if normal font
real area of contact	sum of junction areas, only a small fraction of the apparent area of contact
REBO	recative empirical bond order, reactive force field approach by Brenner [1]
RF	radio frequency
rolling resistance	The resistance a body poses to the initialization or perpetuation of rolling
R	universal gas constant
σ	stress, pressure acting on a body
σ_0	von Mises yield criterion, if elastic energy per unit volume overcomes this threshold, deformation gets plastic
SAM	self-assembled monolayer, formed by molecules from the solution without external driving force
σ_c	critical stress, yield stress, above which a material yields plastically to interaction
sliding friction	by interaction of sliding bodies, directly or mitigated by lubricant, resistance to movement is created
σ_{LJ}	r-axis intersection of a Lennard-Jones interaction potential
static friction	The resistance a resting body poses to the initialization of movement
Stribeck curve	rotation-speed- and lubricant-viscosity-dependent determination of the bearing friction moment, named after Richard Stribeck
T	temperature
TOF	time-of-flight, a mass analyzer used for the determination of the mass of particles
tribology	the science on friction, wear and connected fields
t	time

$\tau_{T/p}$	thermostat/barostat time constant for the exponential decay of the difference between current and target value
united atom representation	common approach to reduce the computational effort in molecular dynamics simulations by uniting atoms of a subgroup, e.g. CH ₃ , into a superatom
v	velocity
V_C	Coulomb potential between two point charges
V_{LJ}	Lennard-Jones interaction potential to model the repulsive and attractive particle interactions
wear	slow process of component destruction e.g. by ripping out material, forming debris or transferring it to the other friction partner
x	the position of the center of mass of the body
XPS	X-ray photoelectron spectroscopy, analyzing the electrons ejected from the specimens by X-rays, also called ESCA



Part I.

Introduction

The history of human technological progress is closely intertwined with the utilization or overcoming of friction. The first tools to ignite a fire utilized the heat generated by friction between a spinning and a static piece of wood. Another breakthrough in human technology was the invention of the wheel, which overcomes friction in the sense that the sliding friction while simply dragging a load, is substituted with the considerably smaller sliding friction at the connection of wheel and axle plus the comparatively minuscule rolling resistance. Utilizing the low rolling resistance, roller bearings reduce friction at the wheel axle connection. Hence bearings facilitate rotation of two bodies against each other, thereby conserving energy because of reduced loss in the form of generated heat. Ball bearings have been developed to the point, where roller and ball bearings are omnipresent.

The general shape of bearings and their parts has been optimized for various purposes, while the specific geometry of the components is subject of the bearing engineering of the bearing manufacturer. Nowadays, bearings that are specialized for the intended application, offer optimized geometrical and *bulk* material properties. However, one *surface* problem is wear, leading to bearing failure under operation conditions and thus machine break-down. Wear is the slow process of mechanical destruction of a bearing starting at the surfaces of the friction partners. One wear mechanism that is dominant in standard steel ball bearings is the formation of so-called “cold-welded junctions”, the formation of chemical metal-metal bonds between the two friction partners [2]. Cold-welded junctions result in ripping out material from one friction partner and transferring it to the other, usually harder partner. Additionally debris may be formed, which often increases friction, but sometimes decreases friction by forming another miniaturized ball bearing in the interface region between the friction partners.

To prevent the formation of cold-welded junctions and drastically reduce wear, ceramics balls have been introduced. In addition to the wear reduction because no cold-welded junctions occur, the elastic modulus of ceramics balls is higher, resulting in less deformation under load and thus less rolling resistance. The resulting bearing made from steel rings and ceramics balls is referred to as “hybrid bearing” and the increase in performance is accompanied by an increase in price. However, still the more cost-intensive bearings may be cost-efficient, because not only the maintenance intervals are enlarged but also break-down becomes less probable, which both reduce the shutdown time of production lines. Even if the bulk material properties of a hybrid ball bearing are optimized for the application in a bearing, improvement of the component performance is still possible, because the surface properties can be tailored nowadays employing surface coating processes. In ball bearings surface properties are relevant on the one hand regarding the direct friction of the two friction partners, and on the other hand for the wetting of a surface with lubricants.

Lubrication, the wetting of sliding surfaces with a special substance to reduce friction, is a very old technique. Already in ancient Egypt the construction of the pyramids was facilitated by pouring lubricant in front of the huge stone blocks that were dragged to the building site [2]. Before the advent of chemical technology, lubricants have been mostly natural oils, either plant oils like olive oil or lard oil made from pig fat, but also whales have been killed to obtain sperm oil, a potent, low-viscosity lubricant [2]. Today progress in chemistry allows for specialized lubricants, containing mainly synthetic and mineral oils and additives, e.g. corrosion protective substances like sodium nitrite. Special high-performance but also high-price lubricants include polymer molecules containing only carbon, oxygen and fluorine. The composition of the perfluoro-polyethers (PFPE) renders them chemically unreactive, inert, as well as nontoxic, which is why these lubricants are approved for direct food contact. Depending on the viscosity of the product, technical lubricants are referred to as oils or fats, if thickeners have been added. The higher the viscosity of the lubricant, the higher the resistance it poses to a body moving through the lubricant. Consequently, lower viscosity lubricants, which means oils compared to fats, would be preferable. However, with increasing speed the wetting of the interacting surfaces with lubricant breaks down the faster, the lower the lubricant viscosity is. Resulting from this interplay, the optimal lubricant has to be chosen depending on the desired application of the bearing.

Since the geometry of a ball bearing is very complex, and this complex component contains different parts, there are several different contributions to the overall resistance to movement posed by a bearing, the so-called friction moment. The classification of different friction states, the detailed discussion of the composition of a bearing and the friction moment contributions will be discussed in the next sections of this chapter. Furthermore, general tendencies for the dependence of the friction on two parameters, stationary time and velocity, will be discussed in the subsections that follow after, as well as the stick-slip phenomenon, which occurs in everyday life. Finally, common approaches to determine the magnitude of friction will be discussed in the last section on friction measurements.

1. Friction

Friction is a phenomenon that is immensely important for the industry and also relevant in every-day life. Sometimes the aim of the science on friction, the tribology, is the reduction of friction, e.g. in case of the bearing in a wheel suspension, where no energy loss at all would be ideal. However, also sometimes the maximization of friction is desired, for example in the contact of car tire with the road upon braking or accelerating. Beyond the pure magnitude of friction and the connected energy loss, the natural scientist is interested in principles and predictions. Regarding the principles of friction, the first step is the classification of different friction states. Generally, there are three friction types relevant for a ball bearing[2]:

1. Static friction

The resistance a resting body poses to the initialization of movement.

2. Kinetic friction

The resistance a moving body poses to the perpetuation of movement.

3. Rolling resistance

The resistance a body poses to the initialization or perpetuation of rolling.

While the static and kinetic friction are different in most of the cases, the difference between “static” and “kinetic” rolling resistance is negligible and usually not explicitly considered.

In connection of kinetic friction with lubrication of sliding interfaces, there are three main lubrication states that are defined in tribology [2]:

1. Hydrodynamic friction

In case of hydrodynamic friction the surfaces of the two friction partners are truly separated by a lubricant film. No direct contact between the surfaces occurs, meaning that there is nothing in between the two bodies. Considering one body as static and the other body as moving relatively to the other, the resistance to the movement is resulting from the lubricant viscosity. If the body is not rotational symmetric, a slight tilting of the body may occur and the buoyancy resulting from movement and tilt angle will conserve the separation of the bodies.

2. Sliding friction

If a normal force F_N , often called load, is acting on the moving body, and this force overcomes the buoyancy, the bodies will come into contact. Resultantly, at some spots on the surface that protrude, which are called asperities, the bodies will be close but without direct contact. However, still the lubricant separates the bodies from each other, and the lubricant molecules are in a liquid state. Yet even without direct contact the bodies interact with each other, either by direct, e.g. electrostatic, interactions of the atoms or mitigated by the lubricant molecules. This interaction poses additional resistance to relative movement.

3. Boundary lubrication friction

Once the normal force is sufficient to squeeze out lubricant from between the asperities, and only few monolayers remain between the sliding bodies, the boundary lubrication regime is reached. In this regime there is direct contact between some of the surface asperities accompanied by the transition of the lubricant molecules into a quasi-solid state, in which the mobility of the molecules is drastically decreased compared to the liquid state. The smaller the molecules, the less perpendicular pressure is necessary to initiate the squeeze-out of a monolayer [3].

Having classified the different friction states, the following step is to note the laws of friction that lay the foundation of predictions. The first tribological studies date back to Leonardo da Vinci, the universal genius living from 1452 to 1519. In addition to friction experiments, da Vinci invented bearings that contained rolling elements [2], thus he is the inventor of roller bearings. One of the successors to da Vinci in the field of systematic tribological studies was Charles Augustin Coulomb (1736-1806). Coulomb conducted experiments regarding the dependence of friction on the materials in contact, the area of contact, normal force, time of stationary contact and ambient conditions. Finally Coulomb arrived at the general friction law, using the friction force F_F , the normal force F_N and the so-called coefficient of friction (COF) μ :

$$F_F = \mu \cdot F_N \tag{1.1}$$

In ordinary cases the COF is a material constant for a given pairing of materials in a given lubrication state. The limitations of this general relationship are: not too high or too low velocities as well as not too high or too low surface roughnesses. The above displayed equation (1.1) states, that there is a linear dependence of the friction force on the normal force.

Having elucidated the different friction states, the geometrical complexity of the bearing component and its parts is the reason, why all of the friction states discussed above are relevant for the overall bearing friction moment, as will be discussed in the next section.

1.1. Friction in Ball Bearings

To be able to name all the different friction interactions in a ball bearing, the different parts of the bearing have to be named and illustrated.

A ball bearing consists of two rings, which are connected to the two bodies which shall rotate relatively to each other on a stable axis. Additionally, as the name ball bearing implies, balls are present to facilitate this rotation by substituting sliding friction with the drastically smaller rolling resistance (very simply put, as we will see hereafter). In some, but not all, bearings a spacer called “cage” is another bearing part that is employed to prevent the direct contact of balls. The bearing parts are illustrated in figure 1.1. The cage exhibits holes, in this case eight, in which the balls reside after assembly. These holes are referred to as pockets, and in this case they are constructed in the open shape, while the closed form exists, too. The concave part of the rings, at which contact of balls and ring occurs is called “track”, and in figure 1.1 the tracks of inner and outer ring are colored blue. The different parts are assembled to a component, the bearing, which in this case is a DIN 623 type 6001 ball bearing. There are two different types of bearings concerning the permanence of the assembly: on the one hand self-retaining bearings and on the other hand not self-retaining bearings, which fall apart if a lateral force acts on the bearing. The type 6001 hybrid ball bearing is the subject of the NANODYN project, part of which the work underlying this thesis was, and is a self-retaining bearing. The assembled type 6001 hybrid ball bearing comprising steel rings, polyether ether ketone (PEEK) cage and silicon nitride balls is shown in figure 1.2.

After the parts of the bearing have been named and illustrated, the next step is the consideration of the contact and friction states between the bearing parts under application conditions. First of all, when a bearing rotates there is an axial force acting on the bearing, e.g. the weight of a car that acts on the bearings in the wheel suspensions. The axial force presses the inner ring in the direction of the weight force against the balls, and thus the balls in that region against the outer ring. Resultantly, at the tracks there is a high pressure associated with the load application, because the area of the ball track interaction is very small. The high pressure is named “Hertz contact stress” after the famous work by Heinrich Hertz (1857-1894) “Über die Berührung fester elastischer Körper” (“On the contact of rigid elastic solids”)[5, 6]. Resulting from the magnitude of this pressure, the lubricant molecules that are trapped between the track and the ball are firstly few because of the squeeze-out, and secondly the molecules enter a quasi-solid state due to the high pressure. Consequently the interaction between ball and track is subject to boundary lubrication friction. Furthermore, under rotation the balls move with half the angular velocity of the turning wheel, which results in interaction of the

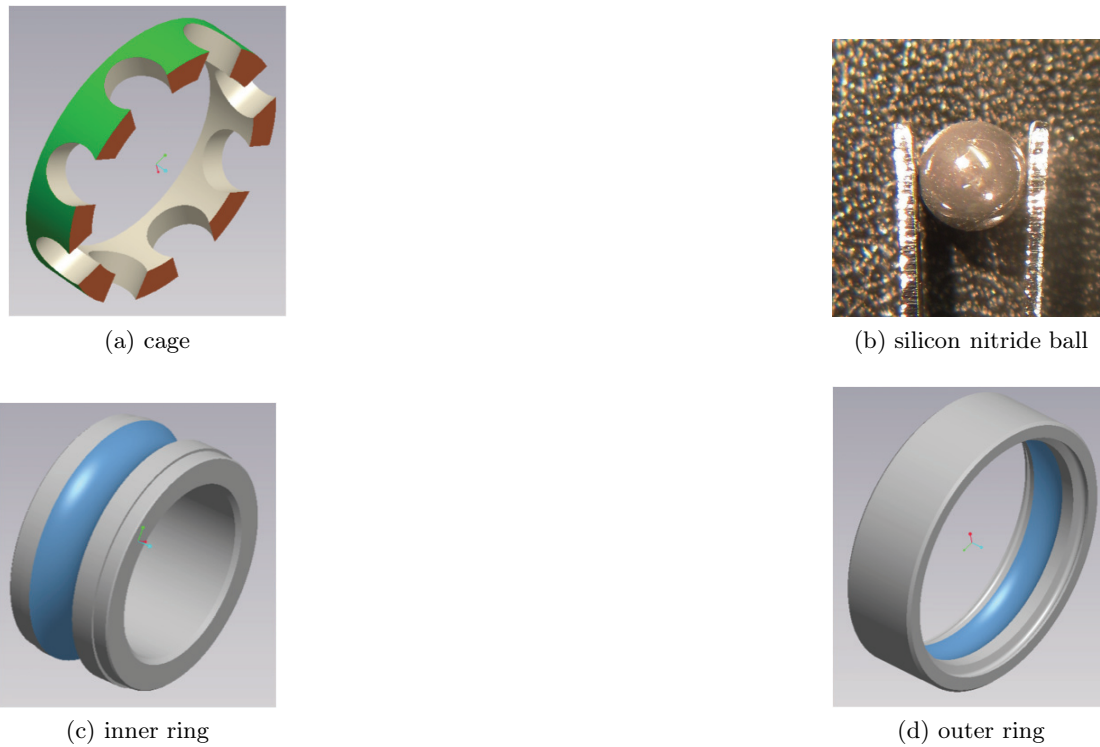


Figure 1.1.: Bearing parts: cage (a)[4], silicon nitride ball (b), inner ring (c)[4] and outer ring (d)[4] and. The ball tracks on the rings (c,d) are highlighted in blue.



Figure 1.2.: Assembled type 6001 hybrid ball bearing comprising a polyether ether ketone (PEEK) cage and eight silicon nitride balls of the diameter 4.763 mm. The bearing steel employed for the inner and outer ring is X30CrMoN 15 1, from ref. [4].

balls with the cage at the side of the pocket in the direction of movement. The pressure at the ball cage interaction is considerably smaller than the Hertz stress at the ball track interface. Yet, depending on the rotation speed, the pressure will become large enough to bring this interaction into the regime of sliding friction. The sliding friction regime of the ball pocket interaction is relatively easily reached, because the radius of curvature of a usual ball is small, and thus at a given force, the pressure in the region of interaction is large. In addition to the first two of the three different interaction states of lubricated friction, also the last one occurs in a bearing under normal conditions: If a bearing is lubricated, the balls move through the lubricant due to the bearing rotation and to some extent without further interaction with solid bodies, e.g. at the openings of open cage pockets. This results in hydrodynamic friction, whose magnitude solely depends on the viscosity of the lubricant and the rotation speed. Additionally the movement of the cage produces lubricant friction. Another contribution to the overall friction moment is the interaction of the cage with the inner ring, which is true sliding friction and is relevant not because of high pressure but because of the large interaction area.

In addition to the interactions of the bearing parts, the rolling resistance of the balls is another factor contributing to the overall friction moment. Depending on the Hertz stress, the balls are flattened by the normal force, because the elastic modulus of any real material is finite. Of course for lower elastic modulus materials, like e.g. steel, the effect is even more pronounced than for ceramics balls. However, nonetheless the contribution is an important contribution, and in addition to that gives rise to sliding friction at the ball track interface: An ideal ball with infinite elastic modulus would not be flattened, thus roll ideally and there would not be any sliding friction in the boundary lubrication regime. Consider a point on the surface of a real ball made from a real material with finite elastic modulus. Starting in a horizontal position the point has a given track speed. Moving towards the surface, the velocity has to decrease, because the flattening reduces the distance the point has to move while maintaining the same *angular* velocity. Moving away from the surface, the same point has to make up for the lost distance, compared to the point where it ideally would be, so the track velocity has to be larger than ideally. The only possibility for the point to reach the ideal position is a limited *slip* instead of rolling of the ball. The sliding speed due to slip is normally very slow, in the order of 1% of the ball velocity [2].

This slip at the ball track interface is a relevant contribution to the overall friction moment. Since it is sliding friction of two surfaces relatively to each other under boundary lubrication conditions, this friction can be calculated by computer simulations.

The respective magnitudes of the different contributions to the overall bearing friction moment certainly vary. The fractions not only depend on the materials the bearing parts are made from, but also on the application conditions, meaning ambient conditions, axial

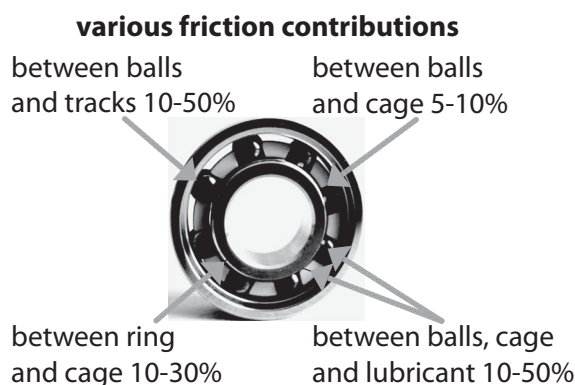


Figure 1.3.: Illustration of the various contributions to the overall bearing friction moment and their relative magnitude.

load, rotation speed and lubrication. Nonetheless in figure 1.3 an attempt is made to illustrate the contributions to the overall bearing friction moment in a type 6001 hybrid ball bearing and their relative magnitude. The percentages of the different contributions do not add up to 100% and the ranges given are rather broad. The reason for the varying fractions is the complexity of the friction in the bearing that has been discussed, and with varying pressure and varying rotation speed the percentages vary for the same bearing and the same lubrication. This behavior was investigated by Richard Stribeck (1861-1950) and the graphs resulting from the investigation are named after him “Stribeck curves”.

Regarding the hybrid ball bearing, the three-dimensional development of the bearing friction moment is depending on rotation speed times lubricant viscosity as well as axial load presents itself in the way schematically depicted in figure 1.4. Three main effects contribute to the overall friction moment [4, 7]: The first is the lubricant friction shown at the bottom, which is only dependent on the rotation velocity and the viscosity of the lubricant. Under low axial load conditions the lubricant friction contribution is the same as for high axial loads. Furthermore, the higher the rotation speed, the higher the lubricant friction, but the rotation speed of a bearing is determined by the application, and because of not being made from metal and more robust, ceramics balls are designed for high speeds. The second contribution, which is solely determined by the axial load, is the sliding friction. This includes all the sliding friction states as well as all the possible contributions to the sliding friction shown in figure 1.3. Since this friction is load dependent, this is the main contribution under hybrid ball bearing application conditions for the most part. Hybrid ball bearings are designed for high axial loads, because the high elastic modulus of the ceramics is of advantage as well as the absence of cold-welded junctions, which reduces wear compared to steel bearings. Furthermore the slip of the ball creates the largest part under high load conditions, because this part increases with axial force while ring-cage-interactions and ball-cage-interactions are nearly independent

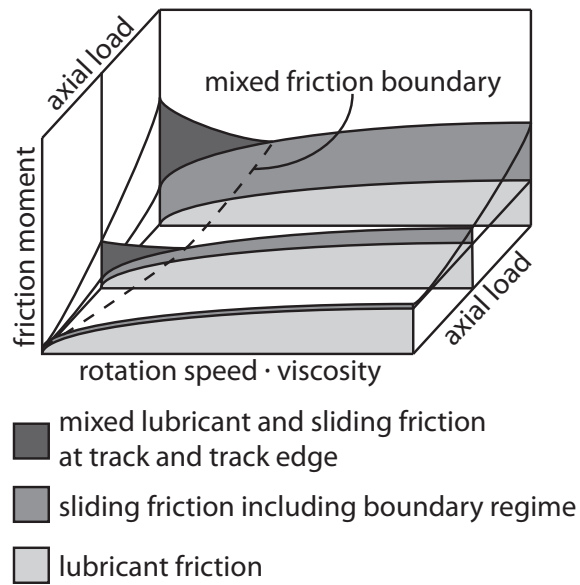


Figure 1.4.: Three-dimensional schematic representation of the development of Stribeck curves for increasing axial load as well as the product of viscosity and relative velocity. The three main different contributions are sketched and the mixed lubrication boundary is depicted as black line. Scheme following references [4, 7].

of the load. The last contribution is the mixed friction. Mixed friction is the contribution resulting from incomplete wetting of the surfaces, which increases with increasing axial load and reaches drastic levels sometimes. Caused by the slow rotation, the squeeze-out (cf. section 2.4) has enough time to be total, resulting in direct contact of ball and track (cf. sections 2.1 to 2.3). Furthermore the slow rotation speed allows for ball rocking in the track, resulting in contact with the track edges. High-price hybrid ball bearings usually are operated under extreme conditions, because here they really pay off, in the truest sense of the word. Consequently the operation conditions are: mixed friction, due to less lubrication or even dry running, high axial loads and high rotation speeds or lots of start-stop-cycles. All these applications would be extremely wear-intensive employing standard steel bearings. Being at the upper load end of the graph in figure 1.4, on the very left or the very right, in both cases the sliding friction is dominant, because it is load dependent. This dominance is the reason, why not only the sliding friction of the ball due to slip is the only contribution to the overall bearing friction moment that can be simulated, but also it is the only constantly important contribution over the whole range of application conditions.

Beyond the different contributions to the kinetic friction in a ball bearing, each bearing motion will begin at some point, and the dependence of the initial static friction on the stationary time, the time a tribological system has been at rest before motion initiation, will be discussed in the following section.

1.2. The Dependence of Static Friction on the Stationary Time

Already Coulomb carried out measurements on the dependence of the static friction force on the stationary time, the time a system rested before motion was initiated by an external force [2]. As reported in the very recommendable and comprehensive monograph “Sliding Friction - Physical Principles and Applications” by Bo N. J. Persson [2], Coulomb arrived at the conclusion, that the initial static friction depends on the stationary time in an exponential way with a very small exponent (at least for oak wood sliding on oak wood). In fact, the dependence is a logarithmic one [2]. Since a complete analysis of the reasons goes beyond the scope of this text and requires a detailed understanding of the chapters to come (sections 2.1 and 2.2), at this point the following remarks shall suffice:

1. The longer friction partners are in stationary contact, the more the surfaces adapt to the other surface.
2. The more the surfaces adapt to each other, the more the surfaces interlock and the stronger the surfaces stick to each other.
3. The stronger the surfaces stick to each other, the higher the static friction.

Resultantly, the longer the friction partners are in stationary contact, the higher the static friction. Furthermore not only the static friction obeys to the relevant dependence on the stationary time, the kinetic friction also exhibits a certain velocity dependence, that is of interest in the context of this thesis, as will be elaborated upon in the next section.

1.3. The Dependence of Kinetic Friction on the Relative Velocity

Coulomb in his general studies on the friction force reported, that for very high and very low relative velocities of the sliding surfaces the friction force is *not* independent from the sliding velocity, while in the very broad intermediate regime the friction force *is* independent of the relative velocity [2]. The question arises, what the reason for this difference is. Persson points out, that Tomlinson in 1929 stated [8], that the velocity dependence of the friction force vanishes, if the processes in the system are rapid enough. Persson further states, that this breaks down, if the relative velocity becomes so small, that thermally activated creep motion becomes relevant, resulting in a friction force proportional to the relative velocity. On the other end of the velocity scale, obviously the motion of the molecules relative to the sliding velocity is not rapid enough any more. In the end, the velocity dependence of the friction force is velocity dependent.

Not only the friction force is velocity dependent, also whether the surfaces move steadily relatively to each other or with interruptions or even in a chaotic way depends on the velocity. Although not only on the velocity, as will be shown in the subsequent section.

1.4. The Stick-Slip Phenomenon

In every day live on a regular basis the so-called stick-slip phenomenon is encountered. This phenomenon is the rapid change from motion to standstill and vice versa. The resulting stuttering movement often produces sound waves, like e.g. in case of a wet finger on a glass substrate, when a squeaking noise results. The fact that stuttering is possible in the first place, stems from the difference between the center of mass (COM) motion of the moving body in contrast to the motion of the surface in contact with the friction partner. Whether stick-slip is observed or not depends on the strength of the coupling between the two movements. In the example of the wet finger, the muscle force acts on the finger bones, while the soft flesh couples the movement of the bone to the movement of the skin. The weak coupling by the soft material results in the stuttering and the noise. The coupling can be viewed as a spring, whose spring stiffness determines the stick-slip behavior. The larger the spring constant, the less likely is stick-slip to occur.

The mathematical expression of the equation of motion including friction looks like the following, using F as the force, x as the position, dots on top of a letter resemble differentiations with respect to the time, k is the spring constant, m is the mass and g is the standard gravity:

$$F = m\ddot{x} \quad (1.2)$$

$$m\ddot{x} = k(\dot{x}t - x) - \mu(\dot{x})mg \quad (1.3)$$

Depending on the velocity, as equation (1.3) states, the COF changes, which can be seen from the Stribeck curves in figure 1.4. At zero velocity the COF is the static friction coefficient, which is higher than the kinetic friction coefficient at low velocities. Once the velocity increases, at first the COF decreases, but soon the COF increases until the motion is dampened to standstill. Supposing a sufficient force, e.g. by elongation of the pulling spring, the motion cycle starts again, which is expressed by the following formula, using the kinetic friction coefficient μ_{kin} and the static friction coefficient μ_{static} and the eigenfrequency $\omega = \sqrt{k/m}$ of the system [9–11]:

$$x(t) = \dot{x}t - \left\{ \frac{g}{\omega^2} [\mu_{kin} + (\mu_{stat} - \mu_{kin}) \cos(\omega t)] + \frac{\dot{x}}{\omega} \sin(\omega t) \right\} \quad (1.4)$$

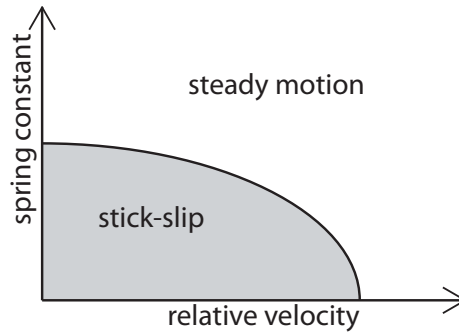


Figure 1.5.: Schematic representation of the dependence of stick-slip and steady motion on the relative velocity and the coupling strength of the motion of the center of mass of the body to the surface motion, which is viewed as a virtual spring of a variable spring constant.

Equation (1.4) states, that depending on the difference between static and kinetic friction coefficients, which modulates a cosine function, the movement will stop. The velocity dependence of the friction coefficient is expressed by the sine function that is modulated by the factor \dot{x}/ω .

In addition to the strength of the coupling of the surface movement to the COM motion, the velocity of the bodies relatively to each other is determining the stick-slip behavior. Again the wet finger on glass may serve as an example: Only slow movement induces noise generation, with increasing velocity the pitch gets higher and then the stuttering stops, which can be felt with the finger tip. A further example is the resonance generation using a wine glass edge and a wet finger: not even a squeaking noise is generated if the finger moves too fast.

Summing up the observations, there is a two-dimensional dependence of stick-slip behavior on the force coupling strength and the relative sliding velocity. Figure 1.5 gives a schematic representation of the stick-slip behavior depending on the spring constant and the relative velocity. The lower both variables are, the more likely stick-slip is, while both variables independently suppress stick-slip from a certain threshold value on. The threshold regarding the relative velocity is called critical velocity, and Persson [2] dedicates a whole subsection on the origin of stick-slip and the critical velocity. Persson presents an arithmetic example resulting in the statement, that the necessary fluctuation in tangential stress is in the order of 10 Pa, which is typically six orders of magnitude smaller than the shear stress. Consequently thermal fluctuations are likely to induce a stick-slip, while it depends on the coupling strength and the material, whether this stopping reaches relevant length scales. Stick-slip may occur on any imaginable length scale, yet the relevance and persistence is variable.

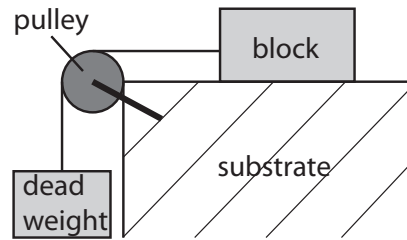


Figure 1.6.: Schematic representation of the apparatus employed by Leonardo da Vinci to determine the static friction of a block resting on a substrate by initiating movement using a dead-weight. The thread connecting the two bodies is diverted by a pulley.

The stick-slip behavior is most important not only in applications, but also upon the attempt to determine the friction force and thus the COF. Most friction measurement techniques discussed in the next section have to deal with some kind of oscillations.

1.5. Friction Measurements

As mentioned before, the measurement of friction forces dates back to da Vinci in the 15th and beginning 16th centuries. To determine the friction force necessary to initiate movement of a block resting on a substrate, da Vinci connected the block to a dead-weight by a thread (see figure 1.6). Neglecting the force necessary to rotate a pulley (roll) that diverts the thread connecting the hanging dead-weight to the block, the weight of the load equals the static friction force once movement is initiated.

Da Vinci stated the independence of the friction force of the apparent area of contact as well as the proportionality expressed in equation (1.1). Unfortunately these results were not accessible for the general public, resulting in the fact, that Guillaume Amontons (1663-1705) again stated these two laws, now called Amontons friction laws. The two laws were verified by Coulomb and extended by a third rule, the independence of the friction force on the relative sliding velocity (which is limited as already discussed, see section 1.3). The next step in friction measurements was the utilization of calibrated springs for dragging the block along a surface. Knowing the spring constant, the friction force can be directly measured by the elongation of the spring. The employment of the spring has the advantage, that thread and pulley do not have to be neglected or their contribution determined, which introduces an additional uncertainty.

More complicated is the further developed “surface force apparatus”. In a common surface force apparatus [2] curved glass bodies (e.g. cylinders) are coated with mica layers. Mica is a mineral, a silicate, which strongly reflects light because the surfaces after cleavage are very smooth. The reason for the smoothness is the layered atomic structure of

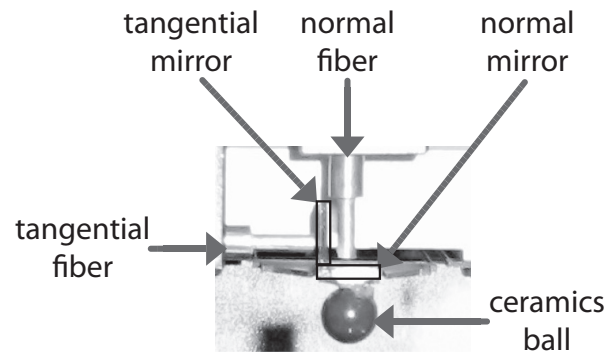


Figure 1.7.: Fiber optics and cantilever unit of the tribometer employed for the work underlying the experimental part of this thesis. A silicon nitride ball is glued underneath the cantilever. Two perpendicular mirrors reflect the light emitted by the fiber optics sensors.

the mineral. Using atomically smooth mica sheets, the contact between the two curved bodies can be studied, and the distance between them, because of condensed water vapor for example, can be measured. For the distance measurements light beam interference is employed. Upon measurement one body is pulled along the other using a spring. Resulting from the atomic smoothness of the interacting surfaces, the influence of lubricants can be studied very accurately.

Nowadays mainly two friction measurement kinds are employed, which both are focusing on spring deflection in tangential but also in normal direction. The one measurement technique is the macroscopic tribometer, the other technique is the atomic force microscope (AFM).

Figure 1.7 illustrates the measurement principle: Knowing the tangential and normal force constants of the cantilever, by the displacements in tangential and normal direction the friction and normal forces are known. The displacements are determined by the voltages induced by the light emitted and received by the fiber optics sensors. This voltage depends on the distance between the end of the fiber and the mirror. The distance between mirror and fiber end can be computed by the tribometer based on the known intensity distribution relatively to the maximum of this distribution. The maximum of the distribution has to be determined before the measurement by the user. The big advantage of course is the contact-less measurement of the acting forces.

The AFM uses the same principle, but the cantilever is so small, that it has to be handled by tweezers. Figure (1.8) schematically displays the measurement approach of an AFM. Underneath the AFM cantilever a tip with an atomically sharp profile is mounted. These tips have diameters of 10 nm and less and are usually etched to this shape by electro-etching. Typical tip materials are silicon or tungsten. The AFM cantilever deflection is measured by the deflection of a laser beam directed onto the cantilever and

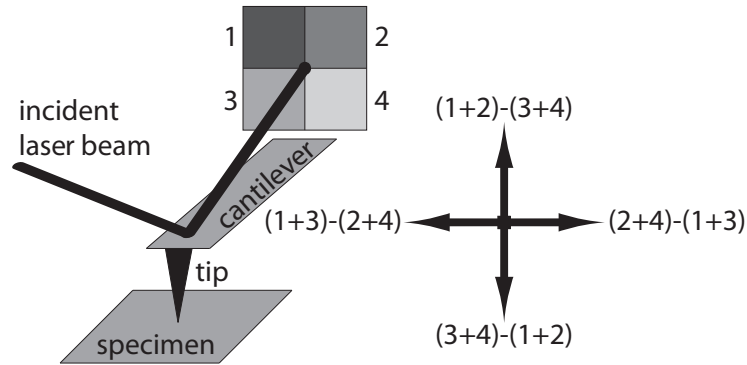


Figure 1.8.: Schematic representation of the atomic force microscope (AFM) measurement unit, the probe is the tip underneath the cantilever.

reflected onto a 2x2 charge-coupled devices (CCD) array. Without any acting forces the beam directly hits the center of the array, giving approximately the same voltage for all four CCDs. Deflection in tangential and normal direction changes the different voltages which produces the measurement signal. Compared to the dimensions of the tip, the normal forces in the range of 1-100 nN are very high. This high forces on areas in the atomic dimensions often leads to the damage of the studied surface, which is why the measurement in full and constant contact of tip and surface is often referred to as “scratching mode”, although the scientifically correct term is “contact mode”. The positioning of the probe on the specimen is performed using piezo-electric materials, because mechanical positioning on nanoscopic length scales with the required accuracy is impossible. The specimen surface is then scanned for the acting forces at a given position, resulting in a two-dimensional force map, the “image”. The employment of piezo-electric materials to position a probe for scanning a certain property renders the AFM among the “scanning probe microscopies”.

The contact of an AFM tip in contact mode with the specimen is obviously direct contact of an atomically shaped tip with a surface. However, for a macroscopic body the surface roughness usually is on a scale that is a lot larger than the diameter of an AFM tip. For the contact of two bodies with surface roughness the question, whether direct contact occurs or not, and if it occurs, where and with what fraction of the surface, is far from obvious and not easily answered. To shed light on the complicated situation at the friction interface between two bodies, the following part of this thesis deals with the general topic of contact, followed by a discussion about the area of contact. Subsequently the deformation resulting from the applied in areas of contact is investigated as well as the influence of lubrication on the molecular scale and finally the squeeze-out and entrapment of lubricant molecules.

2. Contact

When a body of certain dimensions lies on a larger body, these bodies are in contact. However, is there true contact all over the area spanned by the lower horizontal dimensions of the smaller body? Assuming an ideally flat surface for both bodies this statement is true. Considering a real surface, which exhibits protruding “hills” and low-lying “valleys”, corrugations, the answer is not quite obvious. The hills on the average surface levels are called asperities and if two surfaces are brought close to each other, the first interactions will be the interactions of the asperities of the one surface with the asperities of the other surface. The picture gets even more complicated when the deformation of the asperities is considered, elastic and plastic, which gives rise to new contacts. Furthermore, if lubrication gets involved the question is, whether the lubricant molecules are able to separate the asperities or not, because molecules can be squeezed out from between the approaching surfaces. The following sections will try to shed light on the questions presented here, first elaborating upon the area of contact, followed by discussing the consequences of asperity deformation resulting from the applied load. As the next step, lubrication and the change in contact mechanisms by the lubricant molecules is included in the consideration, as well as the process of squeeze-out of the lubricant molecules in the last subsection.

2.1. The Area of Contact

When two bodies are approaching each other, under dry conditions the surface asperities will come into contact. Figure 2.1 shows the schematic representation of two rough bodies in contact as well as the relevant quantities: Once the asperities above the average surface level touch, so-called junctions are formed, the movement will be slowed or stopped, depending on the force pressing the bodies together. The direct contact of asperities will most certainly not occur over the whole area spanned by the dimensions of the smaller body. The whole area, in which contact might occur, is called “apparent area of contact”. There are only some places on the surfaces, at which direct contact really occurs, and the sum of the areas of direct contact is called the “real area of contact”. Consequently two questions arise in case of geometrically more complex bodies compared to ideal cuboids:

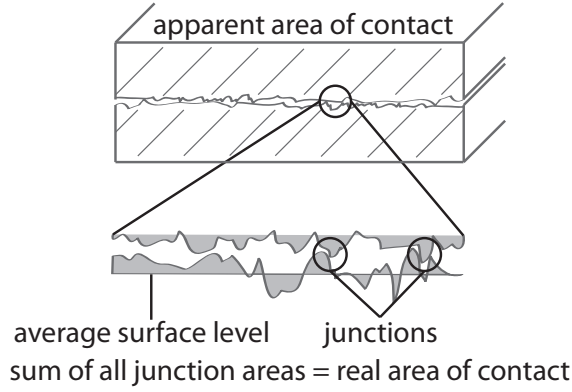


Figure 2.1.: Schematic representation of the apparent area of contact, the junctions that form, the average surface level as well as the explanation of the real area of contact.

1. What is the size of the apparent area of contact?
2. What is the size of the real area of contact?

As the real area of contact depends on the apparent area of contact, we will begin the considerations with the apparent area of contact. Heinrich Hertz considered the topic in his previously mentioned publication [5, 6]. Hertz assumed different ideal geometric bodies and their contact. Concerning the surface force apparatus for example, the contact of two spherically shaped bodies is relevant, which is also the best-known case of Hertz contact. Bringing two spheres into contact by a certain force will deform the spheres. If the force is low, as we assume here, the deformation is completely elastic. The resulting flat will stem from deformations of varying magnitude. Because of the shape of the bodies in contact, more deformation at the center of the flat than at the border of the flat will be observed. Resultantly, the pressure is higher at the center of the flat. Casting Hertz's considerations into formulae the following equations result [2, 5, 6], with the pressure p and the normal force F_N , the effective material behavior β , the elasticity modulus E and the Poisson number ν , the contact area radius r_0 and the radii of the spheres R_1 and R_2 :

$$r_0 = \left(\frac{R_1 R_2}{R_1 + R_2} \right)^{1/3} (\beta F_N)^{1/3} \quad (2.1)$$

$$\beta = \frac{3}{4} \left(\frac{1 - \nu_1^2}{E_1} + \frac{1 - \nu_2^2}{E_2} \right) \quad (2.2)$$

$$p_0 = \frac{F_N}{\pi r_0^2} \quad (2.3)$$

$$p(r) = \frac{3}{2} p_0 \left[1 - \left(\frac{r}{r_0} \right)^2 \right]^{1/2} \quad (2.4)$$

As equation (2.4) states, the pressure at the center of the apparent area of contact is 1.5-times the average pressure. Since the tribometer brings a ceramics ball into contact with a flat steel specimen (see figure 1.7 on page 15), in this thesis the contact of a sphere and a flat is considered. Focusing on the maximum pressure, the above equations transform for a sphere in contact with a flat (one radius is infinite) into the following:

$$p_{max} = \frac{1}{\pi} \sqrt[3]{\frac{6 F_N}{r^2} \cdot \left(\frac{1 - \nu_1^2}{E_1} + \frac{1 - \nu_2^2}{E_2} \right)^{-2}} \quad (2.5)$$

$$F_N = \frac{\pi^3}{6} r^2 \left(\frac{1 - \nu_1^2}{E_1} + \frac{1 - \nu_2^2}{E_2} \right)^2 p_{max}^3 \quad (2.6)$$

The question now is, whether the contact of a spot within the apparent area of contact is direct or not. Even without direct contact, there is interaction of the bodies, but this is not necessarily the most relevant interaction regarding the resulting friction. Where there is direct contact, the resulting friction is higher: The interlocking of asperities comprehensibly gives rise to friction, so the direct contact indeed is of interest. Nonetheless, the Hertz theory gives a good representation of the *average* pressure in the area of contact. Additionally Mo and Szlufarska state in their Physical Review B publication [12] that elaborates more detailed on their work about the friction laws at the nanoscale published in a 2009 Nature article [13] that received great attention (121 citations at the 5th of November 2012 according to ISI web of knowledge): „Friction and contact area directly measured by surface force apparatus (SFA) frequently follow predictions of the Hertz model.“

One single junction will be the first direct contact formed upon bringing two bodies closely together. Consequently, this one single spot will bear all the load, and the resulting stress will be immensely high, because the area of a single junction is minuscule. Resultantly the consideration of the stress and the elastic or plastic deformation of asperities is significant in all contacts, which is the topic of the next section.

2.2. Load and Deformation

The distinguishing between the apparent area of contact, the bottom surface area of the smaller body lying on the larger, and the real area of contact, the area where interactions take place, and especially the fact that there is a huge difference in magnitude dates back to Bowden and Tabor in their monographs on “The Friction and Lubrication of Solids” published in the 1950s [14, 15]. They considered the interactions of bodies as completely

plastic. On the other hand, interactions can also be elastic, but only if the force is small compared to the area.

Any real material has a finite elasticity. The assumption made by Hertz, that all the contact interactions are elastic, is limited to very small contact stresses for very smooth surfaces. In any real case, the surface roughness as well as “regular” macroscopic loads will make this assumption break down. Using the symbol A_{real} for the real area of contact, instead of the distribution of the normal force F_N over the apparent area of contact A_0 , the normal force will be distributed only over the real area of contact. The resulting stress σ on the surfaces will accordingly be:

$$\sigma = \frac{F_N}{A_{real}} \quad (2.7)$$

The threshold value between the regime of lower stress, resulting in elastic deformation of the body, and the regime of high stress, resulting in plastic deformation, is the so-called yield stress σ_c , which is the same as the penetration hardness of a material. It is called yield stress, because if the stress on the body exceeds the yield stress, the body yields plastically to the interaction. In the theory of von Mises [16], which agrees well with experiments [2], the yield stress is related to the von Mises yield criterion s_0 via:

$$s_0 = \sqrt{\frac{8\sigma_c^2}{3}} \quad (2.8)$$

Resulting from the definition, the energetic interpretation of equation (2.8) is, that if the elastic energy per unit volume that stems from shear deformations overcomes the threshold, the body flows plastically.

Now, considering the contradicting theories of Hertz on the one hand and Bowden and Tabor on the other hand, observations and logics contradict both theories. If there would be only *elastic* deformations, as assumed by Hertz, the friction force would not depend linearly on the normal force, because that is also predicted by Hertz theory. However, macroscopic experiments find such a linear relationship between friction and normal force. If there would be only *plastic* deformations, then the fatigue, the gradual degradation of material integrity, would lead to machine failure very fast. For example metals exhibit the so-called “work-hardening”, which changes the material structure in highly stressed areas to a more resilient but less elastic one, leading to fatigue cracks and finally failure. Engines would not surpass a few minutes of running if this would be the case. The reconciliation of both theories was published by Greenwood and Williamson [17] in 1966. The Greenwood-Williamson contact theory assumes a gaussian distribution of heights on the average surface level, which was corroborated by experiments. The resulting equations stated an independence of the friction of the apparent area of contact,

while the friction force was to depend almost linearly on the normal force. Following that, Johnson, Kendall and Roberts [18] developed a model of an elastic contact, which focuses on the compensation of the loss of surface energy by deformation and the increase in stored elastic energy. Utilizing both results, Fuller and Tabor [19] connected the energy change as well as the gaussian height distribution to the result, that the higher asperities try to separate the surfaces, while the lower asperities try to maintain contact. Further augmenting the previous results on spheres in contact with flats, Volmer and Nattermann in 1997 [20] stated, that viewing the surfaces of a cuboid on a surface as self-affine on small length scales gives a COF, which depends on the ratio between elastic and repulsive forces. The resulting equations based upon the elasticity of the majority of asperities in contact directly result in the previously stated friction laws (cf. section 1.5).

Summarizing the theories, upon contact, at first so few junctions occur, that there is plastic deformation of these junctions, which results in further junctions to be formed. The resulting increase in real area of contact reduces the average contact stress per junction, up to the point where only elastic deformations occur. At this point, the junctions support the load, the junction interactions are the load-bearing interactions. The vast majority of the interactions will be elastically, and can be modeled by the theory of elasticity, if a gaussian height distribution as surface roughnesses is assumed, to arrive at the macroscopically observed friction laws.

Finally, the material characteristics determine the behavior of the real area of contact with increasing stationary time. Considering the ideal elastoplastic behavior of a material, the real area of contact should not change over time at all. However, real materials exhibit creep [2], the slow rearrangement of atoms, resulting in the reduction of elastic energy in favor of rearranging atoms, thus creating plastic deformation over time. The relevance of this behavior depends on the time scale of the contact period.

Considering a rectangular block of material under the constant uniaxial tension ϵ in x-direction, the development of the tension over time depends on the length of the block l in the following way

$$\dot{\epsilon} = \frac{\dot{l}}{l(t)} \quad (2.9)$$

There is an initial response of the system to the applied tension, which takes the relaxation time τ . If the contact time is less or equal to τ , there will be no creep. Once the contact time exceeds the relaxation time, the stress distribution has changed accordingly and depends on the von Mises yield criterion. Consequently the length of the block increases over time:

$$l(t) = l_0 e^{\dot{\epsilon}t} \quad (2.10)$$

Since the volume of the block is constant, the cross-sectional area decreases over time, thereby reducing the acting force. The strain rate tensor $\dot{\epsilon}_{ij}$ for uniaxial tension has the form:

$$\dot{\epsilon}_{ij} = \begin{pmatrix} \dot{\epsilon} & 0 & 0 \\ 0 & -\dot{\epsilon}/2 & 0 \\ 0 & 0 & -\dot{\epsilon}/2 \end{pmatrix} \quad (2.11)$$

The resulting stress is uniaxial in x-direction. The creep of a material needs a temperature activation, which allows us to write the uniaxial stress in terms of the activation energy E_A , the temperature T and the Boltzmann constant k_B :

$$\sigma = \sigma_c \left(1 + \frac{k_B T}{E_A} \ln \left(\frac{\dot{\epsilon}}{\dot{\epsilon}_0} \right) \right) \quad (2.12)$$

where the constant $\dot{\epsilon}_0$ is defined as follows, using the Poisson number at zero stress ν_0 and the elastic modulus E :

$$\dot{\epsilon}_0 = \frac{8 \nu_0 (1 + \nu) \sigma_c k_B T}{3 E E_A} \quad (2.13)$$

If we set the stress to zero, meaning complete relaxation of the stress, we arrive at:

$$0 = 1 + \frac{k_B T}{E_A} \ln \left(\frac{\dot{\epsilon}}{\dot{\epsilon}_0} \right) \quad (2.14)$$

where $\dot{\epsilon}$ is the creep rate. Persson [2] states, that for a typical material the activation energy is of the order of 5 eV as determined experimentally and thus the diameter of a stress block is about 3 nm, or an area of about 7 nm².

To obtain the time dependence of the real area of contact, we start from the variation of the block length l and the requirement, that the block volume is constant. In this case we arrive at:

$$\dot{\epsilon} = -\frac{\dot{A}}{A} \quad (2.15)$$

The acting stress is defined as:

$$\sigma = -\frac{F}{A} \quad (2.16)$$

and if the area is the initial area A_0 the yield stress is obtained. Using the above in equation (2.12) deduced result, the yield stress can be expressed as:

$$\frac{\sigma}{\sigma_c} = -1 - \frac{k_B T}{E_A} \ln \left(\frac{\dot{\epsilon}}{\dot{\epsilon}_0} \right) \quad (2.17)$$

Using appropriate definitions and solving the differential equation [2] the following expression can be derived, $B = \frac{k_B T}{E_A}$, $\tau_0 = \frac{k_B T}{E_A \epsilon_0}$:

$$A = A_0 \left[(B - B^2) \ln \left(1 + \frac{t}{\tau_0} \right) + B^2 \ln^2 \left(1 + \frac{t}{\tau_0} \right) + \frac{B^2 t}{(\tau_0 + t)} \right] \quad (2.18)$$

For a metal with a yield stress in the range of GPa the time constant τ_0 is extremely short, reducing equation (2.18) to:

$$A = A_0 \left[(B - B^2) \ln \left(\frac{t}{\tau_0} \right) + B^2 \ln^2 \left(\frac{t}{\tau_0} \right) + B^2 \right] \quad (2.19)$$

With equation (2.19) finally the statement of a logarithmical dependence of the friction force on the static time in section 1.2 has been justified: Since the real area of contact increases over time due to material creep, the friction force increases.

2.3. Lubrication

The situation at the junctions significantly changes, if a tribological system is lubricated. In between the bodies lubricant molecules may act as spacers, preventing direct contact of the bodies. Still there will be interaction of the bodies due to direct electrostatic or dispersive interactions, or by interaction of the surfaces with the lubricant molecules. The interaction of the surfaces with the lubricant molecules results in a lubricant-mitigated interaction of the friction partners. Depending on the surface characteristics the optimal lubricant may have strong or weak interactions with the surface. For some applications a weak interaction of the lubricant with the surface is desirable, because low interaction facilitates the sliding of the junctions. On the other hand, strong interactions may be preferable, e.g. in case of high load, when the lubricant would otherwise easily be squeezed out (see next section 2.4). Without lubricant between asperities in contact, wear is likely to occur, which leads to component failure.

Metal oxide surfaces can effectively be wear-protected by adding longer-chain carboxylic acids, so-called surfactants, to the lubricant mixture. Figure 2.2 schematically shows the mechanism of the chemical bonding of a surfactant to a metal site of the metal oxide surface. With their carboxy group the carboxylic acids chemically coordinate metal sites of the metal oxide surface. The chemical interactions are very strong, resulting in a resilient coverage of the metal surface. Additives which coordinate the surface chemically are called surfactants, and carboxylic acids have proven to be useful because of their amphiphilic character: The hydrophilic carboxy group, often referred to as “head”, coordinates the surface that is to be protected, while the alkyl chain, often called “tail”, is

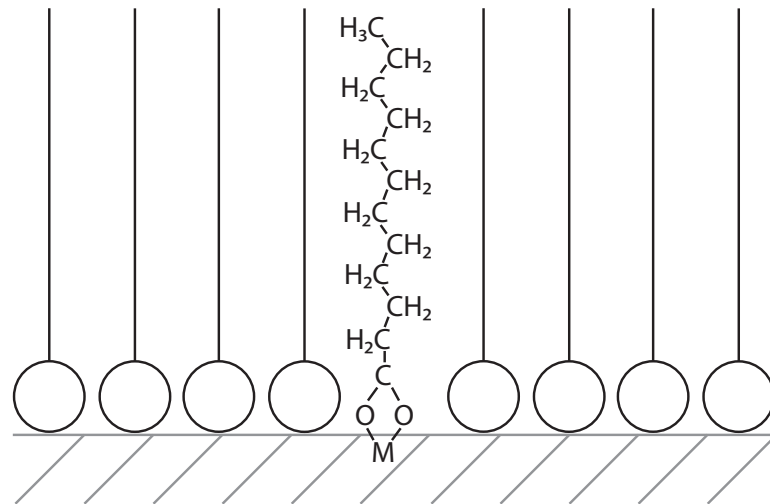


Figure 2.2.: Schematic structure of surfactant molecules of the carboxylic acid kind covering a metal oxide surface, protecting it from wear. The acid shown here is dodecanoic acid, also called lauric acid. Carboxylic “heads”, the carboxy groups of the acid, are displayed as circles, the alkyl chain, the “tail”, is represented as solid lines. M is a metal atom of the metal oxide surface, O is oxygen, C is carbon, H is hydrogen.

lipophilic and thus has favorable interactions with a standard alkyl-based lubricant like mineral or synthetic oils. The lipophilic interactions of the alkyl chains of the surfactant improve the wetting with the lipophilic oils, because a pristine metal oxide surface is oleophobic. The improved wetting in turn reduces the friction coefficient. The strong chemical binding of the surfactant makes the squeeze-out of the molecules difficult, increasing boundary lubrication performance of the lubricant mixture.

Dodecanoic or lauric acid ($C_{11}H_{23}COOH$) is a common additive and it is the parent compound of a surfactant creating one of the least wettable surfaces ever found: Perfluorododecanoic acid ($C_{11}F_{23}COOH$) on a metal oxide [2]. However, is not a wettable surface optimal for the application of a lubricant? That depends on the desired application. Regarding a bearing that has to function in the higher rotation speed regime, a closed lubricant film is vital, because a disrupted lubricant film leads to bearing failure very soon. On the other hand, the Stribeck curve of a bearing has a minimum (see figure 1.4 on page 10) in the region of mixed lubrication. This fact is utilized in hard disk drives (HDD) in a computer, where the disk head flies over the disk at immense rotation speeds, and the friction is minimal, because there is a sub-monolayer coverage of a special surfactant. The coverage is not sufficient to span the whole disk area, resulting in the formation of lubricant islands. Consequently the head is subject to rapid change of physical interactions with the surface, preventing that the system reaches equilibrium. Hence the disk head maintains a distance from the disk that is close enough to scan the data but far enough to avoid frictional interaction, which would instantly destroy the HDD. Perfluorinated

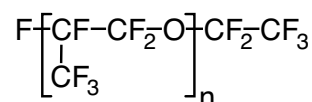


Figure 2.3.: Chemical structure of a perfluoro-polyether of the DuPont Krytox[®] family. C is carbon, F is fluorine, O is oxygen, n is the number of repeating units.

lubricants, regardless of the application as surfactant or as lubricant molecules, reduce the wettability of the surfaces with water- or oil-based lubricants, because perfluorinated molecules are even autophobic and do not interact favorably with other perfluorinated molecules. In addition to that, the friction on perfluorinated molecules is reduced, which led to the development of so-called perfluorinated self-assembled monolayers (SAMs). SAMs spontaneously form once a solution of the surfactant molecules is poured on top of a surface, while the resulting monolayer exhibits a structure that is in principle identical to the surfactant scheme shown in figure 2.2. In contrast to the formation of a SAM, a monolayer coverage of surfactant is usually achieved by employing special dipping techniques, which are also used to get selective coverages of more than one monolayer. The surfactant molecules are spread out over a fluid the surfactant is immiscible with, and then the surface is dipped into the basin slowly. Resultantly the surfactant layer is put over the surface like a sheath, for more than one monolayer the process is repeated.

The chemical interaction of a surfactant with the underlying material is resilient enough to persist under normal shearing conditions. However, as has been shown by molecular dynamics (MD) simulations of perfluorinated SAMs under shearing condition by Lorenz et al. [21], by the external lateral force the structure of the monolayers does not only get tilted: After a short period, the alkyl chains entangle, which will result in SAM wear at first, but finally the coating by the surfactant molecules will be destroyed, leading to wear of the hence as pristine surface. This disadvantage of SAMs regarding high load situations regularly occurring in a bearing may be overcome by an even more resilient, perfluorinated coating of the bearing surface, which will be discussed in the section “Plasma-Enhanced Chemical Vapor Deposition” (section 3.3).

In addition to the stable coverage of the surface by surfactant molecules and SAMs, perfluorinated substances also serve as lubricant molecules that almost do not interact with the surfaces at all. Hence these molecules do not mitigate interaction of the surfaces, which e.g. is the case of water molecules between hydrophilic and even protic surfaces. Between laterally sliding asperities the formation of hydrogen bonds within the water layer and between the water molecules and the surfaces leads to the formation of capillary bridges [2]. These capillary bridges increase the cohesion of the asperities and thus increase the friction. Furthermore perfluorinated molecules offer an increased chemical stability up to inertness compared to alkyl-based lubricants, which is the reason, why

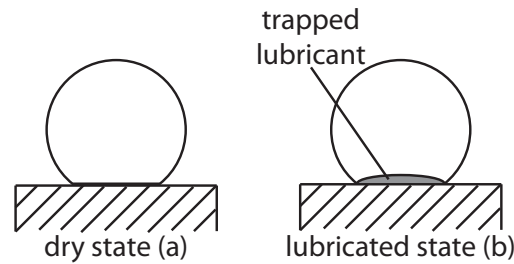


Figure 2.4.: Deformation of a ball on a flat in the dry state (a) and in the lubricated state (b).

the U.S. Food and Drug Administration (FDA) officially allowed a special lubricant class for direct food contact: Perfluorinated Polyethers (PFPE), like e.g the PFPE high performance lubricant, whose chemical formula is shown in figure 2.3. Resulting from the ether bridges, their molecular structure renders PFPEs flexible, yet PFPEs are chemically inert, because of the perfluorinated alkyl segments. Perfluorinated alkyl segments are highly stable because of the very strong carbon-fluorine bond on the one hand, and the high electron density at the fluorine atoms on the other. The high electron density at the fluorine atoms in connection with the rather short carbon-fluorine bonds protects the carbon atoms from nucleophilic attacks. In addition to the chemical inertness, PFPE molecules are advantageous for lubrication because PFPEs are longer chain polymers. The technical data sheet of the Krytox[®] family lubricants states that the number of repeating units n starts from ten for low viscosity lubricants and ranges up to 60. The longer the chain of a lubricant molecule the more difficult the molecules are to squeeze-out, as will be discussed in the next section. Molecules difficult to squeeze out are high-performance boundary lubricants.

2.4. The Squeeze-Out of Lubricant

The fact that a liquid can be squeezed out from between two approaching surfaces or generally by high pressure is an every day fact. However, the process on the molecular scale and the amount of remaining lubricant molecules depends on several parameters: The applied pressure, the chain length of the molecules, the surface roughness and the commensurability, which is the structural likeness of the two approaching surfaces. Obviously a higher pressure will be more effective at squeezing out molecules from in-between asperities. However, in addition to the magnitude of the pressure, the time interval, during which the pressure rises, is essential. The higher the pressure increase rate, the more likely it is that molecules are trapped by surrounding junctions. Furthermore, the macroscopic deformation of the ball bearing ball is different in the lubricated state from the deformation to a flat in the dry state (figure 7 in ref. [3]).

Figure 2.4 exemplary shows the trapping of lubricant by the altered deformation of a ball on a flat with lubricant present. There will be no trapping of lubricant in the limiting case of zero pressure increase rate, because over time all the molecules have the possibility to leave the high pressure area. In contrast to that in the limiting case of infinite pressure increase rate, all lubricant that may be trapped, will be trapped. Balls in a bearing often move with velocities that are in the intermediate regime concerning the entrapment of lubricant. In this case the entrapment is limited to the junction areas, not only because of the speed, but also, because the exaggerated depiction in figure 2.4 and in figure 7 in reference [3] refer to a highly elastic ball, while a ceramics ball with an elastic modulus of 320 GPa most certainly is not very elastic.

In addition to the question, whether there is enough time for the molecules to leave the high pressure area before the liquid enters a quasi-solid state, the length of the molecule backbone is of importance for the squeeze-out. From the review on squeeze-out by Persson and Mugele [3] as well as the underlying article by Sivebaek, Samoilov and Persson [22] it becomes clear from MD simulations of united atom representations of hydrocarbons under squeeze-out conditions, that there is a linear dependence of the pressure necessary for the initiation of a layering transition on the chain length. A layering transition is the transition of n monolayers to $n - 1$ monolayers. Simulations by Persson and Ballone, published in the year 2000 [23, 24], show the influence of density fluctuations on the induction of a layering transition. As with crystallization the layering transition needs a nucleus to start [25]. Density fluctuations stem from thermal molecule motion (Brownian motion) or surface roughness. Persson and coworkers investigated the layering transitions for hydrocarbons from propane on. Extrapolating the linear correlation to one carbon atom, the resulting pressure to squeeze out even the last layer of methane molecules is about 2750 bar. An even smaller pressure will be required for water molecules that are between two approaching hydrophobic surface asperities.

The influence of surface roughness on the layering transition has already been mentioned. Not only the density fluctuations induced by an asperity protruding into the bulk liquid facilitates squeeze-out, also the molecular state of the lubricant is of relevance. Once the molecular state changes to solid-like because of the high pressure, the mobility of the molecules is drastically decreased. Another publication by Persson and coworkers [26] states the fact that “surface roughness hinders the formation of solid-like lubricant structure and liquid-like (disordered) layers are observed. This in turn leads to a reduction in squeeze-out pressure”.

Another hidden factor in squeeze-out was highlighted in the same publication: the surface commensurability. Figure 28 shows a representation of the two different possibilities for friction partner surfaces: Either the surfaces are commensurate, which means the structure is very similar, and thus the molecules may be clamped by the surface, or the

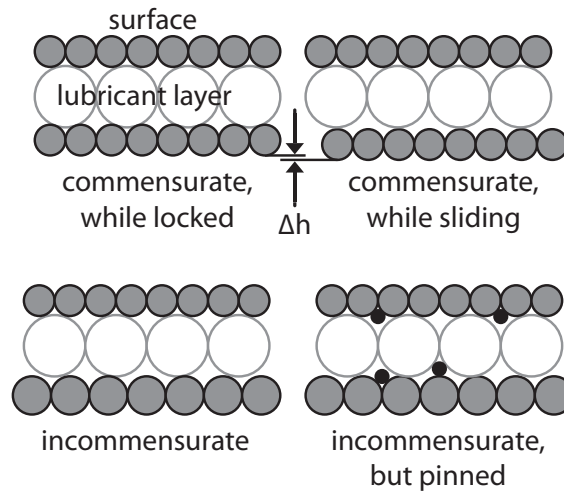


Figure 2.5.: Schematic representation of the commensurability and lubricant pinning. The surfaces are represented by the smaller circles filled grey, while the larger circles represent the lubricant. The height difference Δh has to be overcome when the sliding of a commensurate system takes place. The height difference in the incommensurate but pinned system will be even higher, while it will be less in the incommensurate system.

surfaces are incommensurate, which means that the surface structuring of the one surface does not fit to the other surface structure. In case of surface asperities, the lubricant molecules also may be pinned by the asperities [26]. For the initiation of sliding, the pinning results in the requirement of either a large deformation of the surface or a large height difference. The energy necessary for the deformation or the increase in surface separation increases the friction.

Consequently the surface roughness influences the frictional characteristics of a surface by three main factors: Firstly the surface roughness induces density variations that is necessary for the initiation of the squeeze-out of lubricant molecules, secondly the surface roughness prevents the formation of a quasi-solid lubricant structure thereby facilitating squeeze-out and as a third factor the pinning of the remaining lubricant molecules increases the friction that is created during the sliding process.

3. Plasma Surface Coating

The considerable influence of the surface properties on the frictional characteristics of a tribological system has been elaborated on in detail so far. This chapter is dedicated to the altering of the surface in a selective way to enhance the tribological properties of a material. The bulk properties of a hybrid bearing could only be enhanced by changing the ring material to ceramics in addition to the ceramics balls, but this would be accompanied by an immense increase in price. The surface properties of a hybrid bearing can be optimized employing a coating technique. As stressed in the sections on lubrication and lubricant squeeze-out (sections 2.3 and 2.4) the adhesion of a coating on the bearing surface is of prime importance for the performance of the component under application conditions. Simple surfactant coatings or SAMs cannot withstand the shearing forces occurring when the bearing is running. Hence an interconnection of the molecules and an increase in binding site density is the logical conclusion to achieve an increase in stability. Reactive substances are required, which form many chemical bonds to the underlying substrate and additionally form a network of molecules, or better “reactive molecule remnants”, on the surface. Bringing reactive substances together in close proximity of a substrate is the approach employed by chemical vapor deposition techniques, which is the topic of the following section. The reactivity of these so-called precursor substances may further be increased employing plasma, which is discussed in the section that follows after. The combination of both techniques is called Plasma-enhanced Chemical Vapor Deposition (PECVD) and offers a large variety of different coating possibilities even when focussing on the tribological performance only. PECVD is the last and main subsection of this chapter.

3.1. Chemical Vapor Deposition

While a huge amount of different precursor molecules and resulting deposits is imaginable, the underlying principle of chemical vapor deposition (CVD) is the creation of a film on a substrate by bringing reactive molecules together on the surface or in close proximity to it. The approach is schematically displayed in figure 3.1. The precursor molecules chemically react with each other and the surface to form the desired coating with excellent adhesion between the coating atoms. One example from the study of chemistry is the deposition

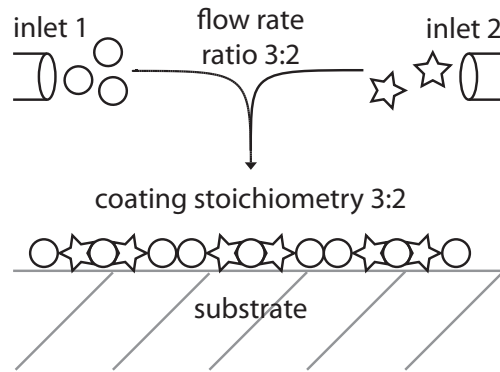


Figure 3.1.: Schematic depiction of the approach to steer the stoichiometry of a coating deposited by chemical vapor deposition (CVD). The reactive gas molecules, represented as circles and stars, stream into the reaction chamber through inlet 1 and 2, the relative flow rates determine the composition of the film deposited on the substrate.

of semiconductor materials, like e.g. gallium arsenide (GaAs). Gallium arsenide may be synthesized via CVD from the toxic precursors trimethyl-gallium(III) and arsane (AsH_3) to form the semiconductor film and methane. The great advantage of CVD is the possibility to steer the reaction to form a coating of defined stoichiometry just by controlling the ratio of the flow rates of the precursor molecules streaming into the reaction chamber. Additionally, a layered structure may be deposited by having more than two inlets and varying the precursor mixtures or just turning off one or more inlets. The reactivity of the molecules may be enhanced by supplying energy to the gas phase, e.g. using electric fields. The resulting mixture of reactive molecule fragments is called a plasma, which is the topic of the next section.

3.2. Plasma Properties

A plasma is created by the addition of energy to a gas. The addition of energy may occur in the form of extreme temperature in the sun, or the supply of an electric field. Plasmas are partly or fully ionized gases, while the ionization of larger molecules probably leads to bond breaking and fragmentation into even more reactive fragments like smaller, less stabilized ions, radicals or carbenes. In coating technology, reactive gases are subject to an electric field to create a plasma, which results in highly reactive species that are present in the gas phase. Commonly, a degree of ionization α of the plasma particles is defined as ratio of the volume electron density n_e to the sum of volume electron density and volume neutral particle density n_0 :

$$\alpha = \frac{n_e}{n_e + n_0} \quad (3.1)$$

There are weakly ionized plasmas of α between 10^{-7} to 10^{-4} to be distinguished from strongly ionized plasmas of α close to 1 [27]. For the molecules and the other particles a temperature, meaning their average energy, can be defined individually, leading to electron, ion and neutral species temperature. If there is an equilibrium in the plasma, all three temperatures are about the same, while in non-equilibrium plasmas the temperature of the electrons is a lot higher than the other two temperatures. In this case the reactive gas phase is called “cold”, and usually non-equilibrium plasmas are used, because the surface damage is reduced when cold plasmas are employed. To prevent the molecules and fragments from reaching high energies, often the operation conditions involve reduced pressure. The resulting diminished molecule density decreases the probability of more than one electron collision with a molecule, or further increasing the energy of already reactive particles. Resulting from the impact of an electron, reactive species like radicals, radical ions and ions and carbenes are formed. Furthermore, the non-equilibrium plasma state can be reached via application of a radio frequency. The high frequency reduces the ion and molecule mobility because of the particle weight in comparison to the electrons. In addition to the highly energetic particles, high energy photons may be created due to secondary effects of the electron impacts. Overall in PECVD processes most frequent is a combination of radio frequency power generation and low pressure in the reaction chamber to ensure a cold plasma atmosphere [27].

Several different gases are employed in classical plasma surface treatments that clean a substrate or alter the chemical properties of the surface, while not depositing a coating on top. The classifications of atomic or molecular gases include inert gases and reactive gases. Inert gas plasma surface treatment has the effect of removing contaminants from the surface. The highly energized e.g. argon atoms activate the contaminant molecules which at least causes desorption, but often molecule fragments are formed due to the high amount of energy transferred from the plasma. Of course the substrate may be affected after time and the result is a sputtering process without changing the chemistry of the substrate or the sputtering deposit [28].

Reactive gases are employed in plasma treatments to alter the surface chemistry of the substrate. Resultantly the treatment duration should be as long as necessary but as short as possible to prevent substrate damage. The reactive gases that are employed are due to abundance and the low cost resulting from that primarily oxygen, but also fluorine is employed because of the high reactivity and different results. While oxygen plasma usually is employed to increase the surface hydrophilicity, in contrast to that fluorine plasma increases the hydrophobicity and induces cross-linking and polymerization [28]. Nitrogen plasmas are utilized e.g. to increase the biocompatibility by adding amino-groups to the surface. In reactive plasma treatments the pressure may be increased while simultaneously keeping a low reactive gas partial pressure by diluting the reactive gas

with inert gas, which is in that case called carrier gas, which most of the time is argon due to the relatively low cost compared to the other noble gases.

Generally, the modification depth can be controlled by the amount of power that is fed into the reaction chamber and the duration of the treatment process. The higher the power and the longer the time, the larger the effect of the modification. However, on the other hand more energy, so a more reactive plasma, and longer exposure to a highly reactive gas atmosphere increase the damage to the substrate. This is also a valid statement for inert gases and not limited to reactive gases only. Especially polymeric materials exhibit significant aging effects after plasma treatment [28]. The introduced functionalities result in reduced cross-linking or destruction of multiple bonds.

Reactive species damage to the substrate is not a problem, if a constantly growing coating is deposited on a surface, which results in effective protection of the underlying material. The deposition of material from a plasma that increases the reactivity of precursor molecules is called plasma-enhanced chemical vapor deposition, the topic of the next section.

3.3. Plasma-Enhanced Chemical Vapor Deposition

Joining CVD with plasma surface treatments results in a highly advanced technique for coating surfaces. Not only does the plasma enhance the chemical reactivity of the precursor molecules, the plasma also increases the adhesion of the resulting coating to the substrate. The adhesion is enhanced not only by previously cleaning and activating the surface via bombardment with reactive particles. The main reason for the greatly improved adhesion is the fact, that the coating is actually not deposited *on* the surface, it is implanted *into* the surface. The high energy of the particles in the plasma gives rise to the implantation, because ionic bombardment of the surface occurs, which results in the impacting plasma particles stopping “in their impact craters” *below* the surface. The according model is the so-called “subplantation model” developed by Lifshitz and co-workers [29]. Focusing on the deposition of diamond-like carbon (DLC), the development of a carbon coating on a metal substrate over time was investigated by Auger electron spectroscopy (AES). Depending on the energy of the C^+ -ions, the impact energy is absorbed sooner or later during penetration into the substrate bulk. At the position where most of the carbon ions are stopped, a carbon film develops, which is intimately connected to the substrate bulk. In contrast to that, the outermost surface of a metal substrate gradually turns from pure metal to metal carbide to carbon film, while the *underlying* film grows (figure 2 in reference [29]).

The coating of a substrate by PECVD requires a sophisticated device that is schematically shown in figure 3.2. As mentioned above, the usual approach to ensure a cold plasma

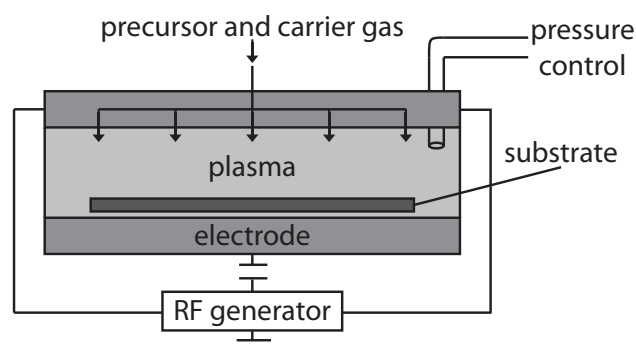


Figure 3.2.: Schematic configuration of a plasma-enhanced chemical vapor deposition device. Precursor molecule(s) and a carrier inert gas (usually Ar) are flowing into the reaction chamber through several pipes to improve even distribution of reactive species. The plasma is ignited by a radio frequency (RF) power generator, which is coupled to one of the electrodes in a capacitive way. A reduced pressure is maintained via pressure control devices connected to the reaction chamber.

is the combination of low pressure in the reaction chamber and high frequency of the electric field. Consequently the power source is a radio frequency (RF) power generator, often the free radio frequency of 13.56 MHz is used or a multiple of that frequency. To ensure an uniform coating, the concentration of reactive species all over the substrate area has to be as equal as possible, which is the reason for the multiple pipe openings spread over the substrate area, through which the precursor molecules enter the reaction chamber.

In the field of PECVD coatings that are meant to improve the tribological properties of a material, the first relevant coatings have been DLC coatings. Since the degree of really “diamond-like” carbon in a DLC coating varies, the more appropriate term is amorphous carbon (a-C). Furthermore, in most a-C coatings hydrogen is present, so that most carbonaceous PECVD coatings are best represented by the term amorphous diamond-like hydrogenated carbon (a-C:H). The first a-C:H coatings have been deposited by Aisenberg and Chabot [30], who published in 1971 their results on ion-beam deposited DLC thin films. From that breakthrough on there has been immense progress in terms of manifold precursors, varying deposition techniques as well as different mechanical and atomic properties [31, 32]. The resulting carbonaceous coatings exhibit some extremely useful properties regarding a large variety of applications. First of all, a-C:H coatings are 1-4 eV bandgap semiconductors, which is a very wide bandgap range. The wide range opens up the possibility of bandgap engineering. Furthermore the mobility of the charge carriers is low, resulting in high resistivity of the material, which renders it useful in semiconductor applications as insulating material. In addition to the semiconductor properties, a-C:H is a material of extraordinary mechanical properties. Being closely related to diamond,

a high hardness (10-30 GPa) of a-C:H films and a high elastic modulus in the range of 60-300 GPa are not astounding. Resulting from the diamond-like bonding situation of carbon atoms in the a-C:H matrix is a high wear resistance. However, the remarkable mechanical properties do come at a cost: The coatings are deposited under conditions, which result in high internal stress within the coating after the deposition process. The internal stress impairs the adhesion to the substrate, which in the end reduces long-term stability and leads to coating failure. Nonetheless, a-C:H coatings are highly successful in a huge variety of different applications, ranging from tribology and mechanics over to electronics and informatics and even to biomedicine as electrodes for bioelectronic applications and because of their anti-fouling properties [31–36]. Amorphous hydrogenated carbon coatings also provide a surface with a low friction coefficient. The reason for this is the metastability of the carbon film: Friction induces a change in molecular structure to a graphitic one in the outermost region of the a-C:H material. Graphite is a layered material that exhibits a very low shear strength, so there results a material transfer to the friction partner, inducing graphite-on-graphite friction. Hence the resulting COF becomes very low.

The fact that an a-C:H coating is metastable, and that friction transforms the outermost part of the film into a graphitic one, makes it less suitable for applications in hybrid bearings. The transformation and transfer of material results in wear of the coating, which is more significant with higher loads, which is common in hybrid ball bearing applications. Furthermore a coating is not of much use, if the adhesion of the surface modification is suboptimal, and the film ruptures and the surface becomes as pristine after a short time under application conditions. Further reducing the friction coefficient while simultaneously increasing the coating adhesion to the substrate are the key benefits of the change from a-C:H surface modifications to fluorine-containing amorphous hydrogenated carbon (a-C:F:H). There is a large variety of possible coating procedures which result in an a-C:F:H coating. Most employ the PECVD route using fluorine containing precursor molecules or a mixture of one carbon source and one fluorine source [33, 37–48]. For the first route, the single precursor route, most often CHF_3 is used, while for the precursor mixture route most often the combination of CF_4 and ethene is used. Furthermore, alternate coating processes lead to similar coating compositions, one being sputtering polytetrafluoroethylene (PTFE, brand name Teflon[®]) [49] and another being sputtering a graphite target in a gas atmosphere containing fluorocarbons [50]. In this case magnetron sputtering was employed, which utilizes pure electric power to ionize carbon atoms from the so-called target and to transport them to the substrate. On their way reactive atoms hit the hexafluoropropene (C_3F_6) or hexafluoroethane (C_2F_6) molecules, creating the reactive species necessary to form the a-C:F:H coating. For all the different routes the different reactive species include not only ions but also radicals like e.g. the trifluoromethyl radical ($\text{F}_3\text{C}^\bullet$). From these radicals further fluorine atoms

can be abstracted, and a CF_2 moiety (difluorocarbene) is created, which readily adds to the film. Since such a CF_2 particle is quite stable, the carbon atoms seldom react further to form more than two carbon carbon bonds, unless another fluorine atom is abstracted. This may only occur while such a film functional group is in the outermost, still growing layer. Resultantly any further reactions are relatively improbable, hence a coating that contains fluorine is less diamond-like than an a-C:H coating and more polymer-like and dominated by $[\text{CF}_2]_n$ -chains.

Depending on specific deposition process parameters, the finally resulting coating even for the exact same precursor may differ. Regarding the PECVD process e.g. the deposition rate, the fluorine content and the density of the resulting film differs between excitation employing RF only or a combined RF and microwave (MW) approach. The RF frequency is preferable over the RF-MW approach [42], but also the applied bias plays an important role. Both wear resistance and fluorine content of an a-C:F:H coating depend on the bias, while the improved wear resistance with increased process bias is unfortunately accompanied by a reduced fluorine content [37], which is preferable from point of view of the COF, the chemical inertness and the facilitation of cleaning. On the other hand again, the higher the fluorine content, not only the lower the wear-resistance, further mechanical properties are also connected to the fluorine content of the deposited a-C:F:H film: The hardness of a coating of higher fluorine content is decreased and the film is more polymer-like [33, 38], but this again means a less brittle and better adhering surface modification [37, 40, 51, 52]. The reason for the improved adhesion is the reduced internal stress, exactly because the deposit is more flexible and more polymer-like. Regarding the fact, that in a ball bearing the coating on ball and track is overrun very often very soon in practice, a less brittle and more flexible and better adhering film is preferable. In the end the application is decisive, which kind of coating is the optimal for the desired application.

There is another fact that has not really been touched so far, which comes into play when the different loads on the coating under application conditions are discussed: the thermal load. The nanoscopic temperatures occurring at the ball track interface at the exact moment when the slip takes place during the overrunning is not measurable, but there is certainly an elevated temperature, if only locally. Regarding the temperature stability, the coating stability does depend on the fluorine content. The higher the fluorine content, the smaller the temperature stability, because the temperature damage proceeds via CF_4 -loss of the coating, which consequently changes its atomic structure from amorphous to graphitic [39, 40]. The transition temperature, at which the temperature damage starts to get severe, decreases with increasing fluorine content, but reassuringly is for a 15 atom-% fluorine coating at 300 °C. So under normal conditions even for 50 atom-% of fluorine in a bearing coating, the temperature stability will be sufficient. Furthermore

it has been reported that the chosen precursor influences the temperature stability of a coating, and that the CHF_3 precursor renders the temperature stability of the film superior to a surface modification resulting from CF_4 precursor molecules [44].

The slip at the ball track interface and the respective occurring temperature as well as the nanoscopic dimensions of junctions have been touched already. In the course of the work underlying this thesis the question was investigated, what the molecular processes in these junctions are. Furthermore it was of interest, what the difference is between a coated bearing part and an uncoated bearing part on the nano-scale under sliding conditions. These questions can only be answered by appropriate computer simulations so far, because the experimental means are not at hand (yet). The respective simulations need to take at least the area of a junction or better more into account including its atomic structure and properties, which excludes macroscopic simulation approaches, and immediately results in a number of atoms, that is only tractable by one simulation approach: classical molecular dynamics simulations.

4. Classical Force Field Simulations

4.1. From Quantum Mechanics to Classical Force Fields

A molecular system can exactly be described by the time-dependent Schrödinger equation:

$$i \hbar \frac{\partial}{\partial t} \Psi(\mathbf{r}, \mathbf{R}, t) = \hat{H} \Psi(\mathbf{r}, \mathbf{R}, t) \quad (4.1)$$

Here, i is the imaginary unit, \hbar is the reduced Planck constant, t is the time, Ψ is the wavefunction, \mathbf{r} and \mathbf{R} are all degrees of freedom of the electrons and nuclei, respectively. The hamilton operator \hat{H} can be split into the operator of the kinetic energy \hat{T} and the operator of the potential energy \hat{V} :

$$\hat{H} = \hat{T} + \hat{V} \quad (4.2)$$

The operators for kinetic and potential energy in turn can be separated into an electronic part and a part acting on the nuclei (index e meaning electrons and index N nuclei):

$$\hat{T} = \hat{T}_e + \hat{T}_N \quad (4.3)$$

$$= \sum_{i=1}^n -\frac{\hbar^2}{2m_e} \nabla_i^2 + \sum_{I=1}^O -\frac{\hbar^2}{2M_I} \nabla_I^2 \quad (4.4)$$

$$\hat{V} = \hat{V}_{ee} + \hat{V}_{Ne} + \hat{V}_{NN} \quad (4.5)$$

$$= \sum_{i<j} \frac{1}{4\pi\epsilon_0} \frac{e^2}{r_{ij}} + \sum_i \sum_J \frac{1}{4\pi\epsilon_0} \frac{-e Z_J e}{r_{iJ}} + \sum_{I<J} \frac{1}{4\pi\epsilon_0} \frac{Z_I Z_J e^2}{r_{IJ}} \quad (4.6)$$

Here, n is the number of electrons, O is the number of nuclei, e is the elementary charge, r_{ij} is the distance of the electrons i and j , r_{iJ} is the distance between electron i and nucleus J , r_{IJ} is the distance of the two nuclei I and J , Z_I is the atomic number of the nucleus I , and ϵ_0 is the permittivity of vacuum. The summation over $i < j$ and $I < J$ means the summation over i and j and accordingly I and J without considering any interactions twice.

Equations 4.3 and 4.5 result in the possibility to define an electronic Hamiltonian \hat{H}_e :

$$\hat{H}_e = \hat{T}_e + \hat{V}_{Ne} + \hat{V}_{ee} \quad (4.7)$$

The wave function of the system is very complex and depends, as stated by equation 4.1, on all degrees of freedom of all electrons and all nuclei. This leads to the necessity of a first approximation, the ‘‘adiabatic approximation’’ [53, 54]. In the limitations of the adiabatic approximation, which is based on the assumption of a slow perturbation of the system, only the diagonal elements of the exact non-adiabatic wave function are used to construct an adiabatic wave function, which enables the separation of an electronic part χ and a nuclei part Φ of the wavefunction:

$$\Psi(\mathbf{r}, \mathbf{R}, t) = \chi(\mathbf{r}, \mathbf{R}) \cdot \Phi(\mathbf{R}, t) \quad (4.8)$$

Using the time-independent expectation value of the electronic Hamiltonian

$$\langle \hat{H}_e \rangle = \int \chi^* \hat{H}_e \chi d\boldsymbol{\tau} \quad (4.9)$$

where $\boldsymbol{\tau}$ is the entirety of all electronic variables, and the star $*$ denotes the complex conjugate of the electronic wave function, the separability of the electronic wave function yields the possibility to define a time-dependent Schrödinger equation for clamped nuclei

$$i\hbar \frac{\partial}{\partial t} \Phi(\mathbf{R}, t) = \left(\hat{T}_N + \langle \hat{H}_e \rangle \right) \Psi(\mathbf{R}, t) \quad (4.10)$$

which is the famous Born-Oppenheimer (BO) approximation [55]. The BO approximation expresses, that the nuclei move so slowly compared to the adaptation of the electronic state to their position variation, that they effectively move in a static potential of electrons. Thus the time-independent electronic energy $\langle \hat{H}_e \rangle$ for clamped nuclei is the BO potential energy hypersurface V_N^{BO} the nuclei move on. Further approximating the nuclei as classical particles, which is justified in many cases due to the relatively high mass of the nuclei [53], the Hamiltonian of the nuclei \hat{H}_N can be expressed as:

$$\hat{H}_N(\mathbf{R}, \mathbf{P}) = \hat{T}_N(\mathbf{P}) + \langle \hat{H}_e \rangle = \hat{T}_N(\mathbf{P}) + \hat{V}_N^{BO}(\mathbf{R}) \quad (4.11)$$

Here \mathbf{P} is the entirety of the momenta of the nuclei. This can be rewritten to yield the Newton equation of motion for the nuclei [53]:

$$M\ddot{\mathbf{R}} = -\nabla V_N^{BO}(\mathbf{R}(t)) \quad (4.12)$$

This equation results in a set of coupled differential equations for the motion of the classical nuclei. By differentiation of the BO pair potential with respect to the atomic distance, the forces acting on the atoms can be determined:

$$\mathbf{F}_I = - \sum_J \frac{dV_{IJ}^{BO}(r_{IJ})}{dr_{IJ}} \frac{\mathbf{r}_{IJ}}{r_{IJ}} = -\mathbf{F}_J \quad (4.13)$$

Here I and J are indices of specific particles, \mathbf{r}_{IJ} is the vector connecting the particles and r_{IJ} is the absolute value of the vector and $\mathbf{F}_{I/J}$ are the forces in particles I and J . In the so-called quantum molecular dynamics (often also called *ab initio* molecular dynamics or Car-Parrinello molecular dynamics [53]), the BO electronic potential is calculated again for every variation of the coordinates of the nuclei using a quantum mechanical method, be it *ab initio* or density functional theory. In contrast to that, in the classical force field calculation approach, the electronic potential between the nuclei is either calculated in advance and fixed, or empiric parameters are used for the construction of a classical potential.

In summary, contrary to quantum mechanical considerations of atomic or molecular systems, the classical simulation approach does not consider electrons explicitly [53, 56]. The nuclei move on the the potential hypersurface based on the BO approximation and a classical, often empirical, potential, that is called the “force field”(FF). In comparison to quantum mechanical calculations this approximation results in a drastic decrease in computational cost per atom, hence the size of systems that can be studied is drastically increased. On the other hand the implicit consideration of electrons in classical FF simulations automatically results in the impossibility to model chemical reactivity within the investigated system. It has to be mentioned, that so-called reactive force fields have been developed, e.g. the REBO force field often applied in tribology simulations [1], which model reactivity by updating the bonding information based on a specific impact threshold for a specific reaction. The updating results in a predefined reaction product either to be established by changed bonded interactions or the product is placed in the updated system, while the reactant molecules are deleted. Still, in the reactive force field description the potential is classical / empirical, while quantum mechanical potentials are inherently capable of describing reactions.

Focusing on simulations that are meant to depict situations without a significant amount of reactions, classical FF simulations are sufficiently accurate. In case of simulations of tribology this means no significant wear should occur. If there is no significant amount of wear to be expected, the system can be sufficiently accurately characterized by its classical BO potential, for which the separation of bonded interactions V_{bond} and non-bonded interactions $V_{\text{non-bond}}$ is common [56]:

$$V^{BO} = V_{\text{bond}} + V_{\text{non-bond}} \quad (4.14)$$

The practical expressions, i.e. functions, used to construct a potential for classical FF calculations are the topic of the following two sections.

4.2. Non-bonded Particle Interactions

Focusing on the non-bonded interactions, there are three interactions included in the FF simulation potential expression [56, 57], the van-der-Waals forces, the repulsive interactions of the atoms and the electrostatic interactions. In classical FF simulations, atomic properties are fixed, resulting in an inflexibility of the model, which results in the exclusion of the current chemical surrounding of an atom in the simulation approach. Consequently, dipole-dipole interactions involving induced dipoles cannot be depicted correctly: The Debye forces, which arise from the dipole induction by a permanent dipole, and the London forces, which arise from the dipole induction by an induced dipole, are not included in the description. Consequently the van-der-Waals forces cannot be calculated exactly and have to be modeled on average by fixed atom-atom interactions. The fixed van-der-Waals interactions are most often represented by a Lennard-Jones interaction potential V_{LJ} [56] that also includes the atomic repulsion of all the atoms I with all the other atoms J :

$$V_{LJ} = 4\epsilon \left[\left(\frac{\sigma_{LJ}}{r_{IJ}} \right)^{12} - \left(\frac{\sigma_{LJ}}{r_{IJ}} \right)^6 \right] \quad (4.15)$$

Here, r_{ij} is the interatomic distance, ϵ is the depth of the potential, σ_{LJ} is the r-axis intersection. The first summand in the Lennard-Jones potential is the positive, thus repulsive, atom-atom interaction, which is due to practical reasons set to r^{-12} , while the dispersive interactions, the second summand, decay with r^{-6} . This approach is common, but in principle the electronic structure is better represented by the Buckingham potential [58], which in contrast to the r^{-12} -dependence exhibits a $[c \cdot \exp(-c' \cdot r)]$ -dependence of the repulsive interactions.

The respective parameters for van-der-Waals interactions are not necessarily explicitly present for all atom combinations in a set of FF parameters. To be able to generate particle interactions from particle interaction parameters that have been specified, combination rules like e.g. the Lorentz-Berthelot mixing rules may be applied [56]:

$$\sigma_{IJ} = \frac{1}{2} [\sigma_{II} + \sigma_{JJ}] \quad (4.16)$$

$$\epsilon_{IJ} = \sqrt{\epsilon_{II} \epsilon_{JJ}} \quad (4.17)$$

Thus the r-axis intersection of the interaction between particles of different type is com-

puted by the arithmetic mean of the interaction parameters for identical partial types, while the depth of the potential is determined using a geometric mean of the respective interaction parameters for identical atom types.

The second part in the non-bonded interactions are the electrostatic interactions. The calculation of the exact electrostatic interactions is the most time-consuming part of an FF simulation, which is carried out based on the Coulomb electrostatic potential V_C :

$$V_C = \frac{1}{4\pi\epsilon_0\epsilon_r} \frac{q_I q_J}{r_{IJ}} \quad (4.18)$$

Here, $q_{I/J}$ is the charge of nuclei I and J and ϵ_r is the relative permittivity of the material.

Hence the potential expression (4.14) has been developed to:

$$V^{BO} = V_{\text{bond}} + \sum_{I<J} 4\epsilon \left[\left(\frac{\sigma_{LJ}}{r_{IJ}} \right)^{12} - \left(\frac{\sigma_{LJ}}{r_{IJ}} \right)^6 \right] + \sum_{I<J} \frac{1}{4\pi\epsilon_0\epsilon_r} \frac{q_I q_J}{r_{IJ}} \quad (4.19)$$

Here, again the sum over $I < J$ means a summation over I and J while not counting any interactions twice. The bonding part of the potential V_{bond} that has not been described yet is elaborated on in the following section.

4.3. Bonded Particle Interactions

The combination of Lennard-Jones parameters and partial charges for the Coulomb interactions are the non-bonding part of a set of simulation parameters. In addition to the non-bonding part, a bonding part is required, which is meant to model the strength of direct bonded interactions, often modeled by harmonic potentials [59–66] as in case of the OPLS-AA force field used in this thesis [67]. Additionally, the model for the angular interactions within a molecule is also part of the bonded interactions, and it is also often a harmonic potential. Last but not least the dihedral interactions or 1-4-interactions are modeled, often by a cosine-expansion of the Fourier type:

$$V_{\text{dihedral}} = \sum_{i=1}^{N_{\text{torsions}}} \sum_{n=1}^4 C_n \left(1 + (-1)^{n+1} \cos(n\phi_i + \phi_{\text{phase},i}^n) \right) \quad (4.20)$$

Here, ϕ_i is the dihedral angle, $\phi_{\text{phase},i}$ is a phase angle and N_{torsions} is the number of torsional angles. This expression can be reformulated to give the Ryckaert-Bellemans potential V_{RB} expression [68, 69]:

$$V_{RB}(\phi_{IJKL}) = \sum_{n=0}^4 C_n (\cos(\phi))^n \quad (4.21)$$

For all the bonded interactions different models than the one for OPLS-AA exist, especially the angular and dihedral interactions are modeled in various ways in literature, most of the different models are included in the MD simulation package employed for the work underlying this thesis: GROMACS 4 [70]. In summary, the potential expression (4.19) including all OPLS-AA and non-bonded terms becomes:

$$\begin{aligned} V^{BO} = & \sum_{\text{bonds}} k_r (r - r_{eq})^2 + \sum_{\text{angles}} k_\theta (\theta - \theta_{eq})^2 \\ & + \sum_{\text{torsions}} \sum_{n=1}^3 C_n \left(1 + (-1)^{n+1} \cos(n\phi_i + \phi_{\text{phase},i}^n) \right) \\ & + \sum_{I < J} 4\epsilon \left[\left(\frac{\sigma_{LJ}}{r_{IJ}} \right)^{12} - \left(\frac{\sigma_{LJ}}{r_{IJ}} \right)^6 \right] + \sum_{I < J} \frac{1}{4\pi\epsilon_0\epsilon_r} \frac{q_I q_J}{r_{IJ}} \end{aligned} \quad (4.22)$$

Here $k_{r/\theta}$ are the harmonic constants of the bond and angle potentials, θ is the angle between two bonds and the index “eq” means the equilibrium value.

How all the different parameters k_r , r_{eq} , k_θ , r_θ , C_n , ϕ_{phase} and the Lennard-Jones parameters for all the different particles are determined is the topic of the next section.

4.4. Force Field Parameters

In general, the values for the parameters that are combined into a force field are empiric. While there is a standard way to arrive at FFs, by using Hartree-Fock quantum mechanical calculations and a 6-31g* basis, the resulting potentials are not as transferable to various applications as desired due to the several approximations discussed in section 4.1 [53, 56]. Therefore, either quantum molecular dynamics is employed in complex systems, or, commonly, FFs are determined by using experimental values of properties that are of interest and adapting the FF parameters to reproduce the desired value. For instance there are many FF models for water molecules, each of them reproducing one or perhaps some more experimental values separately, but none is universal (so far). One of the water models being a workhorse because it is fitted to the accurately reproduce the

self-diffusion coefficient, is the Simple Point Charge Extended model (SPC/E) [71]. Simple means that the water molecule just has three interaction sites, while other possible interaction sites like e.g. the electron lone pairs of the oxygen atom are not explicitly considered. The reason for this simplification is, that especially for water molecules in addition to the proper reproduction of the desired macroscopic property, the computational effort upon employing this model is a very important factor in FF development. Any additional interaction site is an additional particle *per water molecule*, and thus significantly increasing the computation cost, because usually many water molecules are included in a system. According to the chosen FF, after constructing the FF interaction potentials V_{ij} between two particles, the forces acting on the atoms are derived based on equation 4.13.

Having elaborated on the foundations of the potential construction and calculation of the forces, in the following subsections it is discussed how the actual classical FF molecular dynamics (MD) simulation works. Classical MD simulations are not a highly accurate energy calculation like e.g. quantum mechanics single point calculations are, on the contrary, MD is a time-propagation simulation method that is energetically less accurate but capable of describing dynamic effects. In practice, first of all the limited size of a model may pose problems, which is the reason why the first subsection deals with a solution to this issue, the periodic boundary conditions. In the next section the calculation of exact electrostatics is highlighted, which is time-consuming and hence has to be efficient. Following, the propagation of the system state in time is the next step towards a comprehensive explanation of MD simulation procedure in section 4.7. After that, a part of this chapter illustrates the approach for MD simulations of sliding friction. The last two subsections deal with keeping macroscopic conditions, the pressure and the temperature, close to a desired target average during the course of the simulation.

4.5. Periodic Boundary Conditions

Owing to the fact, that any computer model of a real system is limited in size, the simulation volume, which is often called “box”, exhibits free edges. The free edges may lead to artifacts, or more simply put errors. At free surfaces to the vacuum, the particles in the simulation volume would have no interactions with particles beyond that simulation volume, leading to a very poor representation of the respective phase the particles are in. For example in the solid state the surface atoms would lack interactions with neighbors of one half-space, resulting in shorter interatomic distances, hence the representation of the bulk material would not be satisfactory. Furthermore, the atoms move according to the equation of motion 4.12, which is a differential equation and requires boundary conditions. In addition to the boundary conditions, the initial conditions for

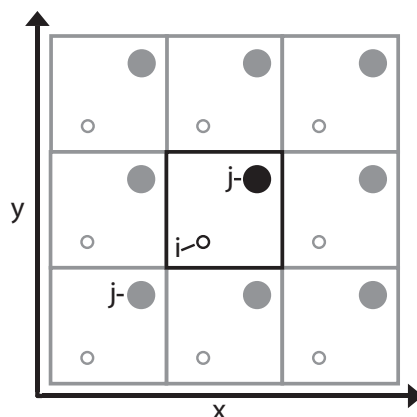


Figure 4.1.: Schematic representation of the periodic boundary condition approach. The simulation system is the black square, while the periodic images are shown in grey.

the particle that shall move are required, which are the initial position and the initial velocity. To provide boundary conditions and erase the unwanted edge effects, a simulation system may be simulated as if it was surrounded by copies of itself. Figure 4.1 shows the approach schematically in two dimensions, a simulation system, represented as black square, is surrounded by identical copies (grey). This approach is called periodic boundary conditions and usually it is applied in all three spacial dimensions [56]. The periodic boundary conditions are one possible choice of boundary conditions for solving the differential equations. Still the method creates errors if the system under consideration is not crystalline [56], but it is a large improvement over a direct edge contact to vacuum. Furthermore, the errors get smaller the larger the systems are. As seen in figure 4.1, the closest interaction of particle i and particle j do not have to be the ones inside of the simulation box. Particle i in the figure has its closest neighbor of kind j not inside the actual simulation system but in the periodic image to the lower left side. Special care is taken, that on the one hand the closest interactions are calculated and on the other hand the interactions are not taken into account (this is the so-called “minimum image convention”). Regarding the electrostatic interactions of a particle another precaution is taken to include not only a single atom, if a group of atoms is effectively acting together electrostatic-wise. Such groups of atoms are called charge groups, and they are defined in the topology in a way, that such a charge group optimally has a net charge of zero. For instance, a group of one carbon atom and three fluorine atoms has an effective charge of zero, which decomposes into the carbon atom carrying three times the positive amount of negative partial charge one of the fluorine atoms carries. In case another particle would only interact with one fluorine atom due to the chosen cut-off that is defined in the input, all atoms of the CF_3 moiety are included in the interactions, although not all of the atoms are below the cut-off distance.

The calculation of exact electrostatics is carried out using the periodic boundary conditions for the Ewald summation approach, which is the topic of the next section.

4.6. Exact Electrostatics Calculation

To calculate the exact Coulomb interaction of all atoms as efficiently as possible the Ewald summation approach [56, 72] may be utilized, which sums up part of the interactions in real space and the other part of the interactions in reciprocal space. The big advantage of the Ewald summation is that the real space short-range interactions sum up quickly in real space, while the real space long-range interactions sum up quickly in reciprocal space. A partitioning of the Coulomb potential hypersurface around a particle is necessary, to decide up to which point the real space summation is carried out:

$$\mathbf{V}_C = \mathbf{V}_{C,\text{short-range}} + \mathbf{V}_{C,\text{long-range}} \quad (4.23)$$

The distance up to which the direct summation is carried out is specified in the simulation input.

Unfortunately, although the Ewald summation is quick, for a large system the reciprocal summation is still not quick enough, because the computational effort scales with the number of particles N as N^2 or when optimized $N^{3/2}$ [69]. In 1993 and 1995 Darden and coworkers introduced an alternate method for Ewald summation [73, 74], that uses a grid on which the charges are assigned by spline interpolation. After assignment of the charges to grid points the grid is Fourier transformed using a three-dimensional fast Fourier transform (FFT) algorithm, hence the electrostatics summation becomes rather simple. This method is called Particle-Mesh Ewald summation and it is highly efficient, because the computation cost scales with $N \cdot \log N$.

Once the interaction potential of the particles is defined by the FF, the geometry and the bonding information are specified and the respective forces have been calculated according to equation (4.13), the sum of all the forces acting on a particle is the net force acting on the atom. Corresponding to this net force the atom shall move for a short amount of time, the time-step, due to the time-propagation step of the MD simulation, which is the topic of the next subsection.

4.7. Molecular Dynamics

Knowing the forces acting on the atoms or particles, be it classical forces or forces derived from quantum mechanical calculations, enables the performance of the actual simulation.

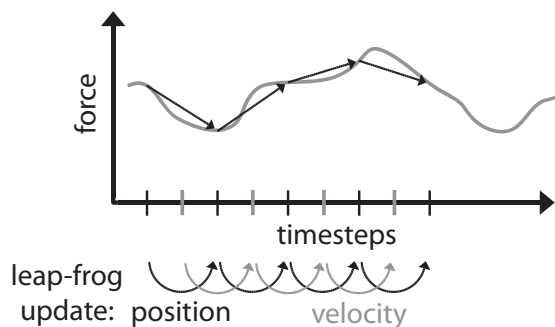


Figure 4.2.: Schematic representation of the fitting of the force development of a system (grey line) by discrete time steps (black arrows) and the “leap-frog” algorithm. The updating of the positions is carried out at the time step intervals, while the velocities are updated in between.

In MD simulations, the so-called time step is performed, which means, that Newton’s equation of motion is integrated to give a velocity and a position after a certain amount of time. In this approach any change of the forces acting on the particle during this time step is neglected. As a result, the system does not evolve continuously in time, more appropriate is the view of subsequent single frames, where nothing is known about the time period between the frames, only the final positions and velocities are known.

Figure 4.2 shows the approximation of a force development (grey line) by discrete time steps, which are represented by the arrows. In principle the arrows would have to be tangential to the force curve at their respective starting points. This shows, that the shorter the time step, the smaller the deviation. The positions of the particles are updated every time step (black arrows), and at that point in time the forces are updated. The velocities of the particles are updated in between, at half the time steps (grey arrows). This way the representation resembles two frogs leaping over each others back. Hence the standard algorithm for the calculation of the new velocity and new position of atoms is called the “leap-frog” algorithm [75, 76]. Since nothing is known about the change of the system state between the discrete steps, the time step Δt used in MD simulations has to be very short with respect to macroscopic time scales and is usually 1 or 2 fs, depending whether high frequency oscillations of e.g. hydroxyl groups shall be resolved or not. To arrive at the updated velocities and positions, the leap frog algorithm uses two different steps for the velocities and the positions separately. Considering the point t in time this means for the equations yielding position \mathbf{r} and velocity \mathbf{v} :

$$\mathbf{v}(t + 1/2\Delta t) = \mathbf{v}(t - 1/2\Delta t) + \frac{\Delta t}{m} \mathbf{F}(t) \quad (4.24)$$

$$\mathbf{r}(t + \Delta t) = \mathbf{r}(t) + \mathbf{v}(t + 1/2\Delta t) \Delta t \quad (4.25)$$

$$\mathbf{r}(t + \Delta t) = 2\mathbf{r}(t) - \mathbf{r}(t - \Delta t) + \frac{\mathbf{F}(t)}{m} \Delta t^2 + \mathcal{O}(\Delta t^4) \quad (4.26)$$

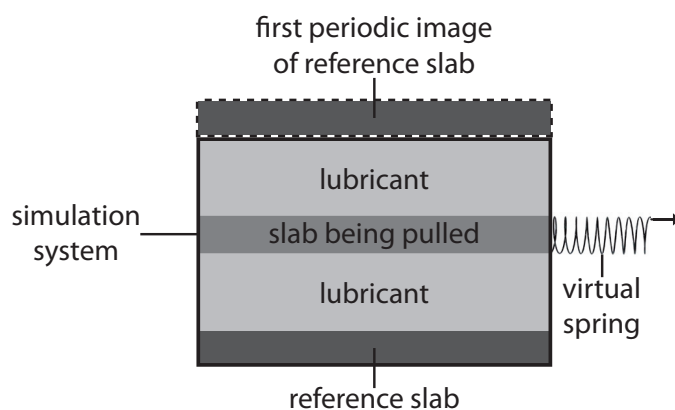


Figure 4.3.: Schematic representation of the simulation approach employed in the work presented here. Two slabs with lubricant between the two are simulated as quasi-infinite stack with periodic boundary conditions in all three dimensions. The upper slab in the simulation volume is pulled by a virtual spring, while the lower slab moves due to “actio equals reactio”.

The above described algorithm for the updating of atomic positions and velocities are performed for the whole system.

In case of MD simulations of sliding friction, the overall acting forces are modified by the pulling of one group of atoms with respect to another group of atoms. The pulling is performed by a virtual spring, and the spring force equals the friction force the simulation system exerts. The next section elaborates more detailed on the virtual spring pulling.

4.8. Virtual Spring Pulling

As mentioned before, the simulations in the course of the work presented here are sliding friction simulations. The reason for the virtual spring pulling of part of the system is the mimicking of a tribometry experiment by lateral pulling of a slab. Figure 4.3 schematically depicts the situation in the simulation volume. The slabs, represented in darker grey, are separated by a lubricant layer (lighter grey). The virtual spring is indicated on the right. Since periodic boundary conditions are applied in all three dimensions, a quasi-infinite stack of slab models results, each slab separated by a lubricant layer from the slabs below and above. The upper lubricant layer separates the upper slab from the first periodic image of the lower slab (box with dashed contour). For applying the pull force, the system has to be partitioned into at least two groups. One group is the reference group, which is treated according to actio equals reactio in the same way as the pulled group, but with the opposite sign. The pull group is defined as the group, on which the virtual spring acts. The force equally acts on all atoms of the pull group, and the spring potential is harmonic. During the course of the simulations the force acting

between the center of mass (COM) of the pulled group and the end of the virtual spring varies and is recorded according to a previously defined step interval. The end point of the spring is moving with a constant velocity that is chosen beforehand. In addition to the friction force, the perpendicular force acting on the system has to be known to calculate the coefficient of friction according to equation (1.1). So the only information that is extracted from the simulations is the average friction force and the average normal force.

Any thermodynamical equilibrium properties are not of interest because the system will not evolve to an equilibrium, because of the virtual spring pulling. In general, the total energy of a system is composed of the kinetic energy and the potential energy of the particles. The kinetic energy of the particles in turn determines the instantaneous temperature of the system. If the system temperature rises, the potential energy on the other hand decreases, because in the microcanonical ensemble the internal energy is constant. Since macroscopic experiments are carried out under conditions of constant temperature and pressure, not under the conditions of constant volume and energy, in order to mimic macroscopic measurement conditions, temperature and pressure have to be maintained at an averaged constant level.

Keeping temperature and pressure constant on average is assured by the so-called barostat and thermostat algorithms, which is the topic of the next subsection.

4.9. Barostat and Thermostat

The pressure of a simulation volume according to the virial theorem [77] is the net force acting in the direction normal to a simulation volume surface divided by the surface area. The pressure in x-direction e.g. results from the net force in x-direction which is calculated as sum of all x-components of the force vectors acting on the plane, divided by the surface area of the simulation volume perpendicular to the x-axis. To keep the pressure over the course of the simulation more or less at the target value, a barostat algorithm is employed, which alters the box vectors that span the surface area to yield the desired pressure by establishing the “correct” area corresponding to the forces.

As mentioned above, the proper reproduction of thermodynamic equilibrium properties of the system depends on the barostat and on the thermostat. However, since the system is not in equilibrium due to the virtual spring pulling, the thermodynamically correct barostat algorithm by Parrinello and Rahman [78, 79] suffers from large volume oscillations [80, 81]. Another possible barostat algorithm is the Berendsen barostat [82]. This Berendsen barostat algorithm is based on scaling the box dimensions at every predefined step interval. According to the box scaling, the positions of the particles are also scaled.

The scaling is based on the time derivative of the pressure, the target pressure \mathbf{p}_0 and the pressure coupling time constant τ_p :

$$\frac{d\mathbf{p}}{dt} = \frac{\mathbf{p}_0 - \mathbf{p}}{\tau_p} \quad (4.27)$$

The deviation of the current simulation pressure from the reference pressure exponentially decreases with time constant τ_p . The scaling of the box vectors and particle coordinates is carried out according to a scaling matrix \mathcal{S} that is defined by the Kronecker δ_{ij} , the pressure coupling interval n_p and the isothermal compressibility κ :

$$\mathcal{S}_{ij} = \delta_{ij} - \frac{n_p \Delta t}{3 \tau_p} \kappa (p_{0,ij} - p_{ij}(t)) \quad (4.28)$$

It can be specified in the simulation input whether complete and isotropic pressure scaling shall be used or not. For a layered system e.g. the x- and y-directions of the plane may be coupled depending on each other, while in the direction of stacking (z-direction) the pressure may scale differently. Such a pressure scaling is called semi-isotropic pressure scaling. Furthermore the scaling in the x-y-plane directions may also be artificially suppressed by setting the compressibility to zero.

Analogous to the pressure coupling, the temperature coupling in MD simulations may also be performed by a so-called thermostat algorithm. The temperature of the system is determined by the Maxwell-Boltzmann distribution and the equipartition theorem, hence the temperature of the system determines the average velocity of the particles \bar{v} via:

$$\bar{v} = \sqrt{\frac{3RT}{M}} \quad (4.29)$$

R is the universal gas constant, M is the molar mass of the particle. In this way by averaging the velocities and taking the particle masses into account the temperature of the system can be determined. According to the deviation of system temperature and target temperature, the velocities of the particles are rescaled to reach the desired target temperature over time. In case of the Berendsen thermostat [82] the temperature of the system is slowly changed to be in accordance with the target temperature:

$$\frac{dT}{dt} = \frac{T_0 - T}{\tau_T} \quad (4.30)$$

The time constant τ_T is again the time constant of the exponential decay, in this case the decay of the temperature deviation. This exponential driving force towards the desired average value suppresses variations of the temperature, which would be needed to compensate the potential energy fluctuations. Again a more accurate algorithm exists, the

Nosé-Hoover thermostat [83, 84], which would be preferable, if thermodynamic equilibrium properties would be of interest. Yet thermodynamic equilibrium properties are not of interest, only the friction force and the force perpendicular to the sliding plane. Thus instead of the Parrinello-Rahman barostat in connection with the Nosé-Hoover thermostat, the more stable Berendsen algorithms are the preferable choice for barostat and thermostat.



Part II.

Experimental Investigations

Chapter 3 highlighted many features of via PECVD deposited coatings that are very useful for tribological applications. Which properties of a coating are key features, and which properties are less important, has to be decided with focus on the desired application. First of all, when hybrid ball bearings are subject of the development of a specialized coating process, different materials and geometries have to be considered in the design of the process. In addition to that some of the materials are insulators, the ceramics ball and the polymer cage, or metal conductors in case of the steel rings, resulting in different electric fields under the same PECVD coating parameters. The different electric fields in turn lead to different coating thicknesses and deposition rates. Furthermore the polymeric cage is insulating, which implies the danger of polymer aging, if the initial conditions of the plasma with inert gas cleaning are too harsh on the material. Nonetheless a single batch process for all bearing parts is desired.

Naming the requirements for a hybrid ball bearing coating that is intended for food and drug industry applications, first of all a good adhesion to the substrate is mandatory to preserve the surface modification throughout the bearing life, which is longer than the lifetime of a standard steel bearing. Additionally improved frictional characteristics as well as facilitated cleaning are desired. For instance in filling lines in the food industry regular cleaning and sterilization are mandatory. This leads to the desire of improved corrosion protection by the coating, which has to be chemically inert to withstand possible chemical sterilization or even steam sterilization. Furthermore often a hybrid bearing is intended for dry running conditions, which means no lubrication, or it may be intended for the lubrication with the medium, which is most of the times water-based.

In the course of the project NANODYN an attempt was made to develop a single batch process for all bearing parts, which offers a multifunctional improvement of as many of the desired features stated above as possible. While the development of the coating was carried out by our colleagues at the “Fraunhofer Institut für Grenzflächen- und Bioverfahrenstechnik” (Fraunhofer IGB) in Stuttgart, part of the work discussed here was the experimental testing of the coating effect on sliding friction by tribometry.

In this chapter first of all the a-C:F:H coating process and analytics will be discussed. *The author had no part in the development of the coating, nor in the characterization. The chapters 5.1 and 6.1 are reproductions of the work of others, our colleagues at the Fraunhofer IGB.* Nonetheless, to give a comprehensive overview of the work it is necessary to highlight the main features of the coating. As a second part of the experimental details, the procedure of the measurements and the employed tribometer are given.

Following, the experimental results will be presented and afterwards discussed, while the chapter closes with conclusions regarding the experiments.

The results discussed here are intended for publication in the journal Langmuir [85].

5. Experimental Details

In the first part of this section the details on the coating process and the analytics on the resulting deposit are given. The second subsection discusses the employed tribometer and the general measurement procedure as well as the chemicals and materials for the experiments.

5.1. Hybrid Ball Bearing Part Coating

5.1.1. PECVD a-C:F:H Coating Process

Bearing components, namely PEEK cages, ceramics balls, inner steel ring, outer steel ring and bearing steel tribometry specimens were coated with fluorocarbon polymeric deposit (a-C:F:H) in a home-built reactor. The process employed continuous wave low-pressure plasma polymerization with trifluoromethane (CHF_3) as precursor molecule. Argon was employed as carrier gas. The schematics of the reactor are displayed in figure 3.2 on page 33. The reactor is a symmetrical, capacitively coupled parallel plate reactor. The RF excitation at the frequency of 13.56 MHz was provided by a Dressler mpg 1306 rf power generator, which was coupled to a Nye Viking Antenna Impedance Matching Network MB-IV-A. The distance between the electrodes was 5 cm and the area and lateral dimensions of the electrodes matches DIN A3 (624 cm²). The gas flow of the precursor was maintained at 25 ccm per minute using a MKS MultiGas Controller 647C and a MKS mass flow controller (maximal range 200 ccm per minute N). To achieve a cold plasma the pressure during the coating process was reduced to 0.12 mbar by a MKS 600 Series pressure Controller and a MKS type 122A baratron and a MKS butterfly valve.

5.1.2. Coating Thickness Analytics

For the determination of the coating thicknesses spectroscopic ellipsometry using a Sen-tech SE801 for silicon wafer test specimens was carried out. Furthermore the coating thickness on coated ceramics balls was determined using a spectroscopic reflectometer microscope (NanoCalc). From spectroscopic ellipsometry the thickness was derived using

a cauchy model for the refractive index. No optical absorption was measured. For thickness measurements on the ceramic balls the respective refractive indices of the ceramics substrate and the a-C:F:H coating were fixed ($n = 2.27$ at 632 nm and $n = 1.4$ at 632 nm, respectively). The refractive index of air was assumed to be 1.

5.1.3. Chemical Analysis of the Film by XPS

To determine the chemical composition of the resulting coating, X-ray photoelectron spectroscopy (XPS) was used with an incident X-ray angle of 90° . The instrument was a Kratos Axis Ultra spectrometer (monochromated Al K alpha radiation, 1486.2 eV) and the investigated spot was of the dimensions of approximately $0.3 \text{ mm} \times 0.7 \text{ mm}$.

5.2. Tribometry

5.2.1. Chemicals and Materials

The following chemicals have been employed in the experiments as received:

- “AnalaR NORMAPUR[®] Acetone” from BDH PROLABO[®] VWR International GmbH
- “ROTIPURAN[®] Ethanol” from Carl Roth GmbH & Co. KG
- “2-Propanol puriss. p.a.” from Sigma Aldrich (#33539)
- “Aqua Ad Injectabilia” from DeltaSelect GmbH in 10 mL ampoules
- “Krytox[®] GPL 104” PFPE oil from DuPont
- “UHU Metall Kontaktkleber” metal glue from UHU GmbH & Co. KG
- “Soluwash[®] S akachemie[®] Spezialreiniger” from PUFAS Werk KG / Decotric GmbH

The following materials have been used in the experiments:

- B.BRAUN Injekt[®] 5 mL syringe
- B.BRAUN size 2 hollow needle ($0.80 \text{ mm} \times 40 \text{ mm}$)

The investigations presented in this thesis are based on a DIN 623 type 6001 hybrid ball bearing supplied by our partner Cerobear GmbH, Herzogenrath, Germany. Hence 4.763 mm diameter silicon nitride balls were used in the coating process and in the tribometry experiments. The steel specimens for the tribometry were also manufactured by Cerobear GmbH from the same X30CrMoN15 1 steel that is employed for the manufacturing of the ball bearings using the exact same machines and cubic boron nitride

lathe tools as for the hybrid ball bearing parts. Prior to lathing the steel was hardened by heat treatment. Three 7.8 mm deep M3 screw threads in 120° angle on a 16 mm diameter were tapped into the bottom side of the 25 mm diameter specimens.

The employed tribometer was a BASALT MUST, Tetra GmbH, Ilmenau, Germany. The two cantilever units used throughout all of the experiments had the order number 91007 at Tetra GmbH. The cantilevers had the springs constants in perpendicular direction of 22.2 N m⁻¹ and 19.196 N m⁻¹, respectively, while the spring constants in tangential direction have been 29.1 N m⁻¹ and 22.459 N m⁻¹, respectively.

5.2.2. Experimental Procedure

5.2.2.1. Preparation

Careful not to touch the sliding surfaces, the bearing steel specimens were handled with powder-free nitrile gloves. Furthermore, with tweezers that were cleaned each time simultaneously with the balls, the silicon nitride balls were also handled with care. Before each of the experiments, ceramics balls and steel specimens were cleaned by brandishing in acetone, ethanol and 2-propanol consecutively. This procedure is in accordance with the general cleaning approach of the hybrid ball bearing manufacturer, Cerobear GmbH, Herzogenrath, Germany. Between the steps and afterwards the parts and tweezers were dried using pressurized air. After the parts have been dried, the silicon nitride balls were glued to the cantilever unit of the tribometer.

Figure 5.1 shows the tribometer with assembled rotation unit, specimen holder and specimen as well as with the mounted cantilever unit. The box in the lower part of the housing is the rotation unit, that rotates the bearing steel specimen, the smallest cylinder visible on top of rotation unit and specimen holder. A silicon nitride ball is glued to the cantilever of the cantilever unit, while both black fiber optics sensor cables are visible in the upper part of the housing. A zoom on the cantilever and fiber optics unit is shown in figure 5.2.

The steel specimens were screwed on top of a specimen holder on the rotating unit (RM120) by three screws. Lubrication was applied using a syringe and a hollow needle. The lubricants have been applied drop-wise on the sliding surface of the steel specimen. For PFPE lubrication 0.2 mL Krytox[®] GPL 104 covered the entire specimen surface, while in case of lubrication with water 0.3 mL lubricant formed a droplet in the middle of the steel specimen.

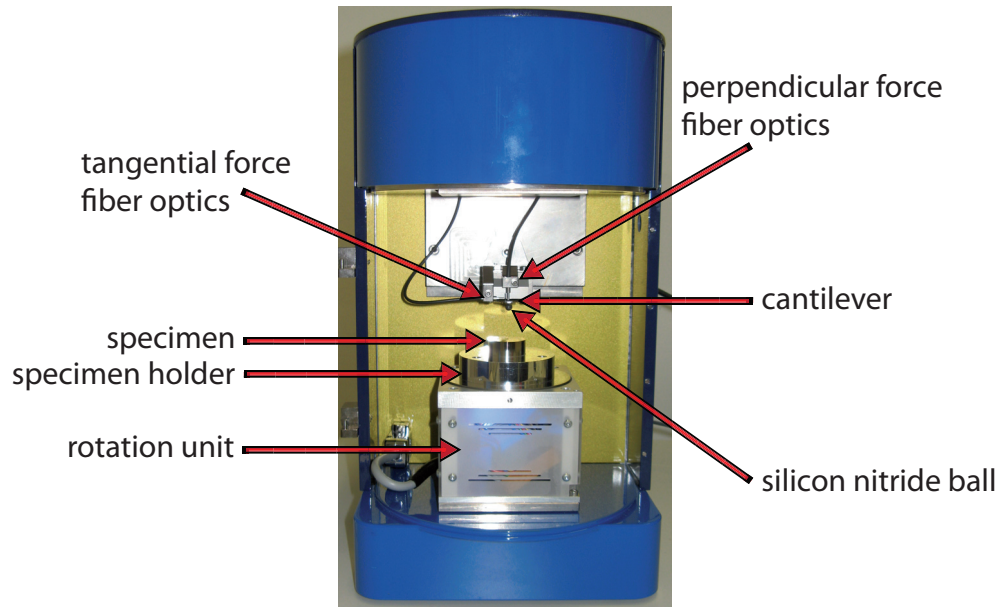


Figure 5.1.: Photograph of the tribometer employed in the tribometry experiments, a BASALT MUST from Tetra GmbH, Ilmenau, Germany.

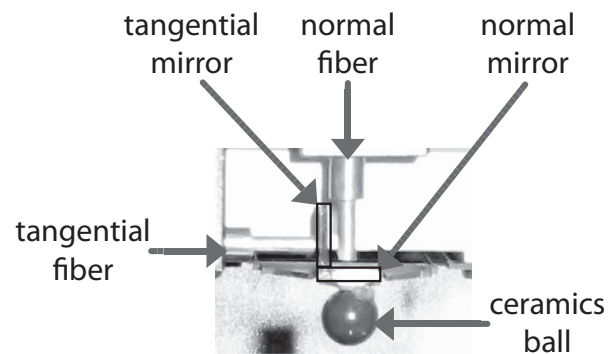


Figure 5.2.: Fiber optics and cantilever unit of the tribometer employed for the work underlying the experimental part of this thesis. A silicon nitride ball is glued underneath the cantilever. Two perpendicular mirrors reflect the light emitted by the fiber optics sensors.

5.2.2.2. Procedure

Due to this droplet formation, for water lubrication only part of the specimen surface was covered. Hence for water lubrication, the experiments were carried out on the same radius of 2.632 mm at 20 RPM three times, after it had been clarified that no significant wear occurred. In case of PFPE lubrication or no lubrication at all (called NEAT) the whole specimen surface could be used. Hence three consecutive experiments employing the same ball and specimen were carried out on three different radii, 2.632 mm, 5.263 mm and 7.519 mm. A constant relative speed of the surfaces of $5.512 \cdot 10^{-3} \text{ m s}^{-1}$ was maintained by rotation speeds of 20 RPM, 10 RPM and 7 RPM, respectively. This relative speed of the surfaces is about the same as the sliding speed due to slip at the ball-track-interface in a type 6001 ball bearing at 850 RPM. The target perpendicular force was 4 mN for all experiments, which results for these materials in a maximum Hertzian pressure of 874 bar. The experiments have been carried out at a temperature of 20 °C and a relative humidity of 50%. The duration of the experiments was 30 minutes. During this time about 100,000 data points each for tangential and perpendicular force were recorded. A cumulative average of the calculated friction coefficients was used as measurement result. All possible different coating situations of ball and steel specimen have been considered: Ball and specimen coated, both uncoated, ball uncoated and specimen coated and vice versa. In combination with three different lubrication states, this results in 12 sets of experiments. One set of experiments comprised at least fifteen experiments each: five different pairs of ball and specimen, for which at least the three usual measurements have been carried out. Longer-term measurements were performed at least once for each coating condition and lubrication state, to determine the wear characteristics of the systems. For water lubrication, longer-term measurements required compensating the evaporating lubricant because no cooling was applied. Hence 6 drops of water were added every half an hour. The shortest longer-term measurements were carried out for water lubrication, in which case the measurement duration was 6 hours, which is 12 times the usual measurement duration and revolutions. The longest measurement has been carried out for PFPE lubrication with 120 hours, while in case of no lubrication 66 hours was the longest measurement duration.

6. Experimental Results

6.1. Coating Analytics Results

6.1.1. Coating Thickness

As determined by spectroscopic reflectometer microscopy, the coating on the silicon nitride balls was the thinner coating of the two different bearing parts employed in tribometry. Depending on the duration of the PECVD coating, the thickness on a silicon wafer according to ellipsometry develops as displayed in table 6.1. The coating thickness is proportional to the PECVD process duration. Coating growth is about 1 nm per 10 seconds. The coating of specimens that have been employed in the tribometry experiments has been carried out for a time of 600 s. The thickness of the coating on the ceramics ball has been determined by reflectometer microscopy to be about 70 nm. The thickness of the coating on the steel parts is beyond 100 nm. These thicknesses mean that the coating resulting from the PECVD coating process is a well adhering closed film. Since the applied load in the tribometry experiments is very low, wear is very unlikely to occur. The maximum Hertz contact stress is only 874 bar in comparison to a usual Hertz contact stress in a hybrid ball bearing of 17,500 bar.

6.1.2. Chemical Analysis of the Coating

The chemical analysis by XPS (also known as ESCA) yielded the data on the atomic composition of the coating as shown in table 6.2. The table shows the different relative amounts for carbon atoms in different chemical environments on the left, and the two rightmost columns are the amounts of oxygen and fluorine detected. Adding up the

Table 6.1.: The coating thickness on silicon nitride balls as determined by spectroscopic reflectometer microscopy, the coating thickness is given in nm, the time of plasma treatment in s. Precursor molecule for the PECVD coating process was trifluoromethane.

time [s]	coating thickness [nm]
600	60 ± 5
1200	120 ± 5

Table 6.2.: The coating atomic composition on silicon wafer as determined by X-ray Photoelectron Spectroscopy (XPS), the binding energy E_B is given in eV, the relative amounts of the different atomic species are given in %. The amount of oxygen is not correctly measured, since at least the same amount as for carbon bound to oxygen should be found. Precursor molecule for the PECVD coating process was trifluoromethane.

<i>atom in moiety</i>	E_B	rel. amount
<i>C in CF₃</i>	294.0	7.8
<i>C in CF₂</i>	291.9	9.5
<i>C in CF</i>	290.3	2.7
<i>C in C=O</i>	289.2	9.5
<i>C in C-CF</i>	287.4	12.1
<i>C in C-H</i>	285.9	4.4
O		3.2
F	689.0	50.8

relative amounts of carbon atoms that are bound to fluorine or in close proximity to a fluorine-substituted carbon atom, this results in 32.1% carbon. Since the spectrum was obtained at an incident X-ray radiation angle of 90°, the penetration in the direction of the thickness of the film is about 5 nm [27]. Therefore the results shown here stem from analyzing a total thickness of 10 nm. Neglecting the amount of carbon bound to oxygen and hydrogen and focusing only on the carbon bound to fluorine directly or indirectly, the ratio of fluorine to carbon atoms is about 1.6.

6.2. Tribometry Results

As stated in the introductory part of this thesis, friction in hybrid ball bearings is very complex. Hence the overall bearing friction moment cannot be concluded from sliding friction measurements, because sliding friction is only one of the contributions to the overall bearing friction moment. However, at the same time, the sliding friction measurements can directly probe the influence of the plasma surface modification on the sliding friction behavior. This is because many different contributions are mixing in the bearing friction, and friction measurements in general are very sensitive to minuscule variations in the measurement parameters [86]. Masking various different contributions by focusing on one main factor seems to be an appropriate way to approach the task of directly investigating surface effects by macroscopic measurements. Furthermore, the sliding friction between ball and track is one constant major contribution to the overall bearing friction moment, which can be seen from the Stribeck-curve (figure 1.4 on page 10). The experiments carried out were designed to specifically probe the influence of the surface modification. To this end, drastic deformations because of a high applied

Table 6.3.: Elastic Moduli E and Poisson numbers ν of the silicon nitride for the ceramics balls and the X30CrMoN15 1 steel for the bearing steel specimens. The elastic moduli are given in GPa.

	Si ₃ N ₄	X30CrMoN15 1
E	320	213
ν	0.27	0.30

load or significant wear of the involved friction partners had to be avoided. With a normal force of 4 mN on the bearing components, the applied load was not very high.

The material constants of the silicon nitride balls and the bearing steel are given in table 6.3. The radius of a type 6001 ball bearing ball is 4.763 mm and the steel specimen is considered a plane. Consequently, according to Hertz theory the maximum pressure in the apparent area of contact at 4 mN perpendicular force on the ball is according to equation (2.5) exactly 874 bar. At such a low pressure, the deformation of the employed parts is negligible considering elastic moduli of at least 213 GPa. Furthermore the contact stress is small enough to prevent significant wear. Hence the experiments are truly designed in a way that is capable of probing the influence of the surface modification by PECVD on the sliding friction.

For all experiments, the respective numbers of data points and obtained cumulative average coefficients of friction are given in tables in the appendix, section B.

6.2.1. Experiments Without Lubrication

Figure 6.1 shows the measured sliding COFs under NEAT conditions as box plots. The median of the results is shown as orange bar while the box starts at the 25%-quartile and reaches up to the 75%-quartile, thus contains 50% of the results. The width from the minimum of the measurement results to the maximum of the various measurement results is indicated as whiskers (min.-max. whiskers). The COFs that result from longer-term measurements are displayed as red crosses and are not included in the box plots shown in the graph. The significant difference between the obtained COFs of the two measurement series with uncoated steel specimen on the left and the two series with surface-modified specimens on the right is the most prominent feature of the graph. In addition to the variation of the results, the absolute value of the COFs also are drastically larger for the measurements with coated specimens. Furthermore, the variation of the results increases from the left part to the right part even when this is viewed relatively, the relative variation increases from about 28% to about 45%. The reference COF of about 0.2 is not significantly changed by coating of the ceramics ball only. In contrast to that, the COF changes drastically to an average of about 0.75, if only the steel specimen is coated, which is not significantly reduced to about 0.7 if the ball surface is modified

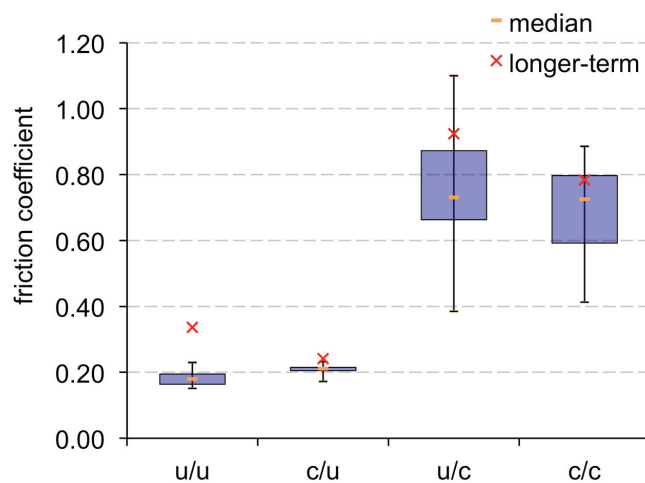


Figure 6.1.: Measured friction coefficients as box plots with whiskers indicating minimum and maximum of the experimental results with no addition of lubricant (NEAT). The median of the results is marked as orange bar, the box starts at the 25%-quartile and reaches to the 75%-quartile, thus contains 50% of the results. From left to right: uncoated ball / uncoated specimen, unmodified reference (10 measurements), c/u only silicon nitride ceramics ball coated (11), u/c only bearing steel specimen coated (15), c/c ball and specimen coated (15). Red crosses: longer-term friction measurement results indicating whether or not wear is observed.

in addition to the steel specimen coating. However, seemingly wear is prevented by the coating of the steel component: If the bearing steel specimen is not modified, the results of the longer-time measurements are not within the width of the min.-max. whiskers. If the surface modification has been applied to the steel specimen, the COFs resulting from longer-time experiments are well within the range of the min.-max whiskers. Thus surface modification of both sliding interfaces may still be useful under dry running conditions in the long run, but further long-time studies are required to corroborate this conclusion.

6.2.2. Experiments with Water Lubrication

In analogy to the measured COFs without lubrication, the results of the four different sets of experiments with addition of pure water as lubricant are displayed in figure 6.2. For a given coating condition the variations of the determined COFs are large. The absolute COF values that have been measured are also rather large. For the reference system with uncoated sliding surfaces the measurements give an average COF of about 0.6. No significant change of the measured COF is observed in case of the pairing of coated ceramics ball with uncoated steel specimen, while the distribution of the results shows a slightly reduced width. In contrast to dry running, in case of water lubrication

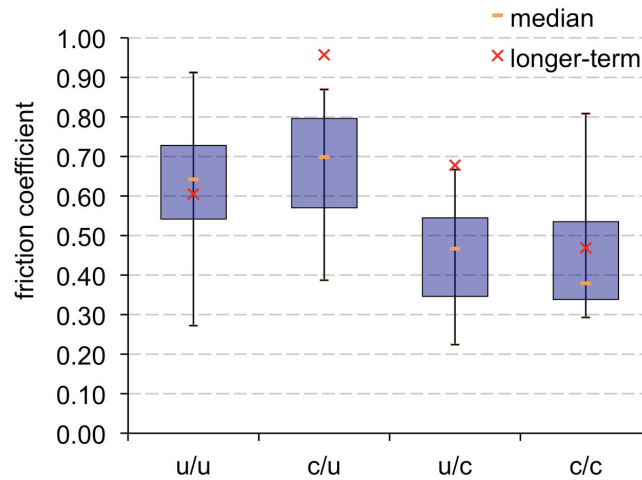


Figure 6.2.: Measured friction coefficients as box plots with whiskers indicating minimum and maximum of the experimental results with water lubrication. The median of the results is marked as orange bar, the box starts at the 25%-quartile and reaches to the 75%-quartile, thus contains 50% of the results. From left to right: uncoated ball / uncoated specimen, unmodified reference (14 measurements), c/u only silicon nitride ceramics ball coated (18), u/c only bearing steel specimen coated (16), c/c ball and specimen coated (16). Red crosses: longer-term friction measurement results indicating whether or not wear is observed.

the surface modification of the bearing steel specimen has a positive influence on the COF: The COF is reduced to about 0.45 by coating of the steel specimen only, while this value is not significantly further reduced by additional modification of the ceramics ball surface. However, the wear behavior does change with additional coating of the ball. If the tribological system is lubricated with pure water and only one sliding surface is modified, the longer-time measurement COFs are not within the min.-max. whisker range. In contrast to that, if both surfaces are coated or both surfaces are uncoated, no significant wear is observed. Concluding, the modification of both surfaces reduces the COF by 27% and wear is effectively prevented.

A further corroboration of this result can be stated based on the experiments on the assembled and completely coated type 6001 hybrid ball bearings *performed by the bearing manufacturer Cerobear GmbH*. Although the measurements employed pairs of assembled bearings and the overall friction moment of this pair of bearings was determined, a significant friction moment reduction for several different lubrication states with water-based lubricants was observed [87]. Using the custom-built test rig the obtained friction moment values at 850 RPM showed a friction moment reduction compared to the un-

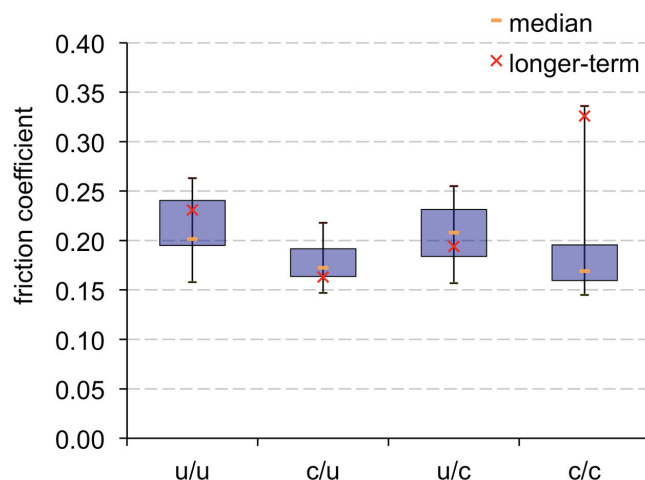


Figure 6.3.: Measured friction coefficients as box plots with whiskers indicating minimum and maximum of the experimental results with perfluoro polyether (PFPE) lubrication. The median of the results is marked as orange bar, the box starts at the 25%-quartile and reaches to the 75%-quartile, thus contains 50% of the results. From left to right: uncoated ball / uncoated specimen, unmodified reference (12 measurements), c/u only silicon nitride ceramics ball coated (14), u/c only bearing steel specimen coated (15), c/c ball and specimen coated (15). Red crosses: longer-term friction measurement results indicating whether or not wear is observed.

modified reference of 42% for lubrication with tap water, a reduction of 20% for milk lubrication and a reduction of 25% employing lubrication with distilled white vinegar (25 weight-% acetic acid in water).

6.2.3. Experiments with PFPE Lubrication

For the lubrication of the specimen surface with PFPE the results of the tribometer experiments are displayed in figure 6.3 analogously to the other two lubrication states. For PFPE lubrication the situation is different from the other lubrication states: Compared to the uncoated state, the coating of the ceramics ball generates a notable reduction in the measured COFs. The modification of the surface of the ceramics ball according to the measurements reduces the friction coefficient by about 14%. The average COF resulting from measurements employing the uncoated reference of 0.225 is reduced to about 0.175 upon coating of the ceramics ball. If only the bearing steel specimen is coated, the reference value is nearly not changed at all. Unfortunately the coating of the steel specimen in addition to coating of the ceramics ball leads to an average COF of about 0.2, which is even higher than the COF for coating the ball only. However, this result is due to two unusually high measurement results, showing how sensitive measurements are to

minuscule changes in measurement conditions. The reasons for the surprising difference has not been unveiled yet. For all other experiments the min.-max. whiskers are more or less symmetric below and above the average values. For PFPE lubrication and both surfaces coated this is not the case, the maximum-result antenna is unusually long. Excluding the two COF values of this one specimen from the calculation of the average, the modified average friction coefficient is with about 0.17 even lower than in case of only the ball surface modified. On the other hand, the longer-time measurement was performed using exactly this specimen in question, hence leaving the two measurements out of consideration would create the false impression, that wear occurred. Consequently, including the two questionable results, the wear behavior of all four systems is not surprising. Since a high-performance lubricant was employed, no wear was observed, just as expected. In summary, the experiments on PFPE lubrication showed that the measured COF is already reduced by 14% if only the ceramics ball surface is coated, which is a large improvement considering the fact that Krytox[®] GPL 104 is a high-price high-performance lubricant. Only when focusing on a multifunctional treatment of the bearing parts in a single batch process, the additional coating of the steel part is advisable, because of the positive results on reduced COF under water lubrication conditions.

As in case of the results with water lubrication, the positive influence of the surface coating with PFPE lubrication is confirmed by the measurements on overall bearing friction moments *carried out by our colleagues at the Cerobear GmbH*. The bearing manufacturer employed the corresponding PFPE fat Krytox[®] GPL 204 that is based on the PFPE oil (Krytox[®] GPL 104) used in the tribometry. Lubricating the employed bearing pair with GPL 204, at 850 RPM the measured friction moment was reduced by 27% [87].

7. Discussion of the Experimental Results

From the determination of the coating thickness on the ceramics ball it can be concluded, that the coating of all bearing parts that have been employed in the experiments is at least of the order of 70 nm and above. This results in a total coverage of the surface, because the surface roughness determined via AFM measurements at the Fraunhofer IGB is below 50 nm. Furthermore the results of the chemical analysis showed, that a highly connected and thus resilient network of fluorinated carbon atoms is the main part of the upper 5 nm of the coating. No trace of the underlying substrate was found in the XPS analysis.

Employing ceramics balls and bearing steel specimens with pristine but also with coated surfaces in tribological experiments, the change in frictional behavior has been investigated. Considering all experimental results on the sliding friction, it is clear, that the lubrication conditions determine the resulting change in tribological behavior of the bearing parts because of the surface modification. For one lubrication condition, namely no lubricant addition, the coating of the steel specimen drastically increases the COF, while the coating of the ball has no significant influence. For water lubrication still the coating of the ball does not significantly change the COF, but the coating of the steel surface now results in a significant decrease of the friction coefficient. Last but not least, for the wetting of the bearing steel surface with PFPE, in contrast to the results under the other lubrication conditions, now the coating of the ball has a significant influence on the COF. By coating the ball, under PFPE lubrication conditions the COF is reduced, while the coating of the steel specimen does not significantly change the frictional behavior any more.

Nonetheless it can be stated, that combining the observed wear behavior during the longer-time measurements, the coating of both surfaces is advisable. In absence of lubricant the coating of the steel surface prevents wear, while for water lubrication the coating of both surfaces is necessary to protect the system from wear. No wear at all is observed for PFPE lubrication in all coating cases, because PFPE is a high-performance lubricant.

Focusing on two of the three lubrication conditions it can be stated, that the coating of both ceramics ball and steel specimen results in a COF decrease of up to 27%. The positive results concerning water and PFPE lubrication are corroborated by the tests on assembled bearing pairs and their overall friction moment carried out by our colleagues at Cerobear GmbH [87].

8. Conclusions of the Experiments

A coating procedure for a-C:F:H PECVD coating of hybrid ball bearing parts has been successfully developed at the Fraunhofer IGB in Stuttgart. The plasma surface modification using the same batch process for all the bearing parts yields the deposition of a closed film, which effectively protects the assembled bearing from corrosion, facilitates cleaning and reduces the friction moment [87]. The deposited coating is predominantly composed of polymeric fluorocarbon which results in a high chemical inertness of the surface modification.

Using tribometry of the unmodified and modified bearing parts, light was shed on the change in sliding friction behavior due to the coating under different lubrication conditions. The measurements have been successfully designed to probe the influence of the plasma surface modification, because the perpendicular force and the resulting contact stress was small enough to prevent relevant deformation and wear. For four different combinations of coated and uncoated balls/specimens in combination with three different lubrication states each, it became clear, that the influence of the lubrication cannot be overestimated. Without lubrication, the coating of the steel specimen increases the friction coefficient, while the COF is reduced by coating of the steel counterpart for water lubrication. For PFPE lubrication there is no significant influence of the steel coating at all; here the coating of the ceramics ball reduces the COF by at least 14%.

For water and PFPE lubrication the coating of both ceramics ball and steel specimen is of significant benefit for sliding friction, and also for the overall bearing friction moment, as determined at Cerobear GmbH. On the other hand in case of no lubrication, similar to dry running conditions of a bearing, the sliding COF is increased by the coating of the steel counterpart, which has not been confirmed by bearing tests yet. Through the sliding friction measurements it was shown, that coating of both ball and specimen does not only reduce the friction coefficient but also protect the system from wear. Furthermore the cleanability of the surfaces is drastically improved [87], so that all in all the application of the coating to hybrid ball bearings for food and drug industry applications is very useful.



Part III.

Computational Investigations

In Part I the complexity of the friction in ball bearings has been elucidated. Utilizing MD simulations, the sliding friction at the ball track interface can be modeled, as pointed out in section 1.1 (page 6). The approach envisaged at the beginning of the work presented here is schematically displayed in figure 4.3 on page 47. In Part II the coating procedure developed by our colleagues at the Fraunhofer IGB, Stuttgart, and the atomic composition as well as the thickness have been studied (analytics performed at the IGB as well). Employing coated and unmodified ball bearing parts, the author devised and carried out tribometry studies under three different lubrication conditions. The results of the tribological experiments are also elaborated upon in Part II. It has to be noted, that the experiments have been successfully designed to probe the influence of the PECVD plasma surface modification on the frictional characteristics of the bearing parts. The experiments were carried out under conditions with no significant deformation of the sliding bodies nor under conditions that result in significant wear. The maximum Hertz contact stress has been very small with 874 bar.

Using the information on contact theory from the introductory part, we can conclude some relevant points for the design of meaningful MD simulations of sliding friction:

1. The maximum Hertz contact stress is the maximum stress occurring in the apparent area of contact (see section 2.1).
2. At the point of maximum pressure there is the highest probability of direct contact, the formation of a junction.
3. The most meaningful pressure surrounding a junction in simulations will be the maximum Hertz contact stress.
4. A junction is of at least 3 nm diameter and at least of 7 nm² area (see section 2.2).

Concluding from these points a computer model directly corresponding to the experiments has to exhibit the following features: Firstly the area of the sliding interfaces has to be a lot more than 7 nm². Secondly, the simulation pressure shall correspond to the maximum Hertz contact stress.

Furthermore, from the analytical results on the coating thickness, the chemical composition of the coating as well as the results on the surface roughness of a ceramics ball relevant information can be extracted for reasonable chemical properties of a coating model:

1. The coating thickness is anywhere on the coated bearing parts at least 70 nm.
2. The roughness of a ball is below 50 nm.
3. Since the coating on the steel parts is a lot thicker than the ceramics ball coating due to the increased electrical field, because metals are conductors, the surface roughness of a steel part is most certainly covered with PECVD coating.

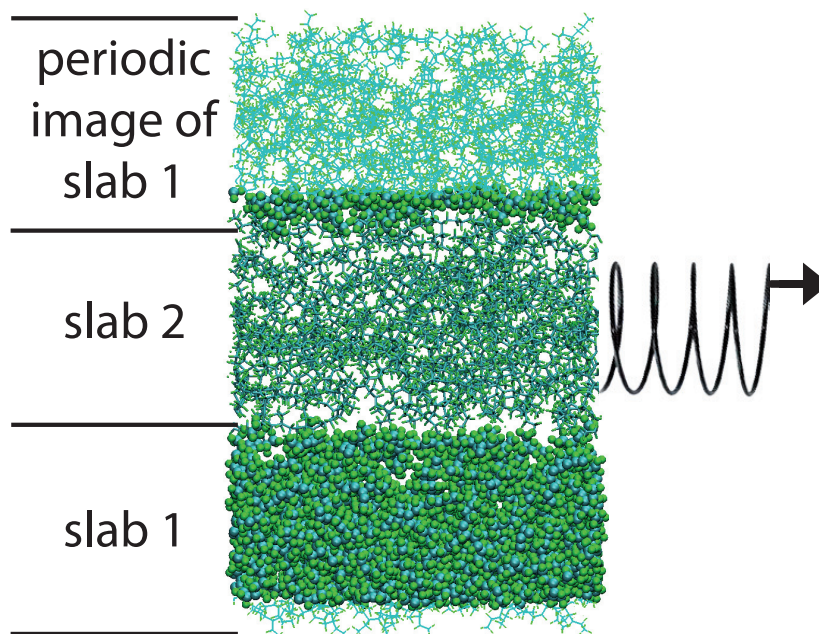


Figure 8.1.: Representation of the simulation volume employed in the simulations. Two identical but differently displayed a-C:F slabs are shown, water is omitted for clarity. The first periodic images of the lower slab in $+z$ - and $-z$ direction are shown in light green below and above the simulation volume image.

4. No trace of the underlying substrate was found in the XPS characterization of the coating.
5. At an incident angle of 90° the penetration depth of the XPS measurements is about 5 nm [27].
6. The ratio of fluorine to carbon atoms on the surface of the coating is at least 1.6, most probably larger, because the outermost surface exhibits CF_3 -moieties, which are not present in the bulk of the coating.

Resulting from the analytics the following conclusions can be drawn: Firstly the coating thickness above the asperities of any of the different bearing part substrates is a lot thicker than anything that can be modeled in MD simulations, because the number of atoms is far too large. Secondly this results in a complete neglecting of the underlying substrate. As a third conclusion, in the MD simulations only the outermost layer of the coating is modeled, which exhibits more fluorine atoms than the bulk material. Groups with higher fluorination orient towards the outside of the coating to minimize the surface energy [88], thus the fluorine to carbon ratio has to be higher than 1.6.

Combining the conclusions from the results of the analytics with the envisaged simulation approach (figure 4.3 on page 47) one of the simulation slab models of the a-C:F:H coating has to model two times the outermost layer. This is because the slabs interact on both

sides with the other slab one time with the upper side and one time with the lower side of the other slab. This fact is shown in figure 8.1. The models of the coating are shown in different representations although they are identical. The first periodic images of the lower slab below and above the simulation volume are shown in light green. Hence it can be seen, that both sides of both slabs directly interact with both sides of the other slab. Due to this modeling approach the friction coefficient μ is defined in variation of equation 1.1 as

$$\mu = \frac{F_F}{2 F_N} \quad (8.1)$$

with an additional factor of $1/2$. One concession to the simplification of the model development was made: Any atom types that are not carbon or fluorine are not included in the model, thus the model is correctly referred to as a-C:F.

The envisaged simulation approach in the work presented here is a classical MD simulation approach not to be found in literature, although it combines two approaches, the constant normal force approach [89] and quasi-infinite stacking including the lubricant twice [90, 91]. Hence the aim of the MD simulations was the successful implementation, verification and validation of the new approach as well as the novel approach for the modeling of an amorphous coating. A common tribology simulation approach in contrast to our constant normal force approach is based on the constant distance of the outermost atoms of two opposing layers. In this approach, the distance between the outermost atoms is kept constant after a certain time under static load, and periodic boundary conditions are applied only in the directions of the sliding plane. Based on the knowledge on the dependence of the static COF on static time (see section 1.2 and section 2.2) the question when to stop the equilibration has to be posed. Because the friction coefficient should increase with static time due to creep on the molecular scale, the friction force in these simulations should depend on the static equilibration time. Nonetheless the approach enables a constant perpendicular force, if a part of the atoms of a slab are subject to pressure coupling [92]. Using the constant distance approach some beautiful simulations on diamond-like carbon and hydrogenated amorphous carbon have provided considerable insight into coating deposition and the tribology at interfaces [92, 93]. For these investigations MD simulations that are able to depict reactions have been employed, on the one hand quantum MD simulations using the density functional tight binding approach [94–96] and on the other hand a reactive empirical bond order (REBO) potential has been used [1, 97].

In literature, to our knowledge, there are no MD simulation studies on sliding friction of a-C:F coatings, but there are studies on a compound that is chemically closely related to a-C:F, Polytetrafluoroethylene (PTFE). PTFE mainly consists of CF_2 -moieties, which is also the case for the a-C:F coating. However, the a-C:F coating is a highly

interconnected network, which is in sharp contrast to the crystalline arrangement of long polymer chains present in PTFE. As mentioned, our simulation approach uses the periodic boundary conditions to simulate a quasi-infinite stack of slabs. The advantage is the fact, that the barostat can be used to maintain a constant perpendicular force, which is the same behavior as for the perpendicular force exerted by the tribometer cantilever. The disadvantage is the fact, that the lubricant has to be modeled twice, but since smaller molecules are squeezed out of the junction area, the number of molecules that have to be modeled is limited.

Regarding the sliding friction of PTFE, Sawyer and coworkers published several papers including both simulations and experiments [98–103]. Since from the chemistry point of view a-C:F and PTFE are closely related, it is reasonable to compare simulation approach and results with the results of Sawyer and colleagues. Focusing on the development of the friction coefficient with increasing load [2, 104](see also the section on contact 2), the comparison has to be made regarding the perpendicular pressures, because the COF of PTFE decreases with increasing normal load, usually in the range of 0.3 to 0.07 [98, 105]. Sawyer and coworkers carried out simulations on the dry sliding friction of PTFE. Their simulations were carried out using an approach, which is in contrast to the approach employed here a constant distance approach, not a constant perpendicular force approach. In their approach, the slabs of crystalline PTFE are equilibrated a certain time under static load, and then the distance between the outermost layers is fixed and kept constant throughout the simulation of relative shearing of the slabs. Based on the knowledge on the dependence of the static COF on static time (see section 1.2 and section 2.2) the question when to stop the equilibration has to be posed. Because the friction coefficient should increase with static time due to creep on the molecular scale, the friction force in their simulations should depend on the static equilibration time, which has not been investigated.

In contrast to the simulations carried out by Sawyer and coworkers, who considered only dry contacts with one exception of perfluoroalkane lubrication [103], our approach includes condensed humidity or water trapped by surface asperities. The trapping by surface asperities is more likely, because water molecules are easily squeezed out, as pointed out in section 2.4. Due to the hydrophobicity of the coating and the small size of a water molecule it is to be expected, that the last monolayer of water molecules may be squeezed out at a pressure considerably lower than 2750 bar. Even in nominally dry contacts, the surfaces of bodies are covered by a water film [106–108]. So even in nominally dry contacts, depending on the squeeze-out conditions, it is at least possible, that water molecules remain between the surface asperities. Furthermore, several publications on tribological experiments show a significant impact of trace water on the friction coefficient [109–111]. The effect of trace moisture on the sliding friction of hy-

drophilic surfaces was studied by Liu and Szlufarska in their publication on quantum mechanical calculations of the sliding of hydroxyl group terminated silicon carbide [112]. Additionally, experimental evidence by AFM studies shows the impact of moisture on silicon (oxide) sliding friction [113, 114]. The formation of hydrogen bonds between the surfaces increases the surface interaction and thus increases the friction force. Even for the impact of water on the friction between an a-C:F:H coated surface and a silicon nitride AFM tip there is evidence. By comparing two publications by Freire Jr. and coworkers [39, 115] on tribological properties of a-C:F:H coated surfaces the influence of humidity becomes obvious: The COF determined by AFM measurements is 0.15 for a relative humidity of 28%, while it is 0.2 for a relative humidity of 38%, so an increase in relative humidity of 10% results in an increase of the COF of 25%.

In our simulations we considered a very thin film of water, which is trapped in the junction area that is simulated. Since the a-C:F slab is highly hydrophobic the interaction with water molecules is very weak. For verification of the approach, additionally a slab made from the cristobalite modification of silicon dioxide has been included in our investigations. The cristobalite slab serves as the complete opposite of the a-C:F slab: The a-C:F slab is rough, rather soft, hydrophobic and amorphous, while the SiO₂-slab is atomically smooth, hard, hydrophilic and crystalline. A steel surface would have been the optimal model of the bearing steel specimen employed in the tribological experiments, but steel surfaces are covered by amorphous oxides of chromium and iron [116–119], which are not the complete opposite of the a-C:F slab. The surface of the silicon dioxide slab has been terminated with hydroxyl groups. Resulting from a possible combination of this second slab model with the a-C:F slab there are in total three different systems modeled throughout these computational investigations of sliding friction:

1. Two a-C:F slabs in a simulations system, referred to as a-C:F.
2. Two cristobalite silicon dioxide slabs in the system, referred to as SiO₂.
3. One a-C:F slab and one cristobalite slab in the system, referred to as MIX.

The overall goal of the MD simulations of a-C:F sliding friction is the implementation, verification and validation of the simulation approach against experiment. Since it has been highlighted that simulation and experiment were designed to be carried out under the same conditions with respect to the parameters like temperature and pressure, an agreement at least regarding the obtained trends was desired.

In the course of the simulations several aspects that influence the friction have been studied. For all aspects all the three systems have been included in the considerations. To study a possible influence on the tribological behavior of the simulation systems we have investigated the following:

-
1. The dependence of the friction force on the perpendicular force for verification and validation of the approach.
 2. The influence of varying temperature on the obtained friction coefficients as sensitivity analysis and for further validation.
 3. The response of the systems when the amount of water between the slabs, the water layer thickness, is varied.
 4. The result of changing the velocity of the virtual spring and thus the relative velocity of the slabs.

For all these four points not only the simulations have been carried out, but also a comparison between our simulations and experiments both of our own and of other researchers is undertaken. For instance the influence of varying temperature on PTFE sliding friction has been investigated by Sawyer and Burris and colleagues [99, 100, 120] experimentally but not computationally.

The rest of this part deals with the details on the creation of material models and the computation approach first, followed by a presentation and discussion of the simulation results and closes with the conclusions of the simulations.

The main results presented here are intended for publication in the journal *Langmuir* [121].

9. Computational Details

This section deals with the details of the creation of different material models as well as with the creation of a material model of the PFPE oil Krytox[®] GPL 104. After that, the specifics of the simulations are given, including the chosen program, simulation parameters and processing of the resulting data.

9.1. Material Models

9.1.1. a-C:F Coating Model

As stated above the model for the coating has to consist of at least 1.6 fluorine atoms per carbon atom. Since the outermost layer of the coating is modeled and CF₃-moieties are present in contrast to the bulk, the fluorine to carbon ratio should be increased. Furthermore two times the outermost layer of the coating is combined into one model slab, which also should increase the content of fluorine. Since the computation resources have been limited, the model of a single slab had to be limited to approximately 6,000 atoms.

The procedure of creating an a-C:F slab model starts with 180 precursor molecules of perfluoro-4,5-diethyl-octane (C₃F₇(CF(C₂F₅))₂C₃F₇), whose chemical structure is shown in figure 9.1. The precursor molecules are placed bond by bond in a fixed volume. To this end the Amorphous Cell tool of Accelrys Materials Studio, Accelrys Inc., San Diego, USA, was used. The placement algorithm used by the Amorphous Cell tool has been published by Theodorou and Suter in 1985 [122]. This algorithm establishes models of amorphous glass states. Based on the estimated interaction energy with already present atoms a new atom of the molecule is placed inside of the box. The box dimensions were 7.2 nm ×

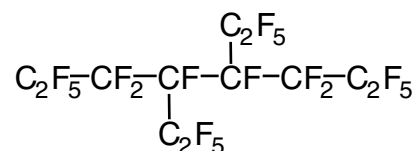


Figure 9.1.: The precursor molecule the a-C:F coating model is built from. C is carbon, F is fluorine.

7.2 nm \times 2 nm with hard walls perpendicular to the z -direction of the box (x - y -plane). Using Materials Studio the molecules have been manually connected to each other by deleting fluorine atoms and creating bonds. If two carbon atoms were close to each other, the fluorine atoms pointing closest to the vector of the new carbon carbon bond have been deleted. After establishing a new bond, the two newly connected fragments have been drawn closer together to a reasonable carbon-carbon distance of about 1.6 Å. This caused other carbon atoms to be close to each other and the interconnection procedure was repeated until a totally interconnected carbon atom network was established. Afterwards the system was relaxed shortly within Materials Studio using the Forcite tool, after which the resulting geometry was exported.

For the generation of a slab model, which is truly two-dimensionally periodic, again close carbon atoms have been connected by bonds after a short equilibration using GROMACS 4.5.3 [70]. To this end the slab model was visualized using VMD [123]. By viewing the slab and its periodic images, close carbon atoms across the simulation volume borders could be identified and again the carbon atoms have been connected, while the fluorine atoms close to the new bond were deleted. In summary, 230 carbon carbon bonds have been defined, which results in a system of 402 CF₃-group carbon atoms, 1266 CF₂-moiety carbon atoms, 483 carbon atoms belonging to a CF group and nine quaternary carbon atoms. Hence 501 cross-links have been established in the coating model, which results in a cross-link density of 28.5% with respect to the total amount of 1758 carbon atoms that are not part of a CF₃-moiety, the backbone carbon atoms. This cross-link density is consistent with the experimental cross-link density. The experimental ratio of CF carbon atoms to CF₂ carbon atoms is 28.4%. The fluorine to carbon ratio resulting from the carbon atoms and 4221 fluorine atoms is 1.95. This value is above the fluorine to carbon ratio of 1.6 resulting from the chemical analysis of the coating. But since the chemical analysis penetrates into depths, which are not depicted by our model, an over-representation of surface CF₃-groups is reasonable. The coating model of 2 nm thickness represent only two times the outermost coating surface. Furthermore, the orientation of groups with higher fluorination towards the surface results in a higher fluorine content at the outermost coating surface [88].

The calculations for the work presented here have been carried out employing the package GROMACS. To create a GROMACS compatible input, a custom-programmed FORTRAN tool was used for the creation of an .itp-file that contains the bonding and force field information of the slab model. Within the program, bond definition cut-offs of 1.3 nm for C-F and 1.8 nm for C-C bonds were employed. The calculations of the distances were performed including the periodic images in the x - y -plane of the slab but not perpendicular to the slab in z -direction. For the bonds beyond the simulation cell border the two closest carbon atoms with less than four bonding partners have been connected.

After the bonds are defined by this algorithm, it was reassured that all atoms had been assigned the correct number of bonding partners, one for fluorine atoms, and four for carbon atoms. Each carbon atom had to possess four bond partners because no multiple bonds were included in the generation of the slab model, because no carbon atoms hybridized different from sp^3 had been detected by XPS analytics of the real a-C:F:H coating. Subsequently a charge group was assigned to every carbon atom and to all fluorine atoms connected to that carbon atom, if applicable. Each carbon atom in sum with the fluorine atoms bound to it has a total charge of zero. Care was taken that the overall charge of the slab was really zero. For the FF parameters the OPLS-AA parameters developed especially for perfluoroalkanes have been used [124]. These parameters have been successfully applied in MD simulations of perfluorinated SAMs by Lorenz et al. [21]. Since in this set of FF parameters no quaternary carbon atoms are present, but the non-bonding interactions for all carbon atoms are the same, for quaternary carbon atoms in the a-C:F model a charge of zero and the same parameters as for the other carbon atoms have been used.

9.1.2. α -Cristobalite Silicon Dioxide Model

Using an α -cristobalite tetragonal unit cell, a slab model was generated by replicating the unit cell a second time in c-direction (the thickness direction of the slab is c-vector of the tetragonal unit cell). Using MOLDEN [125] the surface silicon atoms have been terminated with hydroxyl groups. Afterwards the modified, doubled unit cells have been replicated twelve times in x- and y-direction of the simulation volume each. Subsequently an adapted FORTRAN program that was similar to the one used for the a-C:F model creation was used. The distance cut-offs employed in the program were 1.3 Å for hydroxyl groups and 2.1 Å for the Si-O-bonds. Charge groups have been assigned to each of the silicon or oxygen atoms, because only the whole slab may be neutral (see sections 4.5 and 4.6). The hydrogen atoms are assigned the charge group of the oxygen atom they are bound to. To obtain an electroneutral slab, the negative charge of the oxygen atoms had to be set to the correct value for countering the positive partial charges of the silicon atoms. All in all the silicon dioxide slab model contained 4320 atoms in a simulation volume of 5.968 nm \times 5.968 nm \times 2.8 nm. The FF parameters that have been used for the simulations in this work are the CHARMM parameters [126] and have successfully been applied in our group to the interactions of water with silicon dioxide in cristobalite pores [127].

9.1.3. PFPE Oil Krytox[®] GPL 104 Model

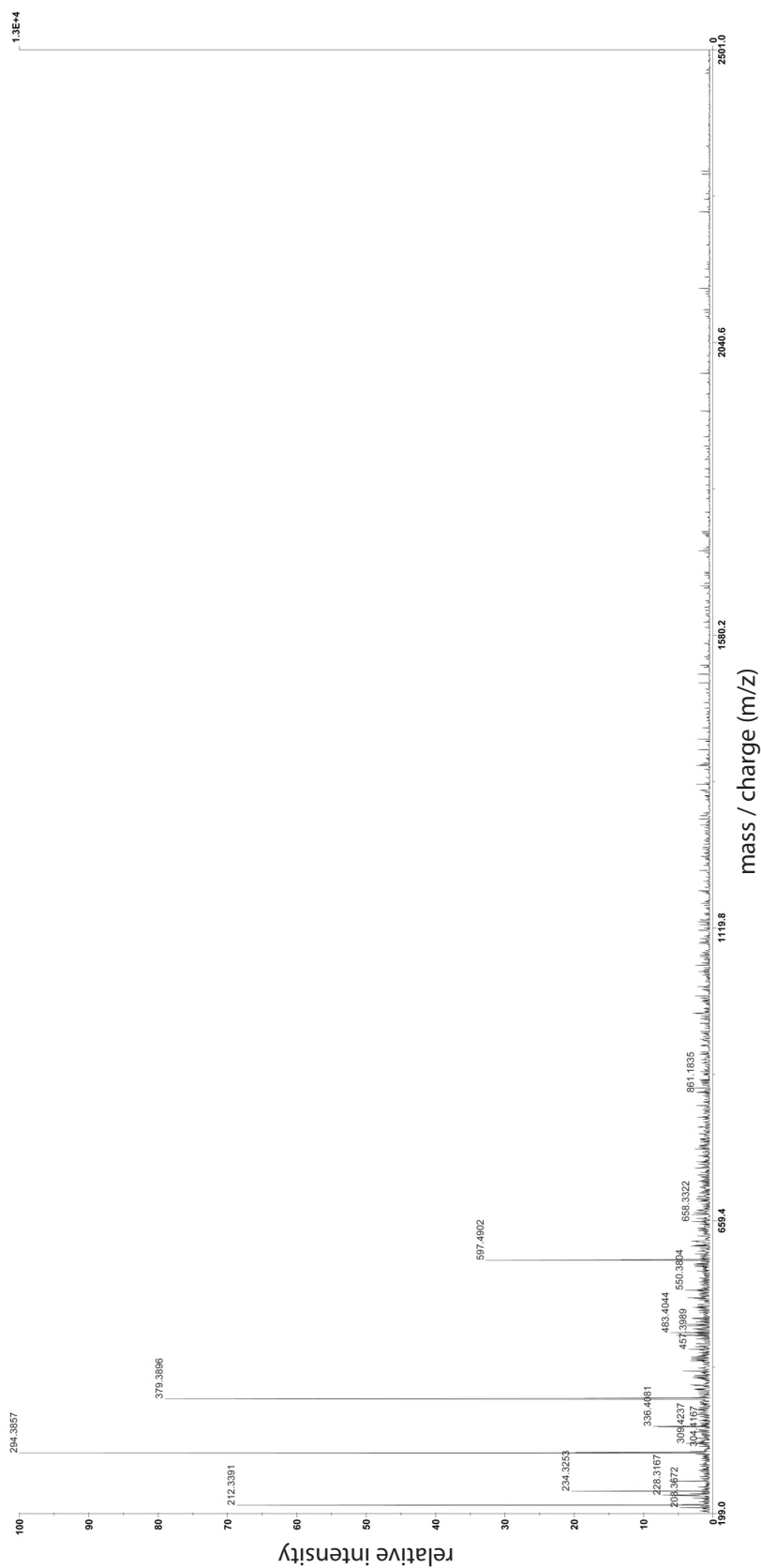
The analytics of the PFPE-based lubricants was kindly carried out by Katharina Richter, Fraunhofer “Institut für Fertigungstechnik und Angewandte Materialforschung” (IFAM), Bremen. Analysis of the spectra was performed by the author.

For analytics of the PFPE lubricants only mass spectrometry is applicable, because PFPE lubricants are only soluble in perfluoroalkane solvents, therefore Nuclear Magnetic Resonance (NMR) spectroscopy was not utilizable, because the signals would be completely overlaid both for ^{13}C and ^{19}F nuclei NMR spectra. Furthermore, IR- or UV/Vis-spectroscopies would not yield any information on the length of the polymer chain, as would elemental analysis. Since analytics of the base oil Krytox[®] GPL 104 were not possible, because crystallization of the oil in a matrix for a Matrix Assisted Laser Desorption Ionization (MALDI) failed, the corresponding fat was analyzed using a MALDI-time-of-flight (TOF) mass spectrometer.

The resulting mass spectrum for the matrix of E-2-cyano-4-hydroxycinnamic acid is shown in figure 9.2, the mass spectrum of matrix and fat in the range of mass to charge ratio (m/z) between 400 and 100 is shown in figure 9.3, the spectrum between 700 and 2,000 m/z is shown in figure 9.4 and in the range between 1,000 and 10,000 m/z in figure 9.5.

A mass spectrum is analyzed in the way, that based on the so-called M^+ -peak, which gives the total mass of the molecule, a hypothesis of the structure is made, which is proven or disproven by means of the other peaks. The other peaks logically are not the peaks of the whole molecule but of fragments of the parent compound. Further fragmentation leads to smaller masses, and by calculation of the masses of possible fragments and verification if these fragments are present in the spectrum, evidence is generated. Furthermore a comparison of the calculated mass differences between peaks in the spectrum may provide evidence, because the difference may be the mass of e.g. a repeating unit. Using evidence for or against the hypothesis, the hypothesis can be proven or disproven.

Fortunately, the technical data sheet provided by DuPont included the basic structure of the lubricant, it is shown in figure 9.6. The question still remains, how large the number of repeating units is. Furthermore, the technical data sheet states the results of a typical elemental analysis: 21.6% carbon, 9.4% oxygen and 69.0% fluorine. Using the provided chemical structure the mass of the M^+ -peak cannot be reproduced, because the mass would be deviating 105 g mol^{-1} if a number of repeating units of 46 is assumed. However, assuming symmetrical end groups this mass difference reduces to 5 g mol^{-1} below the M^+ -peak. Furthermore, in contrast to the technical data sheet, a study on MD simulations of PFPEs by Koike [128], stated, that exactly these symmetric end groups with the same backbone are the “Krytox[®] type” PFPE.



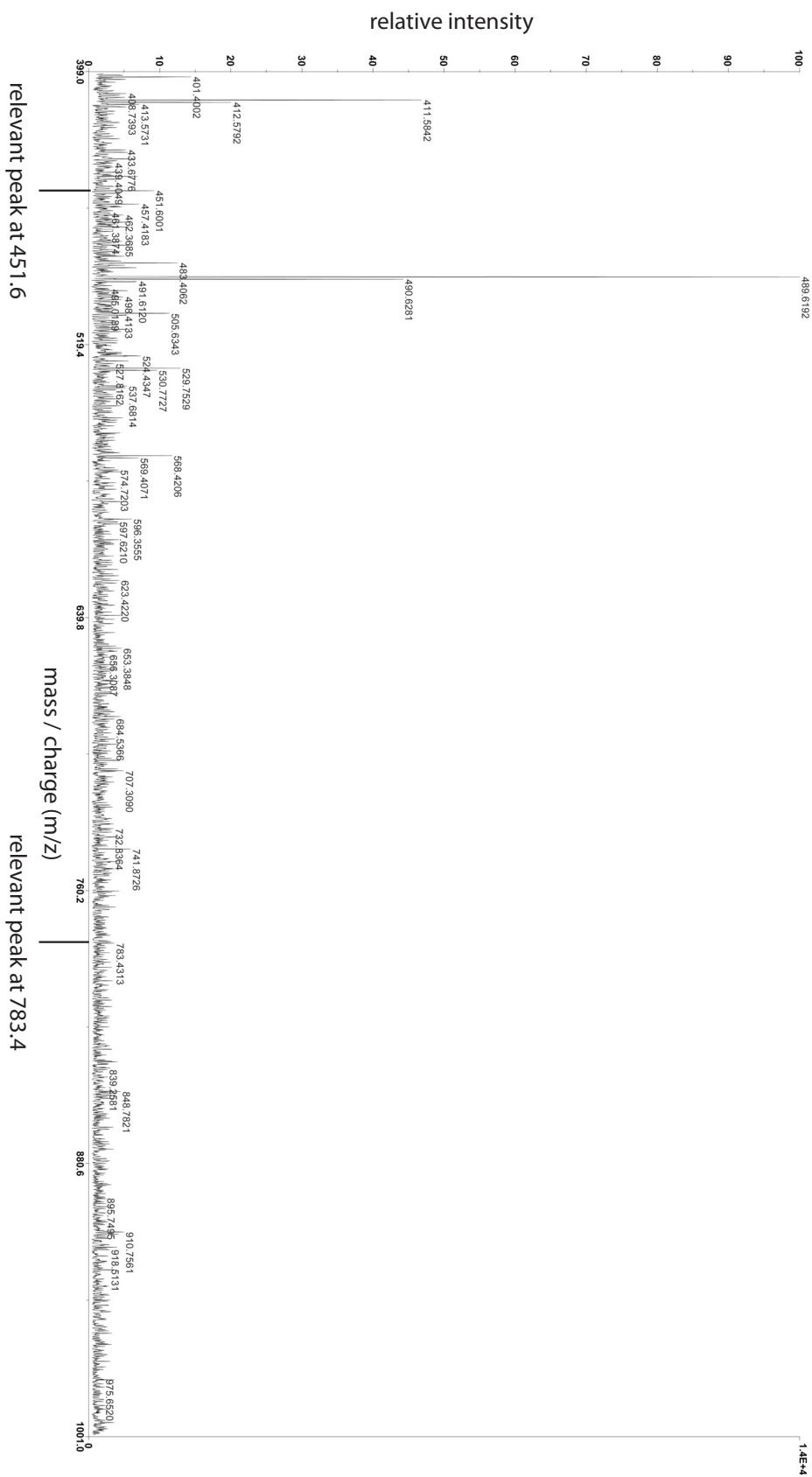


Figure 9.3.: MALDI-TOF mass spectrum of the PFPE fat Krytox® GPL 204, containing GPL 104 PFPE oil. The shown mass per charge range is 400 to 1,000 m/z .

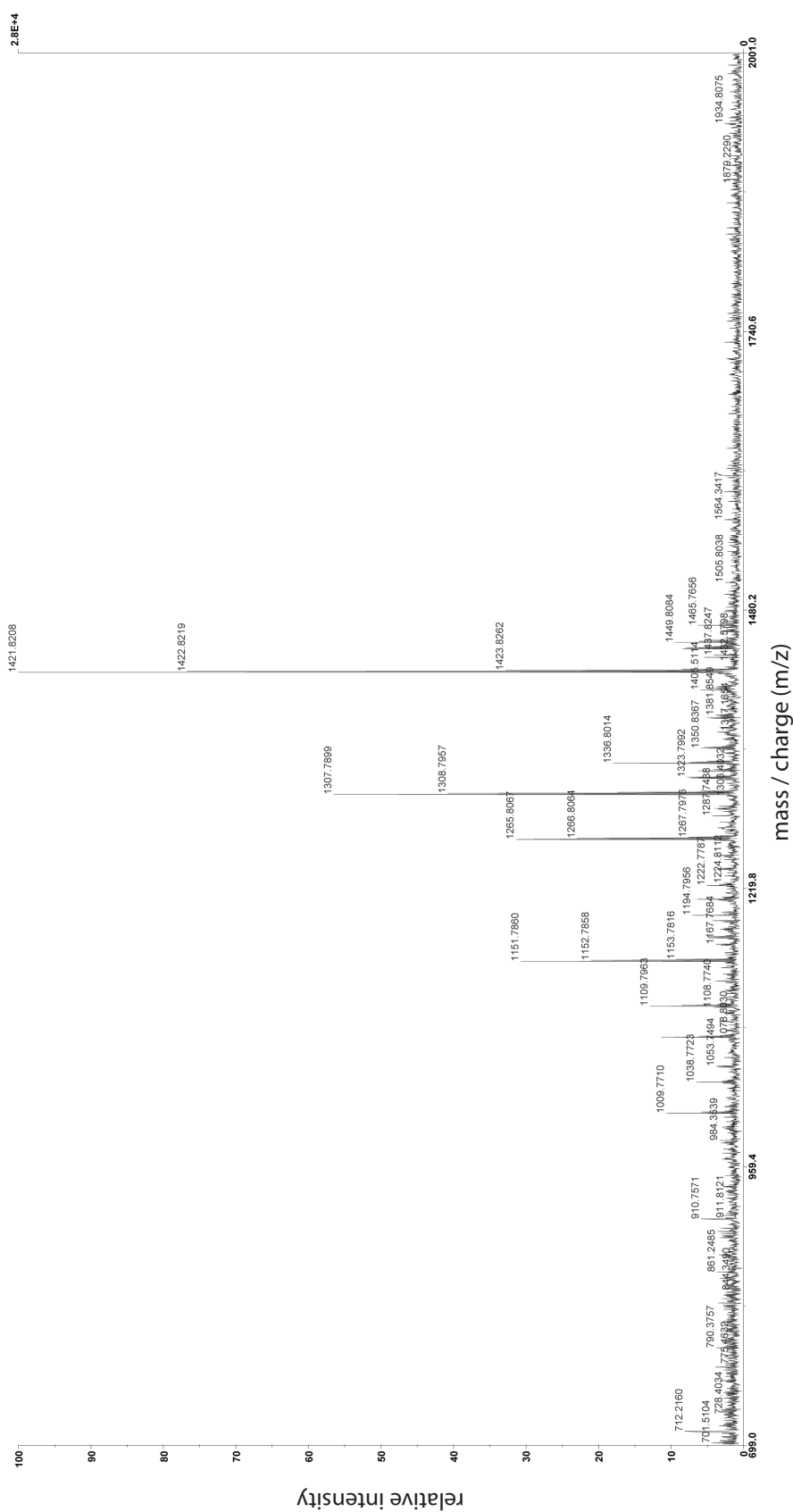


Figure 9.4.: MALDI-TOF mass spectrum of the PFPE fat Krytox® GPL 204, containing GPL 104 PFPE oil. The shown mass per charge range is 700 to 2,000 m/z.

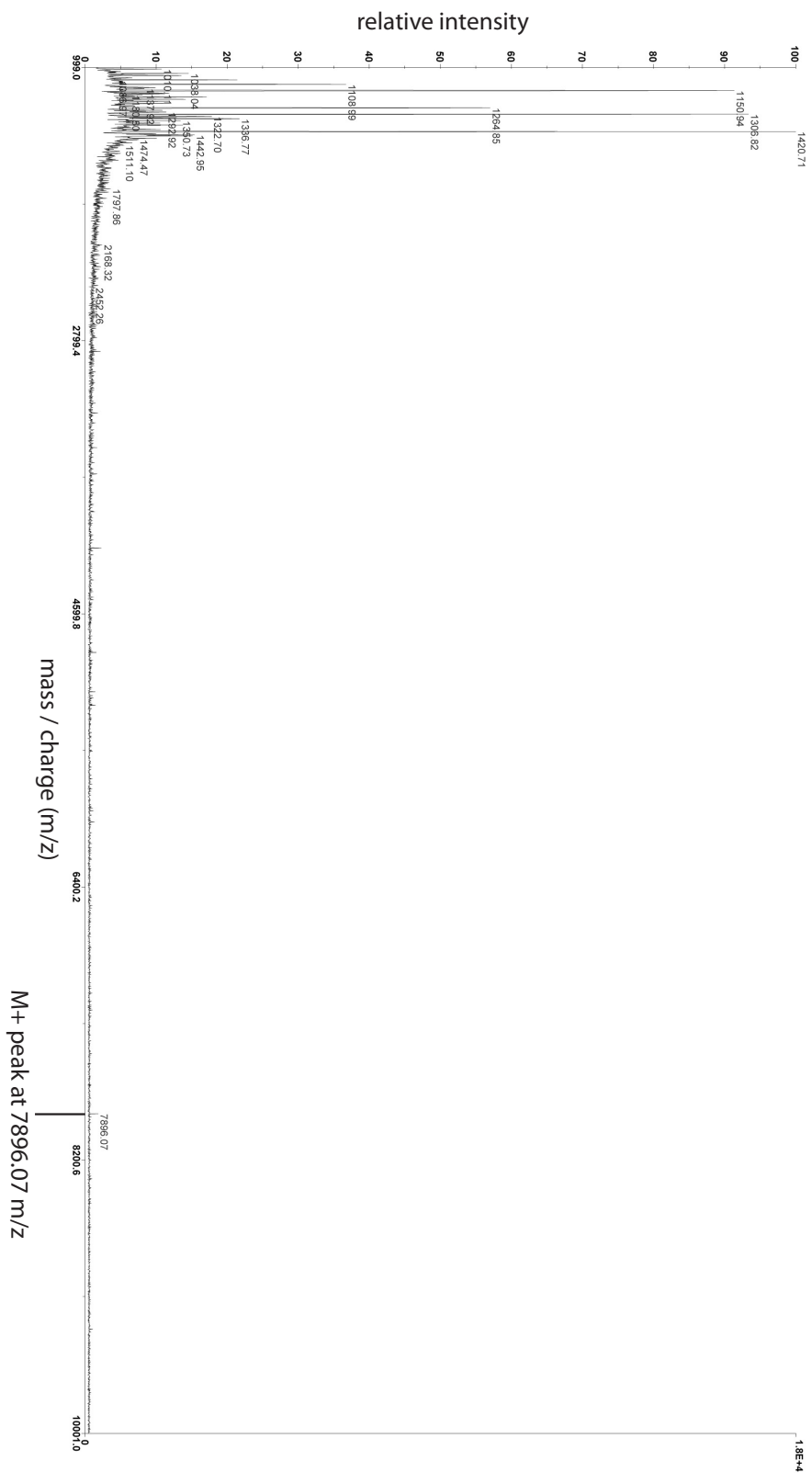


Figure 9.5.: MALDI-TOF mass spectrum of the PFFE fat Kiytox[®] GPL 204, containing GPL 104 PFFE oil. The shown mass per charge range is 1,000 to 10,000 m/z.

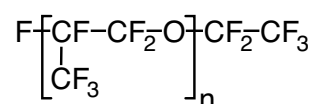


Figure 9.6.: Chemical structure of a perfluoro-polyether of the DuPont Krytox[®] family according to technical data sheet. C is carbon, F is fluorine, O is oxygen, n is the number of repeating units.

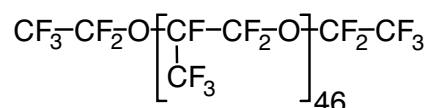


Figure 9.7.: Structure of Krytox[®] GPL 104 according to mass spectrometry and technical data sheet.

In figure 9.7 the supposed structure according to mass spectroscopy is shown. First of all it has to be noted, that the elemental analysis of this compound would yield 21.61% carbon, 68.86% fluorine and 9.53% oxygen, which is almost exactly the composition the technical data sheet gives. Furthermore the fragment signals confirm at least the structure of the backbone. Studying the mass differences of the fragments in the range between 700 and 2,000 m/z, there are several relevant peak differences that belong to very reasonable possible fragments of the parent compound. The peaks, differences and corresponding fragments are listed in table 9.1.

The first of the fragmentations results in a loss of a fragment of the chemical formula CF-CF₂-O. This fragment is once the backbone of the repeating unit, which is a reasonable fragment. The second fragmentation stems from the loss of the connection between two repeating units, namely the connection of head-to-head connected units. The fragment has the chemical formula CF₂-O-CF₂. The head-to-head connection occurs during polymerization. The synthesis of PFPE is an anionic ring opening polymerization of perfluoro-methyloxirane (CF₃CF-μO-CF₂, perfluoro-propene-epoxide), which is not absolutely regioselective, so that head-to-tail is the dominant connection of the monomers in the polymer, but not the only possible connection. The third fragmentation results in

Table 9.1.: Relevant peaks of the Krytox[®] GPL 204 fat MALDI-TOF mass spectrum in the range of 700 to 2,000 m/z. Peak positions in m/z.

higher peak	lower peak	difference	fragment
1421.8	1307.8	113	CF-CF ₂ -O, backbone of the repeating unit
1265.8	1151.8	116	CF ₂ -O-CF ₂ , connection between two head-to-head connected units
1109.8	1009.8	100	CF-CF ₃ , first carbon of repeating unit with side chain

the loss of a CF-CF₃ unit, the first part of a repeating unit. In addition to the differences of main fragments in the range from 700 to 2,000 m/z, a key fragment below 700 m/z distinguishable in the spectrum from 400 to 1,000 m/z (figure 9.3) is the fragment at 451 m/z, which belongs to the fragment CF₃CF₂-O-CFCF₃-CF₂-O-CFCF₃-CF₂ (the starting group plus nearly two repeating units, spectrum not shown). Furthermore the fragment with two more repeating units (166 m/z each) at 783 m/z is also distinguishable in this spectrum.

Concluding the results discussed here it is clear from the fragments that the Krytox[®] GPL 104 was present in the TOF mass spectrometer. Additionally the number of repeating units of the supposed structure is in the range of 10-60 that is provided in the technical data sheet, and the elemental analysis of the supposed structure perfectly agrees with the data from the technical data sheet. However, two minor facts argue against the supposed structure: The mass of the supposed structure is a bit lower than the determined M⁺-peak and the end group deviates from the structure provided in the technical data sheet. However, given the fact, that it is reasonable, that the polymerization is initiated using a perfluoro-ethanolate (CF₃-CF₂-O⁻) both facts are just minor facts.

What further points in the direction of this number of repeating units is the viscosity of all the different Krytox[®] GPL oils given in the technical data sheet. Distributing the number of repeating units evenly over the eight mentioned base oils, the number of repeating units for GPL 104 should be about 38. However, since the entanglement of the polymers gives rise to a viscosity that depends on the molecular mass on the order of M^{3.4} [129], a longer chain for lower viscosity lubricants is very likely.

All in all it is highly probable, that the analysis of the mass spectrum in combination with the data of the technical data sheet yielded a very good model of the real structure of the main compound in GPL 104.

Transferring this analysis into a computer model, based on the supposed structure of the main PFPE substance according to figure 9.7, again Accelrys Materials studio was used to assemble the polyether. As for the other two models an adapted FORTRAN tool was used to generate the input for GROMACS, the charge groups were assigned to the CF₃-moieties and the oxygen atoms, while the CF- and the CF₂-moieties were assigned the same charge group as the oxygen atom they are bound to. As simulation parameters the force field developed by Koike has been used [128].

The focus of the project NANODYN was on water lubrication, and in the beginning of the work, the new simulation approach had not been verified and validated. Furthermore the water lubricated systems required less computational effort compared to the Krytox[®] GPL lubrication. These are the reasons why the Krytox[®] GPL 104 model has not been used further than the successful equilibration of the right number of molecules for one lubrication layer. Extrapolating the results of Persson [3] on squeeze-out of hydrocarbons

to the chain length of the Krytox[®] model, it can be assumed that two monolayers remain in a junction, which according to the dimensions of the a-C:F slab means six molecules between the slabs and another six molecules on top of the upper slab. It has to be noted, that the PFPE model is ready to use.

9.2. Simulation Details

The MD simulations, which are analogous to a tribometer experiment, were carried out using GROMACS 4.5.3 with a time step of 2 fs. Lennard-Jones interactions were calculated using a cut-off of 1.7 nm. Particle-Mesh-Ewald summation was used for the calculation of the electrostatic interactions, which was carried out in real space up to the same cut-off of 1.7 nm. Pressure coupling and temperature coupling were performed using the Berendsen barostat and thermostat algorithms, respectively [82]. The pressure coupling interval was set to 500 steps, the temperature coupling was applied every 100 steps to the whole system. For the pressure coupling the compressibilities of amorphous PTFE at 298 K ($5.884 \cdot 10^{-5} \text{ bar}^{-1}$) was used in the a-C:F case [130], while for the cristobalite slab the cristobalite compressibility was used ($8.695 \cdot 10^{-5} \text{ bar}^{-1}$)[131]. The coupling constants were 20 ps both for the pressure coupling and the temperature coupling. The reference pressure was 874 bar, the reference temperature was 298 K unless otherwise noted. MD simulations were run using an NPT ensemble, the general approach was a single equilibration run of 32 ns for a given set of simulation conditions, meaning temperature, pressure, spring velocity and water layer thickness. During the equilibration run the box was free to relax in all dimensions, but x- and y-dimension have been coupled (semi-isotropic pressure coupling). The semi-isotropic barostat was necessary to prevent elongation in the shearing direction during the subsequent equilibrations. Using the resulting geometry, production runs were started, 9 to 18 for each set of conditions. The simultaneous runs had a duration of 16 ns each, and the dimensions of the slab plane (x-y-plane) were fixed to directly use the barostat as a device maintaining the perpendicular force on a constant level (a dynamostat). The short-time variations in perpendicular force mimic elastic behavior of the materials to some extent.

Regarding the lubrication with water molecules, 0.75 monolayers of water per slab were assumed to be trapped in the simulation area. A monolayer was defined as the complete coverage of the sliding area with a layer of one water molecule thickness. The assumed amount of water results in a total amount of 1.5 monolayers between the two slabs and additional 1.5 monolayers on top of the upper slab. The number of water molecules in total is 2000 water molecules for the a-C:F system, for the SiO₂ system 2284 water molecules are included, while in the MIX system 2022 water molecules are included. The thickness of the water film was 8 Å between the atomically smooth cristobalite slabs,

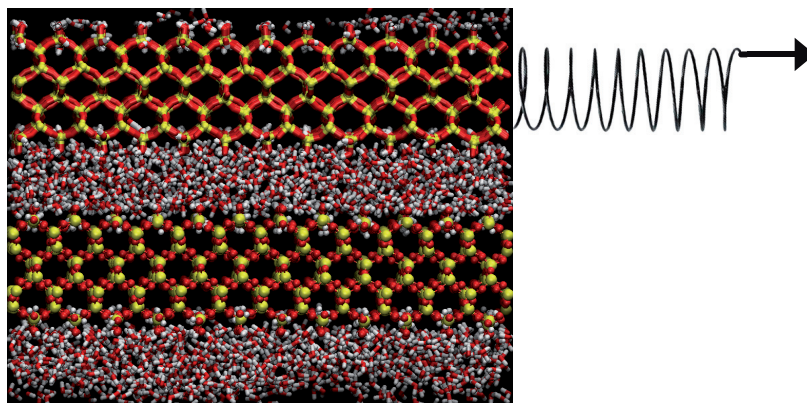


Figure 9.8.: Visualization of a simulation volume containing two cristobalite silicon dioxide slabs (system SiO_2) separated by a water layer of 8 \AA thickness. The virtual spring pulling the upper slab is indicated by a picture. The slabs are identical but differently displayed.

which is reasonable considering squeeze-out and experiments, which yield a thickness of about 10 \AA at 50% relative humidity *per surface* [113, 114, 132]. For the more hydrophobic MIX system and the completely hydrophobic a-C:F system this amount of water may be rather high [113], but it is kept for consistency reason. With respect to the area about 55.7 water molecules per nm^2 have been present in the simulation volumes. The simulation volume set-up was carried out by stacking the geometries of a slab, a water layer, the second slab model and another water layer. Subsequently a conjugate gradient energy minimization (see section A.1 in the appendix) was carried out up to machine precision. The amount of water was only altered for the investigation of the results of a water layer thickness variation. For the water molecules the SPC/E water model was used [71], which performs well for the determination of viscosity, diffusion coefficient and the temperature dependencies thereof [133]. The water molecules were defined to be flexible. As mentioned, the upper slab in the simulation volume was pulled employing a virtual spring. (GROMACS: pull=umbrella) This approach is visualized in figure 9.8 that shows the SiO_2 -system with water lubrication and a picture of a spring indicating the virtual spring and the direction of shearing. The spring end moved with the constant velocity of $5.512 \cdot 10^{-4} \text{ nm ps}^{-1}$ in horizontal x-direction unless otherwise stated. (GROMACS: pull_geometry=direction_periodic, pull_dim=Y N N, pull_vec1=1 0 0) This spring velocity directly corresponds to the ball velocity of a DIN 623 type 6001 [134] ball bearing at 850 RPM. The pull force acting on the virtual spring was recorded during the simulation and the force constant of the spring was chosen so high that stick-slip behavior was strongly dampened. ($6500 \text{ kJ mol}^{-1} \text{ nm}^{-2}$ or 10.8 N m^{-1} relative to average forces in the nN-regime, AFM cantilever spring constants are in the range of 10^{-2} N m^{-1} [135]) Since the slabs interact with the image of the other slab and additionally with the periodic image of the slab, the coefficient of friction is calculated from the friction force

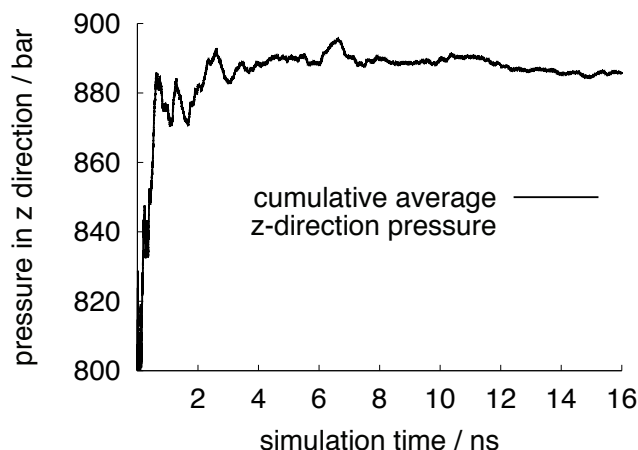


Figure 9.9.: Example of a development of the cumulative average of the pressure in the perpendicular direction of the sliding plane for an a-C:F simulation at 874 bar target pressure. Please note that the y-axis scale starts at 800 bar. In under one nanosecond the error is below ± 10 bar of the overall average, resulting in a deviation of less than 1.2%.

as $\mu = F_F/2F_N$ with an additional factor of $1/2$ (cf. equation 1.1).

Figure 9.9 shows an example of the development of the cumulative average of the pressure in the perpendicular direction of the sliding plane over the course of an a-C:F simulation. The average pressure directly determines the average perpendicular force due to the constant area of the sliding plane. Please note that the y-axis scale starts at 800 bar and that within one nanosecond the error gets below 1.2% of the final value. This error directly translates into the error of the perpendicular force. For the calculation of the perpendicular forces that are used as results for the graphs, the first 2.4 ns of each trajectory have been omitted to exclude any equilibration to the condition, that the x-y-plane area is fixed in the production runs. The final cumulative average value excluding the first 2.4 ns of the simulations is the resulting average perpendicular force.

Figure 9.10 displays the development of the cumulative average of the pull force over the course of an a-C:F simulation. The pull force is the friction force. Please note that the y-axis scale starts at $1000 \text{ kJ mol}^{-1} \text{ nm}^{-1}$. Within one nanosecond the deviation becomes about 14% of the final value. The variation may be optimized by reducing force oscillations by identifying the optimal, reduced spring constant. However, for comparability of the results the force constant is the same for all simulations. Furthermore the oscillations during a-C:F simulations are larger, because two rough slabs are present in the simulation volume, leading to smaller errors for the other two systems. If at least one slab is atomically smooth naturally the resulting variations are smaller.

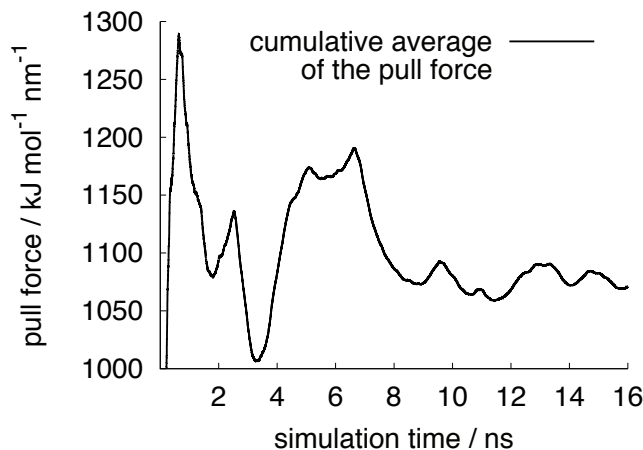


Figure 9.10.: Example of the development of the cumulative average of the pull force for an a-C:F simulation at 874 bar target pressure. Please note that the y-axis scale starts at 1,000 kJ mol⁻¹ nm⁻¹. In less than one nanosecond the error is within ± 150 kJ mol⁻¹ nm⁻¹ of the overall average of the simulation, which results a deviation of 14%.

For the calculation of the cumulative average of the pull force that was used as result only the last 10 ns were considered, because adaptation of the system to the new simulation conditions should not influence the results.

For the determination of the errors, the difference of the maximum to the minimum of the cumulative averages within the last 4 ns of the simulations was determined, and then halved. This applies to the perpendicular pressure and the pull force and thus the perpendicular force and the friction force. In figure 9.11 the procedure is indicated, the difference between the minimum and maximum of the cumulative average is in practice determined using the program “xmgrace” and then half that value is the absolute error of the observable. The reason behind this approach is the following: The first 6 ns are disregarded, and after another 6 ns each point is weighed equally as a possible end point. For a whole set of simulations under the same conditions, the largest of the all the determined errors was used as the one error for the whole set of simulations. Errors of the coefficient of friction have been calculated using the maximum error calculation formula for the error ΔO of a property O that depends on the quantities $r_1 \dots r_N$:

$$\Delta O(r_1, \dots, r_N) = \sum_{i=1}^N \left| \frac{\partial O}{\partial r_i} \Delta r_i \right| \quad (9.1)$$

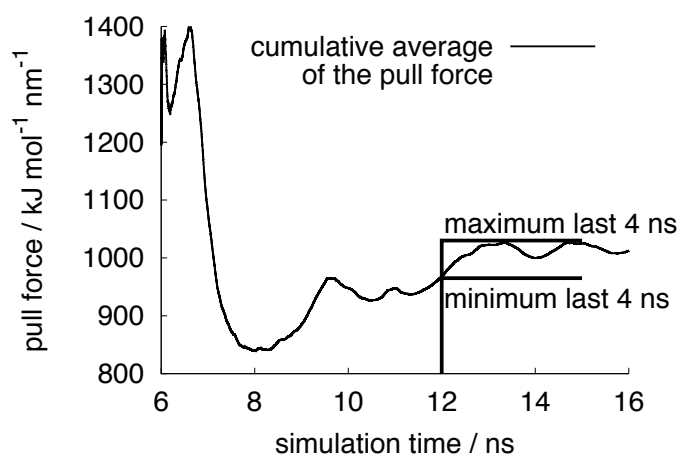


Figure 9.11.: Example of development of the cumulative average of the pull force for an a-C:F simulation for the last 10 ns only. Please note that the y-axis scale starts at $800 \text{ kJ mol}^{-1} \text{nm}^{-1}$. The minimum and maximum of the cumulative average within the last 4 ns are marked in the graph, because they are the basis of the error calculations.

10. Results and Discussion

In this chapter the simulation results using the elucidated approach are presented and discussed. To verify the simulation approach the friction force depending on the perpendicular force has been investigated first. A first step towards validation is performed by comparison between computed and experimental coefficients of friction (COFs). The second section of this chapter elaborates on the influence of the amount of water between the sliding slabs on the coefficient of friction. Subsequently the impact of the variation of the temperature on the COF is discussed and finally the dependence of the friction coefficient on the sliding velocity has been studied, the results are presented in the last part of this chapter.

10.1. The Influence of the Perpendicular Force

In figure 10.1 the dependence of the calculated average friction force on the average perpendicular force during the simulation for the cristobalite (SiO_2) system is shown. For this system in total 216 production runs have been carried out. The results of the friction force are represented by the black crosses, while a linear fit (least squares) is given as dashed line. The linear coherence between friction force on the perpendicular force is observed. The relative errors of the linear fit are minuscule, representing the quality of the linear fit. Furthermore, a very small scattering of the individual results within a given set of simulation conditions is noticeable. In many cases, the simulations ended up with the same results in eight out of nine cases, although new velocities based on the Maxwell distribution were assigned at the beginning of each run. The reason lies within the atomic smoothness of the slabs, as will be discussed in the following.

Replacing one of the slabs with an a-C:F slab, so investigating the MIX system, the scattering of the individual results increases, which can be seen in figure 10.2. Again the friction force results are the black crosses, the least squares fit of the results is the dashed line. For this system 144 simulations have been carried out over the range of target perpendicular pressure from 1 to 10,000 bar. As for the cristobalite system a linear dependence of the friction force on the normal force is observed, and although a larger scattering of results can be seen, the quality of the fit is equivalent.

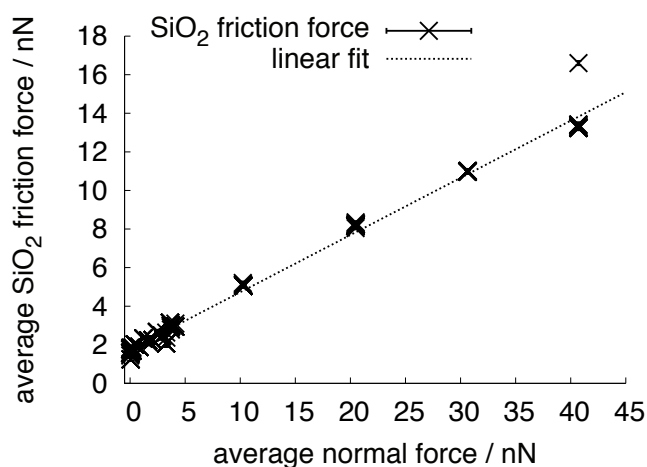


Figure 10.1.: Dependence of the SiO₂ system friction force on the perpendicular force. Solid black: friction force with error bars. Dotted black: linear regression (least squares fit, $0.296 \pm 0.6\% \times F_N + 1.76 \pm 1.6\%$). 216 simulations from 1 to 10,000 bar target pressure perpendicular to the sliding plane, 298 K and 8 Å water layer thickness, errors in the range of 0.7% to 8.3% with respect to the friction force values.

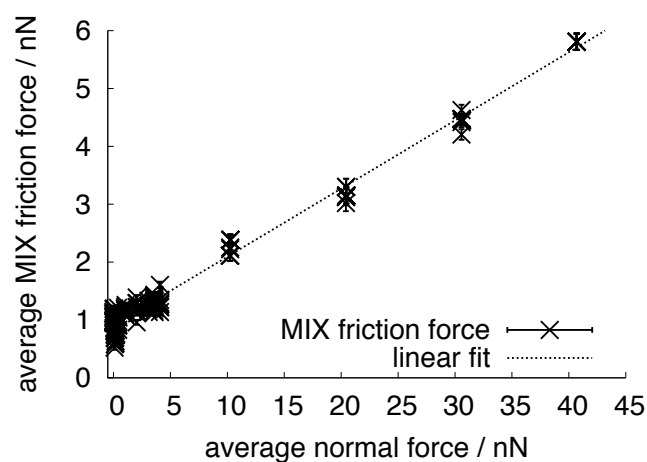


Figure 10.2.: Dependence of the MIX system friction force on the perpendicular force. Solid black: friction force with error bars. Dotted black: linear regression (least squares fit, $0.118 \pm 0.9\% \times F_N + 0.916 \pm 1.6\%$). 144 simulations from 1 to 10,000 bar target pressure perpendicular to the sliding plane, 298 K and 8 Å water layer thickness, errors in the range of 2.0% to 8.3% with respect to the friction force values.

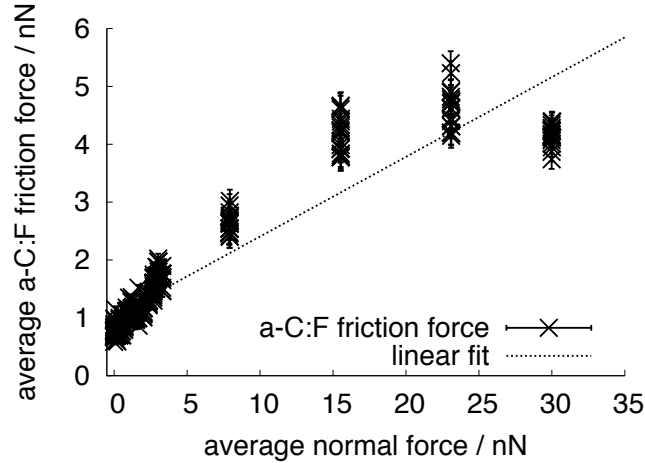


Figure 10.3.: Dependence of the a-C:F friction force on the perpendicular force. Solid black: friction force with error bars. Dotted black: linear regression (least squares fit, $0.138 \pm 2.4\% \times F_N + 1.03 \pm 3.5\%$). 261 simulations from 1 to 10,000 bar target pressure perpendicular to the sliding plane, 298 K and 8 Å water layer thickness, errors in the range of 3.3% to 8.8% with respect to the friction force values.

Changing to the a-C:F system the scattering becomes larger, because now both slabs are rough, and thus the system is less predictable. The results for the dependence of the a-C:F friction force on the average perpendicular force are shown in figure 10.3 in the same manner as for the other two systems. The larger scattering of the results also influences the quality of the linear fit. For this system 261 calculations have been carried out, and although at the first glance a linear dependence of the friction on the perpendicular force is not so obvious, magnifying the lower end of the perpendicular force scale clarifies the situation, because the large majority of the calculations have been performed in the range of 1 bar to 1,000 bar.

The magnification of the lower end of the perpendicular force scale is shown in figure 10.4. Comparing the course of the linear fit with the individual crosses in the low perpendicular force regime a good agreement is to be noted, although a fit with larger slope would represent the lower force regime better and, as mentioned, the scattering of the results is large. These results show, that the friction force depends on the perpendicular force in a linear way over more than five orders of magnitude in perpendicular force (the lowest investigated forces are about $1 \cdot 10^{-4}$ nN). Beyond 3.5 nN normal force, which corresponds to about 1,000 bar target pressure, there is a change in the tribological behavior of the system. The reason is connected to the area of the sliding plane A , which determines the perpendicular force by multiplication with the perpendicular pressure p_N :

$$F_N = p_N \cdot A \quad (10.1)$$

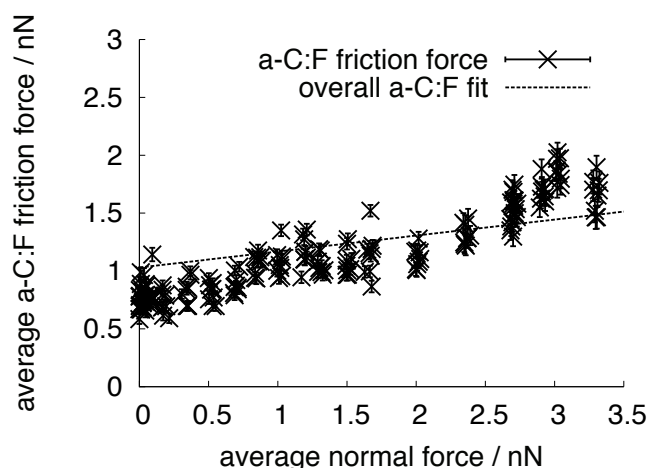


Figure 10.4.: Dependence of the a-C:F system friction force on the perpendicular force. Magnification of same results in Figure 10.3 up to a normal force of 3.5 nN. Solid black: friction force with error bars. Dotted black: linear regression (least squares fit, $0.138 \pm 2.4\% \times F_N + 1.03 \pm 3.5\%$). 189 simulations from 1 to 1,000 bar target pressure perpendicular to the sliding plane, 298 K and 8 Å water layer thickness, errors in the range of 3.3% to 8.8% with respect to the friction force values.

The area of the sliding plane of the MIX and the SiO₂ systems decreases linearly over the target pressure range from 1 to 10,000 bar by only 0.9% (0.37 nm²) and 1.1% (0.45 nm²) with respect to the initial value, respectively, because the SiO₂ slab is crystalline and rigid. For the a-C:F system this is not the case as shown in figure 10.5, at some point beyond 1,000 bar target pressure the compressibility of the slab decreases. In total, the area decreases by 16.7%, only 4.4% area decrease compared to the initial value is observed in the region beyond 1,000 bar. This change in compressibility stems from the compacting of the amorphous slab and is thus resulting from the model construction. Up to a certain point, rings and asperities in the slab may more easily be deformed, after that point, the compressibility decreases. A detailed investigation of the reasons for the change in tribological behavior is a subject of future investigations that include higher pressures, going towards more usual Hertz contact stresses, which occur under application conditions of hybrid bearings. However, the development of the sliding plane area strongly indicates that the slab model is flattened by pressures beyond 1,000 bar.

Comparing the different linear regressions of the results for all systems, the differences in the frictional behavior can be seen from figure 10.6. The fit to the cristobalite results is represented in dashed black, the regression of the a-C:F system results are shown in solid black, while the dotted black line represents the linear fit to the MIX system results. Both, y-axis intersection and slope are largest for the SiO₂ system, although this system consists of two atomically smooth surfaces. The MIX system friction force starts and

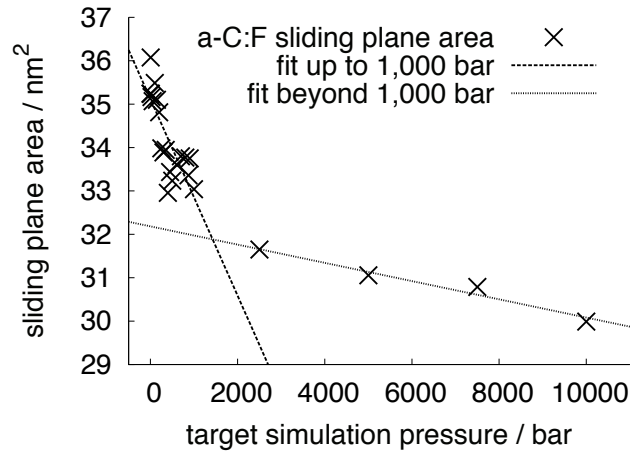


Figure 10.5.: Development of the a-C:F sliding plane area with increasing target simulation pressure. Area of the last frame of the equilibration run is fixed for the production run simulations. Two linear fits of the regimes up to 1,000 bar and beyond 1,000 bar demonstrate the kink in the development. The determination of the onset of the resulting change in tribological behavior needs further simulations.

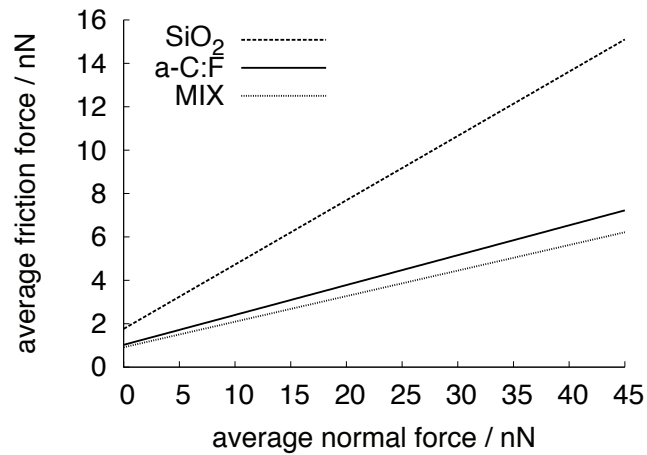


Figure 10.6.: Comparison of the linear regressions of the dependences of the friction on the normal force for the three investigated systems, SiO₂ (dashed black), a-C:F (solid black), and MIX (dotted black).

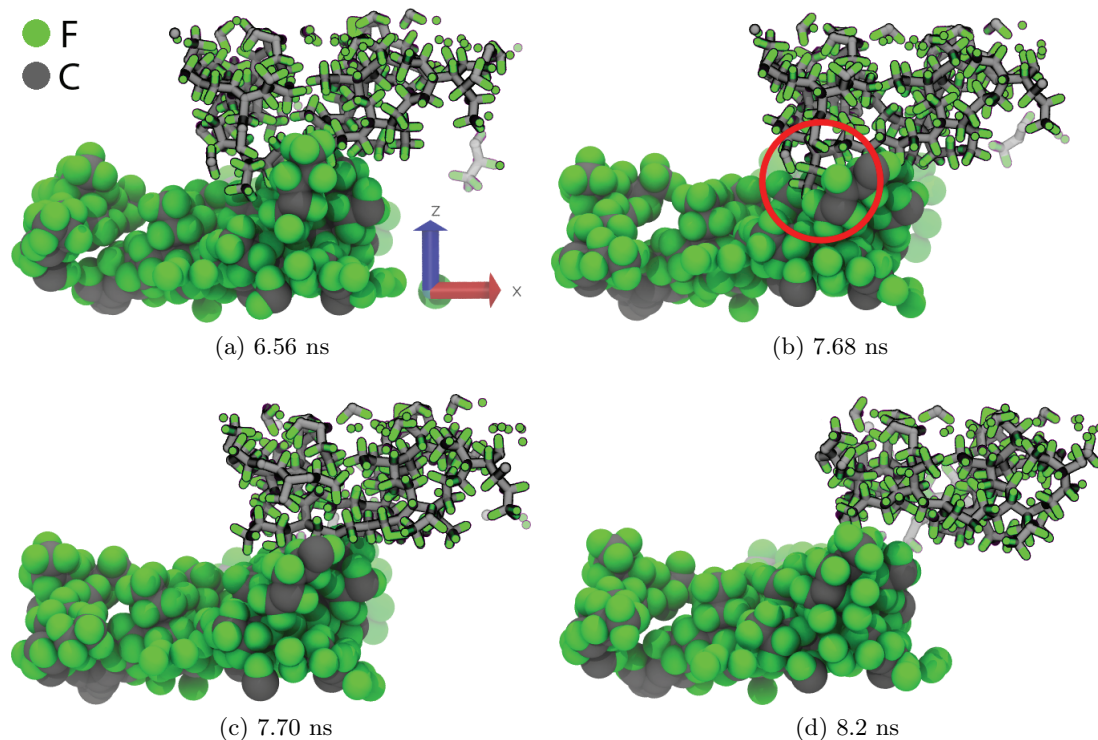


Figure 10.7.: Typical snapshots of interlocking of a-C:F surface asperities. Snapshots taken from a cut of the simulation system. Within 20 ps between snapshot b and snapshot c the interlocking is resolved. Water has been omitted for clarity. The sample trajectory parameters are 874 bar, 298 K and 8 Å water layer thickness.

stays lower than the a-C:F system friction force, but the two results are comparable. The slopes of the fits to the results of both a-C:F containing systems (0.118 MIX, 0.138 a-C:F) are below half the slope of the silicon dioxide system (0.296). This means, that replacing only one hydrophilic slab with a hydrophobic one, already drastically reduces the friction although the a-C:F slab is rougher than the cristobalite surface. Surprisingly the friction force does not drastically increase, if the second slab also becomes a rough slab, although interlocking occurs. Typical snapshots of interlocking between the a-C:F slabs are shown in figure 10.7. At the starting point (snapshot a), an asperity of the upper slab protrudes into a corrugation of the lower slab. In snapshot b the interlocking is visible by the overlap of asperities of upper and lower slab that is highlighted by the red circle. By deformation of the slabs, 20 ps later the interlocking is resolved by deformation of the asperities (snapshot c). Finally the deformed surface asperities slide over each other as shown in snapshot d.

Concluding the first results, for all three systems the friction force depends on the perpendicular force in a linear way. This reproduces the macroscopic behavior according

to equation 1.1. Additionally, the nanoscale friction laws have also been reproduced: Mo and Szlufarska developed a model for the friction laws on the nanoscale [12, 13] and state, that a linear dependence is observed, if the interaction is a nanoscopic, rough, multi-asperity and non-adhesive contact. Their simulations focused on dry DLC on diamond with tip radii of 5 nm to 30 nm and forces ranging from 5-20 nN up to 55-100 nN. Since all the systems in our simulations are not purely adhesive due to the lubrication, our simulation results agree with the model. This is especially interesting, because the cristobalite system is not rough, although the protruding hydroxyl groups might count as nano-asperities. Furthermore the linear behavior is not altered by the surface roughness of the a-C:F slab, although the larger the combined surface roughness of both slabs, the larger the scattering of the results gets. For the roughest contacts in the a-C:F systems the scattering is largest, for the MIX system the scattering is existent but small, and for the silicon dioxide system the scattering is nearly not existent.

Focusing on the friction characteristics of the systems and the expectations from the macroscopic scale point of view, it is reasonable, that the SiO₂ system exhibits the largest friction forces, because the COF of silicon dioxide materials in macroscopic experiments is larger than the COF of PTFE-like materials [99, 100, 136]. Changing one of the hydrophilic slabs to an a-C:F slab, the friction force drops to the value obtained for the MIX system, although the a-C:F slab is rough and not atomically smooth. Replacing only one of the hydrophilic surfaces with a hydrophobic surface already reduces the friction coefficient, which is a fact that has also been observed in the tribometry experiments discussed in this thesis. Considering the a-C:F surface roughness it is astounding, that introducing a second rough slab (a-C:F system) does not increase the friction more than it does due to the interlocking.

The result, that changing one of the surfaces from hydrophilic to hydrophobic already reduces the friction by destroying the hydrophilic interactions directly explains, why in the experimental part of this thesis it was observed, that for water lubrication the friction coefficient drops once the steel surface is coated, independently of the coating state of the ceramics ball. The steel surface is covered by metal oxides that are terminated with hydroxyl groups, hence the surface is highly hydrophilic, just as the SiO₂ slab in the simulations. However, it still remains unclear, why the sole coating of the ceramics ball does not result in the same effect.

The simulation approach may be considered verified by the results presented and discussed above. Over a very wide range of perpendicular force for three very different systems a linear dependence of the friction force on the perpendicular force was observed, which is in accordance with macroscopic and nanoscopic friction laws. Furthermore the comparison between the three systems and the relative values provide a reasonable picture. Additionally the experimental results of this thesis regarding the tribometry of

water lubricated bearing parts corroborate the observations.

Resultantly the next step is validating the sliding friction simulation approach. Validation is achieved by comparing to experimental and computational results and obtaining at least the same trends, if not approximately the same values. As stated in the introduction to this part, the obtained coefficients of friction (COFs) depend on the load [98, 104, 105], hence the comparison of the COFs must be based on the perpendicular pressure. The friction force depends linearly on the normal force with slope a and non-zero y-axis intersection $F_{F,0}$, the adhesive force [12, 13]:

$$F_F = a \cdot F_N + F_{F,0} \quad (10.2)$$

While using equation 10.1 to express the normal force, substituting equation 10.2 in equation 8.1 (page 71) we arrive at a hyperbolic dependence of the friction coefficient on the zz-component of the pressor tensor:

$$\mu = \frac{a}{2} + \frac{F_{F,0}}{2 p_N \cdot A} \quad (10.3)$$

In table 10.1 several experimental and computational results for comparison with our simulation results are listed with the respective denominations and citations.

The comparison between our simulation data and experimental and computational data of others is displayed in figure 10.8 for the a-C:F system results. The simulation results are shown in red with error bars. The hyperbolic dependence of the COF on the perpendicular pressure can be identified in our simulation results. Comparing our simulation results to the experimental and computational work of others, we can state that the results of the Jang et al. (pink, [98]) publication both do not agree very well with our results. The left cross in pink is the experimental result of this publication, and the agreement is not satisfactory, because crystalline PTFE was employed in the experiments and also in the simulations (right pink cross). The main reason for the tribological difference between PTFE and our amorphous coating is the entanglement and knotting and finally rupture of the PTFE chains. Since crystalline PTFE and a-C:F are not comparable, this is also the reason, why the agreement between our simulations and the friction coefficient of the Barry et al. publication (green, [101]) is not very good. Again crystalline PTFE was considered by Sawyer and coworkers, and resultantly in the MD simulations the beautifully observable entanglement increases the friction coefficient. However, in the Chiu et al. publication (blue, [102]) the PTFE chains have been randomly cross-linked, and instantly the friction coefficient agrees perfectly with our results, because the entanglement is reduced or disabled. This coincidence of results is remarkable, because the calculations by Sawyer and colleagues have been carried out for dry contacts, using a

Table 10.1.: Measured or calculated coefficients of friction (COF) published by various researchers, the investigated materials, the kind of study, experimental or simulation, and the corresponding references are listed.

Material	Kind	COF value	Reference
SiO ₂	exp.	0.25-0.35	Reitsma et al. [137]
PTFE	sim.	0.28±0.01	Barry et al. [101]
PTFE	sim.	0.17±0.008	Chiu et al. [102]
PTFE	exp.	0.3±0.1	Jang et.al. [98]
	sim.	0.55±0.15	
a-C:F:H	exp.	0.29-0.81	this thesis and Haupt ed. [87]
Si ₃ N ₄ / a-C:F:H	exp.	0.15±0.02	Prioli et al. [115]
Si ₃ N ₄ / a-C:F:H	exp.	0.2±0.04	Maia da Costa et al. [39]

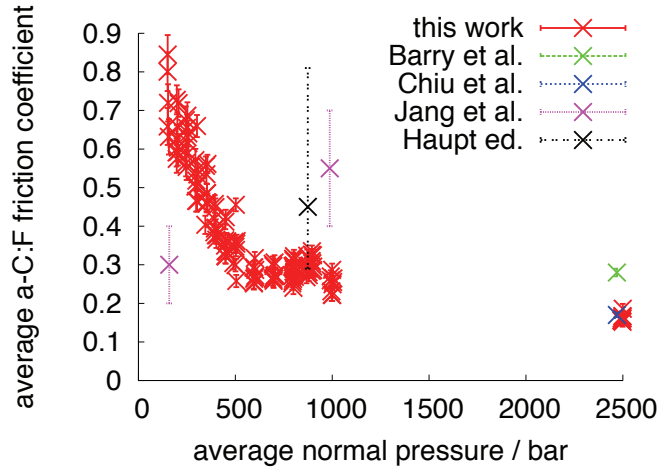


Figure 10.8.: Comparison of the a-C:F friction coefficients calculated in this work (8 Å water layer thickness, 298 K) and the experimental and computational friction coefficients published by other researchers. The data of this work is shown only in the range from 150 bar to 2500 bar average perpendicular pressure. Barry et al. (green, [101]) and Chiu et al. (blue, [102]) are simulation results on the sliding of PTFE chains perpendicularly to each other, in case of Chiu et al. these chains are randomly cross-linked. The errors used here are given in their publications as errors for linear fits of simulation results starting at the pressure displayed here. The lower pressure result of Jang et al. (pink, [98], lefthand side of the graph) is an experimental result for PTFE, while the higher pressure result (pink, righthand side) of that work is obtained by computational perpendicular shearing of crystalline PTFE chains. The friction coefficient oscillations given in that publication were used for the error bars. The friction coefficient of Haupt ed. [87] was experimentally determined in the work underlying this thesis using a-C:F:H coated hybrid ball bearing parts and pure water lubrication for tribometry, the average of the measurements is shown with minimum-maximum results whiskers.

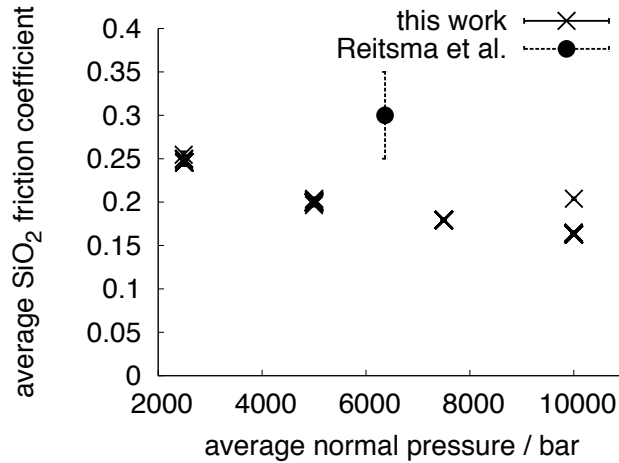


Figure 10.9.: Comparison of friction coefficients resulting from SiO₂ simulations of this work (black crosses) and an experimental friction coefficient of Reitsma et al. [137] (black circle). Reitsma et al. carried out AFM measurements employing a quartz surface and a silicon AFM tip, which presumably is also oxidized. Data of this thesis is shown only between 2500 bar and 10000 bar average pressure perpendicular to the sliding plane.

complex thermostating scheme of only the part farther away from the sliding interfaces, and a reactive force field was employed [1]. However, it has to be mentioned, that also in our case not the whole surface of the slabs was covered with water molecules.

For all three systems, the COF depends on the amount of water between the slabs, as will be discussed in the following section. The amount of water for MIX and a-C:F system may be too high compared to experimental junctions, because less water is adsorbed on hydrophobic surfaces than is absorbed on hydrophilic surfaces [113].

Experimental data to truly validate our computational results regarding the a-C:F systems is only available from our own experiments. These results are shown in black in figure 10.8. The standard simulation pressure and the experimental maximum Hertz contact stress were the same (874 bar) and the temperature was almost exactly the same (exp.: 20 °C, sim.: 25 °C). Furthermore, the PECVD a-C:F:H coating surface was modeled. The agreement between our simulations and the experiments is very good, especially regarding the overlapping of the simulations scattering and the variations of the experimental results.

Additionally, not only for the a-C:F system there is satisfying agreement between simulation and experiment. For the silicon dioxide system a publication by Reitsma et al. [137] gives the friction coefficient between silicon dioxide surface and a presumably oxidized silicon AFM tip. The comparison between those results and the simulations is displayed in figure 10.9. The difference of the experimental friction coefficients and the hyperbolic development of the simulation results stems first from the surface damage the

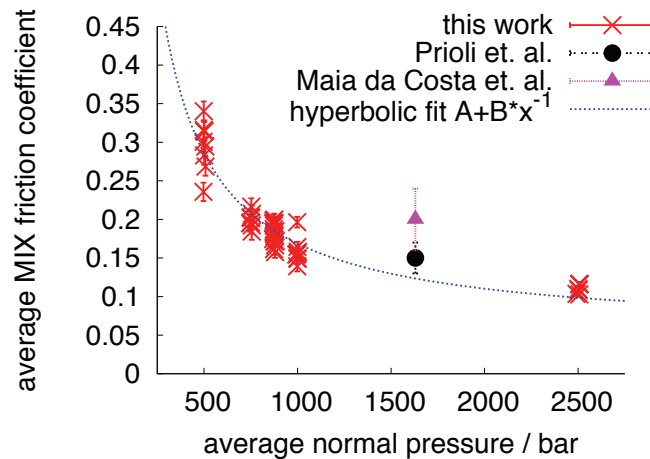


Figure 10.10.: Comparison of the MIX simulation friction coefficients of this work (red) and experimental friction coefficients of other researchers. Data of this thesis is shown only between 500 bar and 2500 bar average pressure perpendicular to the sliding plane. A hyperbolic fit is included to guide the eye (blue). The Freire Jr. group published AFM measurements of a silicon nitride AFM tip on an a-C:F:H coated surface with two rel. humidities, 28% in the Prioli et al. [115] publication (black), 38% in the Maia da Costa et al. [39] publication (pink).

tip produces and second the fact that our slabs are atomically smooth. A third factor is the assumed amount of water, with decreasing water between the slabs, the computed COFs increase. The amount of water that has been assumed is reasonable but rather high. Regarding these facts the agreement is indeed satisfying.

Fortunately also for the MIX system a comparison to the experimental results of other researchers is possible. The result of the comparison of our simulation data with the experimental results of Freire Jr. and coworkers (Prioli et al. [115] and Maia da Costa et al. [39]) is presented in figure 10.10. The agreement between the hyperbolic dependence of our simulation data and the experimental values obtained from silicon nitride tip AFM on a-C:F:H coatings is very good. The surface of the silicon nitride AFM tip is an amorphous silicon oxide, which is chemically very close to our crystalline silicon dioxide. One of the two experimental results is closer to our simulation results, it is the one obtained in an atmosphere of lower relative humidity. The other result is obtained in a more humid atmosphere and the COF with more water in the tribological system is higher. This trend is opposite to the trend we observe for the variation of the water layer thickness, which is the topic of the next section. The reason is the formation of menisci at the sides of the tip due to capillary force [104, 113, 138, 139] that create a retarding force, which is of course not included in our simulations of relative shearing of planar slabs.

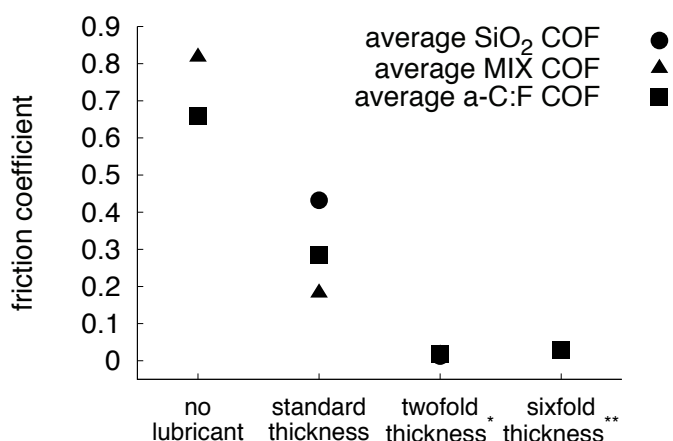


Figure 10.11.: Comparison of the dependences of the average coefficients of friction on the water layer thickness. The three investigated systems are SiO₂ (circles), a-C:F (squares), and MIX (triangles). The standard water layer thickness is 8 Å. Error bars have been omitted for clarity. For no water between the cristobalite slabs no shearing was observed up to a pull force corresponding to a friction coefficient of about 4.7 because of artificial interlocking of the commensurate slabs. This result has been omitted.

* Simulation results are approximately the same and are not distinguishable for twofold water layer thickness.

** a-C:F system only: Simulation conditions for sixfold water layer thickness have been changed. The simulation volume contained only a single a-C:F slab that was pulled through about 6,100 water molecules. The average friction coefficient is approximately the same as the average of the results for twofold thickness.

Concluding the first step towards validation of the approach, simulations of this work agree with simulations of other researchers if the atomic structure of the material models is similar. Most importantly, for all three investigated systems the agreement between our simulations and the experimental work of other researchers and also experiments of this thesis is very good.

10.2. The Influence of the Water Layer

To investigate the influence of the water layer, for all systems three different amounts of water between the slabs has been investigated: No water, the standard amount of water (8 Å water layer thickness) and twice the standard amount of water. The standard amount of water is reasonable considering squeeze-out and experimental results [113, 114, 132] for the silicon dioxide system (see the computational details in section 9.2), but rather high for the more hydrophobic MIX system and the completely hydrophobic a-C:F

system [113]. For all the different sets of simulation conditions 18 production runs each have been carried out at 874 bar and 298 K. Additionally for the a-C:F system another set of simulations was realized, including 6-times the standard amount of water around only one slab in the simulation volume, so any interactions simulated are the interactions with the periodic images below and above the real image. In this case the pull force was not referenced the second slab but to the center of mass (COM) of the water molecules, which is very flexible in time, resulting in a larger scattering of the results. In this case, no significant differences for the COM motion removal of parts or the whole system was found. The COM motion removal prevents the system from developing torques and other artifacts.

In figure 10.11 the resulting different friction coefficients for the three systems are displayed. No water in the simulation systems is labeled as “no lubricant”, the standard water layer thickness is labeled as “standard thickness”, which is 8 Å. Twice the standard amount of water is labeled as “twofold thickness”. For this amount of water the results coincide, which is the reason for the simulation with 6-times the standard amount of water around a single a-C:F slab, which is labeled as “sixfold thickness”. The simulations for the a-C:F slab with sixfold thickness included about 6,100 molecules of water. In this graph, the average COFs for the silicon dioxide system are displayed as circles, for the MIX system as triangles and for the a-C:F system as squares. Error bars have been omitted and only the averages of the 18 production run COFs are shown for clarity reasons. In case of no lubrication the commensurate silicon dioxide slabs interlock with their hydroxyl-groups, resulting in at least a pull force corresponding to a friction coefficient of at least about 4.7. This behavior is of course absolutely artificial, because reactions would occur in the system, but reactions cannot be modeled with our classical MD simulations. Furthermore the artificial atomical smoothness and the commensurability give rise to the interlocking, which is not possible to the same extent even with very limited roughness. Consequently the result for no lubrication in the SiO₂-system has been omitted. The results for the standard water layer thickness are clearly distinguishable, as already stated, the friction coefficient for the MIX system is the lowest, the cristobalite system gives the largest COF and the a-C:F system is in between. Not distinguishable are the results for twice the amount of water between the slabs, because the results coincide. The obtained friction coefficients for all simulations of all systems is about 0.02. The reason is the separation of the slabs, as is proven by the simulations of six-times the amount of water around one a-C:F slab. Even for this slab, the rougher slab, the pulling through a lot more water results in the same friction coefficient. Concluding, the interactions of the slabs decay rapidly with increasing water layer thickness.

To further validate the simulation approach the computational results can again be compared to the experimental results of this thesis. The comparison is shown in figure 10.12.

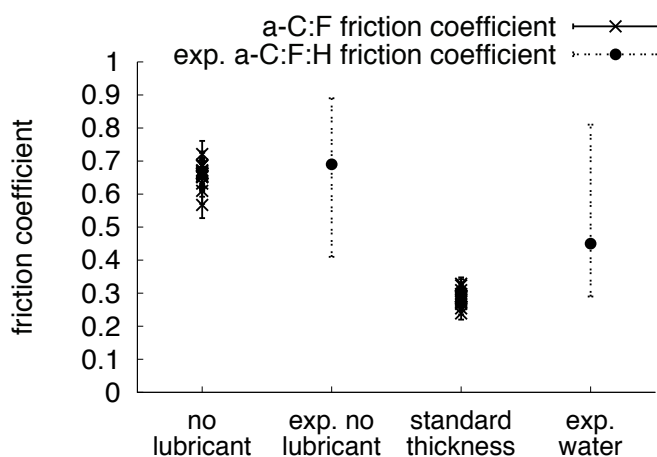


Figure 10.12.: Comparison between the experimental results obtained in this thesis for no lubrication and water lubrication with the simulation results of this thesis for the a-C:F system with no lubrication and water lubrication (874 bar and 298 K). The experimental results are shown as averages with dotted minimum-maximum whiskers as black circles, the simulation results are shown as black crosses with solid error bars.

The experimental results are given with dashed minimum-to-maximum whiskers and black circles, while the simulation results are given with as black crosses with error bars. The comparison for the standard amount of water has already been shown, and the agreement is good. For no lubrication in the experiments and no water in our simulations the agreement between simulation and experiment is quantitative. The average of the simulation results differs from the average of the experimental results by only 0.03, which is less than 5% deviation. For the lubricated state the difference between the two averages is 0.16, which is 35% with respect to the experimental results. Considering the agreement between experiment and simulation without lubricant, the deviation in case of water lubrication may mean, that in experiments less water than in our simulations is involved in the friction of load-bearing junctions. This finding is also corroborated by experimental results on the comparison of the water layer thicknesses on hydrophilic and hydrophobic surfaces [113].

The large difference between the computed COFs of all systems with standard lubrication and with twice that amount of water led to the investigation of the different morphologies of the water layers. These morphologies cannot be compared to experimental morphologies, but they can explain the observed results. In case of the standard lubrication the water layer thickness is assumed to be 8 Å, which results in about 1,000 water molecules between the slabs. In case of the silicon dioxide slab the water slab is strongly shaped, which can be seen from figure 10.13. In this picture one cristobalite slab is shown and one water layer on top, between the two slabs. The hydroxyl groups strongly affect the or-

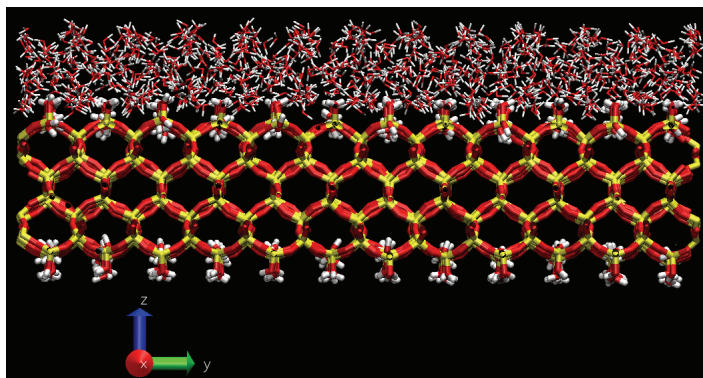


Figure 10.13.: One SiO_2 slab of the SiO_2 system and one water layer with standard water layer thickness of 8 \AA . The view is oriented along the x-axis direction. Shaping of the water layer can be observed, because a zigzag shape of the water layer in z-direction can be identified, which stems from filling the space between the hydroxyl groups. Simulation carried out at 298 K and 874 bar.

dering of the water molecules, which can be seen from the zigzag shape of the upper part of the water layer. The water layer is shaped by filling the space between the hydroxyl groups of the upper SiO_2 slab that is not shown. Since the distance of the slabs is only 1.1 nm from first silicon atom layer of slab one to the first silicon atom layer of slab two, the interactions of the silicon dioxide slabs are direct via electrostatic and Lennard-Jones interactions (cut-off 1.7 nm) and additionally indirect. The water layer of 8 \AA thickness is in the range of nanoconfinement and hence the polar interactions of the surface with the water molecules drastically influence the tribological behavior [91, 140, 141]. The water molecules form hydrogen bonds with the surface and with each other and again to the other surface. Viewed along the z-direction, the water layer of the cristobalite system is a closed layer (picture not shown).

This is not the case for the MIX system, for which due to the surface roughness of the a-C:F slab the water layer is not closed, which can be seen from figure 10.14. Obviously there are two holes in the water layer, where direct contact of the slabs occurs. The holes stem from the asperities of the a-C:F slab. If the amount of water is doubled (twofold thickness in figure 10.11), the water layer is structured by the a-C:F slab but at least one layer of water molecules remains between the slabs (picture not shown). Hence for twice the amount of water complete separation of the slabs occurs and the frictional interactions are drastically reduced, because in the MIX system the water layer does not mitigate any hydrophilic interactions between the slabs.

If both slabs are hydrophobic, the structure of the water layer with the standard water layer thickness changes further. As seen in figure 10.15, in the a-C:F system the water molecules form a string because they prefer interaction with themselves and not with

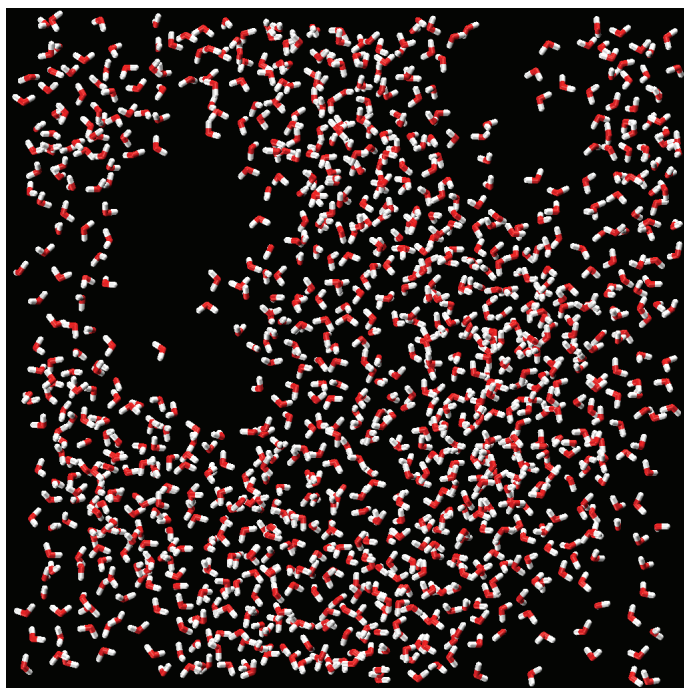


Figure 10.14.: One of the water layers of the MIX system with the standard water layer thickness (8 \AA), viewed along the z -direction perpendicularly to the sliding plane. The holes in the water layer show penetration by surface asperities of the a-C:F material model. Simulation carried out at 298 K and 874 bar.

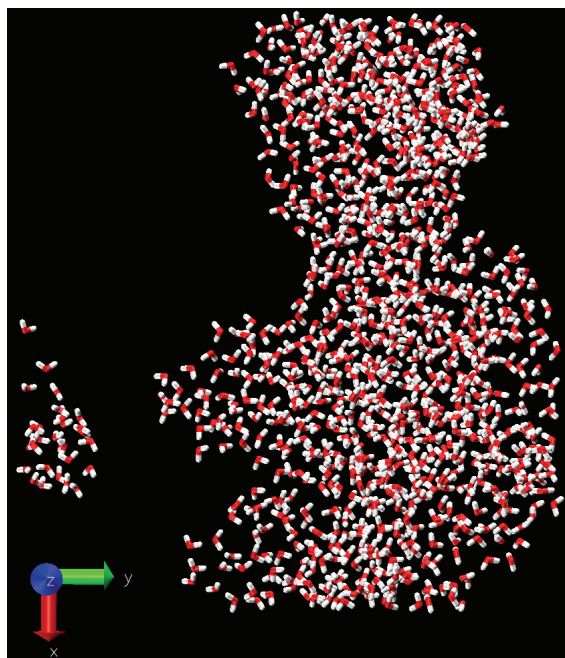


Figure 10.15.: One of the a-C:F system water layers with standard amount of water (8 \AA water layer thickness), viewed from the z -direction. Water forms a string due to the hydrophobic nature of the a-C:F material model. Simulation carried out at 298 K and 874 bar.

the hydrophobic surfaces. Again, if the amount of water is doubled, the two slabs are separated by at least a layer of one water molecule thickness (picture not shown) although a shaping by the surface roughness is observed. Hence also for this system no frictional interactions besides direct electrostatic and Lennard-Jones interactions occur any more, because the surfaces are not hydrophilic.

Concluding, the water layer thickness influences the friction between hydrophilic slabs in a different way than if at least one surface is hydrophobic. In case of two hydrophilic, atomically smooth slabs complete separation is present already with 8 Å water layer thickness. Hydrophilic slab interactions are mitigated by a strongly shaped, nanoconfined water layer of only 8 Å thickness. Phenomenologically, if the amount of water is doubled, the mitigating effect, the indirect and the direct interactions are drastically reduced due to the increased slab distance. As a result the computed COFs drop. If one slab is hydrophobic, no complete separation occurs in the MIX system under standard lubrication conditions due to the surface roughness of the a-C:F slab. But since the hydrophilic interactions are missing, the COF is lower. If the amount of water is doubled in the MIX case, the surfaces are still close in the regions of the asperities, but the direct interactions are missing, and thus the COF is reduced. In the a-C:F case the frictional interactions also are direct in case of the standard amount of water, while these direct interactions are negated by twice the amount of water due to complete separation of the surfaces. In summary, for the MIX and the a-C:F systems the complete separation of the slabs by a water layer of only a single water molecule thickness results in absolute mechanical decoupling of the surfaces. The COF is significantly reduced by this elimination of direct slab-slab interactions. However, no experimental information on the morphology of a water layer in a junction for comparison is at hand, so only the simulation results can be explained.

10.3. The Influence of the Temperature

The influence of the variation of the temperature has been investigated to test the sensitivity of the friction coefficients we obtain with respect to temperature deviations. One reason is the slight temperature difference between the simulations and the experiments, 5 °C. Furthermore obtained thermal activation energies E_A can be compared to experimental results. For all the systems the temperature dependence is investigated by normalization of the results to the average friction coefficient at 298 K $\bar{\mu}_{298 K}$:

$$\mu^* = \frac{\mu}{\bar{\mu}_{298 K}} \quad (10.4)$$

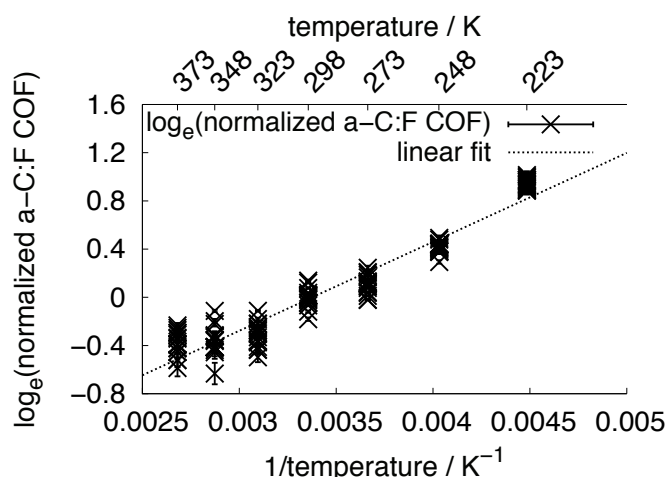


Figure 10.16.: Arrhenius graph of the dependence of the friction coefficients of the a-C:F system that are normalized with respect to the average value at 298 K on the target simulation temperature in the range from 223 K to 373 K, $-50\text{ }^{\circ}\text{C}$ to $+100\text{ }^{\circ}\text{C}$. The natural logarithm of the friction coefficients is represented as black crosses with error bars, a linear fit (least squares) is shown in dotted black, the slope of the linear fit results in a thermal activation energy E_A of $E_A = 6.1\text{ kJ mol}^{-1}$, 18 simulations at each temperature, 874 bar and 8 Å water layer thickness in all cases, friction coefficient errors are between 3.1% and 14% of the respective COFs.

The dependence of the natural logarithm of the normalized friction coefficient of the a-C:F system on the temperature is shown in figure 10.16. For all the different temperatures a set of 18 simulations has been carried out, pressure of 874 bar and water layer thickness of 8 Å were the same as for the standard simulations. In addition to the results shown in black with error bars, a linear fit is given in dotted black. Throughout the investigated temperature range from 223 K (right end of the graph x-axis) to 373 K (left x-axis end) the agreement between fit and curve is very good. The activation energy for the thermally activated friction in the a-C:F system is 6.1 kJ mol^{-1} . Resulting from the observed low temperature dependence the very small temperature difference between our experiments and our simulations of $5\text{ }^{\circ}\text{C}$ influences the friction coefficient only by a negligible amount. It has to be noted, that for the investigated temperature range from 223 K to 373 K ($-50\text{ }^{\circ}\text{C}$ to $+100\text{ }^{\circ}\text{C}$) freezing or evaporation of the water molecules is not possible even without regarding the elevated pressure or the shearing forces. The melting point of water modeled by SPC/E has been determined by Vega and coworkers, and it is with 215 K ($-58\text{ }^{\circ}\text{C}$, [142]) below the investigated temperature range. The normal boiling point of water using this model can be concluded from another publication by Vega et al. [143]. The boiling point of water described by the SPC/E model is 400 K ($117\text{ }^{\circ}\text{C}$), accordingly the SPC/E model does not allow for evaporation of the water molecules in the investigated temperature range even if the pressure would be only 1 bar.

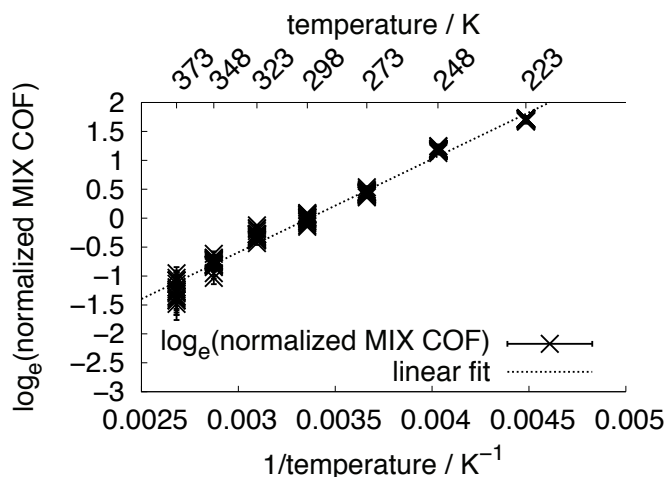


Figure 10.17.: The dependence of the natural logarithm of the friction coefficients of the MIX system that are normalized with respect to the average value at 298 K on the target simulation temperature in the range from 223 K to 373 K, -50 °C to +100 °C. The natural logarithm of the friction coefficients is represented as black crosses with error bars, a linear fit (least squares) is shown in dotted black, the slope of the linear fit results in the the thermal activation energy E_A of 13.4 kJ mol⁻¹, 18 simulations at each temperature, 874 bar and 8 Å water layer thickness in all cases, friction coefficient errors are between 2.0% and 19% of the respective COFs.

For the MIX system the temperature dependence of the normalized friction coefficient is shown in figure 10.17. Again the results are fitted using a linear fit, and in this case the obtained activation energy is 13.4 kJ mol⁻¹. The agreement between the results and the fit is very good.

For the silicon dioxide system the respective results on the temperature dependence of the normalized friction coefficient is shown in figure 10.18. Since the observed behavior is not Arrhenius-like, no linear fit has been calculated.

Comparing the three different dependencies of the simulation results, the activation energy of the MIX system is higher (13.4 kJ mol⁻¹) than the activation energy of the a-C:F system (6.1 kJ mol⁻¹). Arguing on the phenomenological basis of the water layer morphology, the reason for the stronger temperature dependence of the MIX system has to be the water molecule mobility. Since one of the surfaces in the system is atomically smooth and not rough as in the a-C:F case, the temperature dependence should not stem from slab deformation and release of interlocking asperities. As displayed in figure 10.14 there are holes in the water layer, which have to move alongside the asperities during sliding. This movement of the water holes is facilitated or hampered depending on the water molecule mobility that in turn depends on the temperature. For the MIX system the self-diffusion coefficient D of water at 223 K is with $D = 6.10 \pm 2.18 \cdot 10^{-7} \text{ cm}^2 \text{ s}^{-1}$ consid-

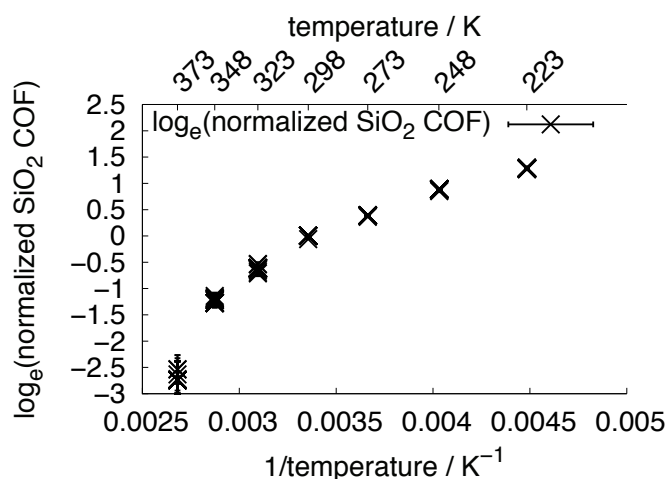


Figure 10.18.: The dependence of the natural logarithm of the friction coefficients of the SiO₂ system that are normalized with respect to the average value at 298 K on the target simulation temperature in the range from -100 °C to +100 °C, friction coefficients are represented as black crosses with error bars. Since there is no Arrhenius behavior no fit is shown, 18 simulations at each temperature, 874 bar and 8 Å water layer thickness in all cases, friction coefficient errors are between 1.5% and 13% of the respective COFs.

erably lower than the diffusion coefficient at 373 K of $D = 1.195 \pm 0.0037 \cdot 10^{-5} \text{ cm}^2 \text{ s}^{-1}$. In other words, the squeeze-out of water molecules from between the junction is increasingly difficult with decreasing temperature. For the a-C:F system, a large part of the friction stems from rearrangements of the slabs because the asperities directly interact. More mobility of the water molecules in the water string (see figure 10.15) is not very beneficial for the overall friction force. Thus the temperature dependence is dominated by the interlocking of the a-C:F asperities only, and apparently the resulting activation energy is smaller than the one of the MIX system. For the cristobalite system the water molecule mobility might be important for the mitigation of the hydrophilic interactions. However, no Arrhenius behavior of the COF is observed. In comparison to the energy of room temperature of 2.5 kJ mol^{-1} , the difference between low temperature and high temperature activation energy is very large: Fitting the lower temperature regime from 223 K to 298 K (righthand part of figure 10.18) an activation energy of 9.54 kJ mol^{-1} is observed (minimum local activation energy 7.3 kJ mol^{-1}), while fitting from 298 K to 373 K an activation energy of 31.8 kJ mol^{-1} results (maximum local activation energy 63.8 kJ mol^{-1}). This trend is also opposite to the trend deduced from experiments on diffusivity and viscosity of bulk water. The activation energy of bulk water diffusion is higher for the low temperature regime at 233 K, 42.3 kJ mol^{-1} , than the activation energy at higher temperatures, 313 K, of 17.9 kJ mol^{-1} [144]. The reason for this difference as well as the detailed study of the water layers is subject of future investigations.

Thermally activated friction and an exponential dependence of the COF on the temperature is well known in literature [99, 100, 120]. We can compare our results with these experimental studies from Sawyer and coworkers. They measured friction coefficients of PTFE depending on the temperature with very little water in the atmosphere and arrive at an activation energy for PTFE of 5 kJ mol^{-1} . This value is in very good agreement with our activation energy of the a-C:F system of 6.1 kJ mol^{-1} , where there is water-free contact between the slabs. In crystalline PTFE, the surface chains entangle and finally rupture, as observed in tribology simulations by Sawyer and colleagues [98, 101–103]. This is the dominating tribological interaction and the reason, why the *absolute* values of the COF for PTFE and highly crosslinked a-C:F are not comparable. In our a-C:F simulations, no entanglement and rupturing is possible due to the crosslinking and the classical force field ansatz. However, the temperature dependencies of the COFs of PTFE and a-C:F are comparable. This means, that the entanglement and rupturing of PTFE chains is not significantly influencing the temperature-dependence of the COF of PTFE, only the absolute value of the COF. Therefore only the sliding of CF_x -moieties over each other, which is relevant for PTFE and a-C:F both, is temperature-dependent, as can be deduced from the matching thermal activation energies.

10.4. The Influence of the Sliding Velocity

In addition to the perpendicular force, the water layer thickness and the temperature, the relative velocities of the sliding surface might influence the coefficient of friction depending on the speed of the processes at the interface (see section 1.3). To investigate this possible dependence of the friction coefficient on the sliding velocity, the velocity of the end of the virtual spring in the simulations has been reduced, while retaining standard temperature (298 K), pressure (874 bar) and amount of water (8 Å water layer thickness). Since the slip velocity at the ball track interface is very slow, usually in the order of 1% of the ball velocity, the velocity of the virtual spring has been decreased in the range from 100% to 1% to test the effect of this variation. For each of the relative velocities 9 simulations have been carried out, except for the 18 simulations that are the standard simulations used in any of the investigations of the simulation condition influences.

The results of the simulations with varying spring velocity for the a-C:F system are shown in figure 10.19. The simulation results are displayed as black crosses with error bars, while a linear fit to the results is represented as dashed line. To be able to compare the slopes more easily, the mean value of all results is given as horizontal solid black line. From comparison of mean value line and the linear fit it can be deduced, that there is no relevant velocity dependence of the friction coefficient in the simulations of

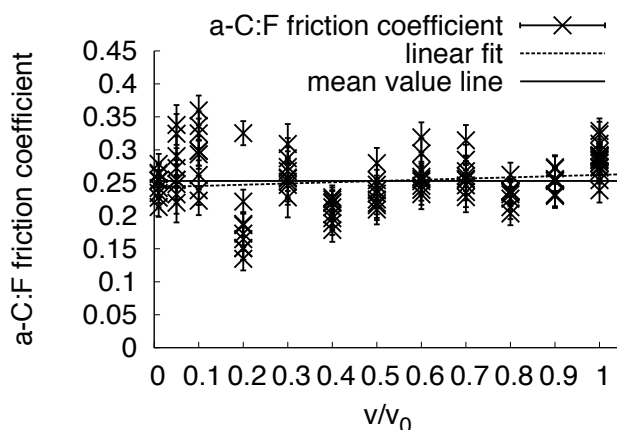


Figure 10.19.: The dependence of the a-C:F friction coefficients on the relative sliding velocity with respect to the original sliding velocity, the friction coefficients with error bars are shown in black, a linear regression (least squares fit, $0.0186 \pm 58.7\% \times v/v_0 + 0.243 \pm 2.7\%$) is represented in dotted black, while the mean value line is displayed in solid black. 9 simulations have been carried out at each velocity from 0.01 to 0.9 and 18 simulations at 1, the errors are in the range from 5.5% to 14% with respect to the COF value. Simulations carried out at 298 K and 874 bar and 8 Å water layer thickness.

the a-C:F system. This result is the macroscopically observed velocity dependence, as stated in section 1.3. The reason for this is the interlocking of asperities and the fact, that apparently the velocities are slow enough to allow for rearrangement of the slab asperities (see interlocking figure 10.7 on page 95). As mentioned in section 1.3 this will not be possible anymore if the relative velocities of the surface become very high.

The investigation of the velocity dependence of the SiO₂ system yielded the simulation results presented in figure 10.20. Again not only the simulation results and the linear fit (dashed line) are given, but also the mean value line. In case of the atomically smooth cristobalite slabs, the slower relative velocities gave the system time to enter a commensurate pinned state (see figure 2.5 on page 28). The slight interlocking resulted in a nano-stick-slip behavior, which influenced the pull force to become close to a sawtooth profile (see figure 10.21). Resultantly the simulations for 1% and 5% of the standard velocity provided no meaningful results, because the velocity was so slow, that the result of a simulation would depend on the starting point of that simulation. This is the reason, why for the silicon dioxide system only the velocity range from 10% to 100% is shown. Considering to the scattering of the results, the difference between the linear fit and the mean value line is very small, so there is no significant velocity dependence or only a very slight one.

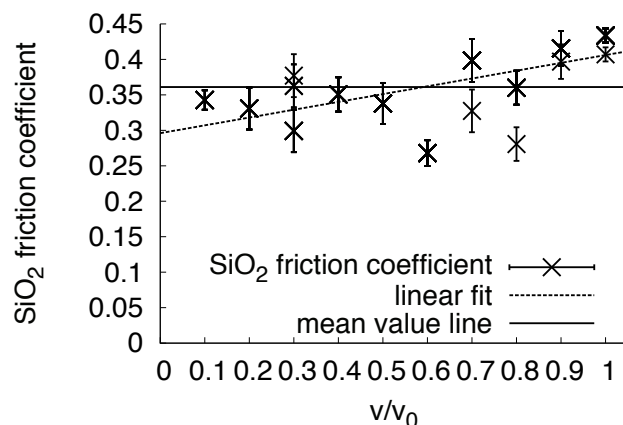


Figure 10.20.: The dependence of the SiO₂ friction coefficients on the relative sliding velocity with respect to the original sliding velocity, the friction coefficients with error bars are shown in black, a linear regression (least squares fit, $0.110 \pm 11.6\% \times v/v_0 + 0.296 \pm 2.9\%$) is represented in dotted black, while the mean value line is displayed in solid black. 9 simulations have been carried out at each velocity from 0.1 to 0.9 and 18 simulations at 1, the errors are in the range from 2.3% to 10% with respect to the COF value. Due to a slight interlocking of the cristobalite slabs and the corresponding saw-tooth profile of the pull force, sliding velocities below 0.1 gave no meaningful results, because these results would depend on the respective starting points of the simulations. Simulations carried out at 298 K and 874 bar and 8 Å water layer thickness.

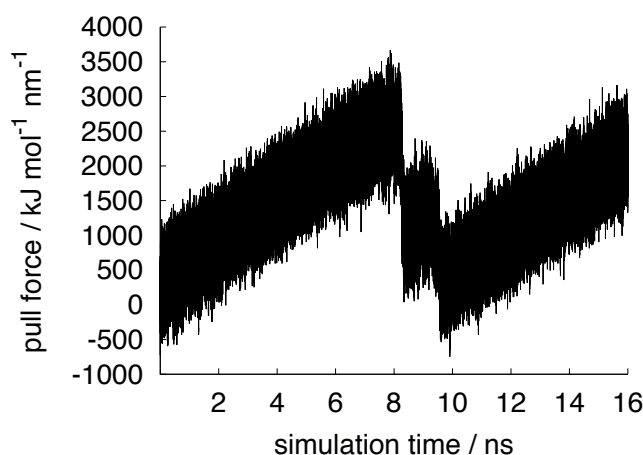


Figure 10.21.: Exemplary sawtooth profile of the friction force of the SiO₂ system at 10% of the original velocity v_0 . Friction force of one trajectory at 298 K and 874 bar perpendicular pressure and standard water layer thickness (8 Å).

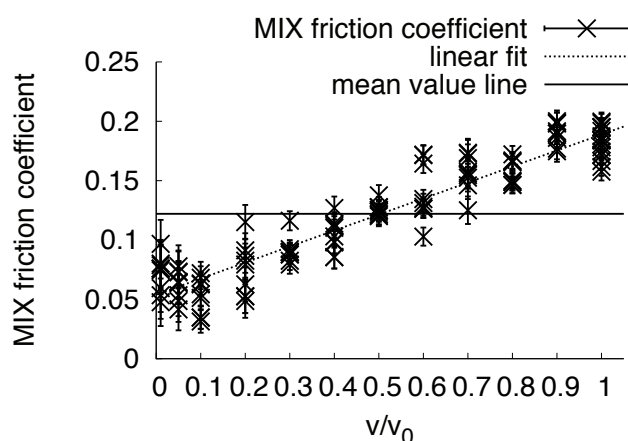


Figure 10.22.: The dependence of the MIX friction coefficients on the relative sliding velocity with respect to the original sliding velocity, the friction coefficients with error bars are shown in black, a linear regression (least squares fit, $0.135 \pm 3.3\% \times v/v_0 + 0.0540 \pm 5.0\%$) is represented in dotted black, while the mean value line is displayed in solid black. 9 simulations have been carried out at each velocity from 0.01 to 0.9 and 18 simulations at 1, the errors are in the range from 3.8% to 42.5% with respect to the COF value. Simulations carried out at 298 K and 874 bar and 8 Å water layer thickness.

For the MIX system the results of the simulations with varying velocity are shown in figure 10.22. The results and the linear fit as well as the mean value line are displayed in the same way as for the other graphs. The velocity dependence for the MIX system is more pronounced than in the case of the other two systems. The slope of the linear regression is 20% larger than in the cristobalite case. Even considering the scattering of the results, for the MIX system there is a noticeable velocity dependence of the friction coefficient.

A comparison of the three velocity dependencies to the results for the velocity variations is shown in figure 10.23. The mean value of the velocity dependent results of the silicon dioxide system is represented as dashed line, the a-C:F system mean value is given in solid black, while the MIX system linear fit is the dotted line. Since the same pressure (874 bar) and temperature (298 K) and water layer thickness (8 Å) conditions as for the standard simulations are employed, the order of the friction coefficients is the same as before, the silicon dioxide system exhibits the largest COF, the a-C:F system is in the middle, while the MIX system results are the lowest friction coefficients. While the a-C:F system certainly exhibits no significant velocity dependence of the COF, the SiO₂ system friction coefficient is approximately constant, while a slight decrease over one order of magnitude in relative velocity results from the linear fit.

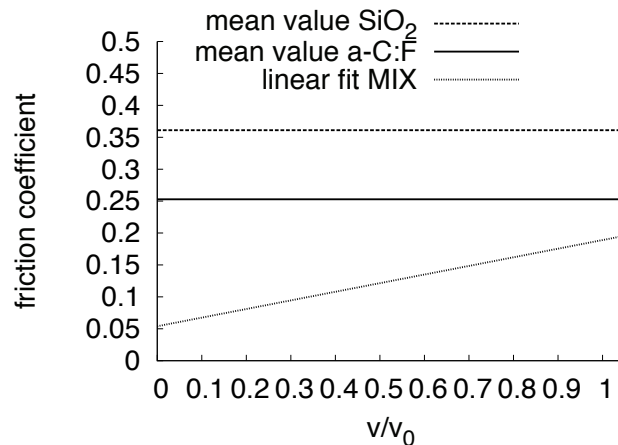


Figure 10.23.: The comparison of the linear regression of the dependence of the friction coefficient on the relative sliding velocity with respect to the original sliding velocity for the MIX system (dotted) with the mean values of the SiO_2 system (dashed) and the a C:F system (solid).

For the MIX system a pronounced velocity dependence is observed, which results in a decrease in friction coefficient by 71% of the standard value over two orders of magnitude in relative spring velocity.

The three velocity dependences have different reasons, which again might be clarified by a phenomenological argumentation. The negligible velocity dependence of the a-C:F system stems from the interlocking of surface asperities, which interlock regardless the relative velocity. Also the shape of the water string in this system is not influenced throughout the investigated velocity range (pictures not shown). Resultantly, for the investigated velocities all interactions and their resolution is fast enough, that the system exhibits no velocity dependence. For the cristobalite system no or only a very slight velocity dependence is observed. A slight dependence of the sliding friction of hydrophilic silicon with small amounts of water is also observed in AFM experiments [104]. The reason for a slight velocity dependence of the friction between hydroxyl group terminated surfaces is known in literature, and has been published by Liu and Szlufarska [112]. They investigated hydroxyl group terminated silicon carbide and found out, that the hydrogen bonds between the surfaces lead to increased friction and additionally to increasing friction with increasing velocity. The rearrangement of the hydrogen bonds retards the hydroxyl groups, and this effect is velocity dependent. It is reasonable to assume, that a similar mechanism affects the nanoconfined water layer of only 8 Å thickness that is strongly shaped by surface hydroxyl groups of the surface, but the effect is negligible, at least over one order of magnitude in relative velocity. In case of the MIX system again the mobility of the holes in the water layer might be the reason for the observed largest variation of the friction coefficient, as it is the case for the temperature variation. The

faster the slabs move, the faster the water hole has to move and the more resistance the water molecules pose to the intermolecular rearrangement. Nonetheless, the detailed investigation of the water layer is a meaningful and important topic of future investigations based on this thesis.

Experimental findings on a possible velocity dependence of the friction coefficient of PTFE depend on the ambient conditions. Several experiments have been carried out using PTFE and steel parts. Shortly after the start of an experiment a transfer layer of PTFE on the steel counterpart will transform the interaction into a PTFE-PTFE interaction, so the different materials are not an issue [145–148]. However, if a comparison of simulations to experiments is desired, the different ambient conditions of the experiments have to be considered. Burris [120] found a slight velocity dependence in pin-on-disk tribometry in dry atmospheres. Using balls instead of flat steel specimens, Karnath et al. [105] found a significant velocity dependence, but equally significant wear tracks were created, which means, that the velocity dependence is the result of the plastic deformation of the PTFE surface. Unal et al. [148] report no significant velocity dependence in a humid atmosphere, which is the experimental condition most similar to our simulations, because water condenses on surfaces in humid atmospheres [106–108]. Concluding, no significant velocity dependence seems to be the experimental result under conditions that correspond to our simulation conditions. This finding agrees well with the observed velocity-independent COF for the a-C:F system.

11. Conclusions of the Simulations

We have developed a modeling approach for simulations of amorphous coatings. The model of an amorphous carbon fluorine PECVD coating has been established by the manual interconnection of molecules that have been placed in a volume resembling an amorphous glass state [122]. Resulting was an amorphous, rough, soft and hydrophobic model of an a-C:F coating. The model depicts only the outermost surface of the actual coating. In addition to this model the complete opposite of this slab has been included in our considerations, a crystalline, atomically smooth, hard and hydrophilic slab of silicon dioxide with hydroxyl group termination. Consequently three different systems have been investigated, the a-C:F system consisting of two a-C:F slabs, the silicon dioxide system of two SiO₂ slabs and the MIX system comprising one slab of a-C:F and one slab of SiO₂.

Furthermore a novel simulation approach for MD simulations of sliding friction has been designed and employed using the program GROMACS 4.5.3. The approach simulates the pulling of one slab relatively to the other slab that is present in the simulation volume by a virtual spring. Knowing the perpendicular force and the pull force a friction coefficient can be calculated. The pull force is recorded during the simulations, and keeping the area of the sliding plane constant, the barostat maintains a constant perpendicular force. Additionally we considered water molecules between the slabs to account for water that has been trapped in the junction area. For the SiO₂ system the considered amount of water resulted in a spread-out, planar water layer with homogeneous thickness of 8 Å.

The dependencies of the friction force or the friction coefficient on several simulation conditions has been studied: A linear dependence of the friction force on the perpendicular force for all three investigated systems over more than five orders of magnitude was observed. According to macroscopic and also nanoscopic friction laws this behavior is expected, since we modeled non-adhesive, rough, multi-asperity contacts. Additionally the friction coefficients obtained could be compared to computational and experimental data of other researchers. If the materials employed in the simulations or experiments were comparable to our simulations, the agreement was very good for the a-C:F system and the SiO₂ system and the MIX system as well.

The second investigated simulation parameter was the thickness of the water layer between the sliding surfaces. A strong dependence of the friction coefficient on the amount

of water for all systems was observed. The systems gave approximately the same friction coefficients for twice the standard amount of water, which results from the complete mechanical decoupling of the slabs (MIX and a-C:F) or the apparently ceased direct, indirect and water-mitigated interactions between the hydrophilic SiO₂ slabs. Complete separation and no mitigated interactions results in the same friction coefficient as for pulling a single a-C:F slab through six times the standard amount of water. A comparison between our experimental results for no lubrication and our simulation results for no water molecules in the a-C:F system showed quantitative agreement with a deviation of less than 5%. This agreement means, that the situation in the junctions of the a-C:F:H coated bearing parts, which bear the load and determine the friction coefficient, is described correctly. If no lubricant is added, no water is present due to the easy squeeze-out of the condensed water molecules from between the hydrophobic surfaces. The agreement between the experimental results with water lubrication and our simulations including water is still good, but in the light of the agreement of the dry friction results, it seems that in our simulations too much water is present. In the real junctions of the water-lubricated coated bearing parts less water plays a role than in our simulations due to the squeeze-out, which is the reason for an increased friction. It has to be noted though, that the coincidence of results is only possible, because the experimentally employed materials and the material models both are highly hydrophobic, so that capillary effects do not play a significant role in the tribometry experiments. Furthermore our simulations depict the simplified situation without wear, which is reproduced in experiments by a Hertz contact stress that is significantly lower than a contact stress under application conditions.

The temperature dependence of the friction coefficients was Arrhenius-like for the MIX and the a-C:F system, but not for the SiO₂ system. In case of the MIX system a water slab is observed, which follows the a-C:F slab shape and has holes where the a-C:F slab asperities are. In contrast to that, for the a-C:F system a water string formation is observed because the two hydrophobic surfaces are not wetted by water. Due to the direct interactions in the a-C:F system the temperature dependence is the least and agrees very well with the temperature dependence of PTFE friction observed in experiments. While we obtain an activation energy of 6.1 kJ mol⁻¹ for a-C:F, the experimental value for PTFE obtained by Sawyer and coworkers is 5 kJ mol⁻¹. The lower the water molecule mobility, the higher the resistance to movement, which is the reason for the more prominent temperature dependence in the MIX system ($D = 6.10 \pm 2.18 \cdot 10^{-7} \text{ cm}^2 \text{ s}^{-1}$ at 223 K, $D = 1.195 \pm 0.0037 \cdot 10^{-5} \text{ cm}^2 \text{ s}^{-1}$ at 373 K, 13.4 kJ mol⁻¹ thermal activation energy). Only at elevated temperatures the holes in the water layer are easily able to move alongside the a-C:F surface asperities, or in other words, the water is more easily squeezed out from the junction area. For the cristobalite system the activation energy obtained from fitting the results from room temperature and below (9.54 kJ mol⁻¹) was very different

from the activation energy obtained from fitting the results from room temperature and above (31.8 kJ mol^{-1}). The reason for this is subject of future investigations.

The dependence of the friction coefficient on the relative sliding velocity was investigated as last parameter. The variation in the MIX system results with decreasing velocity is largest. Again the rearrangement of water molecules due to the movement of the water layer holes might be the reason for this result. For the silicon dioxide system the effect is less pronounced. In fact, the effect over one order of magnitude in spring velocity is so small, that a velocity dependence is disputable. According to literature, the change in hydrogen bonds due to the movement gives rise to a experimentally observed, low velocity dependence. For the a-C:F system no relevant velocity dependence of the obtained friction coefficients has been observed. This is again corroborated by those experimental results for PTFE that are carried out under conditions similar to our simulation conditions.

In summary we designed, verified and validated an MD simulation approach for sliding friction of amorphous coatings by good agreement to experimental data. Not only the experimental data of this thesis, but also data of other researchers was used for the validation. Furthermore the validation was carried out for the dependence of the tribological behavior of our simulation systems on the perpendicular force, and the amount of water between the slabs, and the temperature dependence, and the relative sliding velocities.



Part IV.

Summary and Outlook

12. Summary

This thesis deals with the influence on the tribological performance of hybrid ball bearings exerted by an amorphous carbon fluorine coating that is deposited by plasma-enhanced chemical vapor deposition. Hybrid ball bearings consist of steel rings and ceramics balls, which allow for higher loads in the application and reduce wear. Wear is reduced by the fact that for direct contact, the junctions between the sliding surfaces lead to increased wear, if both friction partners are made from metal. An increased load leads to an increase in direct contact, more junctions, and higher Hertz contact stress in the junctions. The higher contact stress in turn leads to an increased squeeze-out of lubricant, resulting in more junction contacts without any protection by the lubricant. At this point, the surface properties come into play, which can be tailored for the needs of the desired bearing application, while retaining the advantageous properties of the bulk material. Plasma-Enhanced Chemical Vapor Deposition (PECVD) offers a possibility to alter the surface properties in a selective and durable way.

An amorphous fluorine-containing hydrogenated carbon (a-C:F:H) coating has been developed by our colleagues in the project NANODYN at the Fraunhofer “Institut für Grenzflächen- und Bioverfahrenstechnik” (IGB) in Stuttgart. This PECVD coating covers the whole surface of the bearing parts. In this thesis the impact of the coating on sliding friction has been studied experimentally, using bearing parts and a tribometer, as well as computationally by development of a novel approach for modeling amorphous coatings and simulating sliding friction. The results of the tribometry showed a significantly decreased coefficient of friction for coated bearing parts under water and perfluoro-polyether (PFPE) lubrication conditions. These results are corroborated by tests on assembled bearings by our partner Cerobear GmbH, which is a leading hybrid ball bearing manufacturer. Unfortunately, the tribometry also revealed an increased friction coefficient in case of no addition of lubricant.

The atomic composition of the coating has been analyzed at the Fraunhofer IGB, which enabled the modeling of the outermost surface of the coating in classical molecular dynamics (MD) simulations. To this end, a new approach has been devised to model an amorphous coating. Furthermore, to include the direct opposite of the amorphous, rough, soft and hydrophobic coating model, a crystalline, atomically smooth, hard and hydrophilic slab model of hydroxyl group terminated silicon dioxide (cristobalite) has

been included in our considerations. In addition to two systems containing two slabs of either the coating model or the SiO₂ model, a third system consisting of one silicon dioxide and one coating model slab was considered. Furthermore water lubrication has been considered, which is relevant either because of hydrophilicity of the surface, or because of trapping of the lubricant. The sliding friction was simulated by classical non-equilibrium MD simulations of relative shearing of the two-dimensionally infinite slabs via pulling by a virtual spring. The perpendicular force on the system is held constant by a fixed sliding surface area and the simulation barostat, enabling calculation of a coefficient of friction analogously to tribometry.

Simulation results showed a linear coherence between perpendicular and friction force over a range of more than five orders of magnitude. This is in accordance with macroscopic and nanoscopic friction laws and hence verifies the approach. The obtained friction coefficients are in very good agreement with our own experimental results as well as simulations and experiments of other researchers, which validates the simulation approach. Additionally, also for variations of the temperature, the relative surface velocity and the amount of water our simulation results are in very good agreement with experimental results.

In summary, tribometry experiments have been successfully designed and performed to probe the influence of the surface coating on the sliding friction of hybrid ball bearing parts. It was shown, that the surface modification reduces the average friction coefficient under water and PFPE lubrication conditions. The obtained data also provided the means for the validation of a novel approach of sliding friction MD simulations of amorphous coatings. In addition to the verification of the approach against macroscopic and nanoscopic friction laws, a very good agreement between the computational results and experiments of other researchers validated the approach. Comparing to our own experiments, which were designed to exhibit corresponding conditions, the agreement was even up to quantitative.

13. Outlook

Future investigations in the direction of experimental and computational investigations of the impact of surface modification on the tribological properties could be connected to the work of this thesis in several ways.

Regarding further experiments using surface functionalized bearing components, future work could deal with higher perpendicular forces than the very low forces employed in the experiments so far. Higher perpendicular forces result in higher contact stresses and possibly wear, testing the durability of the coating and also, whether the expected behavior of a constant coefficient of friction is fulfilled or not. In connection to this question, different lubrication conditions might alter the picture, e.g. the lubrication with alkanes. Furthermore, experiments on different relative velocities of the friction partners might help to clarify the situation of contradicting experimental results regarding the dependence of the friction coefficient on the relative velocity.

Additionally, a connection between surface modification, tribometry, simulation and micro-sensors might provide further insight into the situation at the ball track interface of bearings under application conditions, as well as further insight into the influence of the coating on the processes at the molecular level. Micro-sensors for the application in bearings are developed by Prof. Walter Lang and Cord Winkelmann at the IMSAS of the Universität Bremen. Especially temperature and pressure at the ball track interface under the application conditions would provide invaluable simulation input for enhanced accuracy of sliding friction simulations.

Future simulations based on the approach developed in this thesis should definitely include the PFPE lubricant model developed here, which has not been used further than establishing and testing the model, because of a different project focus. Other lubricant molecules, e.g. alkanes could also be included in the systems of further simulations. Furthermore, it can be investigated, if the agreement between the computational and experimental results can be improved, if a squeeze-out simulation is carried out to determine the amount of lubricant remaining between the surface models when they approach each other. Additionally it is feasible to include debris of a lubricant thickener, meaning small parts of PTFE, in the simulations and investigate their impact on the tribological behavior. Modeling of a steel surface as amorphous chromium and/or iron oxide might also provide further insight into the tribological processes in hybrid bearings at

the molecular level. In addition to that, comparing classical MD simulation results to computational results using a reactive force field like e.g. the REBO force field developed by Brenner is likely a topic of future investigations. Especially when aiming at higher perpendicular forces the consideration of reactions and wear becomes increasingly important, because at higher stresses, reactions become more and more probable. Another topic that arises from the investigations presented in this thesis is the detailed investigation of the water layers. The shear rates and the nanoconfinement [91, 140, 141] influence the water molecules, and the resulting properties of the water layers between the surfaces is of importance for the understanding of the observed velocity dependencies and thermal activation energies as well as the non-Arrhenius behavior of the silicon dioxide system with varying temperature.

14. Thanks...

... what more can I say to express my deepest gratitude? It goes to

Thomas Frauenheim for giving me the chance to work on this project and being first examiner of this thesis

Lucio Colombi Ciacchi for being the second examiner of this thesis and the advice

Pia Tölle for providing help and useful remarks on the simulation approach

Volker Weiss for being the fellow you have been, all the invaluable advice and all the proof-reading

Christof Köhler for all the technical support, also all the invaluable advice and also all the proof-reading

Bernhard Grundkötter-Stock for being the fellow you have been and all the pleasant breaks

Karin Schütte for all the support making life easier and the friendship including listening and advice

the BCCMS group for the pleasant atmosphere

MY PARENTS for making not only my study of chemistry but also this doctoral thesis possible

my parents-in-law for supporting our family

my dear Claudia for supporting me and being lenient with your “scatterbrained not-professor” (piled higher and deeper...)

Tabea and Daniel for keeping me grounded and giving meaning to my struggling

The work underlying this thesis was carried out as a part of the project NANODYN. This research and development project is funded by the German Federal Ministry of Education and Research (BMBF) within the Framework Concept “Research for Tomorrow’s Production” (Funding No. 02PO2483) and managed by the Project Management Agency Karlsruhe (PTKA). The responsibility for the contents of this publication rests with the author.

References

- [1] D. W. Brenner, O. A. Shenderova, J. A. Harrison, S. J. Stuart, B. Ni, S. B. Sinnott, *J. Phys.: Condens. Matter* **2002**, *14*, 783–802.
- [2] B. N. J. Persson, *Sliding Friction - Physical Principles and Applications*, Springer, Berlin, **1998**.
- [3] B. N. J. Persson, F. Mugele, *J. Phys.: Condens. Matter* **2004**, *16*, R295–R355.
- [4] B. Bergrath, Cerobear GmbH, Herzogenrath, Germany, private communication, **2010**.
- [5] H. Hertz, *Über die Berührung fester elastischer Körper (On the contact of rigid elastic solids)*, MacMillan & Co., London, **1896**.
- [6] H. Hertz "On the contact of rigid elastic solids" as download, **5th of September 2012**, \approx 11 MB, <http://ia600305.us.archive.org/5/items/cu31924012500306/cu31924012500306.pdf>.
- [7] P. Eschmann, L. Hasbargen, K. Weigand, *Die Wälzlagerpraxis. Handbuch für die Berechnung und Gestaltung von Lagerungen*, Oldenbourg R. Verlag, München, **1988**.
- [8] G. A. Tomlinson, *Philos. Mag.* **1929**, *7*, 905–939.
- [9] **27th of September 2012**, <http://www.nano-world.org/nano/Lab/demo/frictionmodule/textbook/macrosopicfriction/sect1/?language=de>.
- [10] T. Baumberger, F. Heslot, B. Perrin, *Nature* **1994**, *367*, 544–546.
- [11] F. Heslot, T. Baumberger, B. Perrin, B. Caroli, C. Caroli, *Phys. Rev. E* **1994**, *49*, 4973–4988.
- [12] Y. Mo, I. Szlufarska, *Phys. Rev. B* **2010**, *81*, 035405.
- [13] Y. Mo, K. T. Turner, I. Szlufarska, *Nature* **2009**, *457*, 1116–1119.
- [14] F. P. Bowden, D. Tabor, *The Friction and Lubrication of Solids Part 1*, Oxford University Press, Ely House, London, **1950**.
- [15] F. P. Bowden, D. Tabor, *The Friction and Lubrication of Solids Part 2*, Oxford University Press, Ely House, London, **1964**.

- [16] R. von Mises, *Göttin. Nachr. Math. Phys.* **1913**, *1*, 582–592.
- [17] J. A. Greenwood, J. B. P. Williamson, *Proc. Roy. Soc. A* **1966**, *295*, 300.
- [18] K. L. Johnson, K. Kendall, A. D. Roberts, *Proc. Roy. Soc. A* **1971**, *324*, 301.
- [19] K. N. G. Fuller, D. Tabor, *Proc. Roy. Soc. A* **1975**, *345*, 327.
- [20] A. Volmer, T. Nattermann, *Z. Phys. B* **1997**, *104*, 363–371.
- [21] C. Lorenz, E. Webb-III, M. Stevens, M. Chandross, G. Grest, *Tribol. Lett.* **2005**, *19*, 93–99.
- [22] I. M. Sivebaek, V. N. Samoilov, B. N. J. Persson, *J. Chem. Phys.* **2003**, *119*, 2314–2321.
- [23] B. N. J. Persson, P. Ballone, *J. Chem. Phys.* **2000**, *112*, 9524–9542.
- [24] B. Persson, P. Ballone, *Solid State Commun.* **2000**, *115*, 599–604.
- [25] B. J. Persson, E. Tosatti, *Phys. Rev. B* **1994**, *50*, 5590–5599.
- [26] B. N. J. Persson, V. N. Samoilov, S. Zilberman, A. Nitzan, *J. Chem. Phys.* **2002**, *117*, 3897–3914.
- [27] N. Vandencastele, F. Reniers, *J. Electron Spectrosc.* **2010**, *178-179*, 394–408.
- [28] C.-M. Chan, T.-M. Ko, H. Hiraoka, *Surf. Sci. Rep.* **1996**, *24*, 1–54.
- [29] Y. Lifshitz, S. R. Kasi, J. W. Rabalais, *Phys. Rev. B* **1990**, *41*, 10468–10480.
- [30] S. Aisenberg, R. Chabot, *J. Appl. Phys.* **1971**, *42*, 2953–2958.
- [31] A. Grill, *Diamond Relat. Mater.* **1999**, *8*, 428–434.
- [32] Y. Lifshitz, *Diamond Relat. Mater.* **1999**, *8*, 1659–1676.
- [33] C. E. Bottani, A. Lamperti, L. Nobili, P. M. Ossi, *Thin Solid Films* **2003**, *433*, 149–154.
- [34] A. Lamperti, P. Ossi, *Appl. Surf. Sci.* **2003**, *205*, 113–120.
- [35] R. Schnupp, R. Kühnhold, G. Temmel, E. Burte, H. Ryssel, *Biosens. Bioelectron* **1998**, *13*, 889–894.
- [36] Q. Xue, D. Kato, T. Kamata, S. Umemura, S. Hirono, O. Niwa, *Jpn. J. Appl. Phys.* **2012**, *51*, 090124.
- [37] L. G. Jacobsohn, D. F. Franceschini, M. E. H. Maia da Costa, F. L. Freire, Jr., *J. Vac. Sci. Technol. A* **2000**, *18*, 2230–2238.
- [38] L. Jacobsohn, M. Maia da Costa, V. Trava-Airoldi, F. Freire, Jr., *Diamond Relat. Mater.* **2003**, *12*, 2037–2041.

- [39] M. E. H. Maia da Costa, I. J. R. Baumvol, C. Radke, L. G. Jacobsohn, R. R. M. Zamora, F. L. Freire, Jr., *J. Vac. Sci. Technol. A* **2004**, *22*, 2321–2328.
- [40] U. Müller, R. Hauert, B. Oral, M. Tobler, *Surf. Coat. Technol.* **1995**, *76-77*, 367–371.
- [41] C. Donnet, J. Fontaine, A. Grill, V. Patel, C. Jahnes, M. Belin, *Surf. Coat. Technol.* **1997**, *94-95*, 531–536.
- [42] L. Valentini, E. Braca, J. Kenny, L. Lozzi, S. Santucci, *Mater. Lett.* **2001**, *51*, 514–518.
- [43] D. Sarkar, M. Farzaneh, R. Paynter, *Appl. Surf. Sci.* **2010**, *256*, 3698–3701.
- [44] Y.-H. Pai, G.-R. Lin, *J. Electrochem. Soc.* **2011**, *158*, G173–G177.
- [45] H. Ji, A. Cote, D. Koshel, B. Terreault, G. Abel, P. Ducharme, G. Ross, S. Savoie, M. Gagné, *Thin Solid Films* **2002**, *405*, 104–108.
- [46] S. R. Coulson, I. S. Woodward, J. P. S. Badyal, S. A. Brewer, C. Willis, *Chem. Mater.* **2000**, *12*, 2031–2038.
- [47] C.-H. Wen, M.-J. Chuang, G.-H. Hsiue, *Thin Solid Films* **2006**, *503*, 103–109.
- [48] J. Barz, M. Haupt, U. Vohrer, H. Hilgers, C. Oehr, *Surf. Coat. Technol.* **2005**, *200*, 453–457.
- [49] L. Li, P. M. Jones, Y.-T. Hsia, *Appl. Surf. Sci.* **2011**, *257*, 4478–4485.
- [50] P. B. Leezenberg, W. H. Johnston, G. W. Tyndall, *J. Appl. Phys.* **2001**, *89*, 3489.
- [51] K. Trojan, M. Grischke, H. Dimigen, *Phys. Status Solidi A* **1994**, *145*, 575–585.
- [52] C. Donnet, *Surf. Coat. Technol.* **1998**, *100-101*, 180–186.
- [53] D. Marx, J. Hutter, *Ab Initio Molecular Dynamics*, Cambridge University Press, Cambridge, **2009**.
- [54] M. Born, V. Fock, *Z. Phys. A* **1928**, *51*, 165–180.
- [55] M. Born, R. Oppenheimer, *Ann. Phys.* **1927**, *84*, 457–484.
- [56] M. P. Allen, D. J. Tildesley, *Computer Simulation of Liquids*, Oxford University Press, USA, **1989**.
- [57] T. Schlick, *Molecular Modeling and Simulation, Vol. 21*, Springer, Heidelberg, 2nd ed., **2010**.
- [58] S. Lifson, A. Warshel, *J. Chem. Phys.* **1968**, *49*, 5116–5129.
- [59] A. T. Hagler, E. Huler, S. Lifson, *J. Am. Chem. Soc.* **1974**, *96*, 5319–5327.
- [60] S. Lifson, A. T. Hagler, P. Dauber, *J. Am. Chem. Soc.* **1979**, *101*, 5111–5121.

- [61] B. R. Brooks, R. E. Bruccoleri, B. D. Olafson, D. J. States, S. Swaminathan, M. Karplus, *J. Comput. Chem.* **1983**, *4*, 187–217.
- [62] S. J. Weiner, P. A. Kollman, D. A. Case, U. Chandra Singh, C. Ghio, G. Alagona, S. Profeta, Jr., P. Weiner, *J. Am. Chem. Soc.* **1984**, *106*, 765–784.
- [63] S. J. Weiner, P. A. Kollman, D. T. Nguyen, D. A. Case, *J. Comput. Chem.* **1986**, *7*, 230–252.
- [64] S. L. Mayo, B. D. Olafson, W. A. Goddard III, *J. Phys. Chem.* **1990**, *94*, 8897–8909.
- [65] R. L. Dunbrack, M. Karplus, *Nature Struct. Biol.* **1994**, *1*, 334–340.
- [66] W. D. Cornell, P. Cieplak, C. I. Bayly, I. R. Gould, K. M. Merz, Jr., D. M. Ferguson, D. C. Spellmeyer, T. Fox, J. W. Caldwell, P. A. Kollman, *J. Am. Chem. Soc.* **1995**, *117*, 5179–5197.
- [67] W. L. Jorgensen, D. S. Maxwell, J. Tirado-Rives, *J. Am. Chem. Soc.* **1996**, *118*, 11225–11236.
- [68] J. P. Ryckaert, A. Bellemans, *Chem. Phys. Lett.* **1975**, *30*, 123–125.
- [69] D. van der Spoel, E. Lindahl, B. Hess, A. R. van Buuren, E. Apol, P. J. Meulenhoff, D. P. Tieleman, A. L. T. M. Sijbers, K. A. Feenstra, R. van Drunen, H. J. C. Berendsen, *Gromacs User Manual version 4.5.4*, www.gromacs.org, **2010**.
- [70] B. Hess, C. Kutzner, D. van der Spoel, E. Lindahl, *J. Chem. Theory Comput.* **2008**, *4*, 435–447.
- [71] H. J. C. Berendsen, J. R. Grigera, T. P. Straatsma, *J. Phys. Chem.* **1987**, *91*, 6269–6271.
- [72] P. P. Ewald, *Ann. Phys.* **1921**, *64*, 253–287.
- [73] T. Darden, D. York, L. Pedersen, *J. Chem. Phys.* **1993**, *98*, 10089–10092.
- [74] U. Essmann, L. Perera, M. L. Berkowitz, T. Darden, H. Lee, L. G. Pedersen, *J. Chem. Phys.* **1995**, *103*, 8577–8592.
- [75] W. Van Gunsteren, H. Berendsen, *Mol. Phys.* **1977**, *34*, 1311–1327.
- [76] W. F. Van Gunsteren, H. J. C. Berendsen, *Mol. Simulat.* **1988**, *1*, 173–185.
- [77] E. N. Parker, *Phys. Rev.* **1954**, *96*, 1686–1689.
- [78] M. Parrinello, A. Rahman, *J. Appl. Phys.* **1981**, *52*, 7182–7190.
- [79] S. Nosé, M. L. Klein, *Mol. Phys.* **1983**, *50*, 1055–1076.
- [80] E. Paci, M. Marchi, *J. Phys. Chem.* **1996**, *100*, 4314–4322.

- [81] A. F. Jakobsen, *J. Chem. Phys.* **2005**, *122*, 124901.
- [82] H. J. C. Berendsen, J. P. M. Postma, A. DiNola, J. R. Haak, *J. Chem. Phys.* **1984**, *81*, 3684–3690.
- [83] S. Nosé, *Mol. Phys.* **1984**, *52*, 255–268.
- [84] W. G. Hoover, *Phys. Rev. A* **1985**, *31*, 1695–1697.
- [85] M. Rullich, M. Haupt, V. Weiss, C. Köhler, J. Barz, C. Oehr, T. Frauenheim, in preparation.
- [86] D. L. Burris, W. G. Sawyer, *Tribol. Lett.* **2009**, *35*, 17–23.
- [87] *Nano-Dynamik tribologischer Paarungen auf plasmastrukturierten Oberflächen und deren Herstellung*, (Ed.: M. Haupt), Fraunhofer Verlag, Stuttgart, **2012**, **In German**.
- [88] H. J. Griesser, D. Youxian, A. E. Hughes, T. R. Gengenbach, A. W. H. Mau, *Langmuir* **1991**, *7*, 2484–2491.
- [89] P. A. Thompson, M. O. Robbins, *Science* **1990**, *250*, 792–794.
- [90] F. Sedlmeier, J. Janecek, C. Sendner, L. Bocquet, R. R. Netz, D. Horinek, *Biointerphases* **2008**, *3*, FC23–FC39.
- [91] C. Sendner, D. Horinek, L. Bocquet, R. R. Netz, *Langmuir* **2009**, *25*, 10768–10781.
- [92] L. Pastewka, S. Moser, M. Moseler, *Tribol. Lett.* **2010**, *39*, 46–61.
- [93] M. Moseler, P. Gumbsch, C. Casiraghi, A. C. Ferrari, J. Robertson, *Science* **2005**, *309*, 1545–1548.
- [94] C. M. Goringe, D. R. Bowler, E. Hernández, *Rep. Prog. Phys.* **1997**, *60*, 1447–1512.
- [95] M. Elstner, D. Porezag, G. Jungnickel, J. Elsner, M. Haugk, T. Frauenheim, S. Suhai, G. Seifert, *Phys. Rev. B* **1998**, *58*, 7260–7268.
- [96] T. Frauenheim, G. Seifert, M. Elstner, T. Niehaus, C. Köhler, M. Amkreutz, M. Sternberg, Z. Hajnal, A. Di Carlo, S. Suhai, *J. Phys.: Condens. Matter* **2002**, *14*, 3015–3047.
- [97] D. W. Brenner, *Phys. Rev. B* **1990**, *42*, 9548.
- [98] I. Jang, D. L. Burris, P. L. Dickrell, P. R. Barry, C. Santos, S. S. Perry, S. R. Phillpot, S. B. Sinnott, W. G. Sawyer, *J. Appl. Phys.* **2007**, *102*, 123509.
- [99] N. McCook, D. Burris, P. Dickrell, W. Sawyer, *Tribol. Lett.* **2005**, *20*, 109–113.
- [100] D. L. Burris, S. S. Perry, W. G. Sawyer, *Tribol. Lett.* **2007**, *27*, 323–328.
- [101] P. R. Barry, P. Y. Chiu, S. S. Perry, W. G. Sawyer, S. R. Phillpot, S. B. Sinnott, *J. Phys.: Condens. Matter* **2009**, *21*, 144201.

- [102] P. Y. Chiu, P. R. Barry, S. S. Perry, W. G. Sawyer, S. R. Phillpot, S. B. Sinnott, *Tribol. Lett.* **2011**, *42*, 193–201.
- [103] P. R. Barry, P. Y. Chiu, S. S. Perry, W. G. Sawyer, S. R. Phillpot, S. B. Sinnott, *Langmuir* **2011**, *27*, 9910–9919.
- [104] A. Opitz, S.-U. Ahmed, M. Scherge, J. Schaefer, *Tribol. Lett.* **2005**, *20*, 229–234.
- [105] M. A. Karnath, Q. Sheng, A. J. White, S. Müftü, *Tribol. Trans.* **2010**, *54*, 36–43.
- [106] R. Nevshupa, M. Scherge, S.-U. Ahmed, *Surf. Sci.* **2002**, *517*, 17–28.
- [107] H. H. Funke, B. L. Grissom, C. E. McGrew, M. W. Raynor, *Rev. Sci. Instrum.* **2003**, *74*, 3909–3933.
- [108] M. Scherge, S. N. Gorb, *Biological Micro- and Nanotribology: Nature's Solutions*, Springer, Berlin, **2001**.
- [109] J.-P. Nabot, A. Aubert, R. Gilet, P. Renaux, *Surf. Coat. Technol.* **1990**, *43-44*, 629–639.
- [110] J. N. Israelachvili, *Surf. Sci. Rep.* **1992**, *14*, 109–159.
- [111] A. Erdemir, C. Donnet, *J. Phys. D: Appl. Phys.* **2006**, *39*, R311–R327.
- [112] Y. Liu, I. Szlufarska, *Appl. Phys. Lett.* **2010**, *96*, 101902.
- [113] A. Opitz, S.-U. Ahmed, J. Schaefer, M. Scherge, *Surf. Sci.* **2002**, *504*, 199–207.
- [114] A. Opitz, M. Scherge, S. I.-U. Ahmed, J. A. Schaefer, *J. Appl. Phys.* **2007**, *101*, 064310.
- [115] R. Prioli, L. Jacobsohn, M. Maia da Costa, F. Freire, Jr., *Tribol. Lett.* **2003**, *15*, 177–180.
- [116] K. Odaka, S. Ueda, *Vacuum* **1996**, *47*, 689–692.
- [117] T. Hanawa, S. Hiromoto, A. Yamamoto, D. Kuroda, K. Asami, *Mater. Trans.* **2002**, *43*, 3088–3092.
- [118] M. Lampimäki, K. Lahtonen, P. Jussila, M. Hirsimäki, M. Valden, *J. Electron Spectrosc.* **2007**, *154*, 69–78.
- [119] I. Saeki, Y. Sugiyama, S. Hayashi, A. Yamauchi, T. Doi, Y. Nishiyama, S. Kyo, S. Suzuki, M. Sato, S. Fujimoto, *Corros. Sci.* **2012**, *55*, 219–225.
- [120] D. L. Burris, *Tribol. Trans.* **2008**, *51*, 92–100.
- [121] M. Rullich, V. C. Weiss, T. Frauenheim, *Langmuir*, submitted.
- [122] D. N. Theodorou, U. W. Suter, *Macromolecules* **1985**, *18*, 1467–1478.
- [123] W. Humphrey, A. Dalke, K. Schulten, *J. Mol. Graphics* **1996**, *14*, 33–38.

- [124] E. K. Watkins, W. L. Jorgensen, *J. Phys. Chem. A* **2001**, *105*, 4118–4125.
- [125] G. Schaftenaar, J. Noordik, *J. Comput.-Aided Mol. Design* **2000**, *14*, 123–134.
- [126] P. E. M. Lopes, V. Murashov, M. Tazi, E. Demchuk, A. D. MacKerell, Jr., *J. Phys. Chem. B* **2006**, *110*, 2782–2792.
- [127] R. Marschall, P. Tölle, W. L. Cavalcanti, M. Wilhelm, C. Köhler, T. Frauenheim, M. Wark, *J. Phys. Chem. C* **2009**, *113*, 19218–19227.
- [128] A. Koike, *J. Phys. Chem. B* **1999**, *103*, 4578–4589.
- [129] R. P. Wool, *Macromolecules* **1993**, *26*, 1564–1569.
- [130] S. P. Andersson, O. Andersson, G. Bäckström, *Int. J. Thermophys.* **1997**, *18*, 209–219.
- [131] R. T. Downs, D. C. Palmer, *Am. Mineral.* **1994**, *79*, 9–14.
- [132] D. B. Asay, S. H. Kim, *J. Chem. Phys. B* **2005**, *109*, 16760–16763.
- [133] G. Guevara-Carrion, J. Vrabc, H. Hasse, *J. Chem. Phys.* **2011**, *134*, 074508.
- [134] *DIN Normblatt-Verzeichnis*, (Ed.: Deutscher Normenausschuss), Beuth Verlag, Berlin, **1973**.
- [135] I. Szlufarska, M. Chandross, R. W. Carpick, *J. Phys. D: Appl. Phys.* **2008**, *41*, 123001.
- [136] K. Deng, W. H. KO, *J. Micromech. Microeng.* **1992**, *2*, 14–20.
- [137] M. Reitsma, R. Cain, S. Biggs, D. Smith, *Tribol. Lett.* **2006**, *24*, 257.
- [138] E. Riedo, F. Lévy, , H. Brune, *Phys. Rev. Lett.* **2002**, *88*, 185505.
- [139] A. Opitz, S.-U. Ahmed, J. Schaefer, M. Scherge, *Wear* **2003**, *254*, 924–929.
- [140] Y. Leng, P. T. Cummings, *Phys. Rev. Lett.* **2005**, *94*, 026101.
- [141] J. M. D. Lane, M. Chandross, M. J. Stevens, G. S. Grest, *Langmuir* **2008**, *24*, 5209–5212.
- [142] C. Vega, J. L. Abascal, I. Nezbeda, *J. Chem. Phys.* **2006**, *125*, 144506.
- [143] C. Vega, J. L. Abascal, I. Nezbeda, *J. Chem. Phys.* **2006**, *125*, 034503.
- [144] H. R. Pruppacher, *J. Chem. Phys.* **1972**, *56*, 101–107.
- [145] J. W. M. Mens, A. W. J. de Gee, *Wear* **1991**, *149*, 255–268.
- [146] A. McNicol, D. Dowson, M. Davies, *Wear* **1995**, *181-183*, 603–612.
- [147] F. Yan, Q. Xue, S. Yang, *J. Appl. Polym. Sci.* **1996**, *61*, 1223–1229.
- [148] H. Unal, A. Mimaroglu, U. Kadioglu, H. Ekiz, *Mater. Design* **2004**, *25*, 239–245.

- [149] F. Jensen, *Introduction to Computational Chemistry*, John Wiley & Sons Ltd., Baffins Lane, Chichester, West Sussex, **1999**.
- [150] R. H. Byrd, P. Lu, J. Nocedal, *SIAM J. Scientific. Statistic. Comput.* **1995**, *16*, 1190–1208.
- [151] C. Zhu, R. H. Byrd, J. Nocedal, *ACM Trans. Math. Softw.* **1997**, *23*, 550–560.



Part V.
Appendix

List of Figures

- 1.1. Bearing parts: cage (a)[4], silicon nitride ball (b), inner ring (c)[4] and outer ring (d)[4] and. The ball tracks on the rings (c,d) are highlighted in blue. 7
- 1.2. Assembled type 6001 hybrid ball bearing comprising a polyether ether ketone (PEEK) cage and eight silicon nitride balls of the diameter 4.763 mm. The bearing steel employed for the inner and outer ring is X30CrMoN 15 1, from ref. [4]. 7
- 1.3. Illustration of the various contributions to the overall bearing friction moment and their relative magnitude. 9
- 1.4. Three-dimensional schematic representation of the development of Stribeck curves for increasing axial load as well as the product of viscosity and relative velocity. The three main different contributions are sketched and the mixed lubrication boundary is depicted as black line. Scheme following references [4, 7]. 10
- 1.5. Schematic representation of the dependence of stick-slip and steady motion on the relative velocity and the coupling strength of the motion of the center of mass of the body to the surface motion, which is viewed as a virtual spring of a variable spring constant. 13
- 1.6. Schematic representation of the apparatus employed by Leonardo da Vinci to determine the static friction of a block resting on a substrate by initiating movement using a dead-weight. The thread connecting the two bodies is diverted by a pulley. 14
- 1.7. Fiber optics and cantilever unit of the tribometer employed for the work underlying the experimental part of this thesis. A silicon nitride ball is glued underneath the cantilever. Two perpendicular mirrors reflect the light emitted by the fiber optics sensors. 15
- 1.8. Schematic representation of the atomic force microscope (AFM) measurement unit, the probe is the tip underneath the cantilever. 16

2.1. Schematic representation of the apparent area of contact, the junctions that form, the average surface level as well as the explanation of the real area of contact.	18
2.2. Schematic structure of surfactant molecules of the carboxylic acid kind covering a metal oxide surface, protecting it from wear. The acid shown here is dodecanoic acid, also called lauric acid. Carboxylic “heads”, the carboxy groups of the acid, are displayed as circles, the alkyl chain, the “tail”, is represented as solid lines. M is a metal atom of the metal oxide surface, O is oxygen, C is carbon, H is hydrogen.	24
2.3. Chemical structure of a perfluoro-polyether of the DuPont Krytox [®] family. C is carbon, F is fluorine, O is oxygen, n is the number of repeating units.	25
2.4. Deformation of a ball on a flat in the dry state (a) and in the lubricated state (b).	26
2.5. Schematic representation of the commensurability and lubricant pinning. The surfaces are represented by the smaller circles filled grey, while the larger circles represent the lubricant. The height difference Δh has to be overcome when the sliding of a commensurate system takes place. The height difference in the incommensurate but pinned system will be even higher, while it will be less in the incommensurate system.	28
3.1. Schematic depiction of the approach to steer the stoichiometry of a coating deposited by chemical vapor deposition (CVD). The reactive gas molecules, represented as circles and stars, stream into the reaction chamber through inlet 1 and 2, the relative flow rates determine the composition of the film deposited on the substrate.	30
3.2. Schematic configuration of a plasma-enhanced chemical vapor deposition device. Precursor molecule(s) and a carrier inert gas (usually Ar) are flowing into the reaction chamber through several pipes to improve even distribution of reactive species. The plasma is ignited by a radio frequency (RF) power generator, which is coupled to one of the electrodes in a capacitive way. A reduced pressure is maintained via pressure control devices connected to the reaction chamber.	33
4.1. Schematic representation of the periodic boundary condition approach. The simulation system is the black square, while the periodic images are shown in grey.	44

-
- 4.2. Schematic representation of the fitting of the force development of a system (grey line) by discrete time steps (black arrows) and the “leap-frog” algorithm. The updating of the positions is carried out at the time step intervals, while the velocities are updated in between. 46
- 4.3. Schematic representation of the simulation approach employed in the work presented here. Two slabs with lubricant between the two are simulated as quasi-infinite stack with periodic boundary conditions in all three dimensions. The upper slab in the simulation volume is pulled by a virtual spring, while the lower slab moves due to “actio equals reactio”. 47
- 5.1. Photograph of the tribometer employed in the tribometry experiments, a BASALT MUST from Tetra GmbH, Ilmenau, Germany. 56
- 5.2. Fiber optics and cantilever unit of the tribometer employed for the work underlying the experimental part of this thesis. A silicon nitride ball is glued underneath the cantilever. Two perpendicular mirrors reflect the light emitted by the fiber optics sensors. 56
- 6.1. Measured friction coefficients as box plots with whiskers indicating minimum and maximum of the experimental results with no addition of lubricant (NEAT). The median of the results is marked as orange bar, the box starts at the 25%-quartile and reaches to the 75%-quartile, thus contains 50% of the results. From left to right: uncoated ball / uncoated specimen, unmodified reference (10 measurements), c/u only silicon nitride ceramics ball coated (11), u/c only bearing steel specimen coated (15), c/c ball and specimen coated (15). Red crosses: longer-term friction measurement results indicating whether or not wear is observed. 61
- 6.2. Measured friction coefficients as box plots with whiskers indicating minimum and maximum of the experimental results with water lubrication. The median of the results is marked as orange bar, the box starts at the 25%-quartile and reaches to the 75%-quartile, thus contains 50% of the results. From left to right: uncoated ball / uncoated specimen, unmodified reference (14 measurements), c/u only silicon nitride ceramics ball coated (18), u/c only bearing steel specimen coated (16), c/c ball and specimen coated (16). Red crosses: longer-term friction measurement results indicating whether or not wear is observed. 62

- 6.3. Measured friction coefficients as box plots with whiskers indicating minimum and maximum of the experimental results with perfluoro polyether (PFPE) lubrication. The median of the results is marked as orange bar, the box starts at the 25%-quartile and reaches to the 75%-quartile, thus contains 50% of the results. From left to right: uncoated ball / uncoated specimen, unmodified reference (12 measurements), c/u only silicon nitride ceramics ball coated (14), u/c only bearing steel specimen coated (15), c/c ball and specimen coated (15). Red crosses: longer-term friction measurement results indicating whether or not wear is observed. 63
- 8.1. Representation of the simulation volume employed in the simulations. Two identical but differently displayed a-C:F slabs are shown, water is omitted for clarity. The first periodic images of the lower slab in +z- and -z direction are shown in light green below and above the simulation volume image. 70
- 9.1. The precursor molecule the a-C:F coating model is built from. C is carbon, F is fluorine. 75
- 9.2. MALDI-TOF mass spectrum of the matrix itself, E-2-cyano-4-hydroxycinnamic acid (α -Cyano-4-hydroxycinnamic acid). The shown mass per charge range is 200 to 2,500 m/z. 79
- 9.3. MALDI-TOF mass spectrum of the PFPE fat Krytox[®] GPL 204, containing GPL 104 PFPE oil. The shown mass per charge range is 400 to 1,000 m/z. 80
- 9.4. MALDI-TOF mass spectrum of the PFPE fat Krytox[®] GPL 204, containing GPL 104 PFPE oil. The shown mass per charge range is 700 to 2,000 m/z. 81
- 9.5. MALDI-TOF mass spectrum of the PFPE fat Krytox[®] GPL 204, containing GPL 104 PFPE oil. The shown mass per charge range is 1,000 to 10,000 m/z. 82
- 9.6. Chemical structure of a perfluoro-polyether of the DuPont Krytox[®] family according to technical data sheet. C is carbon, F is fluorine, O is oxygen, n is the number of repeating units. 83
- 9.7. Structure of Krytox[®] GPL 104 according to mass spectrometry and technical data sheet. 83

- 9.8. Visualization of a simulation volume containing two cristobalite silicon dioxide slabs (system SiO_2) separated by a water layer of 8 Å thickness. The virtual spring pulling the upper slab is indicated by a picture. The slabs are identical but differently displayed. 86
- 9.9. Example of a development of the cumulative average of the pressure in the perpendicular direction of the sliding plane for an a-C:F simulation at 874 bar target pressure. Please note that the y-axis scale starts at 800 bar. In under one nanosecond the error is below ± 10 bar of the overall average, resulting in a deviation of less than 1.2%. 87
- 9.10. Example of the development of the cumulative average of the pull force for an a-C:F simulation at 874 bar target pressure. Please note that the y-axis scale starts at $1,000 \text{ kJ mol}^{-1} \text{ nm}^{-1}$. In less than one nanosecond the error is within $\pm 150 \text{ kJ mol}^{-1} \text{ nm}^{-1}$ of the overall average of the simulation, which results a deviation of 14%. 88
- 9.11. Example of development of the cumulative average of the pull force for an a-C:F simulation for the last 10 ns only. Please note that the y-axis scale starts at $800 \text{ kJ mol}^{-1} \text{ nm}^{-1}$. The minimum and maximum of the cumulative average within the last 4 ns are marked in the graph, because they are the basis of the error calculations. 89
- 10.1. Dependence of the SiO_2 system friction force on the perpendicular force. Solid black: friction force with error bars. Dotted black: linear regression (least squares fit, $0.296 \pm 0.6\% \times F_N + 1.76 \pm 1.6\%$). 216 simulations from 1 to 10,000 bar target pressure perpendicular to the sliding plane, 298 K and 8 Å water layer thickness, errors in the range of 0.7% to 8.3% with respect to the friction force values. 91
- 10.2. Dependence of the MIX system friction force on the perpendicular force. Solid black: friction force with error bars. Dotted black: linear regression (least squares fit, $0.118 \pm 0.9\% \times F_N + 0.916 \pm 1.6\%$). 144 simulations from 1 to 10,000 bar target pressure perpendicular to the sliding plane, 298 K and 8 Å water layer thickness, errors in the range of 2.0% to 8.3% with respect to the friction force values. 91
- 10.3. Dependence of the a-C:F friction force on the perpendicular force. Solid black: friction force with error bars. Dotted black: linear regression (least squares fit, $0.138 \pm 2.4\% \times F_N + 1.03 \pm 3.5\%$). 261 simulations from 1 to 10,000 bar target pressure perpendicular to the sliding plane, 298 K and 8 Å water layer thickness, errors in the range of 3.3% to 8.8% with respect to the friction force values. 92

- 10.4. Dependence of the a-C:F system friction force on the perpendicular force. Magnification of same results in Figure 10.3 up to a normal force of 3.5 nN. Solid black: friction force with error bars. Dotted black: linear regression (least squares fit, $0.138 \pm 2.4\% \times F_N + 1.03 \pm 3.5\%$). 189 simulations from 1 to 1,000 bar target pressure perpendicular to the sliding plane, 298 K and 8 Å water layer thickness, errors in the range of 3.3% to 8.8% with respect to the friction force values. 93
- 10.5. Development of the a-C:F sliding plane area with increasing target simulation pressure. Area of the last frame of the equilibration run is fixed for the production run simulations. Two linear fits of the regimes up to 1,000 bar and beyond 1,000 bar demonstrate the kink in the development. The determination of the onset of the resulting change in tribological behavior needs further simulations. 94
- 10.6. Comparison of the linear regressions of the dependences of the friction on the normal force for the three investigated systems, SiO₂ (dashed black), a-C:F (solid black), and MIX (dotted black). 94
- 10.7. Typical snapshots of interlocking of a-C:F surface asperities. Snapshots taken from a cut of the simulation system. Within 20 ps between snapshot b and snapshot c the interlocking is resolved. Water has been omitted for clarity. The sample trajectory parameters are 874 bar, 298 K and 8 Å water layer thickness. 95

- 10.8. Comparison of the a-C:F friction coefficients calculated in this work (8 Å water layer thickness, 298 K) and the experimental and computational friction coefficients published by other researchers. The data of this work is shown only in the range from 150 bar to 2500 bar average perpendicular pressure. Barry et al. (green, [101]) and Chiu et al. (blue, [102]) are simulation results on the sliding of PTFE chains perpendicularly to each other, in case of Chiu et al. these chains are randomly cross-linked. The errors used here are given in their publications as errors for linear fits of simulation results starting at the pressure displayed here. The lower pressure result of Jang et al. (pink, [98], lefthand side of the graph) is an experimental result for PTFE, while the higher pressure result (pink, righthand side) of that work is obtained by computational perpendicular shearing of crystalline PTFE chains. The friction coefficient oscillations given in that publication were used for the error bars. The friction coefficient of Haupt ed. [87] was experimentally determined in the work underlying this thesis using a-C:F:H coated hybrid ball bearing parts and pure water lubrication for tribometry, the average of the measurements is shown with minimum-maximum results whiskers. 98
- 10.9. Comparison of friction coefficients resulting from SiO₂ simulations of this work (black crosses) and an experimental friction coefficient of Reitsma et al. [137] (black circle). Reitsma et al. carried out AFM measurements employing a quartz surface and a silicon AFM tip, which presumably is also oxidized. Data of this thesis is shown only between 2500 bar and 10000 bar average pressure perpendicular to the sliding plane. 99
- 10.10 Comparison of the MIX simulation friction coefficients of this work (red) and experimental friction coefficients of other researchers. Data of this thesis is shown only between 500 bar and 2500 bar average pressure perpendicular to the sliding plane. A hyperbolic fit is included to guide the eye (blue). The Freire Jr. group published AFM measurements of a silicon nitride AFM tip on an a-C:F:H coated surface with two rel. humidities, 28% in the Prioli et al. [115] publication (black), 38% in the Maia da Costa et al. [39] publication (pink). 100

- 10.11 Comparison of the dependences of the average coefficients of friction on the water layer thickness. The three investigated systems are SiO₂ (circles), a-C:F (squares), and MIX (triangles). The standard water layer thickness is 8 Å. Error bars have been omitted for clarity. For no water between the cristobalite slabs no shearing was observed up to a pull force corresponding to a friction coefficient of about 4.7 because of artificial interlocking of the commensurate slabs. This result has been omitted.
 * Simulation results are approximately the same and are not distinguishable for twofold water layer thickness.
 ** a-C:F system only: Simulation conditions for sixfold water layer thickness have been changed. The simulation volume contained only a single a-C:F slab that was pulled through about 6,100 water molecules. The average friction coefficient is approximately the same as the average of the results for twofold thickness. 101
- 10.12 Comparison between the experimental results obtained in this thesis for no lubrication and water lubrication with the simulation results of this thesis for the a-C:F system with no lubrication and water lubrication (874 bar and 298 K). The experimental results are shown as averages with dotted minimum-maximum whiskers as black circles, the simulation results are shown as black crosses with solid error bars. 103
- 10.13 One SiO₂ slab of the SiO₂ system and one water layer with standard water layer thickness of 8 Å. The view is oriented along the x-axis direction. Shaping of the water layer can be observed, because a zigzag shape of the water layer in z-direction can be identified, which stems from filling the space between the hydroxyl groups. Simulation carried out at 298 K and 874 bar. 104
- 10.14 One of the water layers of the MIX system with the standard water layer thickness (8 Å), viewed along the z-direction perpendicularly to the sliding plane. The holes in the water layer show penetration by surface asperities of the a-C:F material model. Simulation carried out at 298 K and 874 bar. 105
- 10.15 One of the a-C:F system water layers with standard amount of water (8 Å water layer thickness), viewed from the z-direction. Water forms a string due to the hydrophobic nature of the a-C:F material model. Simulation carried out at 298 K and 874 bar. 105

- 10.16 Arrhenius graph of the dependence of the friction coefficients of the a-C:F system that are normalized with respect to the average value at 298 K on the target simulation temperature in the range from 223 K to 373 K, -50 °C to +100 °C. The natural logarithm of the friction coefficients is represented as black crosses with error bars, a linear fit (least squares) is shown in dotted black, the slope of the linear fit results in a thermal activation energy E_A of $E_A = 6.1 \text{ kJ mol}^{-1}$, 18 simulations at each temperature, 874 bar and 8 Å water layer thickness in all cases, friction coefficient errors are between 3.1% and 14% of the respective COFs. 107
- 10.17 The dependence of the natural logarithm of the friction coefficients of the MIX system that are normalized with respect to the average value at 298 K on the target simulation temperature in the range from 223 K to 373 K, -50 °C to +100 °C. The natural logarithm of the friction coefficients is represented as black crosses with error bars, a linear fit (least squares) is shown in dotted black, the slope of the linear fit results in the the thermal activation energy E_A of 13.4 kJ mol^{-1} , 18 simulations at each temperature, 874 bar and 8 Å water layer thickness in all cases, friction coefficient errors are between 2.0% and 19% of the respective COFs. 108
- 10.18 The dependence of the natural logarithm of the friction coefficients of the SiO₂ system that are normalized with respect to the average value at 298 K on the target simulation temperature in the range from -100 °C to +100 °C, friction coefficients are represented as black crosses with error bars. Since there is no Arrhenius behavior no fit is shown, 18 simulations at each temperature, 874 bar and 8 Å water layer thickness in all cases, friction coefficient errors are between 1.5% and 13% of the respective COFs. 109
- 10.19 The dependence of the a-C:F friction coefficients on the relative sliding velocity with respect to the original sliding velocity, the friction coefficients with error bars are shown in black, a linear regression (least squares fit, $0.0186 \pm 58.7\% \times v/v_0 + 0.243 \pm 2.7\%$) is represented in dotted black, while the mean value line is displayed in solid black. 9 simulations have been carried out at each velocity from 0.01 to 0.9 and 18 simulations at 1, the errors are in the range from 5.5% to 14% with respect to the COF value. Simulations carried out at 298 K and 874 bar and 8 Å water layer thickness. 111

- 10.20 The dependence of the SiO₂ friction coefficients on the relative sliding velocity with respect to the original sliding velocity, the friction coefficients with error bars are shown in black, a linear regression (least squares fit, $0.110 \pm 11.6\% \times v/v_0 + 0.296 \pm 2.9\%$) is represented in dotted black, while the mean value line is displayed in solid black. 9 simulations have been carried out at each velocity from 0.1 to 0.9 and 18 simulations at 1, the errors are in the range from 2.3% to 10% with respect to the COF value. Due to a slight interlocking of the cristobalite slabs and the corresponding saw-tooth profile of the pull force, sliding velocities below 0.1 gave no meaningful results, because these results would depend on the respective starting points of the simulations. Simulations carried out at 298 K and 874 bar and 8 Å water layer thickness. 112
- 10.21 Exemplary sawtooth profile of the friction force of the SiO₂ system at 10% of the original velocity v_0 . Friction force of one trajectory at 298 K and 874 bar perpendicular pressure and standard water layer thickness (8 Å). . . 112
- 10.22 The dependence of the MIX friction coefficients on the relative sliding velocity with respect to the original sliding velocity, the friction coefficients with error bars are shown in black, a linear regression (least squares fit, $0.135 \pm 3.3\% \times v/v_0 + 0.0540 \pm 5.0\%$) is represented in dotted black, while the mean value line is displayed in solid black. 9 simulations have been carried out at each velocity from 0.01 to 0.9 and 18 simulations at 1, the errors are in the range from 3.8% to 42.5% with respect to the COF value. Simulations carried out at 298 K and 874 bar and 8 Å water layer thickness. 113
- 10.23 The comparison of the linear regression of the dependence of the friction coefficient on the relative sliding velocity with respect to the original sliding velocity for the MIX system (dotted) with the mean values of the SiO₂ system (dashed) and the a C:F system (solid). 114

List of Tables

- 6.1. The coating thickness on silicon nitride balls as determined by spectroscopic reflectometer microscopy, the coating thickness is given in nm, the time of plasma treatment in s. Precursor molecule for the PECVD coating process was trifluoromethane. 58
- 6.2. The coating atomic composition on silicon wafer as determined by X-ray Photoelectron Spectroscopy (XPS), the binding energy E_B is given in eV, the relative amounts of the different atomic species are given in %. The amount of oxygen is not correctly measured, since at least the same amount as for carbon bound to oxygen should be found. Precursor molecule for the PECVD coating process was trifluoromethane. 59
- 6.3. Elastic Moduli E and Poisson numbers ν of the silicon nitride for the ceramics balls and the X30CrMoN15 1 steel for the bearing steel specimens. The elastic moduli are given in GPa. 60
- 9.1. Relevant peaks of the Krytox[®] GPL 204 fat MALDI-TOF mass spectrum in the range of 700 to 2,000 m/z. Peak positions in m/z. 83
- 10.1. Measured or calculated coefficients of friction (COF) published by various researchers, the investigated materials, the kind of study, experimental or simulation, and the corresponding references are listed. 98

A. Additional Background

A.1. Energy Minimization

Once a system is set up using e.g. a graphical tool, the molecules are highly ordered in most cases, because they are just repeatedly put into a larger volume. Furthermore, the composition of a simulation system by combination of different sub-systems may lead to atoms, which are very close, possibly causing a very large repulsive part of the Lennard-Jones interaction and thus creating a huge force. The huge force, if the system would be used in an MD simulation as assembled, would yield extreme velocities and that in turn would lead to extreme forces on other atoms. Hence a single interaction may create a chain-reaction of immense velocities, which results in a simulation crash often referred to as “system explosion”.

To prevent a system explosion from happening, using energy minimization techniques beforehand the actual MD simulations is highly advisable. The simplest way to minimize the energy is to determine the gradient of the potential with respect to all particle coordinates, and moving a particle in the opposite direction, since the gradient points in the direction of largest positive slope. This approach is called steepest descent [149] and is a very common approach. The new positions are calculated usually under the restraint, that a maximum step size s is given to dampen oscillatory movement around the shortest path:

$$\mathbf{r}_{n+1} = \mathbf{r}_n + \frac{-\text{grad}\mathbf{V}_n}{|\text{grad}\mathbf{V}_n|} s \quad (\text{A.1})$$

As mentioned, the steepest descent method suffers from the simple consideration of only the first derivative of the potential in such a way, that neglecting the curvature of the potential hypersurface may result in too large steps, which in addition to that go at least partially in the wrong direction. While the step size may be truncated, the direction cannot easily be corrected. Resultantly oscillations around the shortest path to the minimum occur.

To overcome the shortcomings regarding the step size of the steepest descent method, the first improvement is connecting the different steps. This method is called conjugate gradient and the performance is increased especially in proximity to the minimum. The

step \mathbf{d} is calculated in the following way:

$$\mathbf{d}_n = -\text{grad}\mathbf{V}_n + \beta_n \mathbf{d}_{n-1} \quad (\text{A.2})$$

The parameter β is determined in various ways according to various implementations. The conjugate gradient method does not cope with the problem of the oscillations themselves, it merely dampens the oscillatory behavior.

To improve the convergence behavior further, the second derivative of the potential must be taken into account. In general, the so-called Newton-Raphson approaches are considering the expansion of the potential around the considered point up to and including the Hessian matrix \mathbf{H} of the second derivatives. Consequently the step \mathbf{d} is calculated in the following way:

$$\mathbf{d}_n = -\text{grad}\mathbf{V}_n \mathbf{H}_n^{-1} \quad (\text{A.3})$$

Unfortunately the calculation of an exact Hessian matrix is very time-consuming, and additionally the step size according to Newton-Raphson is very large in proximity to the minimum. The so-called pseudo-Newton-Raphson algorithms use approximated second derivatives that are computationally less demanding and restrict the step size. One of the methods is the Broyden-Fletcher-Goldfarb-Shanno method (BFGS), but as it is very demanding on the available memory, the so-called low-memory BFGS method (L-BFGS) is used in GROMACS [150, 151].

B. Experimental Results Tables

B.1. No Lubrication

Experimental results with specimen number, number of the experiment and number of data points of the experiment as well as cumulative average of the coefficient of friction. Ball uncoated, specimen uncoated, NEAT

specimen #	experiment #	# of data points	cum. av. COF
77177	1	105719	0.164307469
	2	17344	0.161900998
	4	21828	0.161361067
77185	1	30451	0.150547455
77218	1	137020	0.198043374
77197	1	105369	0.170213556
	2	101327	0.195306456
	3	72185	0.229530907
	4	39587	0.181852953
77199	1	76338	0.202346542
77223	1	677049	0.337005935

Experimental results with specimen number, number of the experiment and number of data points of the experiment as well as cumulative average of the coefficient of friction. Ball coated, specimen uncoated, NEAT

specimen #	experiment #	# of data points	cum. av. COF
77167	1	105618	0.387181033
	2	106030	0.574918317
	3	105541	0.790738776
	4	105537	0.845791214
77179	1	106129	0.439030386
	2	105549	0.658269769
	1	105601	0.615929775

specimen #	experiment #	# of data points	cum. av. COF
77191	2	105570	0.739465260
	3	105655	0.770676967
	4	105741	0.814638618
	1	105475	0.457834518
77209	2	105524	0.657141222
	3	105945	0.798783295
	4	105494	0.868687097
	1	105487	0.399979096
77217	2	105532	0.567587520
	3	105658	0.769223781
	4	105654	0.798323174
77217	1	767326	0.956757103

Experimental results with specimen number, number of the experiment and number of data points of the experiment as well as cumulative average of the coefficient of friction. Ball uncoated, specimen coated, NEAT

specimen #	experiment #	# of data points	cum. av. COF
77187	1	106671	0.665287739
	2	102049	0.662642531
	3	86695	0.975965843
	4	676707	0.923852217
77190	1	105828	0.766203539
	2	101541	0.922897027
	3	86697	1.104459387
77194	1	105648	0.662599152
	2	101318	0.731472497
	3	86696	0.821914031
77212	1	106026	0.717986379
	2	101309	0.787454186
	3	86684	0.973611073
77234	1	105545	0.384645727
	2	101318	0.572373732
	3	86679	0.622849601

Experimental results with specimen number, number of the experiment and number of data points of the experiment as well as cumulative average of the coefficient of friction. Ball coated, specimen coated, NEAT

specimen #	experiment #	# of data points	cum. av. COF
77175	1	105617	0.571916909
	2	101558	0.725469671
	3	101832	0.796617608
77178	1	105473	0.419016083
	2	101307	0.474603855
	3	101825	0.691031212
77198	1	105529	0.413321680
	2	101331	0.613048652
	3	101830	0.641680309
77201	1	106331	0.845760721
	2	101421	0.885630245
	3	101828	0.885251862
77220	1	105502	0.737690124
	2	101387	0.796579918
	3	101822	0.790704285
	4	676640	0.784279285

B.2. Water Lubrication

Experimental results with specimen number, number of the experiment and number of data points of the experiment as well as cumulative average of the coefficient of friction. Ball uncoated, specimen uncoated, WATER

specimen #	experiment #	# of data points	cum. av. COF
77181	1	106024	0.626648969
	2	1164582	0.604982591
77188	1	105536	0.272200753
	2	105545	0.536283306
	3	105546	0.868399346
	4	105542	0.912151491
77189	1	105557	0.559017823
	2	105536	0.423725044
	3	105583	0.657395334
	4	105731	0.709516159
	5	105628	0.739393484
77223	1	105533	0.386217488
	2	105540	0.597265003

specimen #	experiment #	# of data points	cum. av. COF
	3	105550	0.700044048
	4	105561	0.734012315

Experimental results with specimen number, number of the experiment and number of data points of the experiment as well as cumulative average of the coefficient of friction. Ball coated, specimen uncoated, WATER

specimen #	experiment #	# of data points	cum. av. COF
77167	1	105618	0.387181033
	2	106030	0.574918317
	3	105541	0.790738776
	4	105537	0.845791214
77179	1	106129	0.439030386
	2	105549	0.658269769
	1	105601	0.615929775
	2	105570	0.739465260
77191	3	105655	0.770676967
	4	105741	0.814638618
	1	105475	0.457834518
	2	105524	0.657141222
77209	3	105945	0.798783295
	4	105494	0.868687097
	1	105487	0.399979096
	2	105532	0.567587520
77217	3	105658	0.769223781
	4	105654	0.798323174
77217	1	767326	0.956757103

Experimental results with specimen number, number of the experiment and number of data points of the experiment as well as cumulative average of the coefficient of friction. Ball uncoated, specimen coated, WATER

specimen #	experiment #	# of data points	cum. av. COF
77174	1	105708	0.340079028
	2	105549	0.347648795
	3	105798	0.419254607

specimen #	experiment #	# of data points	cum. av. COF
	4	105530	0.507618171
77183	1	509845	0.678429070
77196	1	105944	0.230545706
	2	105950	0.224077558
	3	105532	0.288745916
	4	105537	0.409619072
77207	1	105449	0.465352992
	2	105484	0.469086076
	3	105535	0.547980176
	4	105529	0.616394834
77208	1	106024	0.490672424
	2	105621	0.544260683
	3	105673	0.599134918
	4	105617	0.666844311

Experimental results with specimen number, number of the experiment and number of data points of the experiment as well as cumulative average of the coefficient of friction. Ball coated, specimen coated, WATER

specimen #	experiment #	# of data points	cum. av. COF
77193	1	73673	0.351924037
	2	105547	0.370858050
	3	105516	0.528728948
	4	105563	0.767184917
77200	1	105525	0.340545087
	2	105523	0.388459962
	3	105563	0.453060309
	4	105508	0.553119518
77216	1	760345	0.468722466
77226	1	105446	0.363063967
	2	105504	0.437963403
	3	105605	0.578869124
	4	105511	0.807642553
77235	1	105522	0.319148085
	2	105527	0.293206486
	3	105824	0.330360890
	4	105624	0.316285133

B.3. PFPE Lubrication

Experimental results with specimen number, number of the experiment and number of data points of the experiment as well as cumulative average of the coefficient of friction.

Ball uncoated, specimen uncoated, PFPE

specimen #	experiment #	# of data points	cum. av. COF
77227	1	106013	0.214826048
	2	102510	0.263136622
	3	102510	0.263136622
	4	102510	0.263136622
77166	1	106245	0.233295405
	2	101308	0.199069383
	3	85160	0.203662514
77180	1	105565	0.197247423
	2	57333	0.198509140
	3	85164	0.189113923
77202	1	42988	0.197803569
	3	43395	0.178469788
77130	1	105560	0.157532944
	2	100656	0.175060603

Experimental results with specimen number, number of the experiment and number of data points of the experiment as well as cumulative average of the coefficient of friction.

Ball coated, specimen uncoated, PFPE

specimen #	experiment #	# of data points	cum. av. COF
77171	1	105526	0.200178394
	2	50811	0.203271285
	3	51279	0.195620832
77186	1	105815	0.176432022
	2	50855	0.175384493
77214	1	105525	0.217511533
	2	31013	0.179040307
77219	1	105518	0.147014993
	2	28819	0.169693039
77228	1	32930	0.158185308
	2	105837	0.158660342
	3	105560	0.165724344

specimen #	experiment #	# of data points	cum. av. COF
	4	105954	0.166464829
	5	105895	0.162854147
	6	423223	0.163430781

Experimental results with specimen number, number of the experiment and number of data points of the experiment as well as cumulative average of the coefficient of friction.

Ball uncoated, specimen coated, PFPE

specimen #	experiment #	# of data points	cum. av. COF
77173	1	105889	0.207563765
	2	101307	0.213789988
	3	91580	0.233516807
77192	1	105888	0.253125484
	2	101299	0.255443479
	3	91588	0.244955535
77195	1	105758	0.228855897
	2	101298	0.186855946
	3	101825	0.210393483
	4	676782	0.193798609
77225	1	105644	0.156970774
	2	101305	0.164639147
	3	101853	0.180996263
77231	1	105613	0.195068156
	2	101501	0.170131436
	3	101849	0.196112888

Experimental results with specimen number, number of the experiment and number of data points of the experiment as well as cumulative average of the coefficient of friction.

Ball coated, specimen coated, PFPE

specimen #	experiment #	# of data points	cum. av. COF
77182	1	105522	0.180285368
	2	101499	0.163560316
	3	101822	0.169063977
77211	1	105531	0.162534110

specimen #	experiment #	# of data points	cum. av. COF
77215	2	101295	0.172177968
	3	101824	0.174976384
	1	105456	0.210904205
77221	2	101431	0.312550724
	3	101822	0.336293668
	4	676768	0.326014394
	1	105564	0.145150171
77222	2	101782	0.148893535
	3	101827	0.159064519
	1	105534	0.159592927
	2	101530	0.155324039
	3	101828	0.225759290

C. Computational Results Tables

C.1. Varying Perpendicular Pressures

Computational results for varying cumulative average of the perpendicular pressure, pressure in bar, only values with COF error below 100% are shown and used in the thesis.

a-C:F system

cum. av. perp. pressure	COF	COF error
2.34598610	39.66420285	27.81361901
2.92880110	47.89695062	34.71850292
2.99023384	42.14013722	30.15481982
3.44337583	26.86849922	13.37548103
4.70379489	25.49864705	11.23984591
5.57978913	20.42009939	6.52071388
6.45877630	15.48630620	4.48746284
6.55761081	14.52592328	4.20014927
7.31092354	13.89282396	3.63747413
9.35931416	14.64548087	3.61959096
10.29151384	10.84626941	2.64570104
11.20001454	9.91278750	2.28523592
12.05093451	8.68444773	1.94549899
12.08836955	7.71750627	1.79949275
12.92138810	9.73288436	1.95643416
14.20434573	8.70732785	1.65337578
16.99798988	6.03175666	1.19591521
18.85617932	5.82086592	1.05569494
20.22634147	5.36547616	0.93915124
21.31935459	5.23412476	0.87868001
22.54845850	4.65658656	0.77955725
23.73903195	4.52510371	0.72938310
23.82091284	4.61415282	0.73435250
24.85432608	4.27328197	0.67638950
26.38731453	6.15422445	0.77965835
46.80808571	2.08256947	0.20431432
47.19554036	2.39926102	0.21437984
47.67233719	2.50328651	0.21605437
47.96055829	2.60508839	0.21847056
48.74680115	2.02134896	0.19399070
48.94488345	1.78873293	0.18488854
53.03972641	2.11634737	0.18142389
55.23563808	1.79712196	0.16409748
61.36642865	1.37533249	0.13567512
86.53220323	1.30404149	0.09773279

cum. av. perp. pressure	COF	COF error
96.30053718	1.22426075	0.08616227
96.39717887	1.26318674	0.08688350
96.47908697	1.01873973	0.08174238
98.67723792	0.99731913	0.07948732
98.74579668	0.99667965	0.07941918
99.48563006	1.20713423	0.08305943
103.57754642	1.35841760	0.08269926
103.93246616	1.31122386	0.08150869
142.90950131	0.93608798	0.05448199
143.31578813	0.75133391	0.05174926
145.41356476	0.85945679	0.05248982
147.54482582	0.80973158	0.05105758
150.33105554	0.80045002	0.04998779
150.80933269	0.65856161	0.04794757
150.89104258	0.84511730	0.05039433
152.68045512	0.71976265	0.04816165
157.09496937	0.63163195	0.04568626
196.55426254	0.59112012	0.03635097
197.54159547	0.62658272	0.03652832
197.57463019	0.57455923	0.03599559
198.20308036	0.72769610	0.03742671
200.37135927	0.62570223	0.03600366
200.85339528	0.65930011	0.03625180
203.80790522	0.60370221	0.03518069
204.02465364	0.59267133	0.03503518
207.20811754	0.71901873	0.03571643
244.19448654	0.67499052	0.03554553
245.89890170	0.56353404	0.03439263
245.98780415	0.58521753	0.03455650
248.77270936	0.55367106	0.03391603
250.38498351	0.65507670	0.03450764
252.28482614	0.68660809	0.03449775
252.77657740	0.63053377	0.03398697
257.05407869	0.64054244	0.03349928
257.92580363	0.61515126	0.03318917
302.43170559	0.46567641	0.02738389
297.56463583	0.46551276	0.02783069
302.10297129	0.65966631	0.02869795
303.86418877	0.53416856	0.02770560
300.42518359	0.50427384	0.02782373
293.99996658	0.50270626	0.02842114
303.75144275	0.54660120	0.02779775
293.67663358	0.57144724	0.02892058
299.33065726	0.51822070	0.02801866
350.75333392	0.53483564	0.02397053
351.20975857	0.46192218	0.02352417
356.22575620	0.56139497	0.02375141
352.35398726	0.45917211	0.02343216
356.49937575	0.46144951	0.02317247
345.01108228	0.40364181	0.02360897
353.52278936	0.48578745	0.02350527
348.37188502	0.55633615	0.02425783
353.49742528	0.48567686	0.02350633
402.01783156	0.36524795	0.02152580

cum. av. perp. pressure	COF	COF error
405.61788205	0.37629667	0.02141647
397.46713928	0.44960774	0.02240899
399.28558974	0.37643206	0.02175713
391.20812743	0.41935251	0.02253550
391.84068426	0.38409567	0.02222919
399.64180083	0.39610278	0.02188540
394.02917264	0.45752910	0.02266482
394.68036607	0.39396352	0.02214426
447.89243962	0.32271196	0.01879411
450.46538534	0.32143770	0.01867827
449.18493479	0.33480981	0.01882083
457.98093987	0.36084082	0.01862987
448.13180670	0.36357276	0.01905761
447.29493222	0.34962244	0.01899970
455.56740919	0.33344029	0.01854813
448.63273570	0.41175523	0.01935853
450.44372596	0.42316460	0.01935668
495.43737325	0.35961859	0.01657871
506.96578553	0.36143297	0.01620887
502.27739550	0.45537143	0.01673422
501.11180639	0.29902869	0.01614916
500.48576989	0.34671375	0.01635991
489.91568091	0.30454557	0.01654074
502.98913356	0.33851742	0.01624590
504.90427438	0.25786223	0.01586479
504.87400375	0.35485007	0.01624995
600.60084195	0.26754606	0.01573382
597.21970648	0.29319102	0.01595172
600.34963171	0.31731893	0.01598912
603.78975653	0.27185812	0.01567214
593.32539783	0.29256578	0.01605325
596.01889223	0.25157807	0.01577440
597.34835142	0.26386699	0.01580101
594.60469374	0.25411618	0.01582472
602.56050174	0.28687114	0.01577886
701.76460188	0.27068324	0.01846689
696.68755073	0.29713243	0.01869637
706.98584283	0.27335003	0.01833994
692.66176023	0.30259460	0.01882475
695.47013201	0.26203101	0.01860292
694.57269719	0.26547133	0.01863934
700.68064206	0.27103941	0.01849673
702.60122174	0.30610420	0.01857093
697.67636925	0.25848297	0.01853138
807.51466318	0.26881496	0.01622264
808.54785024	0.28970781	0.01627943
805.12426674	0.28211184	0.01632035
800.33876936	0.29814550	0.01647803
801.32397879	0.29599876	0.01644974
793.92685491	0.25192208	0.01643645
793.72337698	0.27040162	0.01651051
795.32215533	0.29652207	0.01657585
802.42605900	0.32231540	0.01652553
798.44481088	0.31556231	0.01658256

cum. av. perp. pressure	COF	COF error
800.43886037	0.29259966	0.01645519
800.31885778	0.31139842	0.01652812
799.61628431	0.24022164	0.01627560
798.15798731	0.26349326	0.01639281
802.58048784	0.29684229	0.01642714
802.01284348	0.28839731	0.01640717
795.78738173	0.25767923	0.01641973
803.24652738	0.27638067	0.01633709
902.13623970	0.29520101	0.01445323
892.54033826	0.30881092	0.01464674
894.13263844	0.32630658	0.01466958
900.42119330	0.32478338	0.01456289
893.03212815	0.30983005	0.01464153
895.18109514	0.33521766	0.01467728
894.64959672	0.28428280	0.01454367
897.53804861	0.30367712	0.01455089
901.51367115	0.28627774	0.01443847
878.41738580	0.29139535	0.01532743
877.59765820	0.28083593	0.01529963
869.86077275	0.27987292	0.01543184
872.24173231	0.28983355	0.01542968
871.28337006	0.32359857	0.01558229
878.73139425	0.27309793	0.01524907
875.78410052	0.29106332	0.01537218
867.24961507	0.26762323	0.01542886
871.78430039	0.29724741	0.01546754
1000.31878161	0.22165646	0.01573781
1001.72201993	0.24957128	0.01579937
996.09499737	0.23100511	0.01583270
997.90083151	0.22186269	0.01577657
992.31958653	0.25974501	0.01597983
1006.11922378	0.26485831	0.01577590
999.78604958	0.28701673	0.01594232
1004.52918753	0.25564104	0.01577335
992.61650662	0.26977344	0.01600536
2502.64806584	0.16858208	0.01261972
2501.52237944	0.17833879	0.01264295
2506.24819878	0.19041461	0.01264079
2494.72827839	0.15705440	0.01263899
2498.76360161	0.16628230	0.01263519
2504.16147695	0.16574375	0.01260699
2493.17939483	0.15596198	0.01264487
2504.82233637	0.16014202	0.01259360
2493.52044534	0.16089363	0.01265204
2500.11227417	0.17221432	0.01263906
2503.33319483	0.15157786	0.01258570
2497.63603205	0.16703783	0.01264226
2493.21783184	0.15590066	0.01264456
2498.94558748	0.16106499	0.01262488
2498.69887461	0.15231643	0.01261037
2504.63763016	0.17446686	0.01262027
2500.38638935	0.17002834	0.01263374
2499.34514349	0.18602516	0.01266780
5004.34328746	0.12638187	0.00758043

cum. av. perp. pressure	COF	COF error
4998.47859595	0.12262707	0.00758632
4999.71750976	0.13969790	0.00759810
4988.30884486	0.14998542	0.00762372
4996.53762683	0.13544939	0.00759953
5002.11130861	0.15023585	0.00760289
4993.70282995	0.12619285	0.00759643
4995.19686132	0.13681540	0.00760267
5002.65741967	0.14141033	0.00759500
5003.67338314	0.14284777	0.00759461
5003.63990135	0.12169273	0.00757775
5002.31641994	0.12358656	0.00758127
4995.86375389	0.13046900	0.00759657
4997.22859547	0.14836546	0.00760882
4996.68530857	0.12846608	0.00759372
4997.12211040	0.13618430	0.00759923
4999.23754265	0.13823545	0.00759766
4998.07150459	0.12149269	0.00758603
7500.07387514	0.09628459	0.00454603
7507.52670664	0.10248672	0.00454482
7505.76800169	0.09320485	0.00454094
7497.17771055	0.09349060	0.00454629
7500.89948052	0.10644316	0.00455094
7497.77483300	0.10193548	0.00455044
7500.81676654	0.08977582	0.00454211
7491.51759847	0.10622851	0.00455653
7496.20011002	0.10349572	0.00455222
7490.65671095	0.11707180	0.00456284
7494.79764227	0.09621463	0.00454919
7494.57860081	0.10441956	0.00455370
7497.01629451	0.09532485	0.00454737
7503.74547561	0.09975349	0.00454565
7504.35941613	0.09062327	0.00454041
7499.83121665	0.11322160	0.00455521
7493.78418793	0.09110708	0.00454708
7496.54424433	0.10019781	0.00455026
9996.63680516	0.07052146	0.00279784
9995.59780536	0.06788089	0.00279708
10011.46658056	0.07306075	0.00279471
10001.36905399	0.07298713	0.00279750
9998.92213410	0.06234881	0.00279393
9999.20054990	0.06940484	0.00279668
9996.32244527	0.06959625	0.00279756
9996.45671359	0.06453546	0.00279550
10001.36479972	0.06684448	0.00279505
10002.74652449	0.06580301	0.00279425
9995.01098641	0.06896086	0.00279767
9999.83532491	0.06867909	0.00279621
10003.04037713	0.07035512	0.00279598
9997.31957747	0.07094291	0.00279782
9999.30583898	0.07224762	0.00279779
10002.49901752	0.07327966	0.00279730
9999.45310959	0.07142173	0.00279741
10002.42700796	0.06861391	0.00279546

cum. av. perp. pressure	COF	COF error
2503.42999614	0.24579633	0.00388043
2499.71132068	0.25000640	0.00389041
2495.46653341	0.24853662	0.00389556
2503.42999614	0.24579633	0.00388043
2494.23513459	0.24979132	0.00389874
2503.42999614	0.24579633	0.00388043
2503.42999614	0.24579633	0.00388043
4999.05543322	0.20271505	0.00176463
5008.37295320	0.20127733	0.00176034
5001.66649898	0.20381226	0.00176447
4994.47406368	0.19958471	0.00176405
4994.47406368	0.19958471	0.00176405
4994.47406368	0.19958471	0.00176405
4994.47406368	0.19958471	0.00176405
4998.34474651	0.19663181	0.00176062
4997.44081766	0.20118304	0.00176412
4994.47406368	0.19958471	0.00176405
4994.47406368	0.19958471	0.00176405
4994.47406368	0.19958471	0.00176405
5002.85808700	0.20070495	0.00176188
5000.60670237	0.19892758	0.00176143
5002.57496818	0.19847423	0.00176042
4994.47406368	0.19958471	0.00176405
4994.47406368	0.19958471	0.00176405
4994.47406368	0.19958471	0.00176405
7502.16792641	0.17987351	0.00156158
7494.14022243	0.17940634	0.00156307
7494.14022243	0.17940634	0.00156307
7494.14022243	0.17940634	0.00156307
7494.14022243	0.17940634	0.00156307
7494.14022243	0.17940634	0.00156307
7494.14022243	0.17940634	0.00156307
7496.48681881	0.17911745	0.00156246
7494.14022243	0.17940634	0.00156307
7494.14022243	0.17940634	0.00156307
7494.14022243	0.17940634	0.00156307
7503.57484099	0.17872199	0.00156083
7494.14022243	0.17940634	0.00156307
7494.14022243	0.17940634	0.00156307
7494.14022243	0.17940634	0.00156307
7494.14022243	0.17940634	0.00156307
7503.50189854	0.17939131	0.00156111
7494.14022243	0.17940634	0.00156307
7494.14022243	0.17940634	0.00156307
9998.23346196	0.16282430	0.00137504
9998.51246340	0.16253035	0.00137492
9998.23346196	0.16489864	0.00137566
9993.20628482	0.16459933	0.00137627
10003.35499567	0.16274094	0.00137431
9998.23346196	0.16282430	0.00137504
9998.23346196	0.16282430	0.00137504
9998.23346196	0.16282430	0.00137504
9998.23346196	0.16282430	0.00137504
9998.23346196	0.16410049	0.00137543
10005.65572312	0.16270352	0.00137399

cum. av. perp. pressure	COF	COF error
9998.23346196	0.16372184	0.00137531
10002.09957587	0.16277757	0.00137450
9997.44230177	0.16283719	0.00137516
9998.23346196	0.16282430	0.00137504
9998.23346196	0.16282430	0.00137504
9998.23346196	0.16482719	0.00137564
10000.93040016	0.20393766	0.00138700

Computational results for varying cumulative average of the perpendicular pressure, pressure in bar, only values with COF error below 100% are shown and used in the thesis.

MIX system

cum. av. perp. pressure	COF	COF error
4.4163841495	32.8588228263	23.1223403066
4.5583614575	29.1479017867	19.959885796
4.9288039535	24.2969997538	16.0201785125
4.9511513909	25.9067903021	16.4125540184
6.2644403196	18.5874180411	14.2005262869
7.7630372978	16.293686583	10.1296122707
8.2721674544	17.4099274802	6.7419393402
9.658575285	12.2957002668	4.1856866419
10.2977857821	13.1817560802	4.1840001241
11.6786589627	11.1404390557	3.1649169682
11.9175931865	9.6746052993	2.9446495845
14.1897034619	10.2924299103	2.603761929
15.183690596	7.8085313055	1.9425391776
15.1862681628	6.9372269208	1.7700860015
17.7103542259	7.5223638078	1.6169304682
17.9630960015	6.9071112054	1.4914273988
18.9929609371	6.0435350712	1.2741523147
19.3184917409	5.1385554159	1.034158167
23.2676428773	3.8998981427	0.6989278748
24.6524061708	2.5829938188	0.4994113407
26.0879014119	3.9288458621	0.6266984488
27.3357531067	3.3852677282	0.5384345142
28.546366431	2.4742787937	0.4198624077
29.0639034643	2.8992701827	0.4562539345
31.2072651866	2.6915015583	0.4049446294
33.4658452518	2.5463859962	0.3646065909
43.2007265456	1.6958580634	0.3173965608
44.4993471651	2.0615350008	0.3451131135
44.8058873591	1.7251543172	0.308968218
47.6057886603	1.8877009861	0.3061614058
47.9522258553	2.4187013411	0.353780382
49.4387244942	2.0157172333	0.3064627668
56.2312543326	1.8780872899	0.2584291196
58.5083518962	1.9347868642	0.2527321511
58.7156082614	1.5833084765	0.2249025307
95.748185612	1.5401912555	0.1332639454

cum. av. perp. pressure	COF	COF error
97.0708578783	1.1608824152	0.111910382
99.1944906508	1.1074873576	0.1068230849
99.622573727	1.1997593901	0.1109951414
100.1036596608	1.1674964464	0.1088502356
100.2691318499	1.1051654659	0.10078941
100.5821820748	1.1017257682	0.1050628782
100.8902194391	1.2960831525	0.1143742231
105.0679798536	1.2080186417	0.1056355888
242.9506094384	0.5990995843	0.0269817449
244.5909331961	0.5428484812	0.0262258438
247.3961044558	0.5478683186	0.0259792013
248.8698218378	0.5750784873	0.0260986992
249.3089916766	0.5972198993	0.0262747529
250.1353859997	0.5304593958	0.025520703
253.990788851	0.5556042984	0.0253808147
258.5360841722	0.5458362785	0.0248401422
259.8494317835	0.5896761758	0.0251363753
496.9128723548	0.235696955	0.0118676755
497.6418717213	0.3005755157	0.0123065924
498.7271806441	0.340247435	0.0125582235
499.0787069384	0.3160697372	0.0123798218
500.4565141898	0.2830087893	0.0121145234
501.2876670245	0.3140954968	0.012311485
501.8990385748	0.31429364	0.01229787
506.9849734382	0.2944647156	0.012037611
507.8501899915	0.2684768361	0.0118379995
745.8580481955	0.1950131947	0.0108286443
748.7550812242	0.2023309819	0.0108356132
750.3241254114	0.2025245012	0.0108142439
751.0625661804	0.1960771659	0.0107606899
752.4720039969	0.2164235823	0.0108757315
752.6194656501	0.2019068416	0.0107771592
755.1730259306	0.18428453	0.0106240397
755.8010813741	0.1922309766	0.010667781
755.8470529037	0.2071522302	0.0107658377
869.6238662703	0.1745152636	0.0075920822
869.897017839	0.1951711229	0.0076609338
871.3431896426	0.1948471966	0.0076471037
871.3563590553	0.1840436482	0.0076097925
871.4407815964	0.1985145002	0.0076588722
873.4654690944	0.1872986134	0.007602597
873.5285453509	0.1918894075	0.0076178144
874.4708999996	0.161560482	0.0075055574
875.2717617456	0.1838527816	0.0075750969
875.5214623878	0.1805540889	0.0075616334
875.994992324	0.1997335803	0.0076232295
876.4195003435	0.1780597524	0.0075453471
876.7158928422	0.1715065156	0.007520372
877.9120087059	0.1949674984	0.0075902967
879.7372034245	0.1575909616	0.007447091
880.0712460748	0.1665357788	0.0074747556
881.8404152084	0.1845595809	0.0075210761
883.8133837898	0.1718095409	0.007461008
992.9754902459	0.1544301934	0.0067473236

a-C:F system

perp. force	friction force	friction force error
3.30505848	1.46517512	0.09963467
3.30969479	1.65200954	0.09963467
3.29110307	1.52052323	0.09963467
3.29706956	1.46299342	0.09963467
3.27862910	1.70321512	0.09963467
3.32422317	1.76089629	0.09963467
3.30329833	1.89620377	0.09963467
3.31896968	1.69692972	0.09963467
3.27961012	1.76950339	0.09963467
3.04465938	1.79757308	0.08302889
3.01227375	1.86044603	0.08302889
3.01764768	1.96935658	0.08302889
3.03887120	1.97394972	0.08302889
3.01393352	1.86761432	0.08302889
3.02118616	2.02550991	0.08302889
3.01939238	1.71672265	0.08302889
3.02914075	1.83976149	0.08302889
3.04255825	1.74203338	0.08302889
2.93049109	1.70786294	0.08302889
2.92775639	1.64443836	0.08302889
2.90194534	1.62435186	0.08302889
2.90988847	1.68676661	0.08302889
2.90669128	1.88120231	0.08302889
2.93153865	1.60119430	0.08302889
2.92170618	1.70080302	0.08302889
2.89323425	1.54859341	0.08302889
2.90836243	1.72900642	0.08302889
2.72691480	1.46607101	0.08302889
2.73040379	1.58203862	0.08302889
2.71884261	1.53403536	0.08302889
2.70268236	1.61158518	0.08302889
2.70600933	1.60195080	0.08302889
2.68102982	1.35082124	0.08302889
2.68034269	1.44953799	0.08302889
2.68574164	1.59276333	0.08302889
2.70973097	1.74677604	0.08302889
2.69628661	1.70169288	0.08302889
2.70302036	1.58180567	0.08302889
2.70261512	1.68318014	0.08302889
2.70024258	1.29731340	0.08302889
2.69531802	1.42039626	0.08302889
2.71025247	1.60903509	0.08302889
2.70833558	1.56215341	0.08302889
2.68731267	1.38492933	0.08302889
2.71250163	1.49936603	0.08302889
2.37190276	1.28406864	0.08302889
2.35474277	1.39934090	0.08302889
2.38955010	1.30636717	0.08302889
2.34113595	1.41683018	0.08302889
2.35062800	1.23187485	0.08302889
2.34759475	1.24643818	0.08302889

perp. force	friction force	friction force error
2.36823907	1.28377225	0.08302889
2.37473046	1.45382992	0.08302889
2.35808489	1.21904955	0.08302889
2.01842433	1.08004295	0.05812023
2.00706143	1.17690478	0.05812023
2.01758009	1.28043272	0.05812023
2.02914123	1.10327703	0.05812023
1.99397392	1.16673709	0.05812023
2.00302588	1.00783478	0.05812023
2.00749376	1.05942267	0.05812023
1.99827322	1.01558713	0.05812023
2.02501011	1.16183391	0.05812023
1.64663737	1.18432280	0.04981734
1.68495324	1.21799531	0.04981734
1.66937089	1.52036761	0.04981734
1.66549693	0.99606273	0.04981734
1.66341624	1.15345856	0.04981734
1.62828545	0.99177424	0.04981734
1.67173642	1.13182380	0.04981734
1.67810159	0.86543805	0.04981734
1.67800099	1.19087753	0.04981734
1.49758369	0.96657632	0.04981734
1.50618666	0.96829035	0.04981734
1.50190531	1.00570527	0.04981734
1.53131584	1.10512254	0.04981734
1.49838405	1.08954323	0.04981734
1.49558586	1.04578074	0.04981734
1.52324590	1.01582311	0.04981734
1.50005897	1.23531426	0.04981734
1.50611424	1.27466846	0.04981734
1.32491556	0.96784539	0.04981734
1.33678012	1.00605181	0.04981734
1.30991801	1.17789856	0.04981734
1.31591101	0.99070217	0.04981734
1.28929041	1.08133435	0.04981734
1.29137511	0.99202319	0.04981734
1.31708496	1.04340204	0.04981734
1.29858763	1.18828326	0.04981734
1.30073374	1.02488328	0.04981734
1.19061220	1.27356367	0.04981734
1.19216151	1.10137168	0.04981734
1.20918803	1.35766414	0.04981734
1.19604553	1.09838149	0.04981734
1.21011681	1.11681563	0.04981734
1.17112045	0.94542636	0.04981734
1.20001296	1.16590247	0.04981734
1.18252851	1.31576671	0.04981734
1.19992686	1.16555341	0.04981734
1.02486505	0.95451095	0.04981734
1.00837177	0.93881986	0.04981734
1.02375105	1.35066816	0.04981734
1.02971938	1.10008743	0.04981734
1.01806545	1.02676754	0.04981734
0.99629201	1.00168445	0.04981734

perp. force	friction force	friction force error
1.02933731	1.12527402	0.04981734
0.99519631	1.13740437	0.04981734
1.01435638	1.05132093	0.04981734
0.82981242	1.12023103	0.04981734
0.85897576	1.08322645	0.04981734
0.87351140	1.11904224	0.04981734
0.83560430	0.94178293	0.04981734
0.83590640	0.97837417	0.04981734
0.85084873	1.11474235	0.04981734
0.87647366	1.07832776	0.04981734
0.85730471	1.17726470	0.04981734
0.84536996	0.93611377	0.04981734
0.68998061	1.00419239	0.04151445
0.69920683	0.92197428	0.04151445
0.71024655	0.84188553	0.04151445
0.68767786	0.86177413	0.04151445
0.68779286	0.79035547	0.04151445
0.72132876	1.03729779	0.04151445
0.70949201	0.85664378	0.04151445
0.68424077	0.80893698	0.04151445
0.69752878	0.87289062	0.04151445
0.50303170	0.75588955	0.04151445
0.52765496	0.84472285	0.04151445
0.55139598	0.69655863	0.04151445
0.52962049	0.89518287	0.04151445
0.50160565	0.93909404	0.04151445
0.52933369	0.69719770	0.04151445
0.51787542	0.83868017	0.04151445
0.51039480	0.87732454	0.04151445
0.53590124	0.77144340	0.04151445
0.36758425	0.99866583	0.04151445
0.35306253	0.85238774	0.04151445
0.30709238	0.80092241	0.04151445
0.36884382	0.96727363	0.04151445
0.34175902	0.83680432	0.04151445
0.34210199	0.86427740	0.04151445
0.34239267	0.69761804	0.04151445
0.35043695	0.69854676	0.04151445
0.35019365	0.69850965	0.04151445
0.17094730	0.69108828	0.04151445
0.16550727	0.79419029	0.04151445
0.18600191	0.78728929	0.04151445
0.19370262	0.69621446	0.04151445
0.17164194	0.61404318	0.04151445
0.16717932	0.83699549	0.04151445
0.21520233	0.59194951	0.04151445
0.16414853	0.68370143	0.04151445
0.16819007	0.87629999	0.04151445
0.05976829	0.72101561	0.05812023
0.07928484	0.73839343	0.05812023
0.08375904	0.77295402	0.05812023
0.07496307	0.78473209	0.05812023
0.06630206	0.77187075	0.05812023
0.08347113	0.75543104	0.05812023

perp. force	friction force	friction force error
0.08739273	0.74690751	0.05812023
0.07111982	0.76318336	0.05812023
0.09278302	1.14201501	0.05812023
0.03626310	0.78663866	0.05812023
0.00114175	0.77835175	0.05812023
0.04259448	0.65744641	0.05812023
0.03946428	0.78240212	0.05812023
0.01657426	0.84524216	0.05812023
0.03297841	0.96596924	0.05812023
0.04552970	0.88627066	0.05812023
0.04246258	0.73752810	0.05812023
0.05005032	0.87160913	0.05812023
0.00446902	0.78467135	0.04151445
-0.01642220	0.68190214	0.04151445
0.02329942	0.72164400	0.04151445
0.00846292	0.67135015	0.04151445
0.02012856	0.82205441	0.04151445
0.02365596	0.68724930	0.04151445
0.01242165	0.66750229	0.04151445
-0.01097402	0.76186468	0.04151445
0.02637346	0.73280378	0.04151445
0.00024468	0.67022876	0.04151445
0.01053858	0.88819442	0.04151445
0.00708656	0.67531147	0.04151445
0.00369381	0.69627400	0.04151445
0.00453233	0.70427429	0.04151445
0.00337818	0.83404217	0.04151445
-0.00368586	0.79549866	0.04151445
0.00018972	0.58380836	0.04151445
0.01032207	0.98879142	0.04151445
7.92093721	2.67065614	0.19511790
7.91737439	2.82394996	0.19511790
7.93233172	3.02086371	0.19511790
7.89587091	2.48016250	0.19511790
7.90864280	2.63013458	0.19511790
7.92572719	2.62727948	0.19511790
7.89096866	2.46138224	0.19511790
7.92781883	2.53915385	0.19511790
7.89204809	2.53956058	0.19511790
7.91291138	2.72543337	0.19511790
7.92310566	2.40193474	0.19511790
7.90507401	2.64089286	0.19511790
7.89109031	2.46045240	0.19511790
7.90921879	2.54779644	0.19511790
7.90843794	2.40917004	0.19511790
7.92723423	2.76607929	0.19511790
7.91377896	2.69113334	0.19511790
7.91048339	2.94309791	0.19511790
15.54138696	3.92829904	0.23248090
15.52317369	3.80712261	0.23248090
15.52702123	4.33818454	0.23248090
15.49159072	4.64702534	0.23248090
15.51714585	4.20357590	0.23248090
15.53445537	4.66766411	0.23248090

perp. force	friction force	friction force error
15.50834217	3.91408383	0.23248090
15.51298200	4.24482974	0.23248090
15.53615136	4.39394450	0.23248090
15.53930651	4.43951051	0.23248090
15.53920253	3.78201583	0.23248090
15.53509236	3.83985714	0.23248090
15.51505309	4.04846700	0.23248090
15.51929171	4.60505368	0.23248090
15.51760449	3.98697170	0.23248090
15.51896101	4.22687767	0.23248090
15.52553066	4.29235750	0.23248090
15.52190943	3.77159693	0.23248090
23.09090409	4.44659659	0.20757224
23.11384954	4.73772517	0.20757224
23.10843492	4.30763654	0.20757224
23.08198750	4.31589794	0.20757224
23.09344593	4.91627863	0.20757224
23.08382590	4.70612177	0.20757224
23.09319127	4.14642015	0.20757224
23.06456139	4.90022819	0.20757224
23.07897771	4.77715099	0.20757224
23.06191093	5.39979886	0.20757224
23.07465985	4.44023972	0.20757224
23.07398547	4.81875088	0.20757224
23.08149054	4.40047916	0.20757224
23.10220805	4.60905162	0.20757224
23.10409823	4.18753782	0.20757224
23.09015700	5.22860920	0.20757224
23.07153967	4.20396126	0.20757224
23.08003721	4.62513834	0.20757224
29.97840510	4.22824186	0.16605779
29.97528929	4.06949852	0.16605779
30.02287736	4.38698770	0.16605779
29.99259640	4.37814685	0.16605779
29.98525845	3.73909012	0.16605779
29.98609338	4.16235992	0.16605779
29.97746238	4.17263792	0.16605779
29.97786503	3.86927047	0.16605779
29.99258364	4.00967702	0.16605779
29.99672722	3.94774964	0.16605779
29.97352951	4.13400077	0.16605779
29.98799698	4.11909646	0.16605779
29.99760844	4.22097087	0.16605779
29.98045263	4.25380082	0.16605779
29.98640913	4.33289357	0.16605779
29.99598499	4.39619118	0.16605779
29.98685077	4.28342547	0.16605779
29.99576904	4.11625414	0.16605779

Computational results for varying cumulative average of the perpendicular force, all forces in nN.

SiO₂ system

perp. force	friction force	friction force error
2.05724137	2.24498758	0.18681501
1.63828253	2.13211996	0.16605779
1.65265781	2.22484820	0.16605779
1.65265781	2.22484820	0.16605779
1.65265781	2.22484820	0.16605779
1.65265781	2.22484820	0.16605779
1.65265781	2.22484820	0.16605779
1.65265781	2.22484820	0.16605779
1.65265781	2.22484820	0.16605779
1.20793670	2.32924141	0.03321156
1.20793670	2.32924141	0.03321156
1.20793670	2.32924141	0.03321156
1.20793670	2.32924141	0.03321156
1.20793670	2.32924141	0.03321156
1.20793670	2.32924141	0.03321156
1.20793670	2.32924141	0.03321156
1.20793670	2.32924141	0.03321156
1.20793670	2.32924141	0.03321156
1.20793670	2.32924141	0.03321156
1.20793670	2.32924141	0.03321156
0.83451020	1.88564681	0.05812023
0.83451020	1.88564681	0.05812023
0.83451020	1.88564681	0.05812023
0.83451020	1.88564681	0.05812023
0.83451020	1.88564681	0.05812023
0.83451020	1.88564681	0.05812023
0.83451020	1.88564681	0.05812023
0.83451020	1.88564681	0.05812023
0.83451020	1.88564681	0.05812023
0.83451020	1.88564681	0.05812023
0.43074846	2.01807073	0.02490867
0.43074846	2.01807073	0.02490867
0.43074846	2.01807073	0.02490867
0.43074846	2.01807073	0.02490867
0.43074846	2.01807073	0.02490867
0.43074846	2.01807073	0.02490867
0.43074846	2.01807073	0.02490867
0.43074846	2.01807073	0.02490867
0.43074846	2.01807073	0.02490867
0.43074846	2.01807073	0.02490867
0.20732013	1.68807082	0.04981734
0.20732013	1.68807082	0.04981734
0.20732013	1.68807082	0.04981734
0.21006864	1.79223653	0.04981734
0.21507856	1.87827681	0.04981734
0.20732013	1.68807082	0.04981734
0.20732013	1.68807082	0.04981734
0.20732013	1.68807082	0.04981734
0.20732013	1.68807082	0.04981734
0.20732013	1.68807082	0.04981734
0.20732013	1.68807082	0.04981734
0.08702404	1.82230475	0.03321156
0.08702404	1.82230475	0.03321156
0.08702404	1.82230475	0.03321156
0.08702404	1.82230475	0.03321156
0.08702404	1.82230475	0.03321156
0.08702404	1.82230475	0.03321156
0.08702404	1.82230475	0.03321156
0.08702404	1.82230475	0.03321156
0.08702404	1.82230475	0.03321156
0.08702404	1.82230475	0.03321156

perp. force	friction force	friction force error
10.27876703	5.05296651	0.07472600
20.46684809	8.29787626	0.06642312
20.50499535	8.25438148	0.06642312
20.47753817	8.34714676	0.06642312
20.44809131	8.16225278	0.06642312
20.44809131	8.16225278	0.06642312
20.44809131	8.16225278	0.06642312
20.46393844	8.04772235	0.06642312
20.46023763	8.23250546	0.06642312
20.44809131	8.16225278	0.06642312
20.44809131	8.16225278	0.06642312
20.44809131	8.16225278	0.06642312
20.48241670	8.22184485	0.06642312
20.47319921	8.14536776	0.06642312
20.48125757	8.13000367	0.06642312
20.44809131	8.16225278	0.06642312
20.44809131	8.16225278	0.06642312
20.44809131	8.16225278	0.06642312
30.65540607	11.02819121	0.09133178
30.62260322	10.98777834	0.09133178
30.62260322	10.98777834	0.09133178
30.62260322	10.98777834	0.09133178
30.62260322	10.98777834	0.09133178
30.62260322	10.98777834	0.09133178
30.62260322	10.98777834	0.09133178
30.63219190	10.97352044	0.09133178
30.62260322	10.98777834	0.09133178
30.62260322	10.98777834	0.09133178
30.62260322	10.98777834	0.09133178
30.66115502	10.95964552	0.09133178
30.62260322	10.98777834	0.09133178
30.62260322	10.98777834	0.09133178
30.62260322	10.98777834	0.09133178
30.62260322	10.98777834	0.09133178
30.62260322	10.98777834	0.09133178
30.66085696	11.00058229	0.09133178
30.62260322	10.98777834	0.09133178
30.62260322	10.98777834	0.09133178
40.69471088	13.25217593	0.10793756
40.69584647	13.22862033	0.10793756
40.69471088	13.42100476	0.10793756
40.67424931	13.38990855	0.10793756
40.71555649	13.25217593	0.10793756
40.69471088	13.25217593	0.10793756
40.69471088	13.25217593	0.10793756
40.69471088	13.25217593	0.10793756
40.69471088	13.25217593	0.10793756
40.69471088	13.35604383	0.10793756
40.72492089	13.25217593	0.10793756
40.69471088	13.32522555	0.10793756
40.71044670	13.25349477	0.10793756
40.69149071	13.25217593	0.10793756
40.69471088	13.25217593	0.10793756
40.69471088	13.25217593	0.10793756
40.69471088	13.41519004	0.10793756

perp. force	friction force	friction force error
40.70568793	16.60284534	0.10793756

Computational results for varying cumulative average of the perpendicular force, all forces in nN.

MIX system

perp. force	friction force	friction force error
-0.03330513	1.11380691	0.04981734
-0.01583731	0.95654743	0.04981734
-0.00264431	0.99494710	0.04981734
0.00000483	1.06608627	0.04981734
0.00001346	0.99090389	0.04981734
0.00061279	1.14237982	0.04981734
0.00184417	0.95992628	0.04981734
0.00318634	1.03253817	0.04981734
0.00647354	1.05486251	0.04981734
0.01231492	0.98635409	0.04981734
0.01812378	1.19105233	0.04981734
0.01870642	1.09050599	0.04981734
0.02022796	0.98295733	0.04981734
0.02031834	1.05276591	0.04981734
0.02568858	0.95496889	0.04981734
0.03183388	1.03738249	0.04981734
0.03394699	1.18202940	0.04981734
0.03963648	0.97471654	0.04981734
0.04225965	1.11411270	0.04981734
0.04792642	1.06784270	0.04981734
0.04891015	0.94637288	0.04981734
0.05823496	1.19875853	0.04981734
0.06231431	0.97316655	0.04981734
0.06232489	0.86472385	0.04981734
0.07268382	1.09350823	0.04981734
0.07372108	1.01839935	0.04981734
0.07794767	0.94215899	0.04981734
0.07909739	0.81289263	0.03736300
0.09526674	0.74306119	0.03736300
0.10093650	0.52143671	0.03736300
0.10681397	0.83931128	0.03736300
0.11192316	0.75777974	0.03736300
0.11687988	0.57838683	0.03736300
0.11899888	0.69001980	0.03736300
0.12777463	0.68781124	0.03736300
0.13702213	0.69782249	0.03736300
0.17697395	0.60024542	0.04981734
0.18229382	0.75161018	0.04981734
0.18354958	0.63330269	0.04981734
0.19501951	0.73627706	0.04981734
0.19643871	0.95025315	0.04981734
0.20252823	0.81647928	0.04981734

perp. force	friction force	friction force error
0.23035417	0.86525047	0.04981734
0.23968241	0.92746877	0.04981734
0.24053145	0.76167097	0.04981734
0.39287119	1.21019355	0.04566589
0.39829834	0.92475508	0.04566589
0.40701197	0.90152122	0.04566589
0.40876847	0.98084762	0.04566589
0.41074245	0.95908069	0.04566589
0.41142141	0.83061735	0.04566589
0.41270591	0.90937746	0.04566589
0.41396984	1.07307866	0.04566589
0.43111190	1.04158243	0.04566589
0.99713251	1.19476334	0.04151445
1.00386482	1.08989299	0.04151445
1.01537798	1.11258685	0.04151445
1.02142649	1.17480081	0.04151445
1.02322896	1.22218540	0.04151445
1.02662070	1.08916119	0.04151445
1.04244428	1.15837304	0.04151445
1.06109935	1.15837304	0.04151445
1.06648967	1.25776710	0.04151445
2.03351736	0.95858770	0.04151445
2.03650065	1.22424446	0.04151445
2.04094206	1.38885060	0.04151445
2.04238061	1.29106940	0.04151445
2.04801901	1.15921476	0.04151445
2.05142034	1.28868378	0.04151445
2.05392226	1.29106940	0.04151445
2.07473544	1.22187276	0.04151445
2.07827616	1.11593802	0.04151445
3.05210434	1.19040124	0.05812023
3.06395921	1.23986775	0.05812023
3.07037985	1.24365430	0.05812023
3.07340160	1.20524775	0.05812023
3.07916912	1.33280962	0.05812023
3.07977255	1.24365430	0.05812023
3.09022190	1.13896018	0.05812023
3.09279195	1.18906083	0.05812023
3.09298006	1.28143544	0.05812023
3.56344882	1.24375242	0.04981734
3.56456811	1.39140152	0.04981734
3.57049408	1.39140152	0.04981734
3.57054804	1.31427338	0.04981734
3.57089398	1.41774847	0.04981734
3.57919052	1.34075484	0.04981734
3.57944899	1.37371669	0.04981734
3.58331046	1.15784273	0.04981734
3.58659215	1.31880989	0.04981734
3.58761534	1.29551724	0.04981734
3.58955572	1.43390963	0.04981734
3.59129522	1.27893028	0.04981734
3.59250975	1.23227766	0.04981734
3.59741106	1.40275647	0.04981734
3.60489014	1.13619621	0.04981734

perp. force	friction force	friction force error
3.60625895	1.20114228	0.04981734
3.61350845	1.33381521	0.04981734
3.62159307	1.24444848	0.04981734
4.06656671	1.25600137	0.05562936
4.08728860	1.22178309	0.05562936
4.08745531	1.60575405	0.05562936
4.08752476	1.13810504	0.05562936
4.08856702	1.26680388	0.05562936
4.09315859	1.34490463	0.05562936
4.09358028	1.27659782	0.05562936
4.10240948	1.22178309	0.05562936
4.10461920	1.29704955	0.05562936
10.20439584	2.11159187	0.09133178
10.24627908	2.25165429	0.09133178
10.25279456	2.22316761	0.09133178
10.26792898	2.11159187	0.09133178
10.26792898	2.38494406	0.09133178
10.26792898	2.38494406	0.09133178
10.26792898	2.38494406	0.09133178
10.26792898	2.38494406	0.09133178
10.26792898	2.38494406	0.09133178
10.26792898	2.38494406	0.09133178
20.41089312	3.12425679	0.14114912
20.41515475	3.02028424	0.14114912
20.42601860	3.29986765	0.14114912
20.43856235	3.12425679	0.14114912
20.44715709	3.29900131	0.14114912
20.44725065	3.15133628	0.14114912
20.44725065	3.15133628	0.14114912
20.44725065	3.15133628	0.14114912
20.44725065	3.15133628	0.14114912
20.44725065	3.15133628	0.14114912
30.56613333	4.47038351	0.09133178
30.56839196	4.41940215	0.09133178
30.56958400	4.62750710	0.09133178
30.57230873	4.20503479	0.09133178
30.58887716	4.47038351	0.09133178
30.58887716	4.47038351	0.09133178
30.58887716	4.47038351	0.09133178
30.58887716	4.47038351	0.09133178
30.58887716	4.47038351	0.09133178
30.62829952	4.44857713	0.09133178
40.68910891	5.80853684	0.14114912
40.68910891	5.80853684	0.14114912
40.68910891	5.80853684	0.14114912
40.68910891	5.80853684	0.14114912
40.68910891	5.80853684	0.14114912
40.68910891	5.80853684	0.14114912
40.68910891	5.80853684	0.14114912
40.68910891	5.80853684	0.14114912
40.68910891	5.80853684	0.14114912
40.68910891	5.80853684	0.14114912

C.3. Varying Water Layer Thicknesses

Computational results for varying water layer thickness, standard amount is 0.75 monolayers per slab between the slabs, which means in total 1.5 monolayers between the slabs.

a-C:F system

	COF	COF error
no water	0.6665564096	0.039861284
	0.6610710162	0.0398272611
	0.6319527248	0.0398596597
	0.7211983632	0.0397964761
	0.6861865851	0.0394386935
	0.6721280012	0.0394630471
	0.6632556029	0.0396652105
	0.6096566938	0.0394258251
	0.6511734489	0.0397490085
	0.6616317813	0.0389625192
	0.6891927427	0.0398743258
	0.6547345159	0.0393651396
	0.5670902774	0.0397540961
	0.6628686972	0.0395839472
	0.6700177667	0.0394863524
	0.6854887708	0.0397890802
	0.6548256164	0.0392909915
0.6515589056	0.0401233007	
0.75 monolayers	0.2913953476	0.018658293
	0.2808359274	0.01861556
	0.2798729243	0.0187755987
	0.28983355	0.0187814448
	0.3235985747	0.0189958693
	0.2730979339	0.0185475129
	0.2910633236	0.0187124987
	0.2676232338	0.0187615054
	0.2972474133	0.0188338208
	0.2886809195	0.0187242049
	0.2861122602	0.0188221202
	0.2540775893	0.0184739329
	0.2386303603	0.0184762359
	0.3287582057	0.0189480361
	0.2744961691	0.0186030684
	0.3090934315	0.0189337798
	0.2918915403	0.0187175428
0.2841903179	0.0184442469	

	COF	COF error
1.5 monolayers	0.0155712339	0.002846878
	0.0188724688	0.0028368613
	0.0180940298	0.0028369127
	0.0131574658	0.0028381653
	0.014432784	0.002848467
	0.0188826386	0.0028480986
	0.0167048628	0.0028534529
	0.014034792	0.002860995
	0.0183593848	0.0028488703
	0.0130962106	0.0028316978
	0.0169502759	0.0028360999
	0.0190727166	0.0028440525
	0.015445833	0.0028611547
	0.0215515929	0.0028459042
	0.0196340396	0.0028536888
	0.0197284073	0.0028488381
	0.0139151365	0.0028447702
	0.0152624406	0.0028350647
4.5 monolayers	0.0080491102	0.0201960999
	0.0267608866	0.0202619326
	0.0592404365	0.0202619326
	0.0290655943	0.0204011895
	0.0101743007	0.0203727886
	0.014024892	0.0202968529
	0.018806514	0.0204322139
	0.0396796778	0.0201902548
	0.0361315327	0.0204759386
	0.0303417481	0.0202452729
	0.0216891718	0.0203570908
	0.0830273315	0.0203526351
	0.0166946827	0.0202923957
	0.0165962222	0.0203691761
	0.0385747457	0.0203686297
	0.025025399	0.0203763271
	0.0080491102	0.0201960999

Computational results for varying water layer thickness, standard amount is 0.75 monolayers per slab between the slabs, which means in total 1.5 monolayers between the slabs. In this case, for no water the commensurate slabs interlocked ideally, which resulted in an overflow of the friction force at the given COF, which is totally artificial.

SiO₂ system

	COF	COF error
no water	4.7385429479	0.8133053604
	4.7385429479	0.8133053604
	4.7385429479	0.8133053604
	4.7128428536	0.8088942947
	4.7385429479	0.8133053604
	4.7385429479	0.8133053604
	4.6804164849	0.803328757
	4.7385429479	0.8133053604
	4.7385429479	0.8133053604
	4.7385429479	0.8133053604
	4.7385429479	0.8133053604
	4.7385429479	0.8133053604
	4.7385429479	0.8133053604
	4.7385429479	0.8133053604
	4.7385429479	0.8133053604
	4.7385429479	0.8133053604
	0.75 monolayers	0.4337328051
0.4337328051		0.0100038771
0.4337328051		0.0100038771
0.4337328051		0.0100038771
0.4337328051		0.0100038771
0.4337328051		0.0100038771
0.4337328051		0.0100038771
0.4337328051		0.0100038771
0.4337328051		0.0100038771
0.4337328051		0.0100038771
0.4337328051		0.0100038771
0.4337328051		0.0100038771
0.4337328051		0.0100038771
0.4337328051		0.0100038771
0.4337328051		0.0100038771
0.4070498653		0.009964984
0.4337328051		0.0100038771
0.4337328051	0.0100038771	
0.4337328051	0.0100038771	
0.4337328051	0.0100038771	
0.4337328051	0.0100038771	
0.4337328051	0.0100038771	
0.4337328051	0.0100038771	
0.4337328051	0.0100038771	
0.4337328051	0.0100038771	
1.5 monolayers	0.0103942273	0.0011593325
	0.0103942273	0.0011593325
	0.0126478477	0.0011563917
	0.0143854629	0.0011679361
	0.0103942273	0.0011593325
	0.0103942273	0.0011593325

	COF	COF error
	0.0151949778	0.0011501092
	0.0145485141	0.0011451139
	0.0162768384	0.0011573374
	0.0103942273	0.0011593325
	0.0124565747	0.0011566298
	0.0120104078	0.0011538657
	0.0148664394	0.0011588551
	0.0151549746	0.0011577344
	0.0141809676	0.0011463539
	0.0123437523	0.0011582774
	0.0111418351	0.0011536999
	0.0103942273	0.0011593325

Computational results for varying water layer thickness, standard amount is 0.75 monolayers per slab between the slabs, which means in total 1.5 monolayers between the slabs.

MIX system

	COF	COF error
no water	0.7463524319	0.0229792922
	0.8718127728	0.023492427
	0.834823865	0.02352545
	0.8344708762	0.0235142779
	0.7643765665	0.0229096191
	0.7779068625	0.0230856988
	0.7789901262	0.0228323426
	0.8246382964	0.0231058554
	0.8820154041	0.0234668317
	0.8778904632	0.0233334416
	0.7502985694	0.0228650143
	0.806725515	0.023172129
	0.8229736946	0.0232264092
	0.8808265955	0.0236809276
	0.7927043552	0.0230742456
	0.7440451067	0.0227024762
	0.9067472503	0.0233492549
	0.8133871365	0.0231815737
0.75 monolayers	0.1872986134	0.007602597
	0.1985145002	0.0076588722
	0.1948471966	0.0076471037

	COF	COF error
	0.1951711229	0.0076609338
	0.1997335803	0.0076232295
	0.1805540889	0.0075616334
	0.1575909616	0.007447091
	0.1780597524	0.0075453471
	0.1718095409	0.007461008
	0.1840436482	0.0076097925
	0.1838527816	0.0075750969
	0.1949674984	0.0075902967
	0.1918894075	0.0076178144
	0.1845595809	0.0075210761
	0.1745152636	0.0075920822
	0.161560482	0.0075055574
	0.1665357788	0.0074747556
	0.1715065156	0.007520372
1.5 monolayers	0.0163020656	0.0014297234
	0.0150122154	0.0014303423
	0.0183070774	0.0014464241
	0.018403099	0.0014543407
	0.0157901588	0.0014480945
	0.0213794059	0.0014635089
	0.0180293256	0.001463032
	0.0166956674	0.0014540308
	0.016810377	0.0014504873
	0.0182288298	0.0014563811
	0.0177076284	0.0014470248
	0.018380343	0.0014587793
	0.0174448639	0.0014412996
	0.0161232862	0.001443675
	0.0170577102	0.0014564361
	0.0156238988	0.0014545442
	0.0186899175	0.001455183
	0.0169760644	0.0014467538

C.4. Varying Temperatures

Computational results for varying target average simulation temperature. μ^* is the normalized friction coefficient with respect to the average of the COF results at 298 K.

a-C:F system

temperature	COF	COF error	μ^*	
223	0.71215992	0.02426011	2.48786490	
	0.70194383	0.02422668	2.45217592	
	0.78919681	0.02468940	2.75698617	
	0.69331187	0.02440667	2.42202099	
	0.75630192	0.02442120	2.64207091	
	0.72878865	0.02424838	2.54595584	
	0.74623470	0.02438509	2.60690199	
	0.72517907	0.02406429	2.53334610	
	0.73221562	0.02434633	2.55792763	
	0.73746813	0.02431771	2.57627681	
	0.75905851	0.02448046	2.65170081	
	0.76065108	0.02455535	2.65726429	
	0.70503888	0.02398284	2.46298820	
	0.77170922	0.02460340	2.69589489	
	0.71805660	0.02431741	2.50846442	
	0.69475544	0.02420271	2.42706395	
	0.74828709	0.02444491	2.61407185	
	0.78054050	0.02460743	2.72674614	
	248	0.46877318	0.01885439	1.63761582
		0.44446903	0.01862735	1.55271149
0.44535405		0.01852070	1.55580324	
0.41927058		0.01871860	1.46468305	
0.43210499		0.01876475	1.50951886	
0.44229094		0.01880406	1.54510255	
0.46226882		0.01876110	1.61489342	
0.44726902		0.01875276	1.56249301	
0.43761411		0.01868224	1.52876447	
0.42959495		0.01874099	1.50075030	
0.43390942		0.01864068	1.51582247	
0.38386571		0.01881349	1.34099941	
0.44475524		0.01861352	1.55371134	
0.44518655		0.01859092	1.55521809	
0.42562228		0.01852758	1.48687211	
0.41873580		0.01876804	1.46281483	
0.42106803		0.01877315	1.47096228	
0.41687186		0.01872013	1.45630335	
273		0.36566570	0.02566681	1.27741934
		0.29694188	0.02567160	1.03733905
	0.28008082	0.02565644	0.97843647	
	0.32097649	0.02587899	1.12130174	
	0.31815143	0.02585628	1.11143263	
	0.32490826	0.02579029	1.13503701	

temperature	COF	COF error	μ^*
	0.35049422	0.02590617	1.22441920
	0.31328502	0.02573036	1.09443227
	0.32686255	0.02592121	1.14186414
	0.31494076	0.02588670	1.10021645
	0.28055130	0.02581580	0.98008006
	0.35288926	0.02589506	1.23278603
	0.32375001	0.02566726	1.13099076
	0.29901443	0.02560831	1.04457930
	0.30932822	0.02599540	1.08060955
	0.33757456	0.02581928	1.17928553
	0.28973374	0.02574430	1.01215806
	0.34478515	0.02567008	1.20447508
298	0.29139535	0.01865829	1.01796273
	0.28083593	0.01861556	0.98107437
	0.27987292	0.01877560	0.97771021
	0.28983355	0.01878144	1.01250674
	0.32359857	0.01899587	1.13046173
	0.27309793	0.01854751	0.95404241
	0.29106332	0.01871250	1.01680284
	0.26762323	0.01876151	0.93491705
	0.29724741	0.01883382	1.03840638
	0.28868092	0.01872420	1.00848013
	0.28611226	0.01882212	0.99950676
	0.25407759	0.01847393	0.88759659
	0.23863036	0.01847624	0.83363312
	0.32875821	0.01894804	1.14848643
	0.27449617	0.01860307	0.95892701
	0.30909343	0.01893378	1.07978935
	0.29189154	0.01871754	1.01969614
	0.28419032	0.01844425	0.99279263
323	0.20550672	0.01427771	0.71791874
	0.19989234	0.01432164	0.69830544
	0.18962157	0.01420178	0.66242543
	0.22345363	0.01442964	0.78061463
	0.18500584	0.01434333	0.64630082
	0.19696127	0.01422547	0.68806601
	0.23036674	0.01429766	0.80476495
	0.21125169	0.01440157	0.73798826
	0.23900198	0.01414129	0.83493134
	0.19858680	0.01439386	0.69374466
	0.22097964	0.01430300	0.77197195
	0.25597215	0.01431082	0.89421505
	0.17401262	0.01422290	0.60789702

temperature	COF	COF error	μ^*
	0.21720818	0.01418491	0.75879672
	0.18556425	0.01420529	0.64825155
	0.21428029	0.01443373	0.74856841
	0.22949393	0.01427344	0.80171585
	0.21837567	0.01442872	0.76287525
348	0.20898408	0.02173677	0.73006658
	0.18916024	0.02177470	0.66081384
	0.22950274	0.02190447	0.80174662
	0.23478822	0.02186950	0.82021097
	0.15207201	0.02136286	0.53124952
	0.20785234	0.02191062	0.72611294
	0.20086608	0.02173491	0.70170711
	0.18477236	0.02168418	0.64548516
	0.18886834	0.02174000	0.65979410
	0.20661347	0.02195005	0.72178509
	0.18149266	0.02162435	0.63402785
	0.19926102	0.02172618	0.69609996
	0.18994495	0.02159485	0.66355514
	0.18922423	0.02171643	0.66103737
	0.18883070	0.02149192	0.65966261
	0.18901124	0.02160334	0.66029331
	0.20111697	0.02184695	0.70258355
	0.25561398	0.02236974	0.89296381
373	0.18180878	0.01874850	0.63513218
	0.21352876	0.01877529	0.74594300
	0.22677085	0.01925188	0.79220301
	0.17031114	0.01879082	0.59496622
	0.20322443	0.01897469	0.70994579
	0.18784275	0.01893908	0.65621128
	0.21823237	0.01894765	0.76237462
	0.21287864	0.01912220	0.74367186
	0.20474293	0.01894375	0.71525050
	0.16984740	0.01883534	0.59334620
	0.19328159	0.01902230	0.67521139
	0.19303380	0.01896964	0.67434575
	0.19456918	0.01894732	0.67970945
	0.18732652	0.01889755	0.65440790
	0.15921690	0.01878103	0.55620955
	0.22218539	0.01921862	0.77618413
	0.18188549	0.01876112	0.63540016
	0.21007789	0.01925157	0.73388771

Computational results for varying target average simulation temperature. μ^* is the normalized friction coefficient with respect to the average of the COF results at 298 K.

SiO₂ system

temperature	COF	COF error	μ^*	
223	1.55466693	0.02325533	3.59740685	
	1.57038351	0.02335797	3.63377408	
	1.58656611	0.02344101	3.67121966	
	1.54217534	0.02327464	3.56850204	
	1.58554292	0.02360334	3.66885206	
	1.56702816	0.02328372	3.62600999	
	1.55466693	0.02325533	3.59740685	
	1.55466693	0.02325533	3.59740685	
	1.55723789	0.02322399	3.60335591	
	1.55650444	0.02346264	3.60165874	
	1.53900440	0.02317404	3.56116470	
	1.55466693	0.02325533	3.59740685	
	1.55466693	0.02325533	3.59740685	
	1.55345251	0.02335792	3.59459677	
	1.55466693	0.02325533	3.59740685	
	1.56140019	0.02327020	3.61298721	
	1.55466693	0.02325533	3.59740685	
	1.55466693	0.02325533	3.59740685	
	248	1.03636430	0.02200268	2.39808538
		1.03466991	0.02207350	2.39416466
1.05158084		0.02215976	2.43329555	
1.05158084		0.02215976	2.43329555	
1.05158084		0.02215976	2.43329555	
1.05158084		0.02215976	2.43329555	
1.05158084		0.02215976	2.43329555	
1.05158084		0.02215976	2.43329555	
1.05158084		0.02215976	2.43329555	
1.05158084		0.02215976	2.43329555	
1.05158084		0.02215976	2.43329555	
1.05158084		0.02215976	2.43329555	
1.05158084		0.02215976	2.43329555	
1.05158084		0.02215976	2.43329555	
1.05158084		0.02215976	2.43329555	
1.05158084		0.02215976	2.43329555	
1.05158084		0.02215976	2.43329555	
1.05158084		0.02215976	2.43329555	
1.04149877		0.02207133	2.40996623	
1.05158084		0.02215976	2.43329555	
1.05158084	0.02215976	2.43329555		
273	0.63773346	0.01372872	1.47567731	
	0.63773346	0.01372872	1.47567731	

temperature	COF	COF error	μ^*
	0.23029308	0.01593917	0.53288449
	0.21223625	0.01580356	0.49110206
	0.23459692	0.01611312	0.54284332
	0.25359460	0.01603495	0.58680282
	0.23459692	0.01611312	0.54284332
	0.21767667	0.01594996	0.50369088
	0.23459692	0.01611312	0.54284332
	0.23459692	0.01611312	0.54284332
	0.23459692	0.01611312	0.54284332
348	0.12790912	0.00767661	0.29597411
	0.12017352	0.00764066	0.27807439
	0.12095130	0.00764180	0.27987411
	0.12126042	0.00756028	0.28058940
	0.12758752	0.00765959	0.29522993
	0.13147692	0.00767077	0.30422977
	0.12095130	0.00764180	0.27987411
	0.12115473	0.00764931	0.28034484
	0.12095130	0.00764180	0.27987411
	0.12951610	0.00774235	0.29969256
	0.12095130	0.00764180	0.27987411
	0.13803232	0.00772338	0.31939858
	0.12691657	0.00773209	0.29367739
	0.12114429	0.00767595	0.28032068
	0.13069953	0.00765752	0.30243094
	0.13440111	0.00765347	0.31099617
	0.12095130	0.00764180	0.27987411
	0.13118541	0.00770700	0.30355524
373	0.03407741	0.00366915	0.07885309
	0.02844106	0.00362731	0.06581093
	0.02784479	0.00362913	0.06443120
	0.02784479	0.00362913	0.06443120
	0.02784479	0.00362913	0.06443120
	0.02784479	0.00362913	0.06443120
	0.03109091	0.00363361	0.07194251
	0.02784479	0.00362913	0.06443120
	0.02784479	0.00362913	0.06443120
	0.02784479	0.00362913	0.06443120
	0.02784479	0.00362913	0.06443120
	0.02784479	0.00362913	0.06443120
	0.03428978	0.00363017	0.07934451
	0.02784479	0.00362913	0.06443120
	0.02784479	0.00362913	0.06443120
	0.02784479	0.00362913	0.06443120

temperature	COF	COF error	μ^*
	0.02784479	0.00362913	0.06443120
	0.02784479	0.00362913	0.06443120

Computational results for varying target average simulation temperature. μ^* is the normalized friction coefficient with respect to the average of the COF results at 298 K.

MIX system

temperature	COF	COF error	μ^*
223	0.98602504	0.02071272	5.39765097
	1.02992965	0.02087442	5.63799149
	1.00673489	0.02060937	5.51101989
	1.01651151	0.02085427	5.56453858
	0.99753078	0.02072412	5.46063517
	1.02033061	0.02093111	5.58544491
	1.01478478	0.02100882	5.55508617
	1.02039233	0.02095583	5.58578276
	0.97077155	0.02079355	5.31415110
	1.02325132	0.02099880	5.60143333
	1.00006600	0.02074088	5.47451333
	1.01346407	0.02083506	5.54785641
	1.01223305	0.02074995	5.54111764
	0.98893434	0.02072460	5.41357697
	0.97694670	0.02058361	5.34795477
	1.01682955	0.02093386	5.56627958
1.03086837	0.02095401	5.64313022	
1.01611499	0.02062593	5.56236794	
248	0.60984766	0.01434831	3.33839884
	0.57831973	0.01425242	3.16581012
	0.60477080	0.01461028	3.31060732
	0.59241534	0.01424133	3.24297164
	0.59808302	0.01445076	3.27399740
	0.59109072	0.01429699	3.23572047
	0.60163868	0.01434371	3.29346159
	0.60035119	0.01419492	3.28641369
	0.58350422	0.01421084	3.19419080
	0.56396883	0.01415631	3.08725113
	0.58931848	0.01422605	3.22601896
	0.58395714	0.01422082	3.19667019
0.60503895	0.01423811	3.31207522	

temperature	COF	COF error	μ^*
	0.58263710	0.01429949	3.18944407
	0.60183462	0.01439181	3.29453420
	0.63544741	0.01448480	3.47853575
	0.62909969	0.01443909	3.44378736
	0.60560895	0.01449962	3.31519545
273	0.30090232	0.01144897	1.64718506
	0.27547749	0.01135569	1.50800569
	0.28628949	0.01132221	1.56719222
	0.28775227	0.01138507	1.57519970
	0.27756141	0.01135133	1.51941337
	0.28089532	0.01134463	1.53766367
	0.26832385	0.01126811	1.46884554
	0.27773999	0.01140892	1.52039092
	0.27093623	0.01132229	1.48314611
	0.27737836	0.01134289	1.51841130
	0.26927529	0.01126712	1.47405389
	0.29147327	0.01139954	1.59556899
	0.29227195	0.01142585	1.59994109
	0.28347866	0.01134453	1.55180528
	0.28582976	0.01150253	1.56467558
	0.26205249	0.01132752	1.43451516
	0.28365110	0.01140506	1.55274925
	0.31170463	0.01161551	1.70631856
298	0.18729861	0.00760260	1.02530109
	0.19851450	0.00765887	1.08669856
	0.19484720	0.00764710	1.06662318
	0.19517112	0.00766093	1.06839640
	0.19973358	0.00762323	1.09337199
	0.18055409	0.00756163	0.98838054
	0.15759096	0.00744709	0.86267689
	0.17805975	0.00754535	0.97472616
	0.17180954	0.00746101	0.94051155
	0.18404365	0.00760979	1.00748292
	0.18385278	0.00757510	1.00643808
	0.19496750	0.00759030	1.06728173
	0.19188941	0.00761781	1.05043179
	0.18455958	0.00752108	1.01030721
	0.17451526	0.00759208	0.95532309
	0.16156048	0.00750556	0.88440664
	0.16653578	0.00747476	0.91164218
	0.17150652	0.00752037	0.93885275
323	0.16139120	0.00889691	0.88347998
	0.12482964	0.00876258	0.68333641

temperature	COF	COF error	μ^*
	0.13785253	0.00873920	0.75462573
	0.13866468	0.00879442	0.75907157
	0.12608503	0.00866737	0.69020864
	0.13456089	0.00878779	0.73660675
	0.13257891	0.00867950	0.72575709
	0.12679862	0.00869944	0.69411494
	0.13892884	0.00873132	0.76051761
	0.12428005	0.00868367	0.68032788
	0.13082589	0.00868242	0.71616084
	0.13750129	0.00870667	0.75270297
	0.15146671	0.00884931	0.82915177
	0.15403289	0.00882574	0.84319944
	0.13936677	0.00880172	0.76291490
	0.12899929	0.00869269	0.70616173
	0.11869207	0.00866245	0.64973844
	0.14629311	0.00880987	0.80083071
348	0.08895051	0.00687619	0.48692861
	0.08678421	0.00692761	0.47506997
	0.09232965	0.00690771	0.50542655
	0.09159914	0.00684891	0.50142760
	0.08144923	0.00681561	0.44586547
	0.08832531	0.00688425	0.48350620
	0.08282889	0.00692623	0.45341793
	0.09857912	0.00690464	0.53963708
	0.08195528	0.00676259	0.44863567
	0.08056472	0.00679429	0.44102355
	0.08514506	0.00691121	0.46609702
	0.08832425	0.00694066	0.48350038
	0.08180131	0.00681085	0.44779280
	0.07061135	0.00676620	0.38653725
	0.09049762	0.00694703	0.49539774
	0.06500857	0.00680487	0.35586678
	0.07841245	0.00684613	0.42924169
	0.08000710	0.00682470	0.43797104
373	0.04968424	0.00781470	0.27197911
	0.04154003	0.00785769	0.22739644
	0.06222447	0.00786430	0.34062621
	0.06236617	0.00788302	0.34140191
	0.05887528	0.00791472	0.32229222
	0.06222099	0.00791719	0.34060714
	0.04405985	0.00772865	0.24119031
	0.04410501	0.00776436	0.24143753
	0.07050664	0.00790434	0.38596405

temperature	COF	COF error	μ^*
	0.05534485	0.00776980	0.30296613
	0.05177059	0.00781798	0.28340007
	0.04538464	0.00779473	0.24844244
	0.05094092	0.00783981	0.27885834
	0.06516738	0.00789694	0.35673617
	0.04744472	0.00770621	0.25971963
	0.05131432	0.00771872	0.28090239
	0.04678485	0.00784579	0.25610737
	0.05343189	0.00780700	0.29249429

C.5. Varying Relative Velocities

Computational results for varying virtual spring velocity, resulting in a variation of the relative velocities of the slabs. Relative velocity given as v/v_0 .

a-C:F system

rel. velocity	COF	COF error
0.01	0.21327253	0.01487529
	0.22751931	0.01489427
	0.25405338	0.01513106
	0.26509626	0.01523770
	0.25295375	0.01504485
	0.23449395	0.01506103
	0.26314159	0.01525542
	0.24208936	0.01504851
0.05	0.27863503	0.01517818
	0.25465034	0.02975434
	0.33770644	0.03017647
	0.25456791	0.02983814
	0.21989040	0.02991160
	0.23261439	0.02947849
	0.27238126	0.03005581
	0.32444237	0.02991704
0.1	0.24819764	0.02996189
	0.29042079	0.03002590
	0.22299027	0.02193983
	0.26187742	0.02221455
	0.32498124	0.02233665

rel. velocity	COF	COF error
	0.29850986	0.02230287
	0.35984660	0.02251790
	0.23863843	0.02226194
	0.29838669	0.02230251
	0.29327216	0.02212049
	0.33618131	0.02238289
0.2	0.13477531	0.01763349
	0.22160163	0.01798841
	0.32529028	0.01829608
	0.18768571	0.01796754
	0.15080596	0.01786905
	0.18583221	0.01778585
	0.16463245	0.01785097
	0.17295982	0.01802739
	0.15125780	0.01775226
0.3	0.25163997	0.02980074
	0.27384526	0.03007948
	0.28723540	0.03058692
	0.25799643	0.03022648
	0.25634232	0.03005497
	0.26776069	0.03010074
	0.24687264	0.03012214
	0.22785934	0.03030241
	0.30890991	0.03028804
0.4	0.22488131	0.01803487
	0.21284794	0.01814501
	0.18882686	0.01777366
	0.22806068	0.01789823
	0.17845695	0.01790991
	0.21934134	0.01803327
	0.20220231	0.01796414
	0.19632096	0.01790036
	0.22088626	0.01806884
0.5	0.21937350	0.02266378
	0.24709719	0.02275957
	0.21609466	0.02258718
	0.23848364	0.02254736
	0.27990502	0.02303455
	0.22482006	0.02249832
	0.23372128	0.02257833
	0.20956557	0.02258963
	0.25415353	0.02270462
0.6	0.23269864	0.02267634

rel. velocity	COF	COF error
	0.29478709	0.02304692
	0.25252661	0.02288806
	0.25558521	0.02323232
	0.23934197	0.02258775
	0.26850435	0.02285860
	0.31885056	0.02291972
	0.24550331	0.02249388
	0.25912021	0.02285901
0.7	0.25418046	0.02270341
	0.24616586	0.02269504
	0.23590265	0.02266796
	0.25618351	0.02289263
	0.28488612	0.02290147
	0.26049240	0.02280546
	0.22829638	0.02284708
	0.26764069	0.02272426
	0.31446561	0.02308004
0.8	0.23797879	0.01814713
	0.20362417	0.01787962
	0.23541343	0.01814296
	0.26215824	0.01841837
	0.21308994	0.01813983
	0.23713848	0.01814559
	0.22610794	0.01814026
	0.23745248	0.01820004
	0.23250880	0.01812149
0.9	0.25359917	0.01830759
	0.27358139	0.01828822
	0.25404207	0.01816506
	0.25576066	0.01815779
	0.25265971	0.01819286
	0.23134609	0.01848441
	0.23259418	0.01817719
	0.23012015	0.01827001
	0.27186854	0.01830621
1	0.29139535	0.01865829
	0.28083593	0.01861556
	0.27987292	0.01877560
	0.28983355	0.01878144
	0.32359857	0.01899587
	0.27309793	0.01854751
	0.29106332	0.01871250
	0.26762323	0.01876151

rel. velocity	COF	COF error
	0.29724741	0.01883382
	0.28868092	0.01872420
	0.28611226	0.01882212
	0.25407759	0.01847393
	0.23863036	0.01847624
	0.32875821	0.01894804
	0.27449617	0.01860307
	0.30909343	0.01893378
	0.29189154	0.01871754
	0.28419032	0.01844425

Computational results for varying virtual spring velocity, resulting in a variation of the relative velocities of the slabs. In this case, due to interlocking of the commensurate slabs and water molecule pinning, at relative velocities below 0.1 v_0 no meaningful results were obtained. Relative velocity given as v/v_0 .

SiO₂ system

rel. velocity	COF	COF error
0.1	0.34270299	0.01382010
	0.34277066	0.01383153
	0.34277066	0.01383153
	0.34277066	0.01383153
	0.34277066	0.01383153
	0.34277066	0.01383153
	0.34277066	0.01383153
	0.34277066	0.01383153
	0.34277066	0.01383153
0.2	0.33069486	0.02958534
	0.33069486	0.02958534
	0.33069486	0.02958534
	0.33069486	0.02958534
	0.33069486	0.02958534
	0.33069486	0.02958534
	0.33069486	0.02958534
	0.33069486	0.02958534
	0.33069486	0.02958534
0.3	0.36302168	0.03040923
	0.37709892	0.03030032
	0.29919127	0.02996568

rel. velocity	COF	COF error
	0.29919127	0.02996568
	0.29919127	0.02996568
	0.36235882	0.03019020
	0.29919127	0.02996568
	0.29919127	0.02996568
	0.29919127	0.02996568
0.4	0.35066863	0.02420490
	0.35066863	0.02420490
	0.35066863	0.02420490
	0.35066863	0.02420490
	0.35066863	0.02420490
	0.35066863	0.02420490
	0.35066863	0.02420490
	0.35066863	0.02420490
	0.35066863	0.02420490
	0.35066863	0.02420490
0.5	0.33790117	0.02894570
	0.33790117	0.02894570
	0.33790117	0.02894570
	0.33790117	0.02894570
	0.33790117	0.02894570
	0.33790117	0.02894570
	0.33790117	0.02894570
	0.33790117	0.02894570
	0.33790117	0.02894570
	0.33790117	0.02894570
0.6	0.26786320	0.01822114
	0.26786320	0.01822114
	0.26786320	0.01822114
	0.26786320	0.01822114
	0.26786320	0.01822114
	0.26786320	0.01822114
	0.26786320	0.01822114
	0.26786320	0.01822114
	0.26786320	0.01822114
	0.26786320	0.01822114
0.7	0.39844345	0.03037175
	0.39844345	0.03037175
	0.39844345	0.03037175
	0.39844345	0.03037175
	0.32736176	0.03007507
	0.39844345	0.03037175
	0.39844345	0.03037175
	0.39844345	0.03037175
	0.39844345	0.03037175
0.8	0.36012191	0.02400101

rel. velocity	COF	COF error
0.01	0.05947199	0.02015353
	0.09676320	0.02017256
	0.07585046	0.02020966
	0.07595448	0.02023797
	0.04755227	0.02002391
	0.07874510	0.01999315
	0.05349002	0.01991982
	0.08014649	0.01993694
	0.07451723	0.02026640
0.05	0.05344444	0.01756410
	0.07787566	0.01763683
	0.07275915	0.01762834
	0.07336188	0.01777714
	0.06483183	0.01750719
	0.04856845	0.01758216
	0.04149759	0.01761940
	0.06425663	0.01777572
	0.06359561	0.01773769
0.1	0.03139880	0.00951116
	0.06820751	0.00965249
	0.03462279	0.00949777
	0.03474266	0.00953135
	0.07206794	0.00959084
	0.06256569	0.00964016
	0.05428241	0.00951094
	0.05117680	0.00954929
	0.06345950	0.00957311
0.2	0.08261201	0.01434537
	0.08668534	0.01433246
	0.05267784	0.01415233
	0.05243236	0.01408512
	0.04858343	0.01415521
	0.07938610	0.01429010
	0.09132367	0.01435809
	0.06268949	0.01435029
	0.11503879	0.01446685
0.3	0.07932454	0.00777953
	0.09220796	0.00777642
	0.09011104	0.00778845
	0.08979608	0.00776016
	0.08251310	0.00782288
	0.08783390	0.00786250

rel. velocity	COF	COF error
	0.08944931	0.00778879
	0.08782139	0.00782183
	0.11621890	0.00806868
0.4	0.11374904	0.00969821
	0.09848912	0.00970170
	0.08564000	0.00957403
	0.08544820	0.00955193
	0.11030070	0.00964488
	0.11179096	0.00959564
	0.09798435	0.00956206
	0.10304801	0.00954251
	0.12691243	0.00967005
0.5	0.12118380	0.00852311
	0.12380237	0.00854239
	0.12010497	0.00849873
	0.12188286	0.00863168
	0.12773709	0.00860769
	0.12518261	0.00861954
	0.12733936	0.00860144
	0.13765709	0.00861380
	0.12518706	0.00859444
0.6	0.12632497	0.00779640
	0.12656326	0.00778666
	0.17145885	0.00801092
	0.17191612	0.00803516
	0.13448954	0.00778397
	0.13113672	0.00785427
	0.12796523	0.00773263
	0.16439024	0.00800212
	0.10284715	0.00761772
0.7	0.15247833	0.01165215
	0.12506682	0.01158210
	0.15463352	0.01146096
	0.15593771	0.01156212
	0.16898068	0.01157202
	0.17258675	0.01170176
	0.15746312	0.01153657
	0.17350828	0.01173476
	0.14605680	0.01157242
0.8	0.16611506	0.00704975
	0.14655037	0.00703149
	0.14884063	0.00709037
	0.14891615	0.00709431

rel. velocity	COF	COF error
	0.17213164	0.00712002
	0.15009219	0.00708064
	0.14625147	0.00705401
	0.16547250	0.00714491
	0.16706828	0.00703720
0.9	0.17477723	0.00890264
	0.19812772	0.00902036
	0.19159650	0.00903672
	0.18970025	0.00893863
	0.17691100	0.00890478
	0.20004896	0.00902701
	0.18977034	0.00898951
	0.19869712	0.00895002
	0.18609607	0.00901936
1	0.18729861	0.00760260
	0.19851450	0.00765887
	0.19484720	0.00764710
	0.19517112	0.00766093
	0.19973358	0.00762323
	0.18055409	0.00756163
	0.15759096	0.00744709
	0.17805975	0.00754535
	0.17180954	0.00746101
	0.18404365	0.00760979
	0.18385278	0.00757510
	0.19496750	0.00759030
	0.19188941	0.00761781
	0.18455958	0.00752108
	0.17451526	0.00759208
	0.16156048	0.00750556
	0.16653578	0.00747476
	0.17150652	0.00752037
